AD-A072 426 DELAWARE UNIV NEWARK CENTER FOR COMPOSITE MATERIALS F/G 13/5
DESIGN OF THE SPAR-WINGSKIN JOINT.(U)
MAR 79 R D COPE, R B PIPES F33615-77-C-3132

UNCLASSIFIED AFFDL-TR-79-3015 NL

| OF
AD
A072426

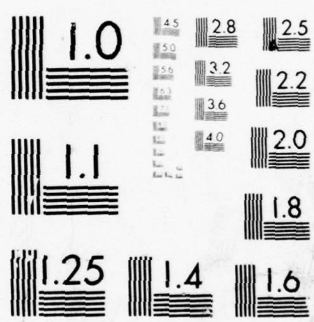
1.0
4.5
5.0
5.6
6.3
2.8
3.2
3.6
4.0
2.5
2.2
2.0
1.1
1.8
1.25
1.4
1.6

AFFDL-TR-79-3015

DESIGN OF THE SPAR-WINGSKIN JOINT

Center for Composite Materials
University of Delaware
Newark, Delaware 19711

March 1979

Technical Report AFFDL-TR-79-3015
Final Report for period 1 September 1977 to 15 December 1978

Approved for public release; Distribution unlimited

Air Force Flight Dynamics Laboratory
Air Force Wright Aeronautical Laboratory
Air Force Systems Command
Wright-Patterson Air Force Base, Ohio 45433

NOTICE

When Government drawings, specifications, or other data are used for any purpose other than in connection with a definitely related Government procurement operation, the United States Government thereby incurs no responsibility nor any obligation whatsoever; and the fact that the Government may have formulated, furnished, or in any way supplied the said drawings, specifications, or other data, is not to be regarded by implication or otherwise as in any manner licensing the holder or any other person or corporation, or conveying any rights or permission to manufacture, use, or sell any patented invention that may in any way be related thereto.

This report has been reviewed by the Information Office (IO) and is releasable to the National Technical Information Service (NTIS). At NTIS, it will be available to the general public, including foreign nations.

This technical report has been reviewed and is approved for publication.

Billy L. White

BILLY L. WHITE
Project Engineer

Francis J. Janik Jr.

FRANCIS J. JANIK, JR., Chief
Structural Concepts Branch
Structures and Dynamics Division

FOR THE COMMANDER

Ralph L Kuster Jr

RALPH L. KUSTER, JR., Col, USAF
Chief, Structures and Dynamics Division
Air Force Flight Dynamics Laboratory

Copies of this report should not be returned unless return is required by security considerations, contractual obligations, or notice on a specific document.

AIR FORCE/56780/5 June 1979 — 100

SECURITY CLASSIFICATION OF THIS PAGE (When Data Entered)

REPORT DOCUMENTATION PAGE

READ INSTRUCTIONS BEFORE COMPLETING FORM

1. REPORT NUMBER: AFFDL-TR-79-3015	2. GOVT ACCESSION NO.
	3. RECIPIENT'S CATALOG NUMBER
4. TITLE (and Subtitle): DESIGN OF THE SPAR-WINGSKIN JOINT.	5. TYPE OF REPORT & PERIOD COVERED: FINAL REPORT. Sept. 1977 – Dec. 1978
	6. PERFORMING ORG. REPORT NUMBER
7. AUTHOR(s): Ralph D. Cope, R. Byron Pipes	8. CONTRACT OR GRANT NUMBER(s): F33615-77-C-3132
9. PERFORMING ORGANIZATION NAME AND ADDRESS: Center for Composite Materials, University of Delaware, Newark, Delaware 19711	10. PROGRAM ELEMENT, PROJECT, TASK AREA & WORK UNIT NUMBERS: 188p.
11. CONTROLLING OFFICE NAME AND ADDRESS: Air Force Flight Dynamics Laboratory, Structures Division, Wright-Patterson AFB, OH 45433	12. REPORT DATE: March 1979
	13. NUMBER OF PAGES: 174
14. MONITORING AGENCY NAME & ADDRESS (if different from Controlling Office)	15. SECURITY CLASS. (of this report): Unclassified
	15a. DECLASSIFICATION/DOWNGRADING SCHEDULE

16. DISTRIBUTION STATEMENT (of this Report)

Distribution Unlimited 2401 03

17. DISTRIBUTION STATEMENT (of the abstract entered in Block 20, if different from Report)

18. SUPPLEMENTARY NOTES

19. KEY WORDS (Continue on reverse side if necessary and identify by block number)

EMBEDDED SPAR, FINITE ELEMENT MODELING, OUT-OF-PLANE JOINT, SPAR-WINGSKIN JOINT

20. ABSTRACT (Continue on reverse side if necessary and identify by block number)

A variety of spar-wingskin joint concepts have been investigated to optimize out-of-plane strength while still providing low weight and ease of fabrication. The spar-wingskin configuration consists of a thin spar which overlaps and is co-cured perpendicular to a thick wingskin. Investigation parameters were the joint geometry in the immediate vicinity of the base of the spar, and the spar-to-spar spacing. It was found that by varying the overlap geometry and decreasing the interspar spacing, a significant

DD FORM 1 JAN 73 1473 EDITION OF 1 NOV 65 IS OBSOLETE

410 035

(continued over)

SECURITY CLASSIFICATION OF THIS PAGE (When Data Entered)

20. (continued)

increase in out-of-plane strength could be realized. A theoretical analysis was made by the extended use of the finite element technique. Joint strength was predicted through the application of Tsai-Wu and maximum stress failure criteria. These results were verified by comparison to experimental results in which all significant concepts were fabricated and tested.

FOREWARD

The work reported herein was sponsored by the Air Force Flight Dynamics Laboratory, Structures Division, Wright-Patterson Air Force Base, Ohio under contract F33615-77-C-3132. The program title was Advanced Composite Design Program and the Project number was 24010301. Mr. Bill White (AFFDL/FBS) was the project engineer and the work was performed during the period from 1 September 1977 to 15 December 1978. Initial report submission date was 25 January 1979. The contractor was the University of Delaware, Center for Composite Materials, Newark, Delaware. The principal investigators were Ralph D. Cope and Dr. R. Byron Pipes.

The authors would like to thank Mr. J. W. Gillespie, Mr. Joseph J. Quigley IV, Mr. Richard Walsh, Ms. T. K. Moon and Mr. J. K. Faye for their guidance and assistance throughout the program.

TABLE OF CONTENTS

Table of Contents (concluded)

LIST OF ILLUSTRATIONS

List of Illustrations (continued)

List of Illustrations (continued)

List of Illustrations (continued)

List of Illustrations (continued)

List of Illustrations (concluded)

LIST OF TABLES

CHAPTER I

INTRODUCTION

Although the use of unidirectional lamina in the construction of multidirectional laminates provides the designer with a unique ability to tailor the in-plane strength and stiffness of the laminate, the out-of-plane properties are difficult to adjust and are severely limited by the properties of the matrix phase. The low strength and stiffness in the matrix dominated laminate directions poses a significant problem for the designer and often necessitates the use of mechanically fastened joints in situations where out-of-plane load carrying members are required. Unfortunately, such joints require penetration through the original laminate. These penetrations significantly reduce the load carrying capacity of the laminate and may also result in more rapid deterioration of laminate properties when the structure is subjected to a harsh environment. For these reasons, the need for investigation of out-of-plane joints utilizing no mechanical fasteners is of great importance. Typical requirements for such a joint are high strength, ease of fabrication, reduced number of parts, low weight, and environmental stability.

The objective of the research recorded in this report was to quantitatively evaluate the influence of local joint geometry on the properties of a typical out-of-plane joint. Laminates and dimensions have been chosen to match those used by Gillespie and Pipes [1] and model the prototype spar-wingskin joint in the General Dynamics F-16 aircraft. All joint geometries were analyzed by finite element methods with theoretical predictions validated through comparison to experimental data.

CHAPTER II

JOINT GEOMETRY AND LOADING

2.1 General Joint Description

All joint concepts investigated consisted of a 24 ply, $[(\pm 45)_6]_s$ spar which overlapped, 12 plies on each side of the centerline, and was co-cured perpendicular to a 56 ply $[(\pm 45/90_2)(0/\pm 45/0)_6]_s$ wingskin laminate with the enclosed void filled by an adhesive. All laminates were fabricated of graphite-epoxy material (Hercules, Inc., AS3501-6) with Reliable Manufacturing, Inc. Reliabond 398 used as the adhesive for the insert at the base of the spar. The 0° ply direction is taken parallel to the spar in the plane of the laminate and, for all included figures, lies normal to the joint cross-section.

All joint concepts investigated can be termed "no-insert". This implies that a suitable epoxy, as opposed to a metallic insert, has been used to fill the void created at the base of the spar between the overlap and the wingskin. The use of an epoxy filler provides the following advantages:

- Raw material is relatively inexpensive
- Insert is easy to manufacture (machine or extrude)
- Insert requires no extensive surface preparation

- Insert is thermally compatible with the graphite-epoxy material system

2.2 Specific Joint Concepts

Five joint concepts were chosen for investigation and are shown schematically in figures 1 through 5. Concept "A" (Figure 1) employed a 0.64 cm (0.25 in) radius at the base of the spar and provided the lower bound for geometries having a smooth, radial transition from the vertical spar to the horizontal wingskin. Concept "B" (Figure 2) was chosen as the upper bound for radial geometries and employed a 1.27 cm (0.50 in) fillet radius. The third concept, "C", shown in Figure 3, was constructed using an insert of equilateral triangular cross-section and an apex angle of 90°. The height of the triangle was 1.27 cm (0.50 in) and the base was 2.54 cm (1.00 in) in length. This concept differed from concept "B" in that the radius of curvature of the overlap from the apex of the insert to the overlap-wingskin contact point was greatly increased while maintaining approximately the same distances from overlap-wingskin contact point to overlap-wingskin contact point. Both the fourth concept, "D", (Figure 4) and concept "C" utilized straight overlap sections of approximately equal lengths in joining the spar to the wingskin. However, concept "D" possessed a height-to-base ratio of 2.4 compared to a value of 0.5 for concept "C". The final configuration, concept "E" (Figure 5), had no insert and employed a 90° angle at the junction between the spar and the overlap. Although this concept could not be fabricated, it was evaluated analytically. Concept "E" differed from the

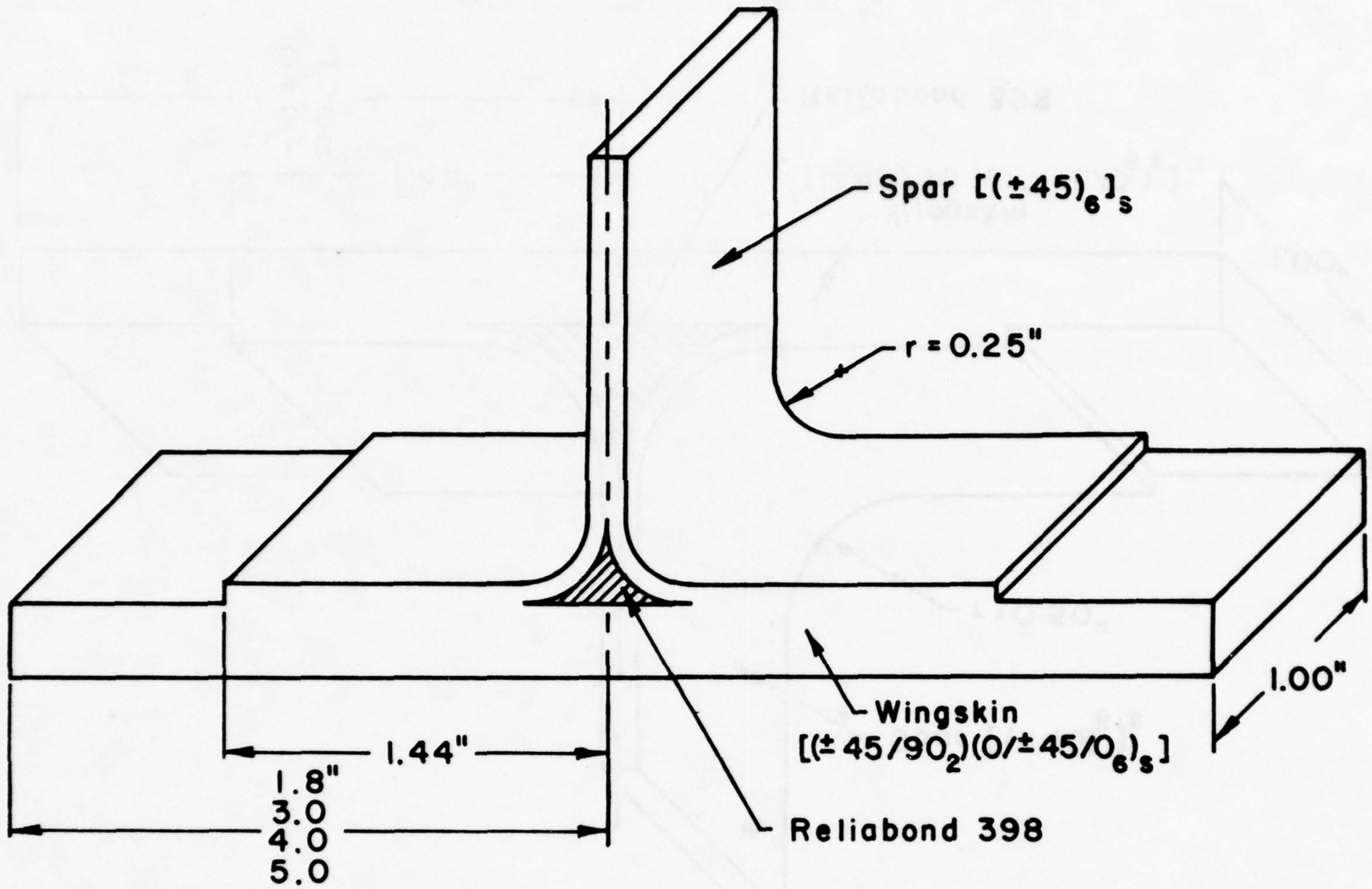

Figure 1: Schematic of Concept "A"

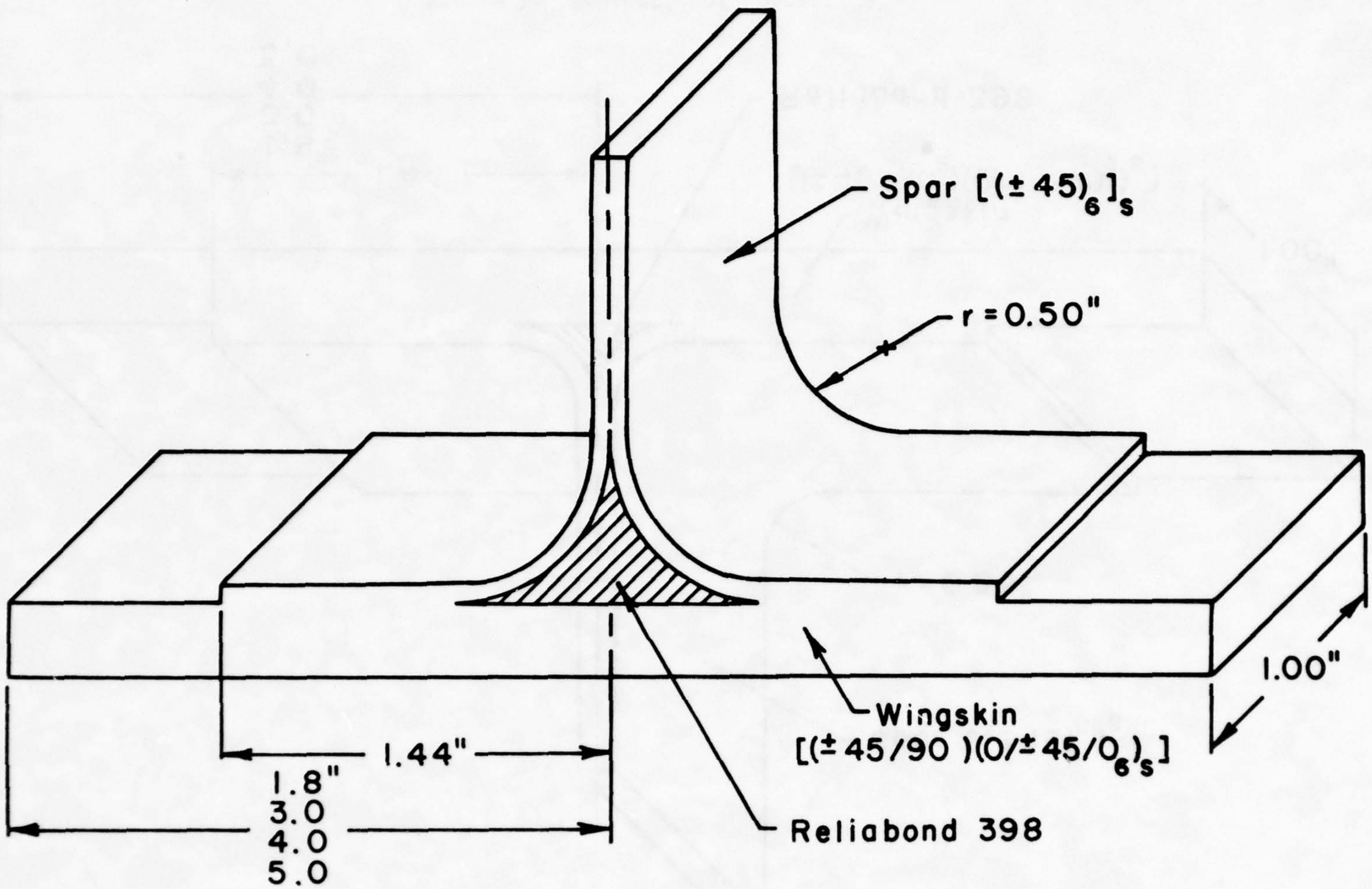

Figure 2: Schematic of Concept "B"

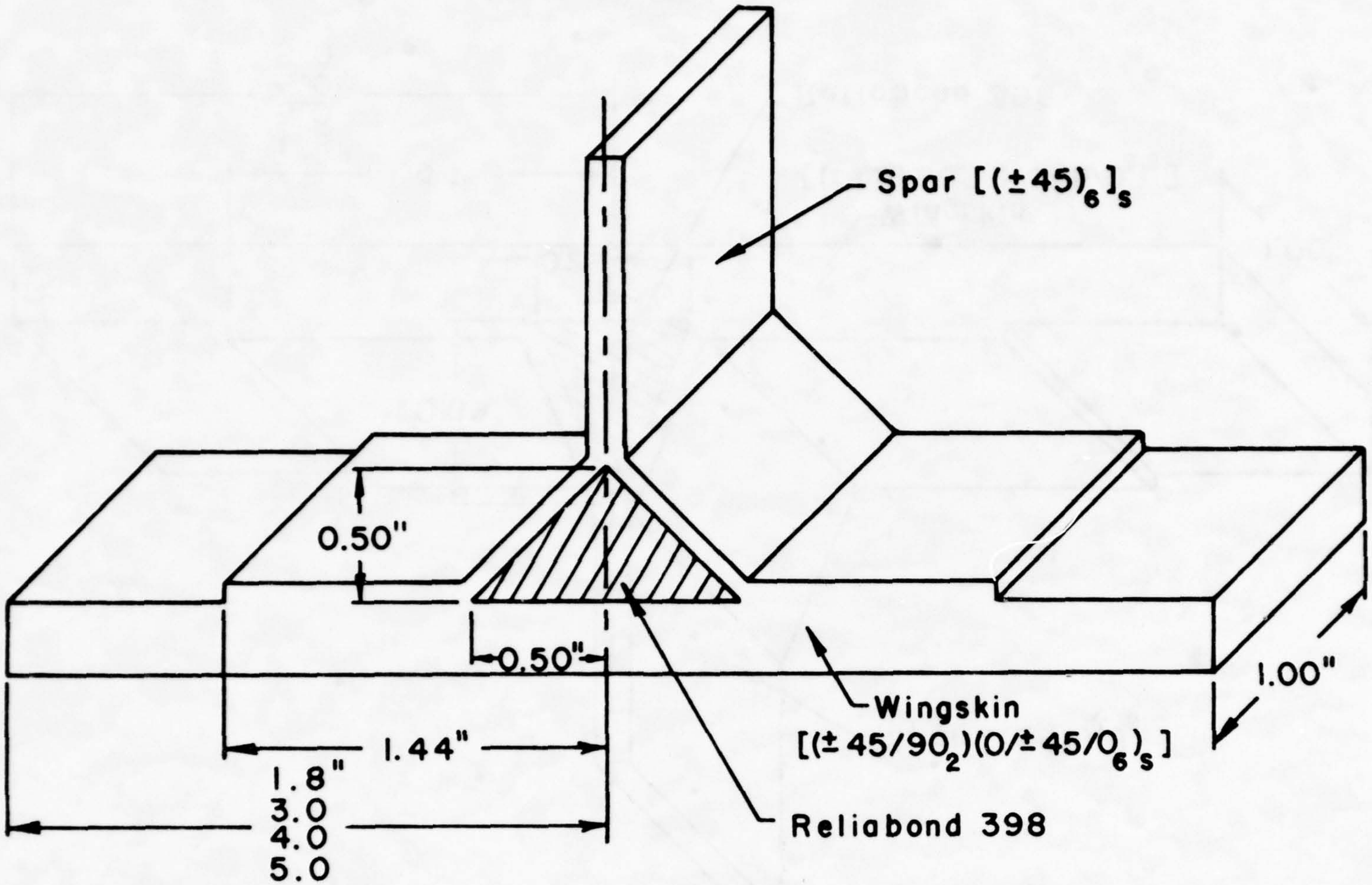

Figure 3: Schematic of Concept "C"

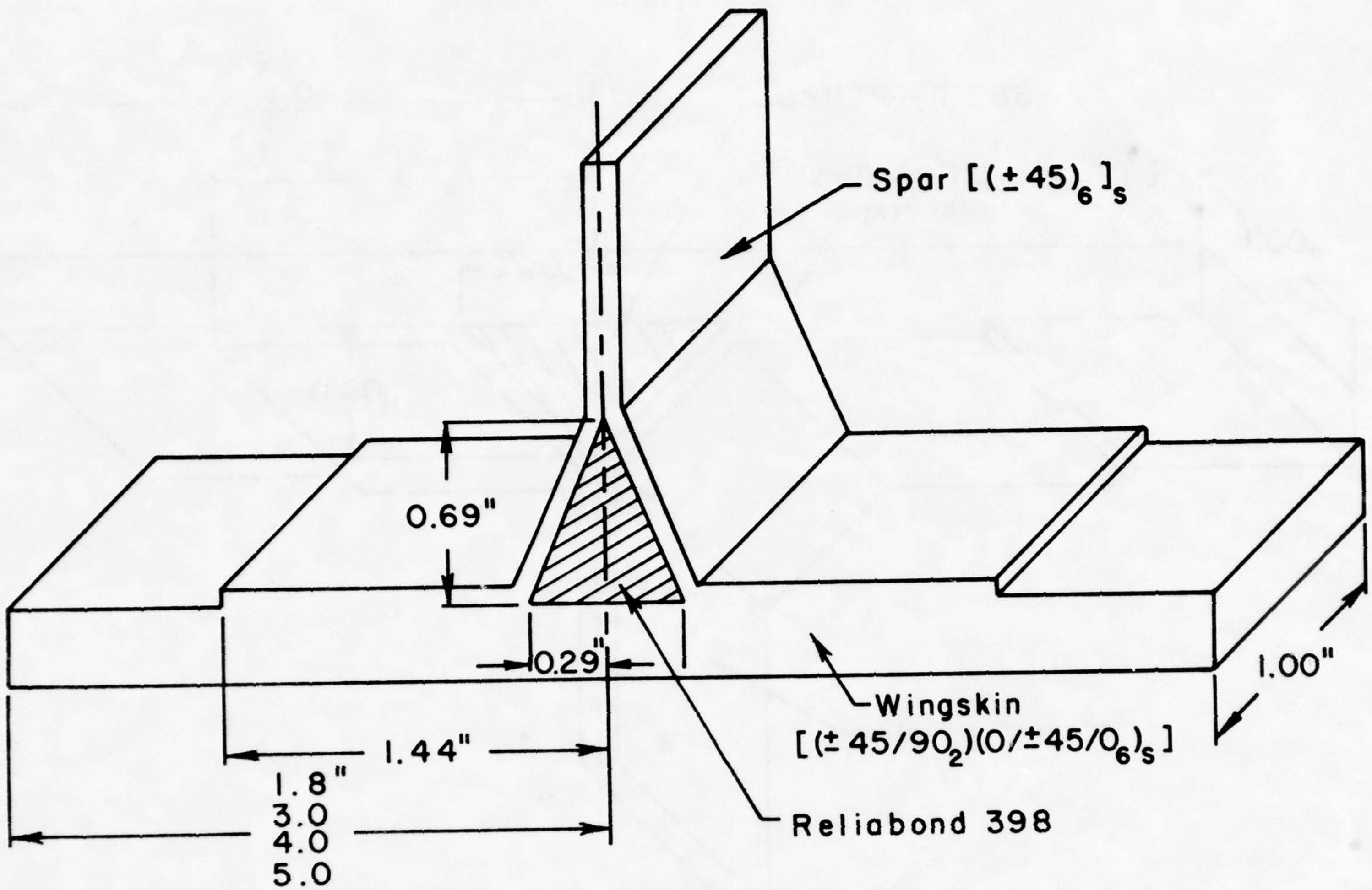

Figure 4: Schematic of Concept "D"

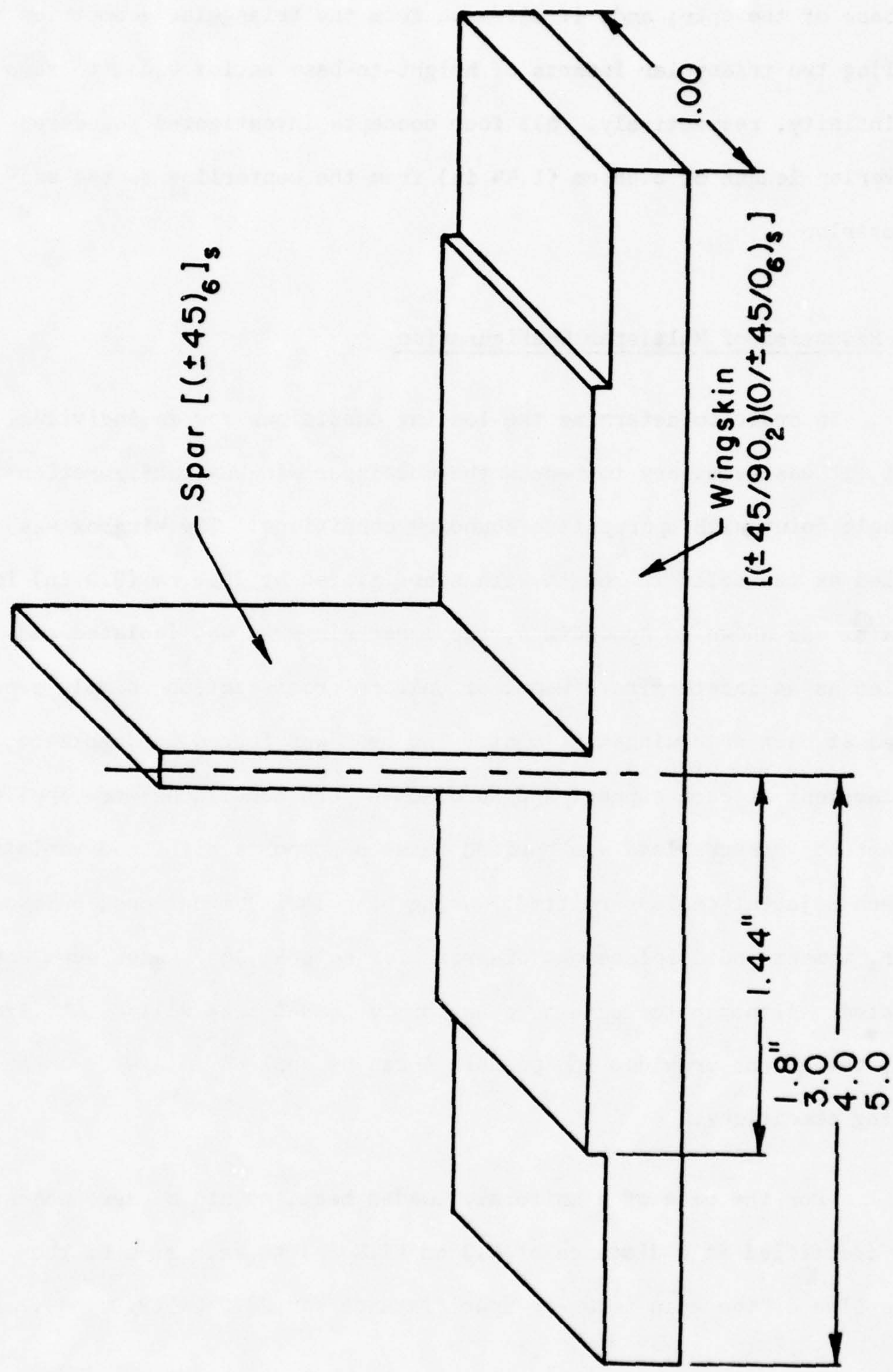

Figure 5: Schematic of Concept "E"

radial joint geometries in that it provided a geometry of zero radius at the base of the spar; and, it differed from the triangular geometries by modeling two triangular inserts of height-to-base ratios equal to zero and infinity, respectively. All four concepts investigated possessed an overlap length of 3.66 cm (1.44 in) from the centerline to the end of the overlap.

2.3 Reduction of Multispar Configuration

In order to determine the loading conditions for an individual joint, it was necessary to reduce the multispar wingbox configuration to a single joint with appropriate boundary conditions. The wingbox was modeled as ten cells in length with spars placed at 20.3 cm (8.0 in) intervals. As shown in Appendix A, the lower wingskin was isolated and modeled as an indeterminate beam, of uniform cross-section, simply supported at each spar-wingskin joint. The beam was forced through zero displacement at each support and zero moment end conditions were applied. A constant pressure load was applied between supports with load variation between adjacent cells permitted. Using singularity functions, pressure, shear, moment and displacement diagrams for several load cases were constructed. Although the case of a uniformly loaded beam will be utilized here, the graphs provided in Appendix A can be applied to a wide array of loading conditions.

For the case of a uniformly loaded beam, points of zero moment were identified at a distance of 4.3 cm (1.7 in) to each side of the centerline of the spar (spar-to-spar distance was 20.3 cm (8.0 in)). The shear load at these points was determined to be 2.2 times the applied pressure.

2.4 Joint Loading Conditions

The experimental loading conditions for each joint concept consisted of two simple supports applied at the top of the wingskin and positioned symmetrically about the spar, with a tensile load applied through the spar (see Figure 6). The span length or distance between simple supports was chosen as a test parameter. As indicated in the preceding section, the span length in this study is analogous to the distance between points of zero moment in the wingskin of a pressurized wingbox. Span lengths analyzed were 9.1 (3.6), 15.2 (6.0), 20.3 (8.0) and 25.4 cm (10.0 in) which correspond to spar-to-spar distances of 21.5 (8.5), 35.9 (14.1), 47.8 (18.8) and 59.8 cm (23.5 in), respectively. The first of these spans was chosen to be identical to that used by Gillespie and Pipes [1] and is representative of the actual F-16 prototype wing while the other three spans provide a significant range for investigation.

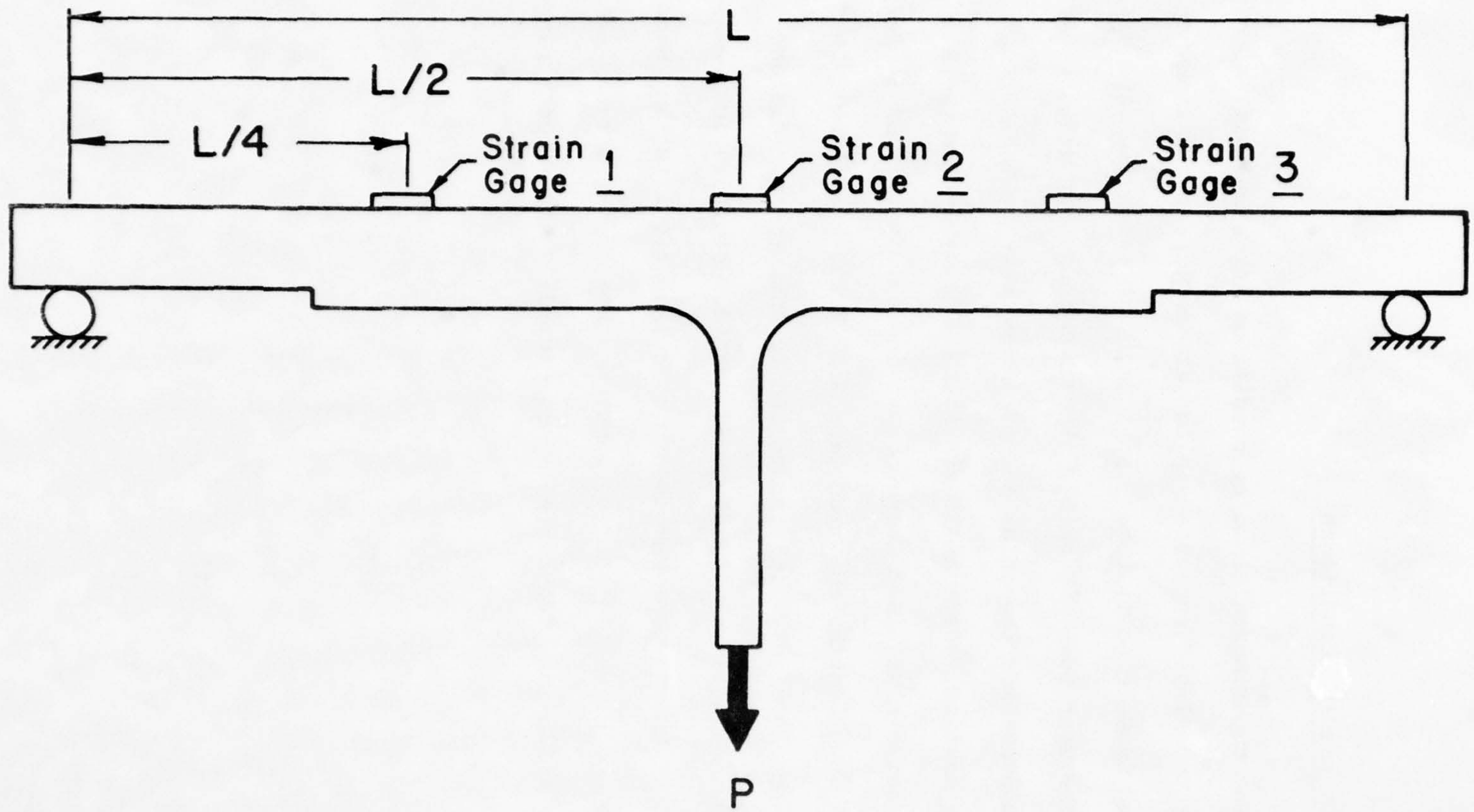

Figure 6: Schematic of Test Apparatus

CHAPTER III

FINITE ELEMENT MODELING

3.1 Finite Element Method

The theoretical evaluation of each concept was accomplished through the use of a linear-elastic finite element analysis. The finite element computer program utilized was the structural analysis program, SAP V [2]. A two-dimensional, four-node, quadrilateral element with orthotropic material properties was employed; and, a plane stress analysis was chosen in order to decouple the in-plane displacements and stresses due to wing flexural and torsional loads from the same due to internal pressure loads. The intrinsic bandwidth minimization routine was utilized to reduce solution time and computer costs.

3.2 Development of Finite Element Mesh

As a result of the symmetry of the joint, it was possible to model one half of the structure, as shown in Figure 7. The conditions of symmetry were enforced by fixing all horizontal displacements along the left side of the model or centerline of the joint, and fixing all vertical displacements at the top of the spar. Loading conditions for a given span length were modeled by applying downward point-loads on the top surface of the wingskin at a distance of half the span length from

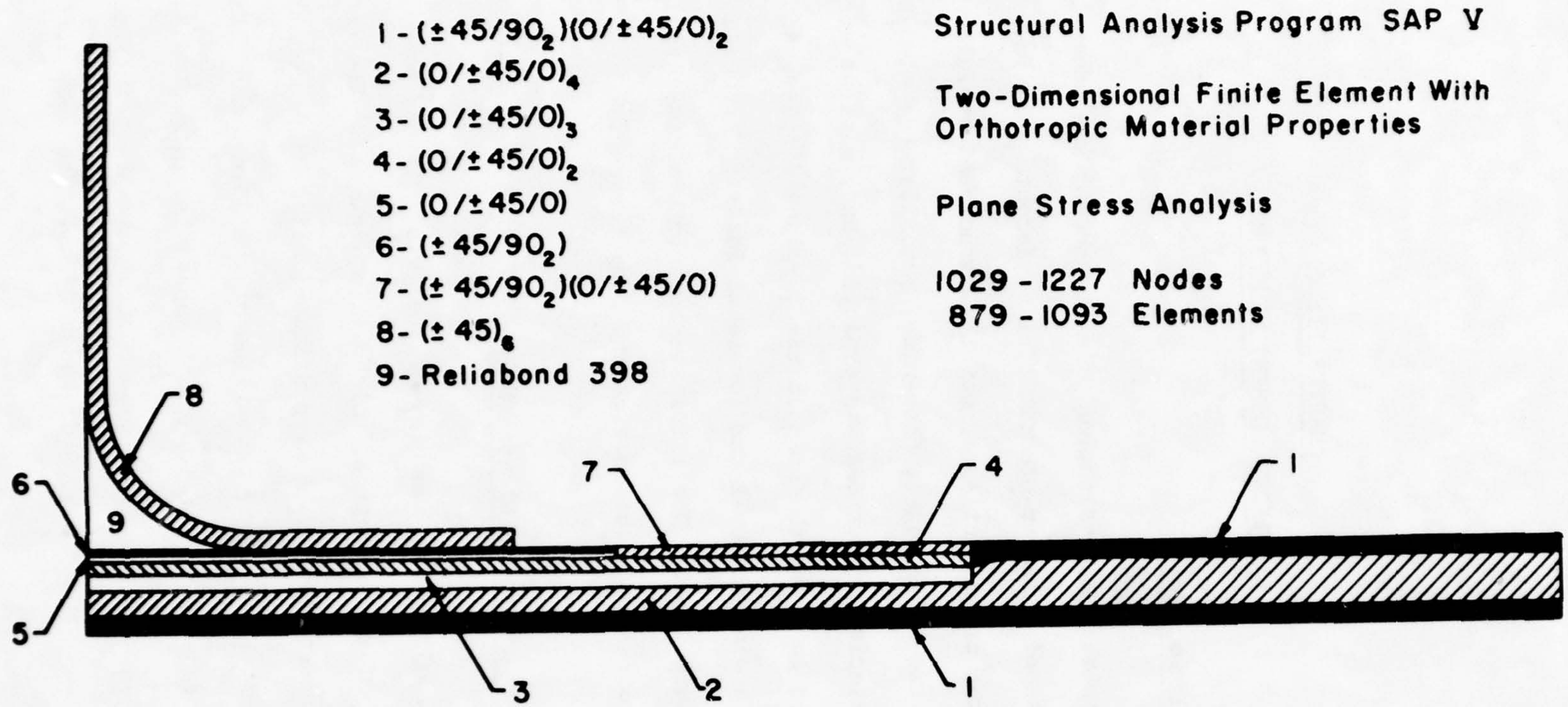

Figure 7: Schematic of Finite Element Mesh

the spar centerline.

The wingskin, common to all concepts, was modeled as a multi-layered laminate consisting of seven sublaminates as illustrated in Figure 7. An eighth sublaminate was used to model the spar, and the adhesive insert was modeled as an isotropic material. Determination of material properties for all sublaminates and the insert is contained in Appendix B.

Complete finite element meshes for each joint concept, shown in Figures 8 through 12, consisted of approximately 1100 nodes and 900 elements. Specific node and element totals are given as follows:

Concept A	1076 Nodes	931 Elements
Concept B	1167 Nodes	1035 Elements
Concept C	1227 Nodes	1094 Elements
Concept D	1167 Nodes	1030 Elements
Concept E	1029 Nodes	879 Elements

Using a single ply thickness of 0.013 cm (0.005 in), obtained from fabricated specimen measurements, each row of elements represented a minimum of four and a maximum of sixteen plies. Four ply thickness was used for regions in the immediate vicinity of the spar and overlap and sixteen ply thickness was allowed near the midplane of the wingskin at the right end of the mesh. Surfaces of the wingskin were modeled using elements of smaller height as compared to elements near the laminate midplane in order to more accurately represent the flexural stiffness of the wingskin. As can be seen in the mesh enlargements, triangular elements were

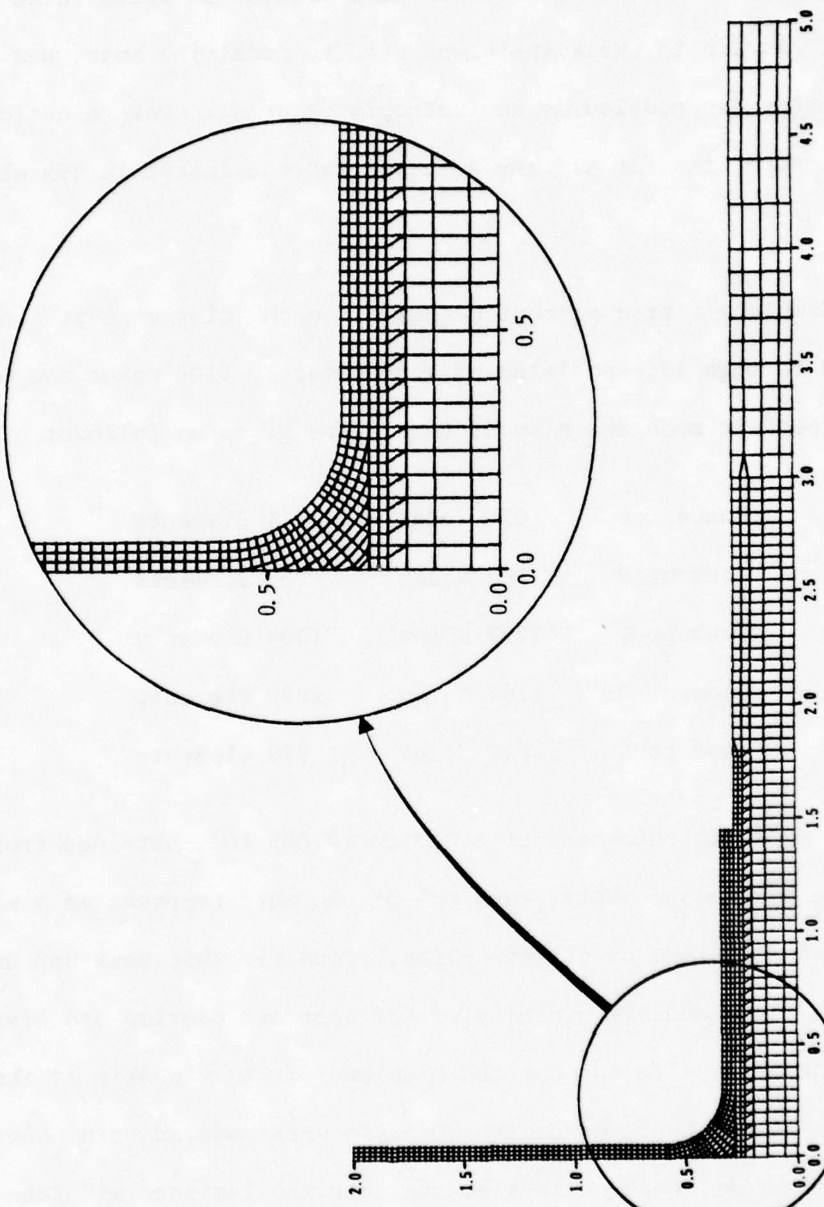

Figure 8: Finite Element Mesh for Concept "A"

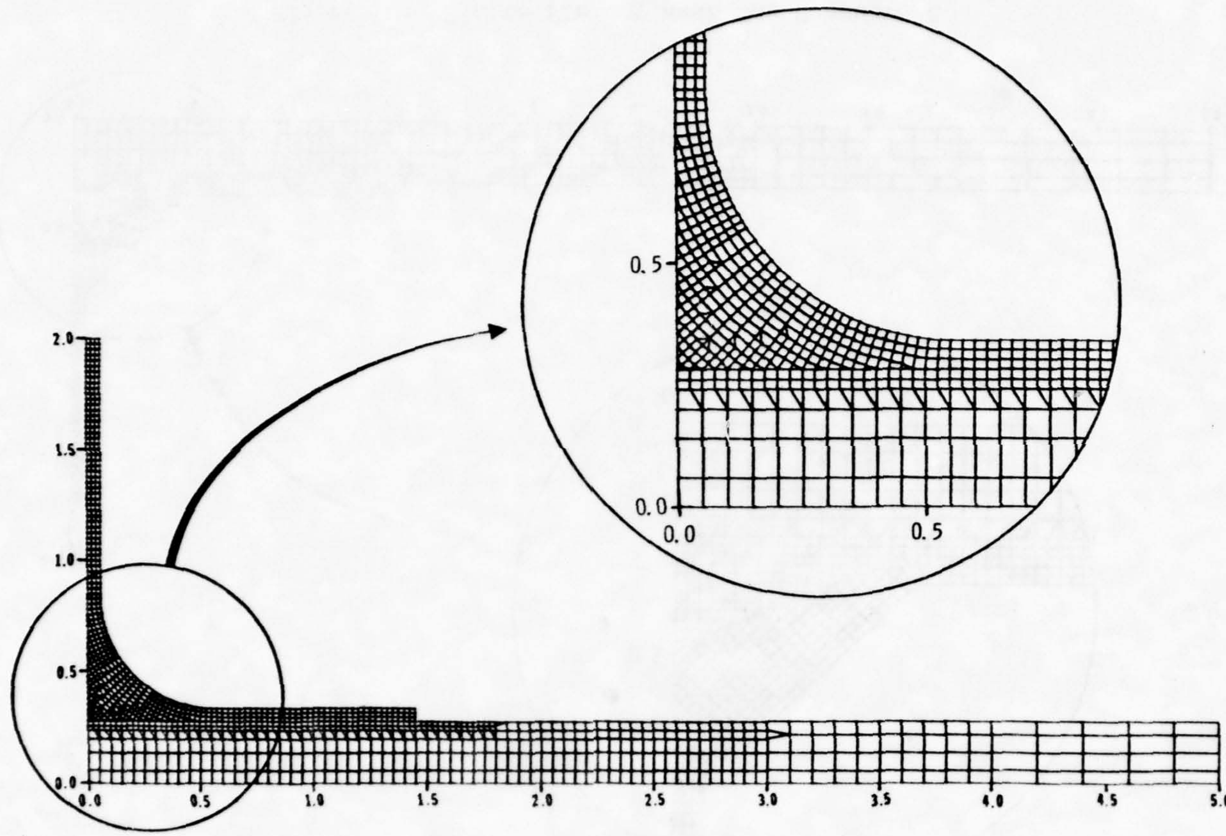

Figure 9: Finite Element Mesh for Concept "B"

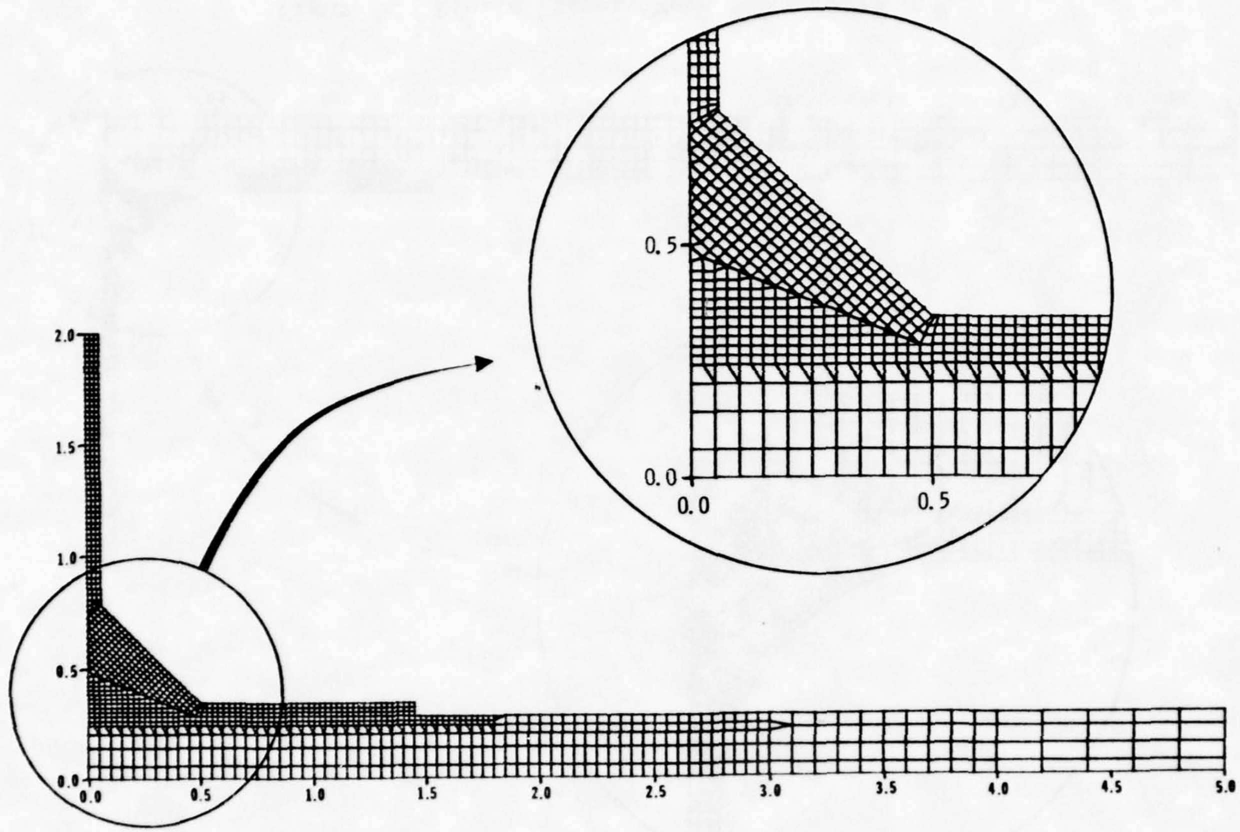

Figure 10: Finite Element Mesh for Concept "C"

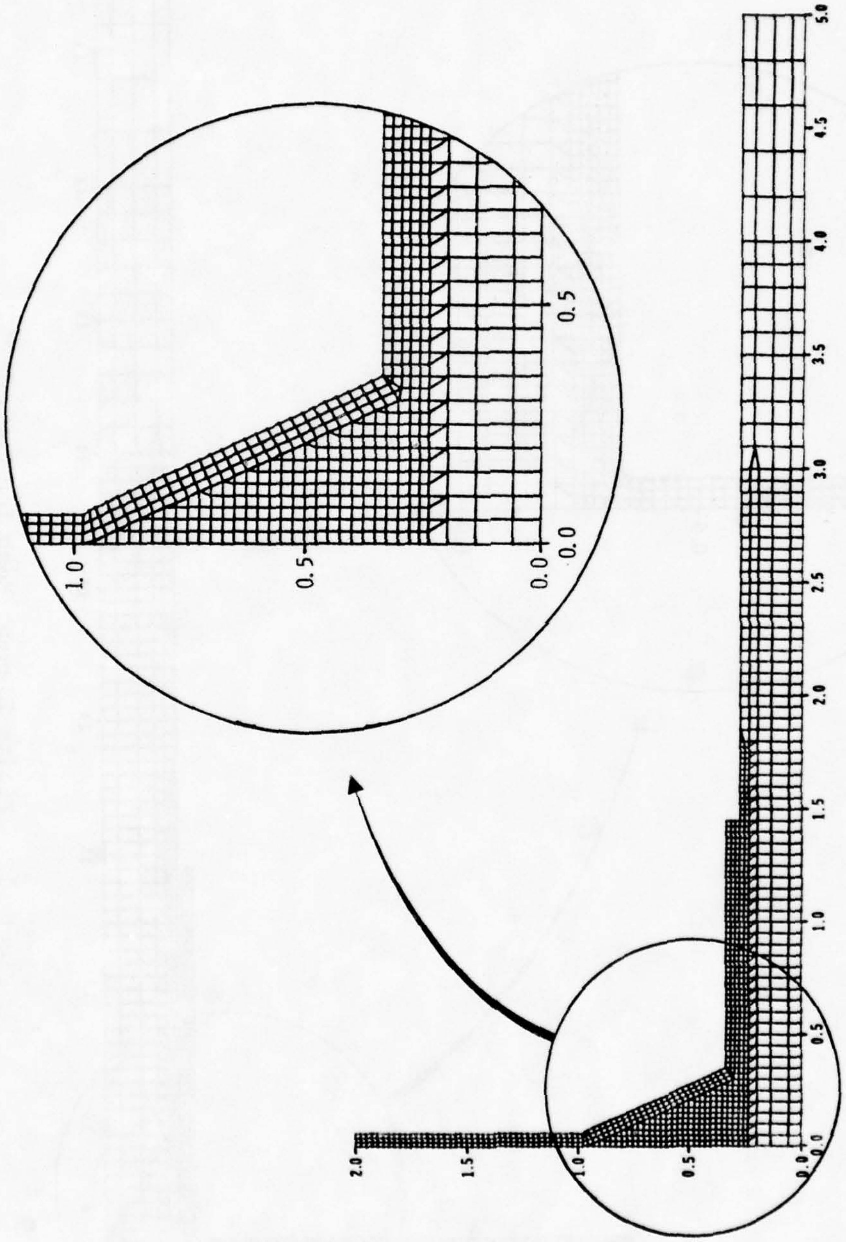

Figure 11: Finite Element Mesh for Concept "D"

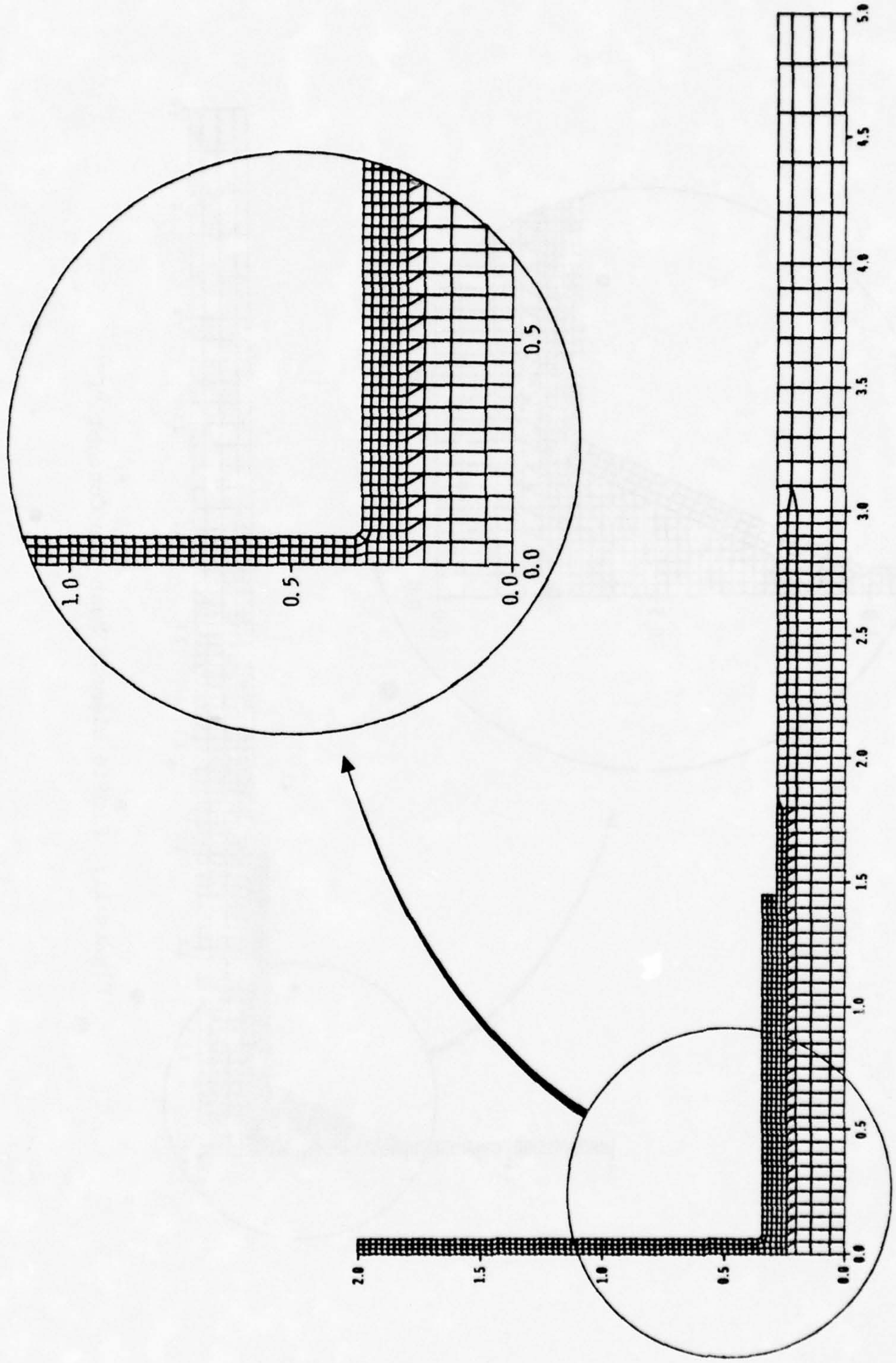

Figure 12: Finite Element Mesh for Concept "E"

used only to refine the mesh and an element aspect ratio of approximately 1.25 was maintained for all elements in the immediate vicinity of the spar and overlap. The finite element mesh of the insert for concept "D" (Figure 11) was developed to allow for the possible inclusion of a triangular cross-section tube having a wall consisting of multiples of four plies with variable properties allowed for each set of four plies.

CHAPTER IV

ANALYTICAL AND EXPERIMENTAL STIFFNESS RESULTS

4.1 Load, Strain and Stiffness

The first means for correlation of finite element and experimental results was accomplished by comparison of predicted and actual load-strain response. Load-strain response not only provides an adequate means of data comparison, it also represents a significant parameter for consideration by the designer when determining local joint geometry and maximum allowable spar spacing. For this comparison, load is defined as the load per unit specimen width applied at the top of the spar and strain as the compressive strain on the bottom surface of the wingskin at half-span, directly opposite the spar (strain gage 2 in Figure 6). It follows that modulus or apparent stiffness is defined as the slope of the load-strain curve.

4.2 Load-Strain Response

Plots of experimental and predicted load-strain response were made for concepts "A", "B", "C" and "D" over all spans and are supplied in Figures 13 through 28. Experimental load-strain responses were obtained directly from the test results after dividing the test loads by the sample width. Each figure represents from one to three test speci-

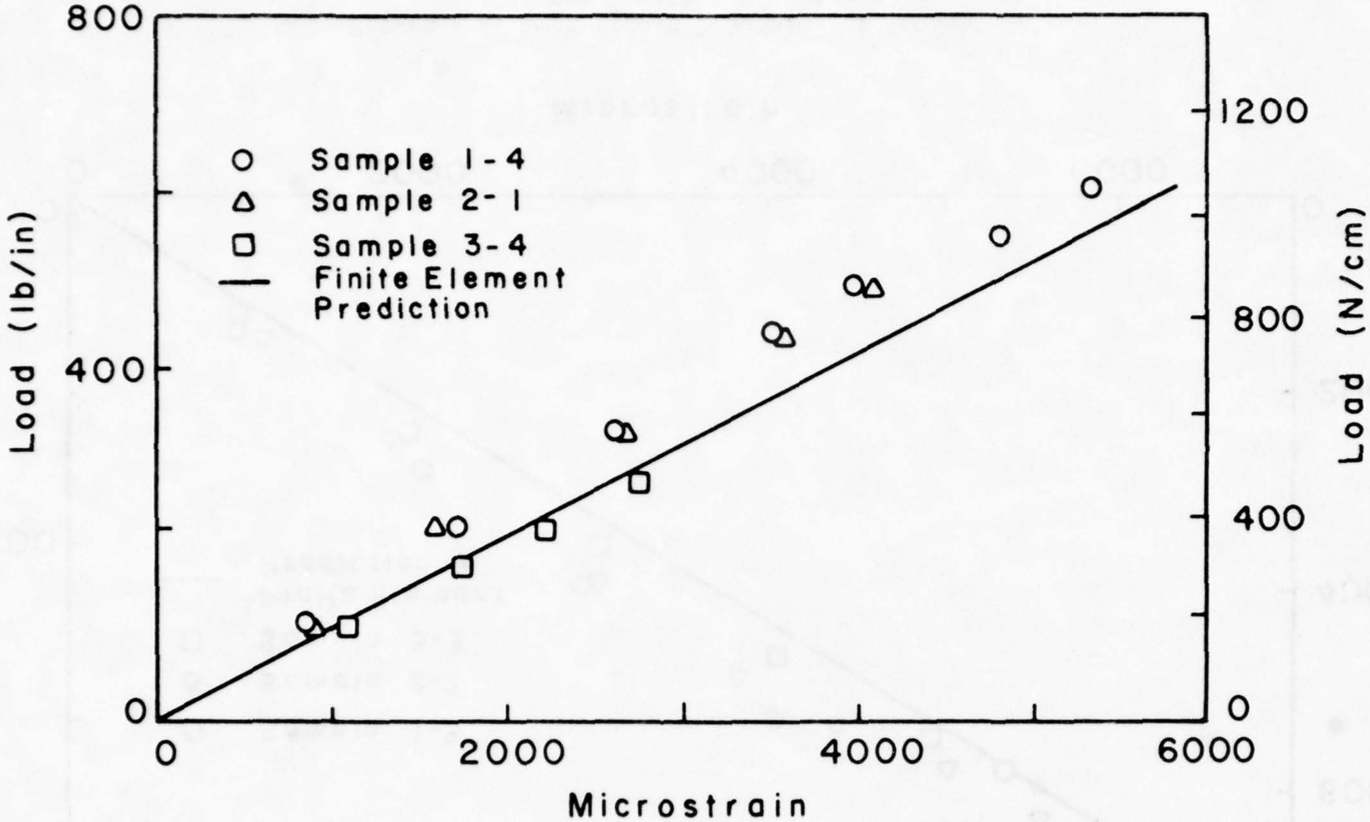

Figure 13: Load-Strain Response for Concept "A"
(Span Length = 3.6 inches)

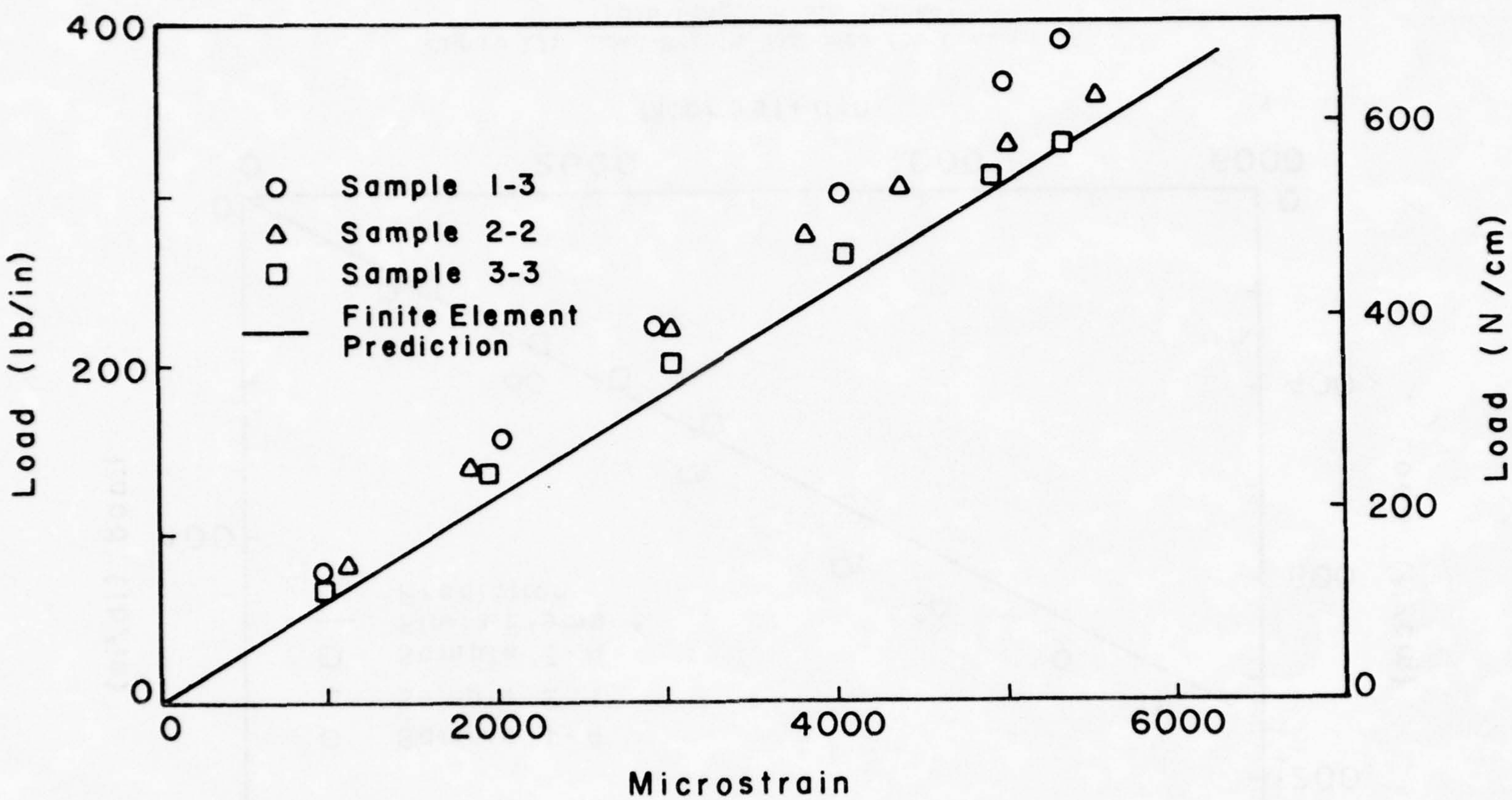

Figure 14: Load-Strain Response for Concept "A"
(Span Length = 6.0 inches)

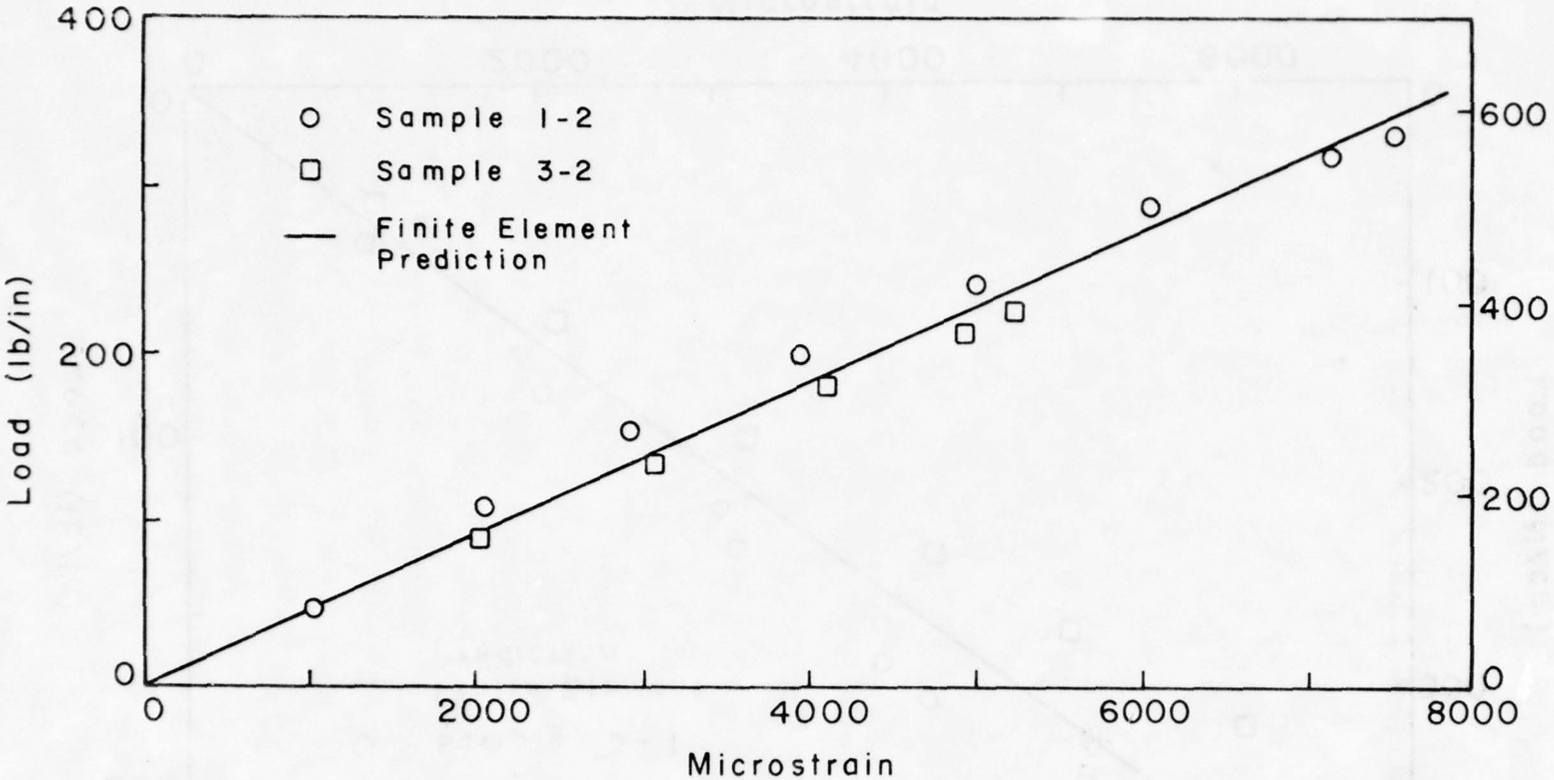

Figure 15: Load-Strain Response for Concept "A"
(Span Length = 8.0 inches)

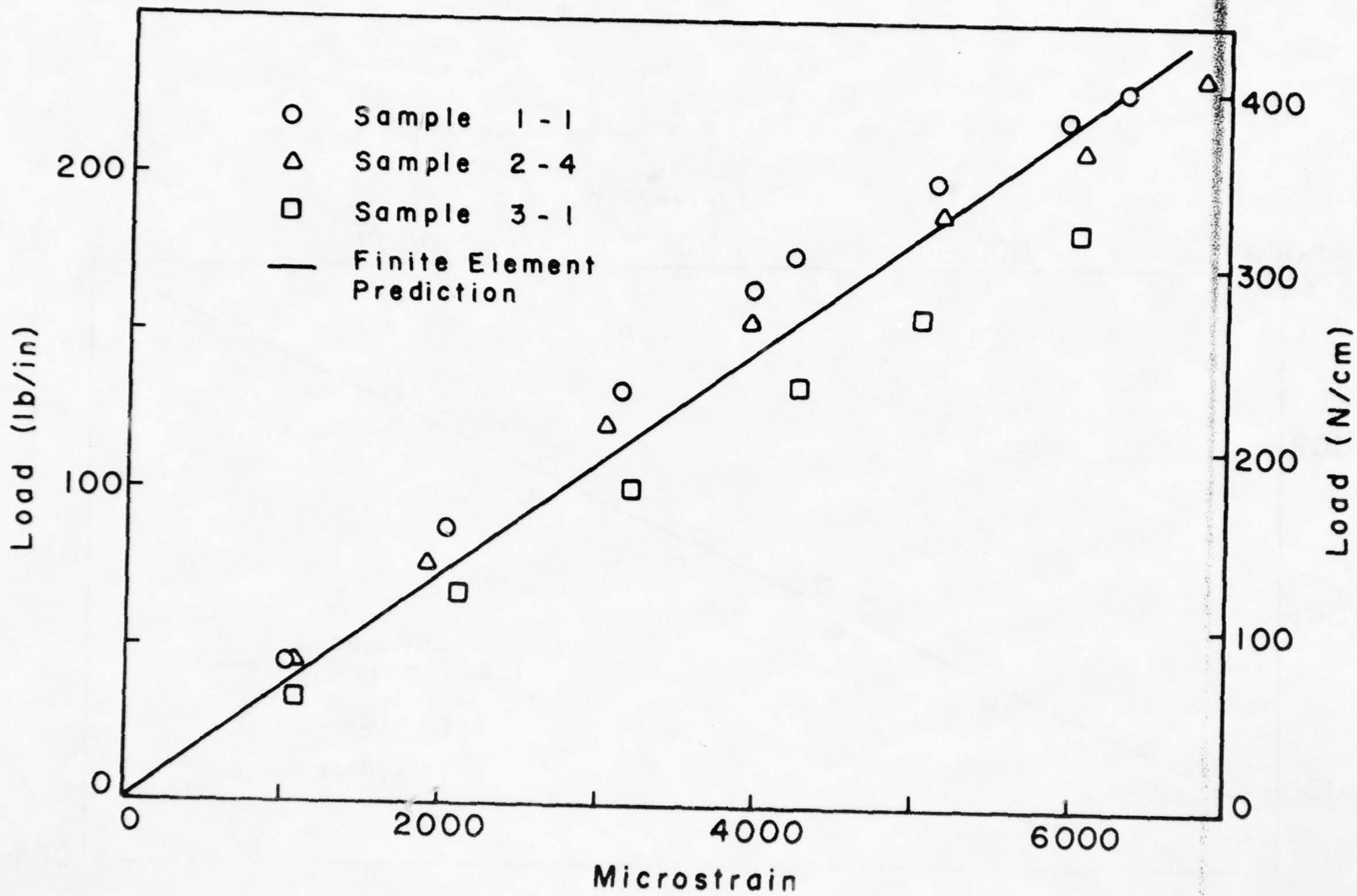

Figure 16: Load-Strain Response for Concept "A"
(Span Length = 10.0 inches)

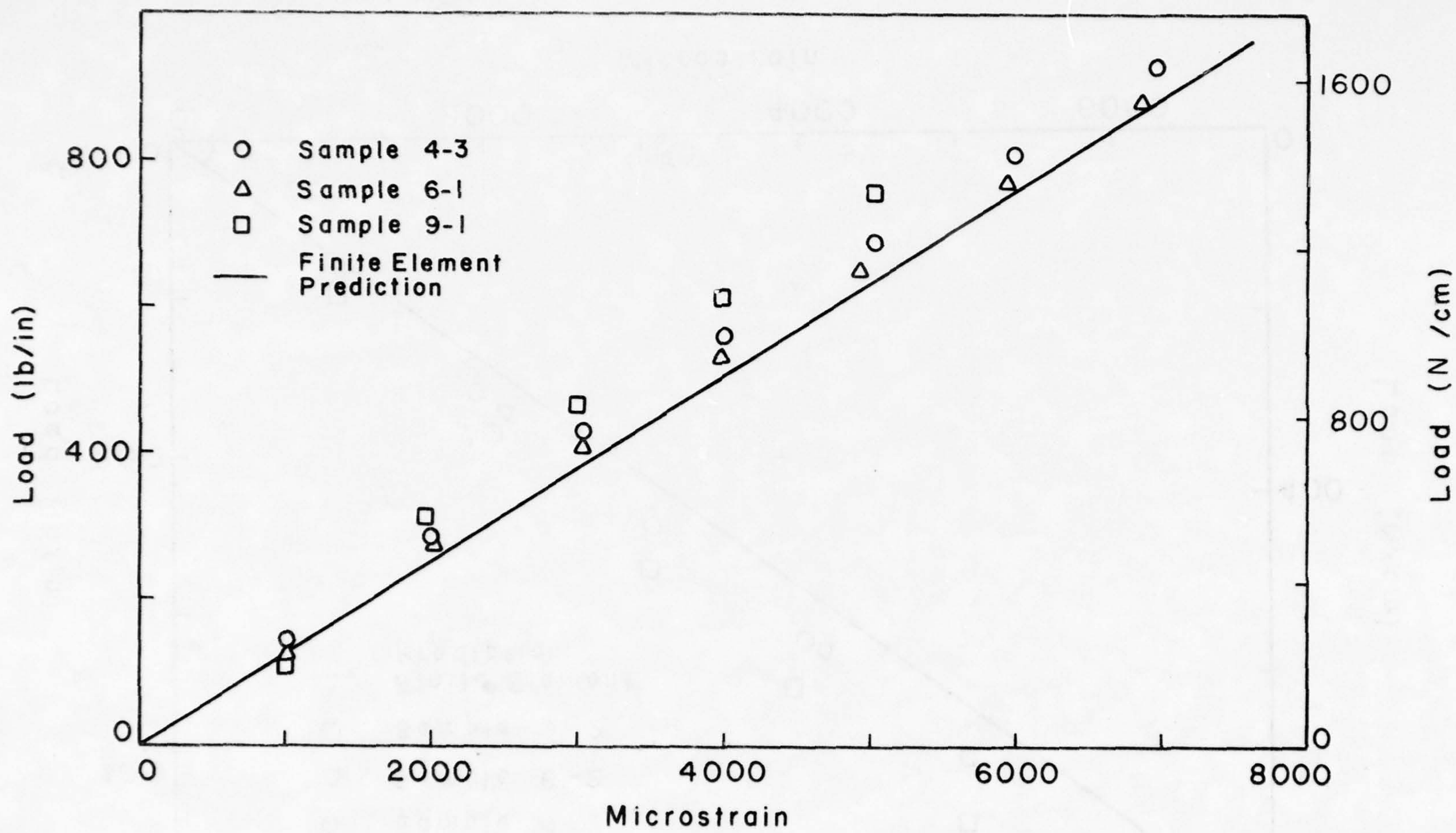

Figure 17: Load-Strain Response for Concept "B"
(Span Length = 3.6 inches)

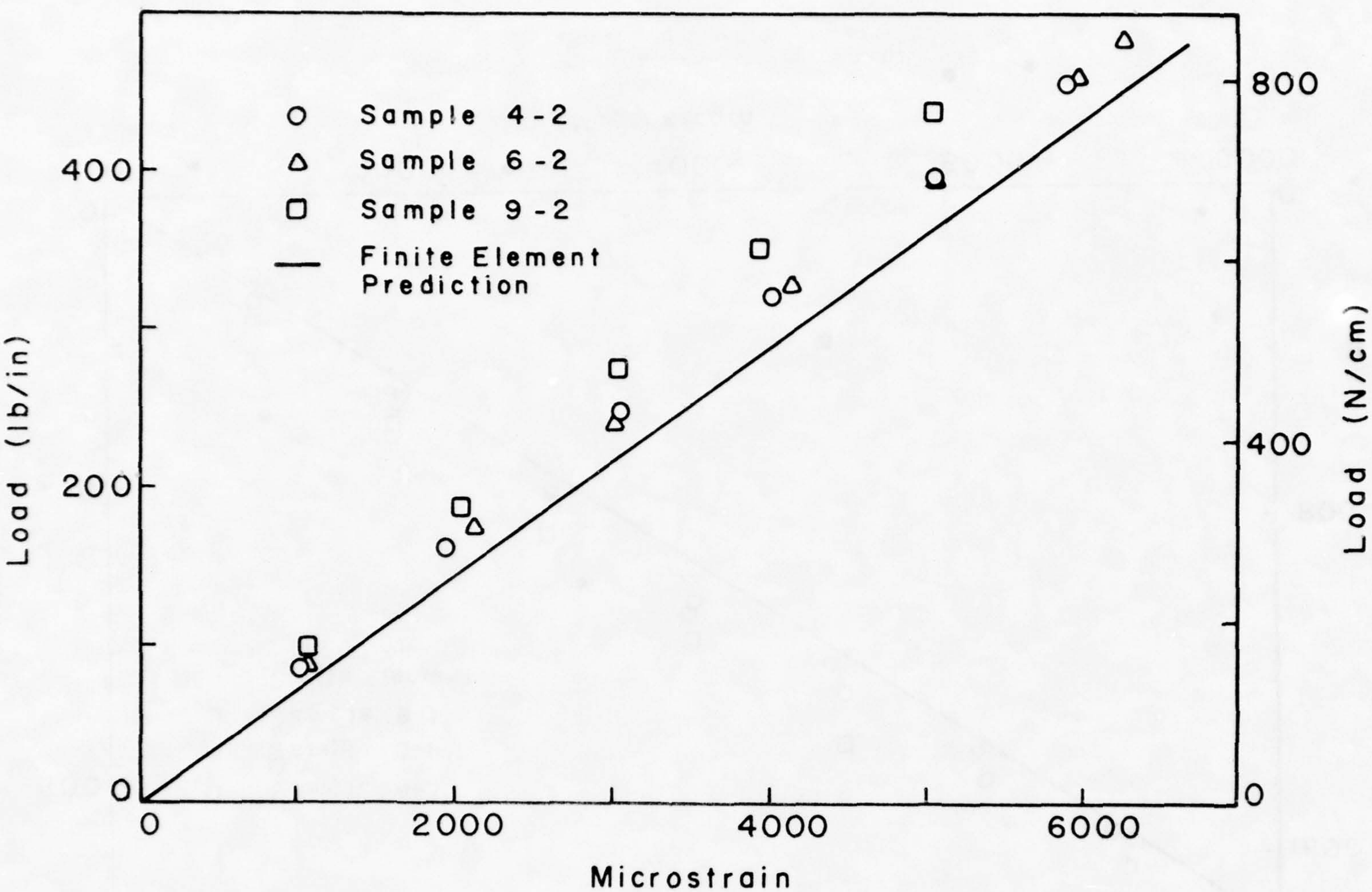

Figure 18: Load-Strain Response for Concept "B"
(Span Length = 6.0 inches)

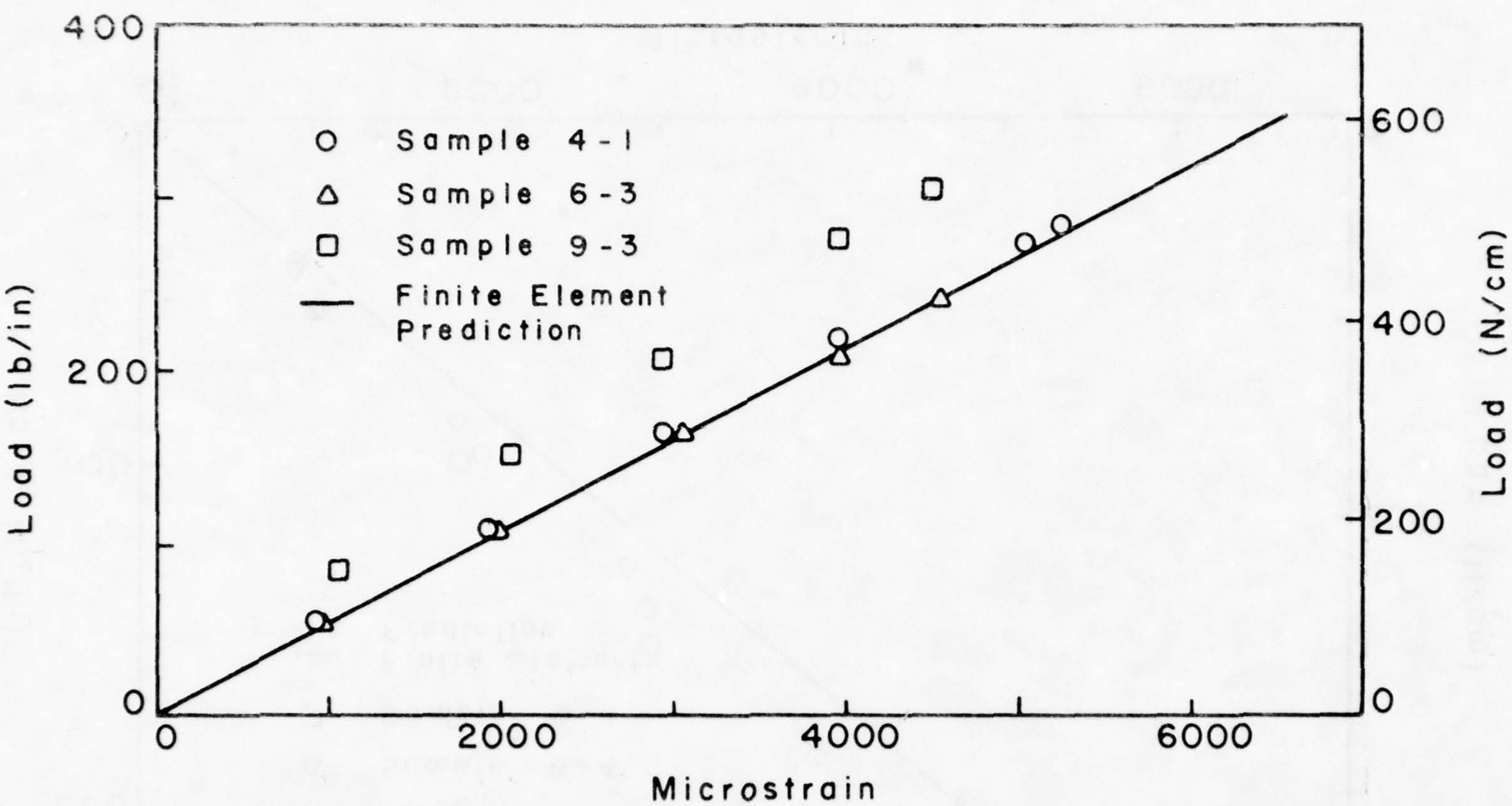

Figure 19: Load-Strain Response for Concept "B"
(Span Length = 8.0 inches)

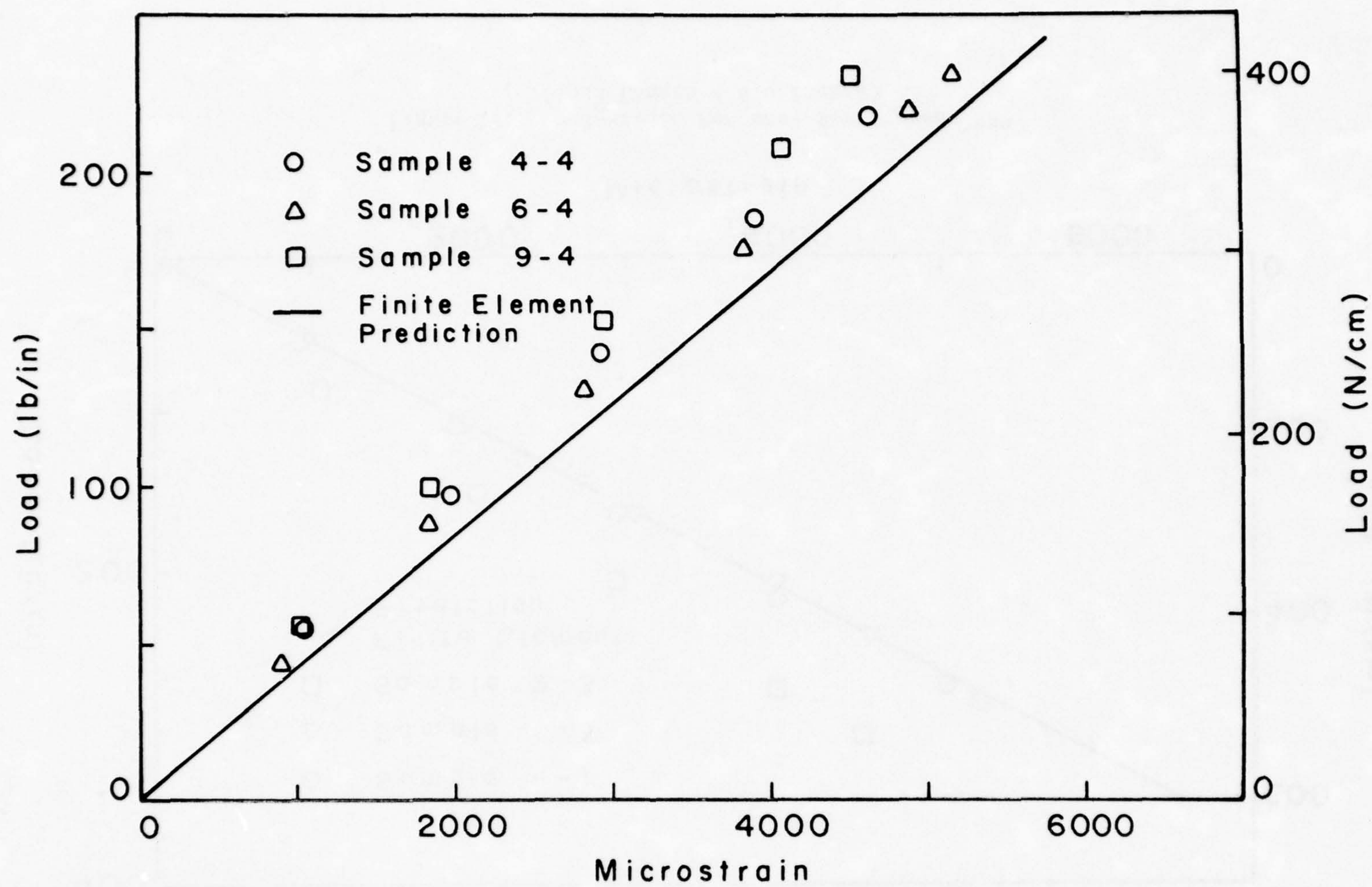

Figure 20: Load-Strain Response for Concept "B"
(Span Length = 10.0 inches)

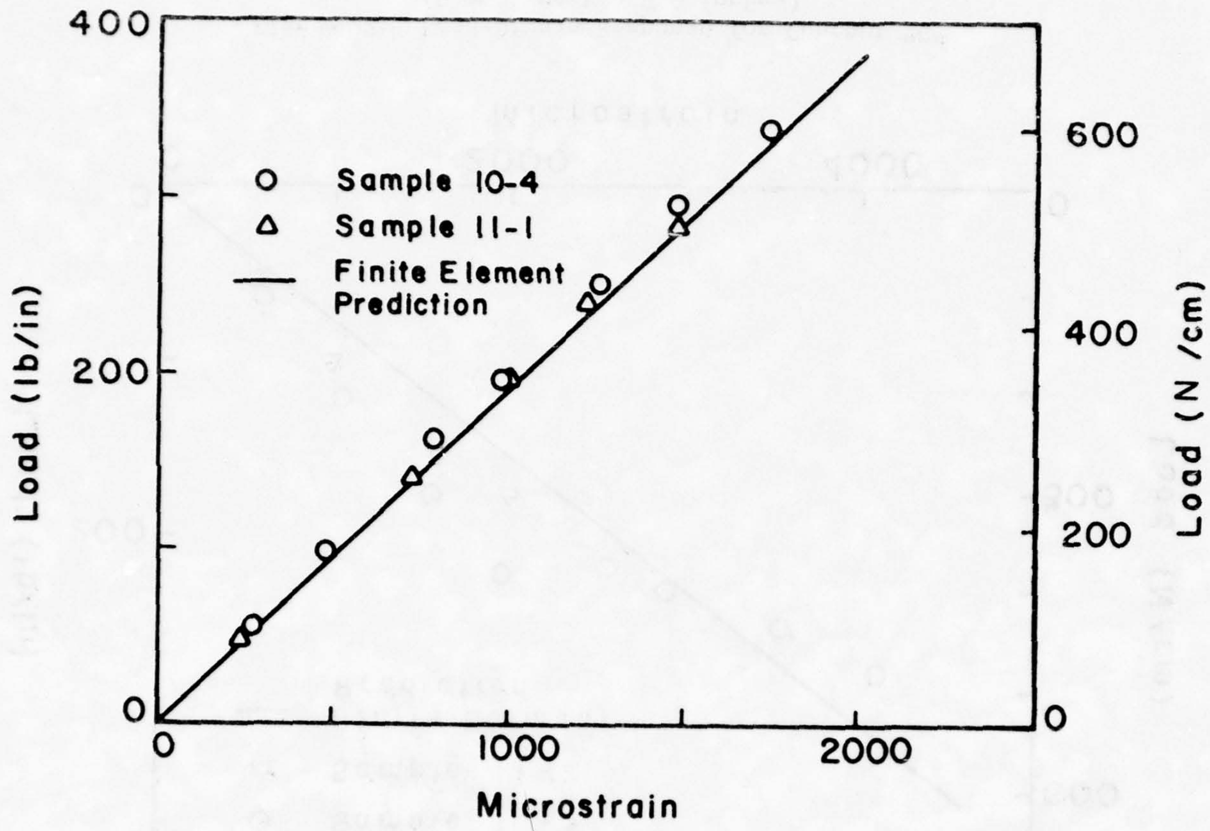

Figure 21: Load-Strain Response for Concept "C"
(Span Length = 3.6 inches)

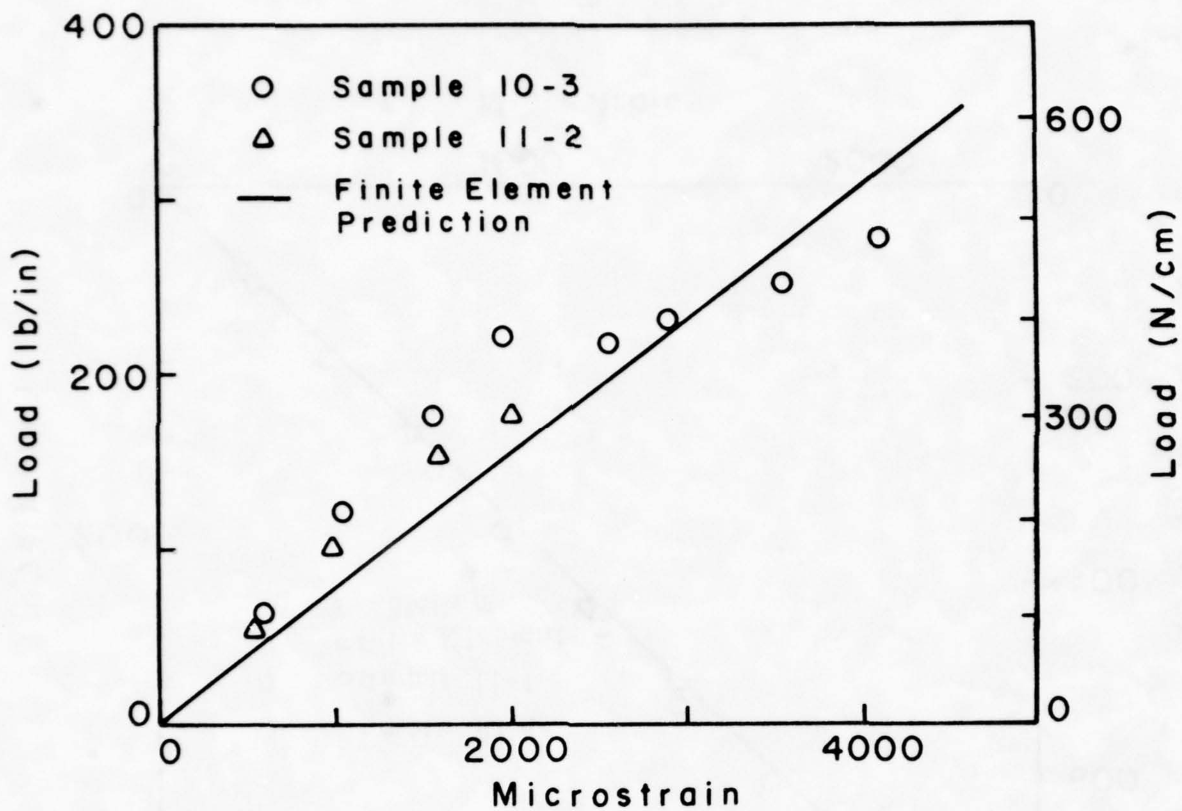

Figure 22: Load-Strain Response for Concept "C"
(Span Length = 6.0 inches)

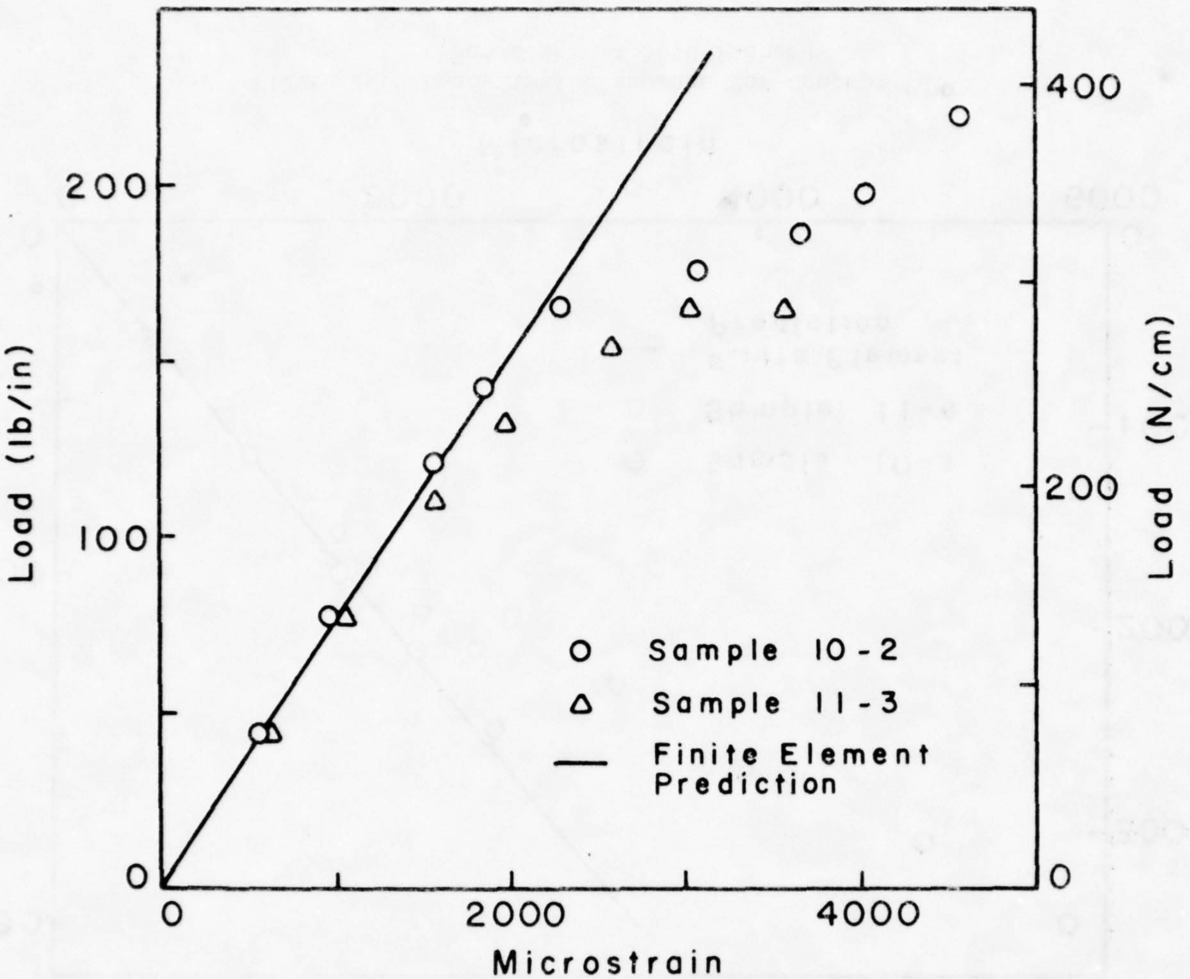

Figure 23: Load-Strain Response for Concept "C"
(Span Length = 8.0 inches)

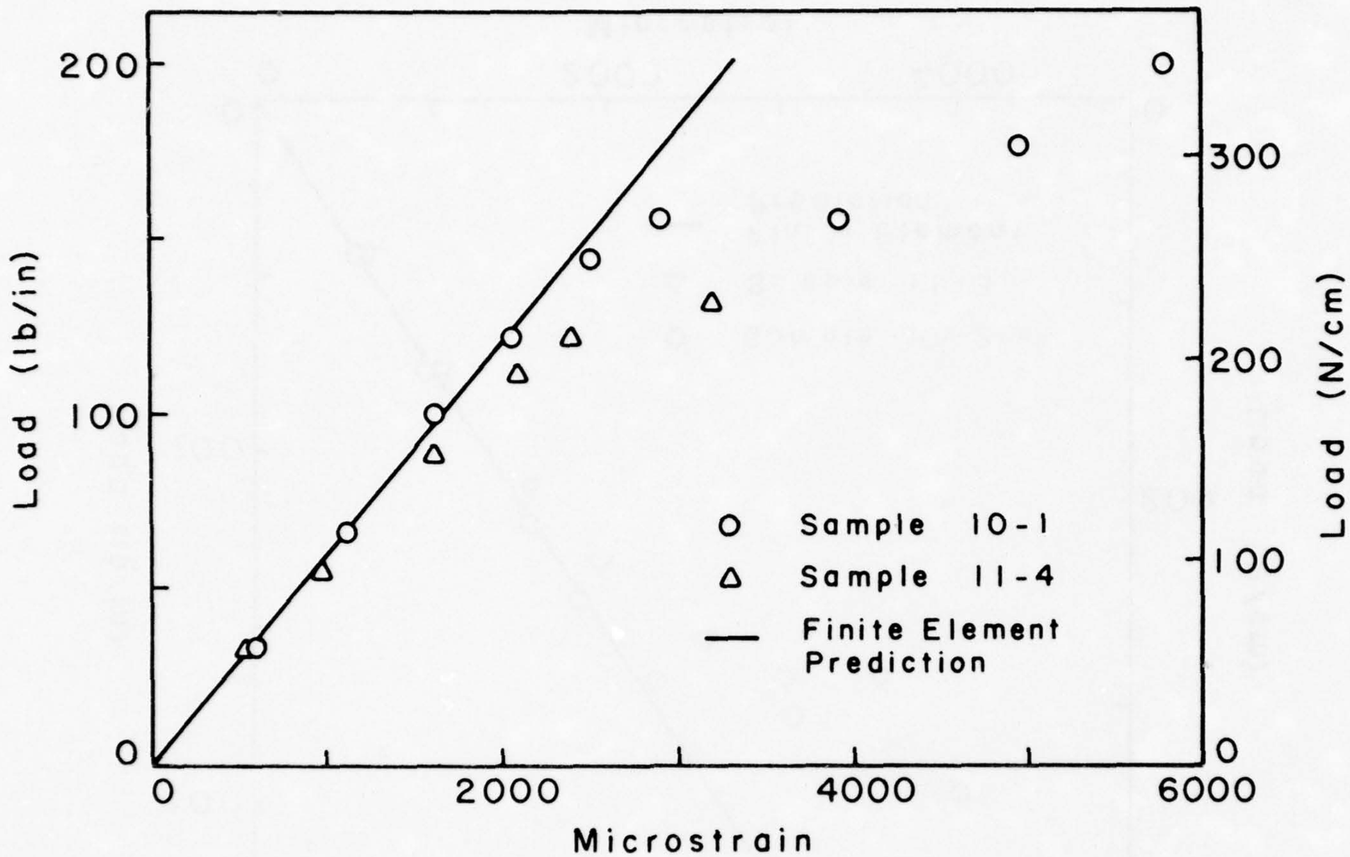

Figure 24: Load-Strain Response for Concept "C"
(Span Length = 10.0 inches)

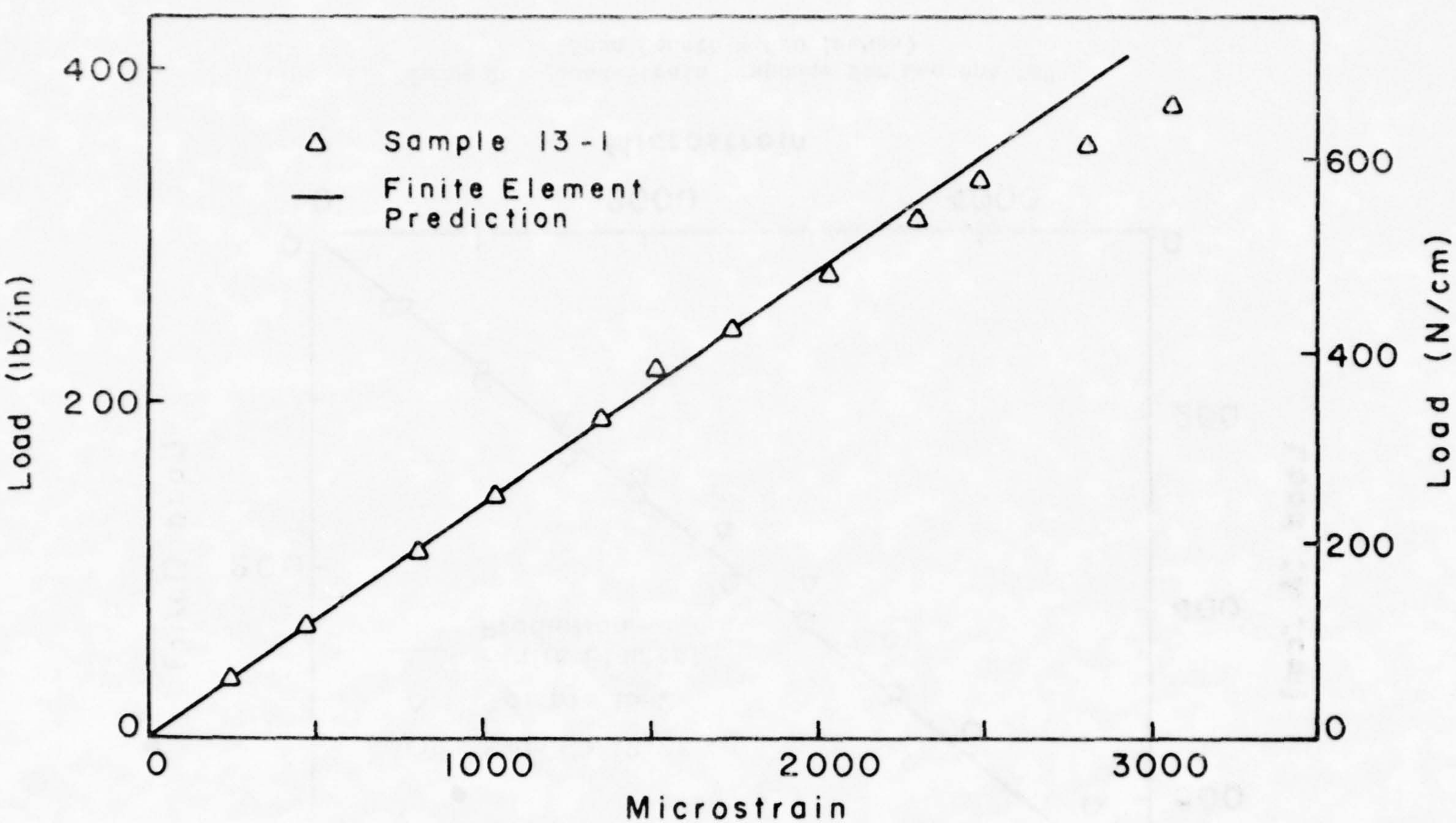

Figure 25: Load-Strain Response for Concept "D"
(Span Length = 3.6 inches)

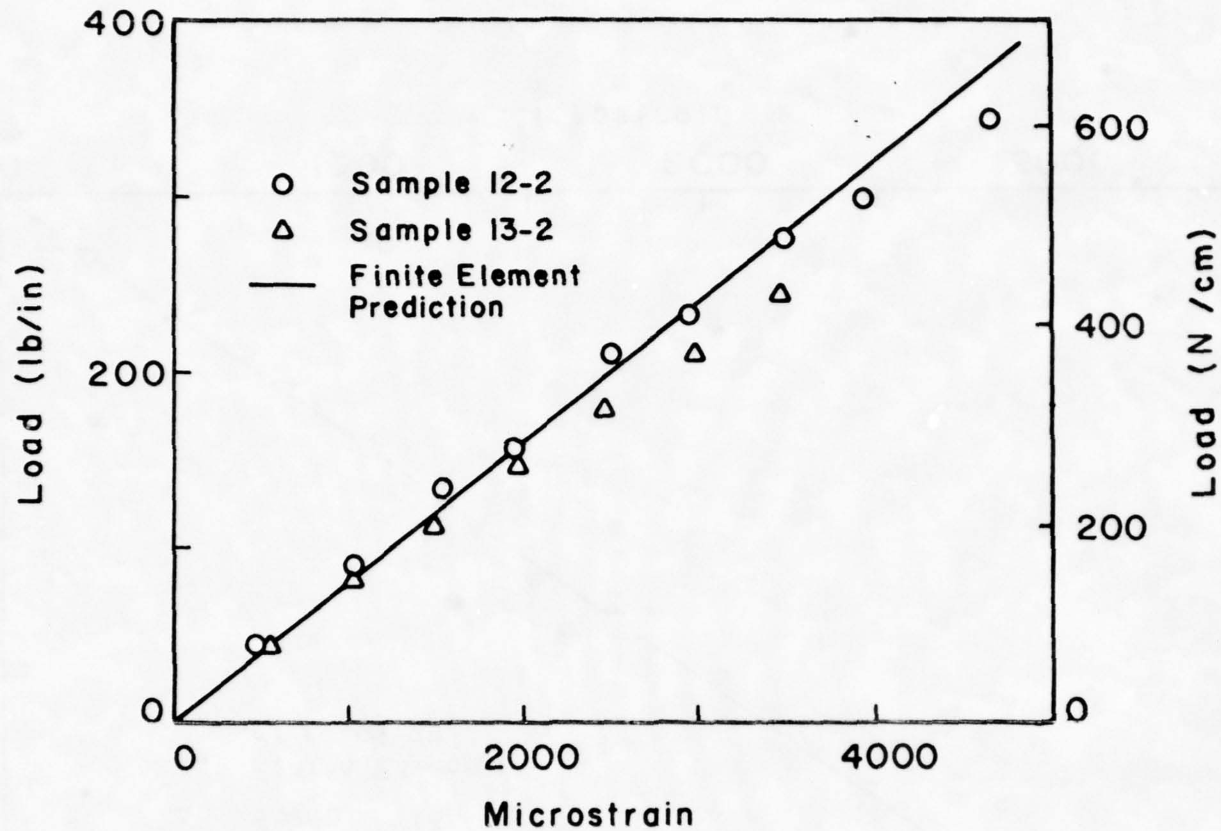

Figure 26: Load-Strain Response for Concept "D"
(Span Length = 6.0 inches)

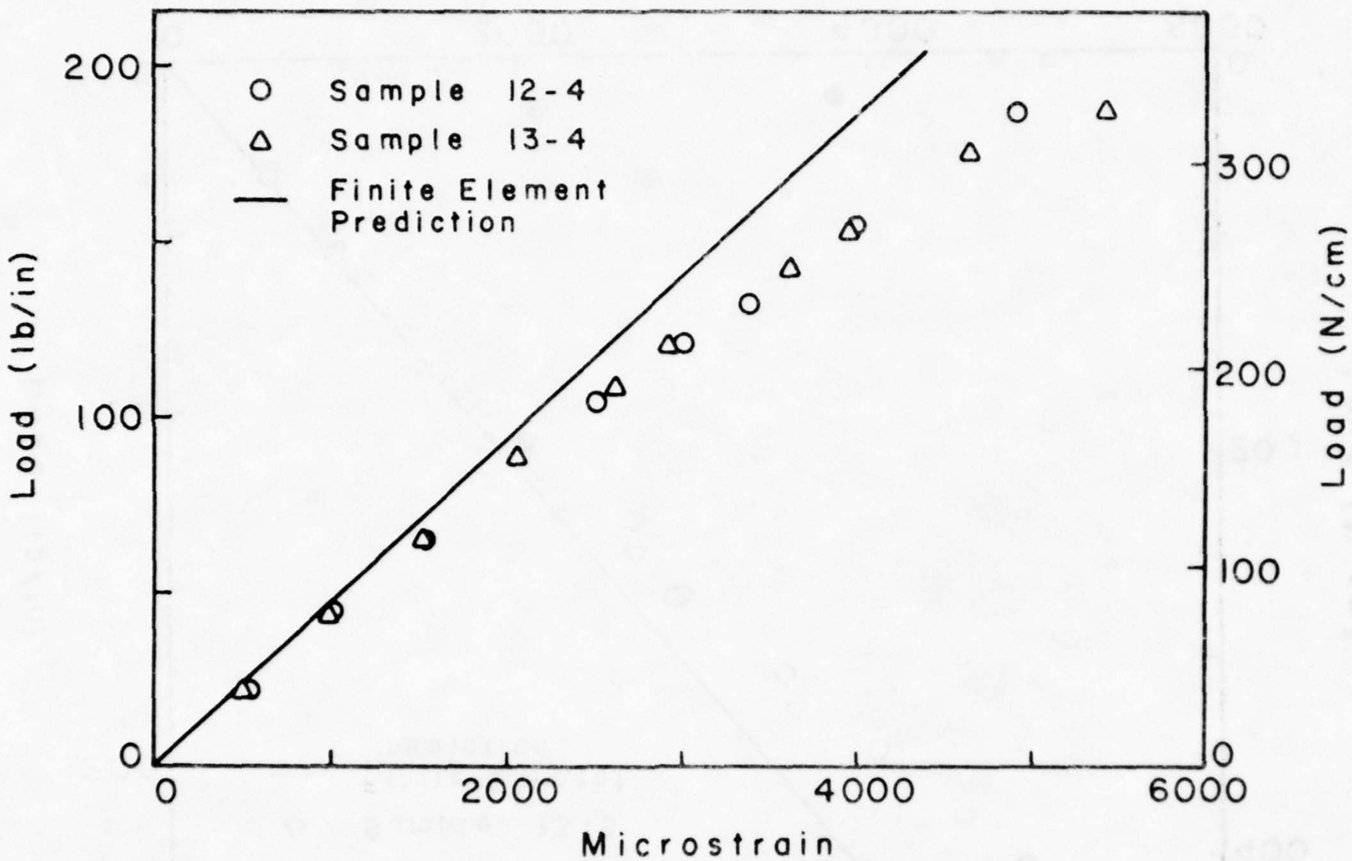

Figure 27: Load-Strain Response for Concept "D"
(Span Length = 8.0 inches)

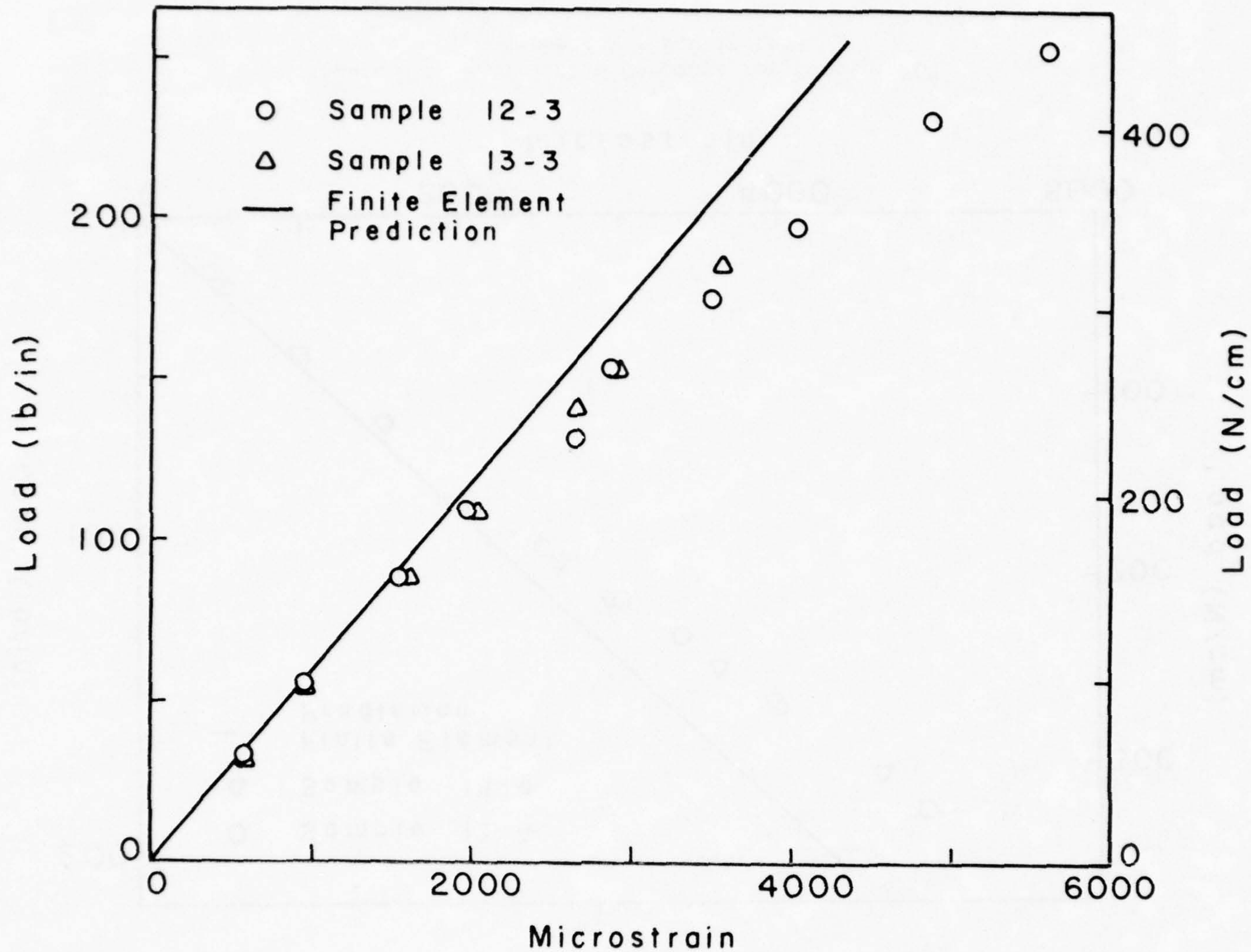

Figure 28: Load-Strain Response for Concept "D"
(Span Length = 10.0 inches)

mens with many of the recorded data points omitted for clarity. Sample numbers indicate processing cycle and are referenced in table 15. Since the finite element analysis yielded only stress and displacement results, it was necessary to employ the orthotropic stress-strain relationship to determine the strain at the bottom surface of the wingskin. Once the finite element prediction of half-span strain was determined, the predicted load-strain response was superimposed over the experimental results for comparison. Examining figures 13 through 28, the correlation between analytical and experimental results may be considered excellent. For all joint concepts and spans, experimental results showed excellent reproducibility, and finite element predictions generally exceeded observed stiffnesses. Concepts "C" and "D" demonstrated some non-linearity while "A" and "B" remained linear almost until failure. Due to the linear-elastic finite element modeling, any non-linear experimental results were not predicted.

4.3 Modulus-Span Results

Apparent stiffness or modulus (defined in section 4.1) provides a quantitative measure of the joint stiffness. The experimental value of this property was determined by performing a linear regression analysis on the initial portion of the load-strain response for all samples tested of a given concept at a single span. Since the finite element prediction of load-strain response was linear, the apparent stiffness could be obtained directly from strain calculations. Modulus versus span results for all concepts, shown in Figures 29 through 33, further illustrate the excellent correlation between experimental and analytical re-

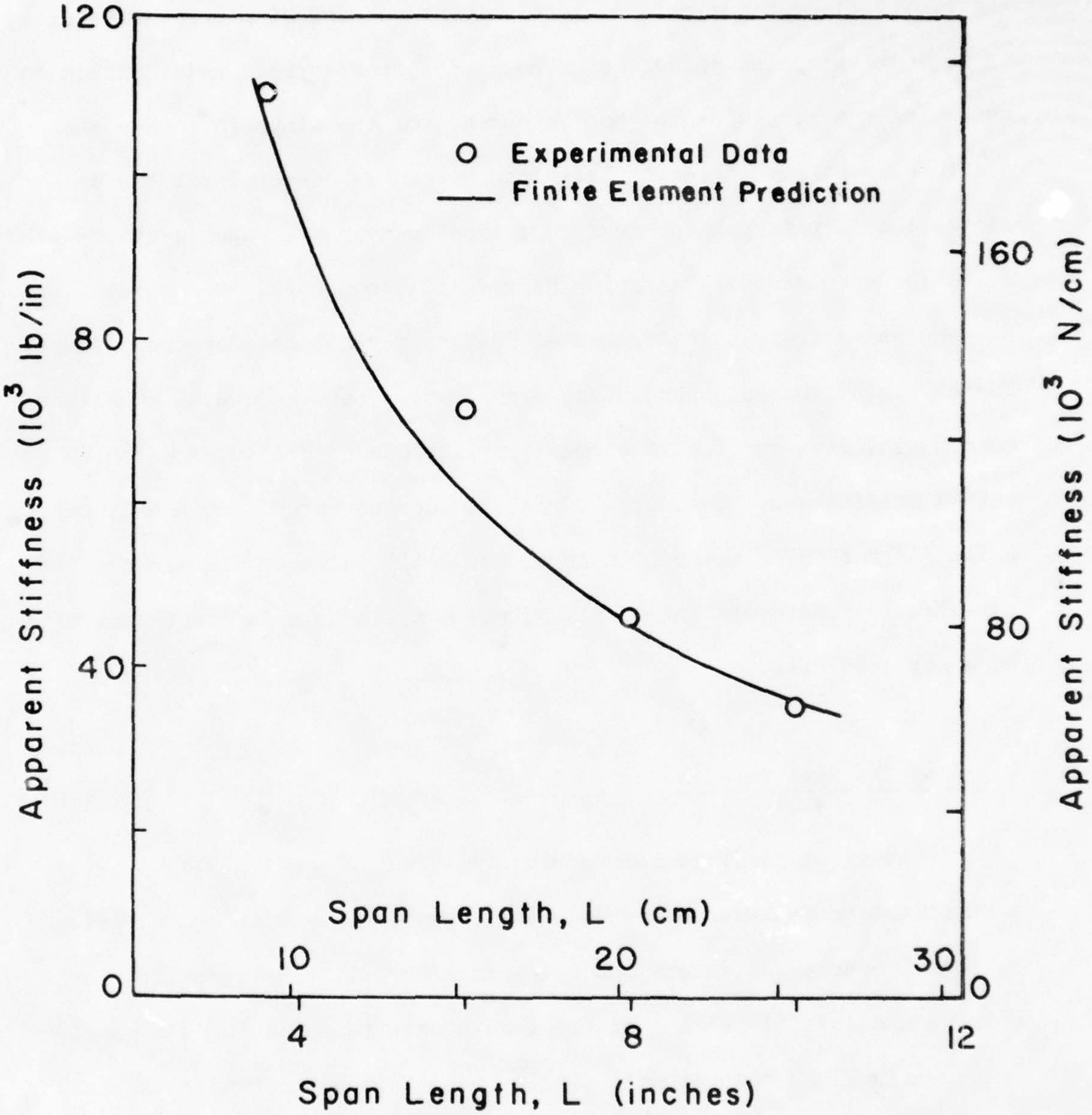

Figure 29: Influence of Span on Modulus for Concept "A"

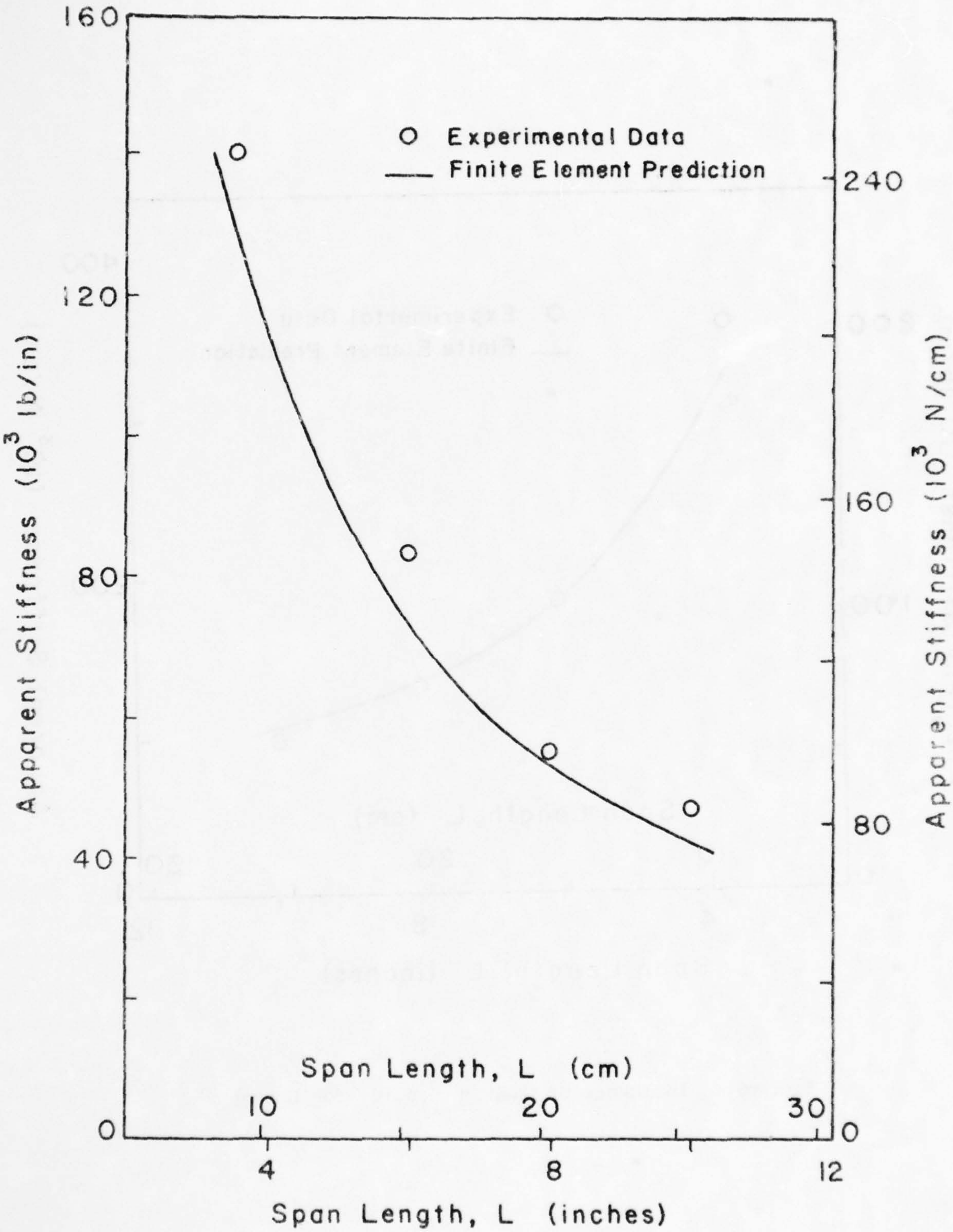

Figure 30: Influence of Span on Modulus for Concept "B"

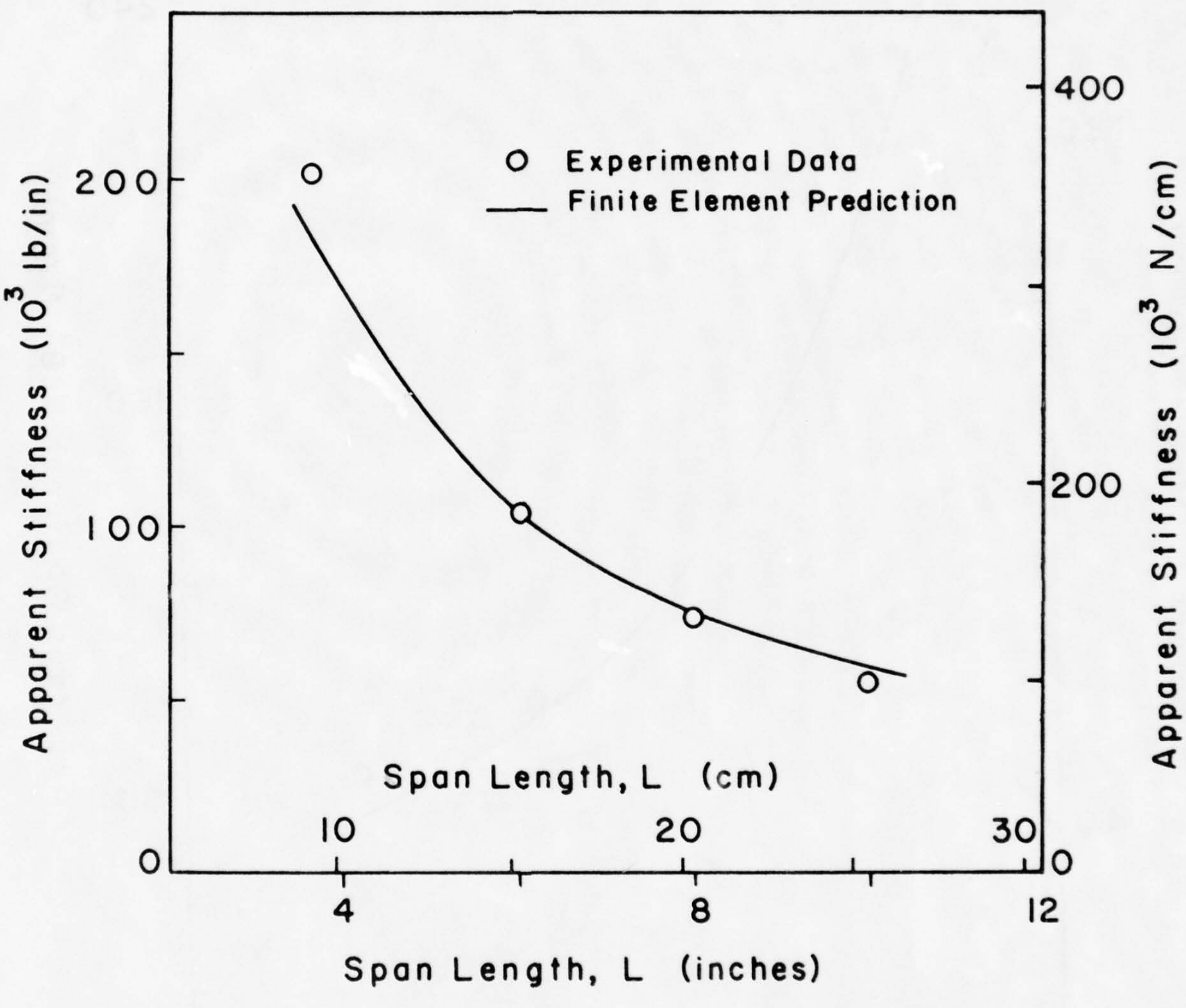

Figure 31: Influence of Span on Modulus for Concept "C"

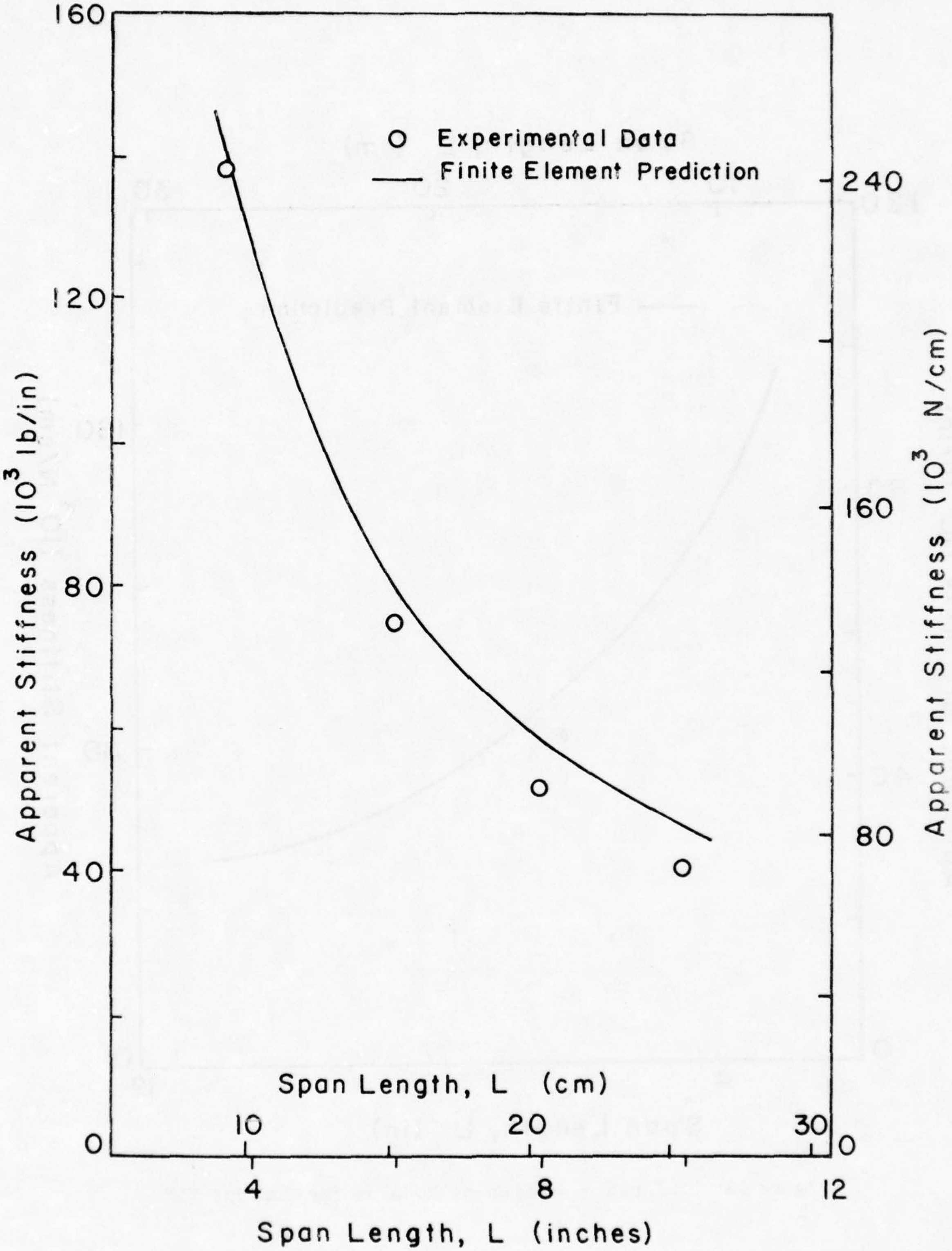

Figure 32: Influence of Span on Modulus for Concept "D"

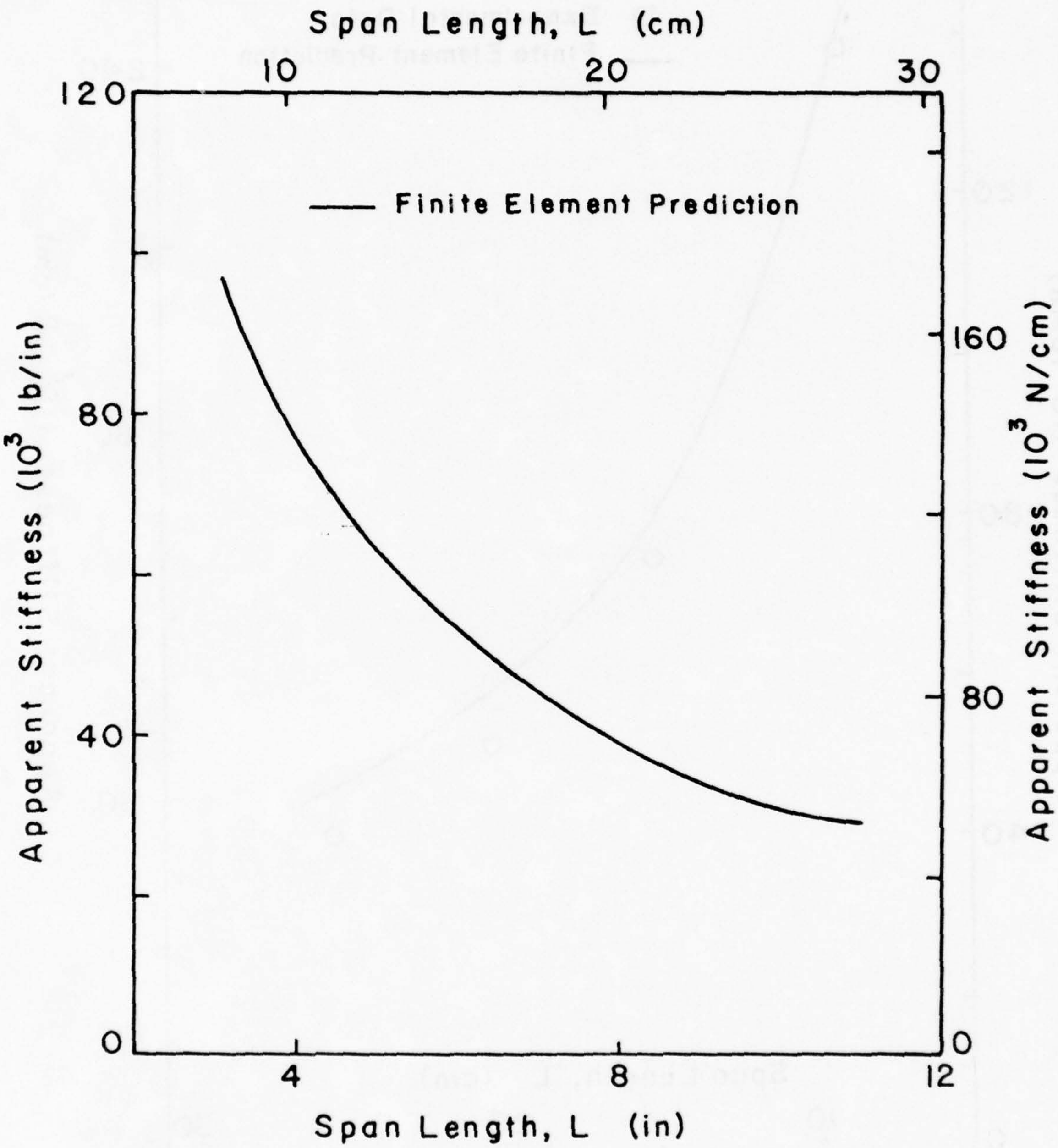

Figure 33: Influence of Span on Modulus for Concept "E"

sults for all span lengths. All numerical results are provided in Table 1. Finite element predictions were conservative for all concepts, except "D" for which predictions exceeded test data by a maximum of 12%.

A first approximation to the modulus-span relationship can be obtained by examining classical beam theory. For a uniform beam of length $2L$, thickness $2h$, simply supported and subjected to a normal load, F, at $x = L$ (see Figure 34), beam theory predicts

$$M = \text{moment} = F(x-L) - \frac{F}{2}x$$

$$y = \text{deflection} = \frac{F}{6EI}(x-L)^3 - \frac{F}{12EI}x^3 + \frac{FL^2}{4EI}x$$

where EI = Flexural Rigidity

The strain at the bottom surface of the beam for $x = L$ is

$$\varepsilon\Big|_{x=L} = \frac{-M\Big|_{x=L} h}{EI} \tag{1}$$

Evaluating the moment at $x = L$ and substituting into equation (1)

$$\varepsilon\Big|_{x=L} = \frac{FLh}{2EI}$$

$$= \frac{L}{K}F \tag{2}$$

where

$$K = \frac{2EI}{h}$$

is a constant for a given beam. Clearly, equation (2) represents the

Table 1: Summary of Modulus versus Span Results

Concept	Span	MODULUS	
		Fin. El.	Exper.
	inches	10^3 lb/in	10^3 lb/in
A	3.6	105	110
A	6.0	61	71
A	8.0	46	46
A	10.0	36	35
B	3.6	127	140
B	6.0	73	83
B	8.0	53	55
B	10.0	42	47
C	3.6	184	202
C	6.0	104	104
C	8.0	76	73
C	10.0	60	56
D	3.6	141	138
D	6.0	80	75
D	8.0	59	52
D	10.0	47	41
E	3.6	85	-
E	6.0	50	-
E	8.0	38	-
E	10.0	30	-

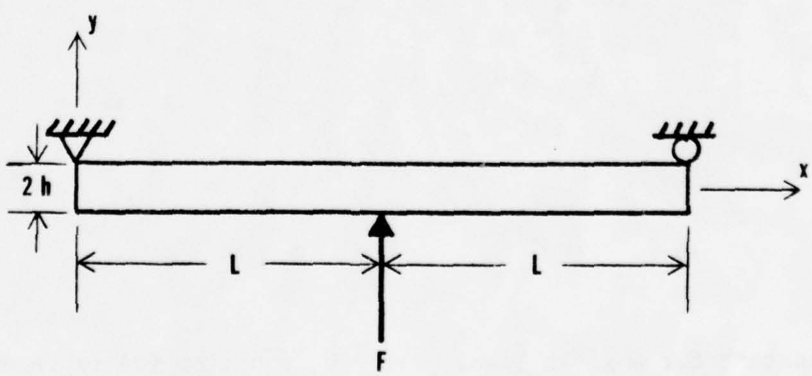

Figure 34: Model of Simply Supported Beam

load-strain response and the quantity K/L represents the apparent stiffness or modulus. Applying this result to the determination of the spar-wingskin modulus, "K" can be calculated from a single experimental test or finite element solution and the complete modulus-span response can, in turn, be determined. Table 2 lists "K" values for each concept and span as determined by both experimental and finite element data. Variations in "K" values for a given span are due to the assumption of uniform cross-section and constant flexural rigidity made in the beam theory solution. Nevertheless, the maximum K variation over span for the finite element results is 10% and reaches 23% for the experimental results. Agreement is considerably better for the concepts having a small insert ("A" and "E") and accuracy decreases as span length decreases.

When experimental modulus-span data for concepts "A" through "D" is plotted on a single graph (Figure 35), several trends can be noted. Concept "C" exhibits the greatest stiffness. This can be attributed to the increased moment of inertia over an extended range near the base of the spar exhibited by this concept. Although concept "B" has a similar length, high inertia range, the value of the apparent moment of inertia is significantly greater for concept "C". Consequently, concept "B" exhibits a lower stiffness. Concept "D" falls slightly below "B" and the lowest stiffness is exhibited by concept "A" which has the smallest apparent moment of inertia over the shortest range. Referring to the modulus equation from beam theory where modulus equals K/L, as span increases the length of the span, $2L$, becomes the dominate term and the effects of local, joint configurations are insignificant. Similarly,

Concept	$K=\frac{2EI}{t}$ $[10^3 lb]$ Experimental (Theoretical)			
	3.6" span	6.0" span	8.0" span	10.0" span
A	396 (378)	426 (366)	368 (368)	350 (360)
B	504 (457)	498 (438)	440 (424)	470 (420)
C	727 (662)	624 (624)	584 (608)	560 (600)
D	497 (508)	450 (480)	416 (472)	410 (470)
E	- (306)	- (300)	- (304)	- (300)

Table 2: K Values

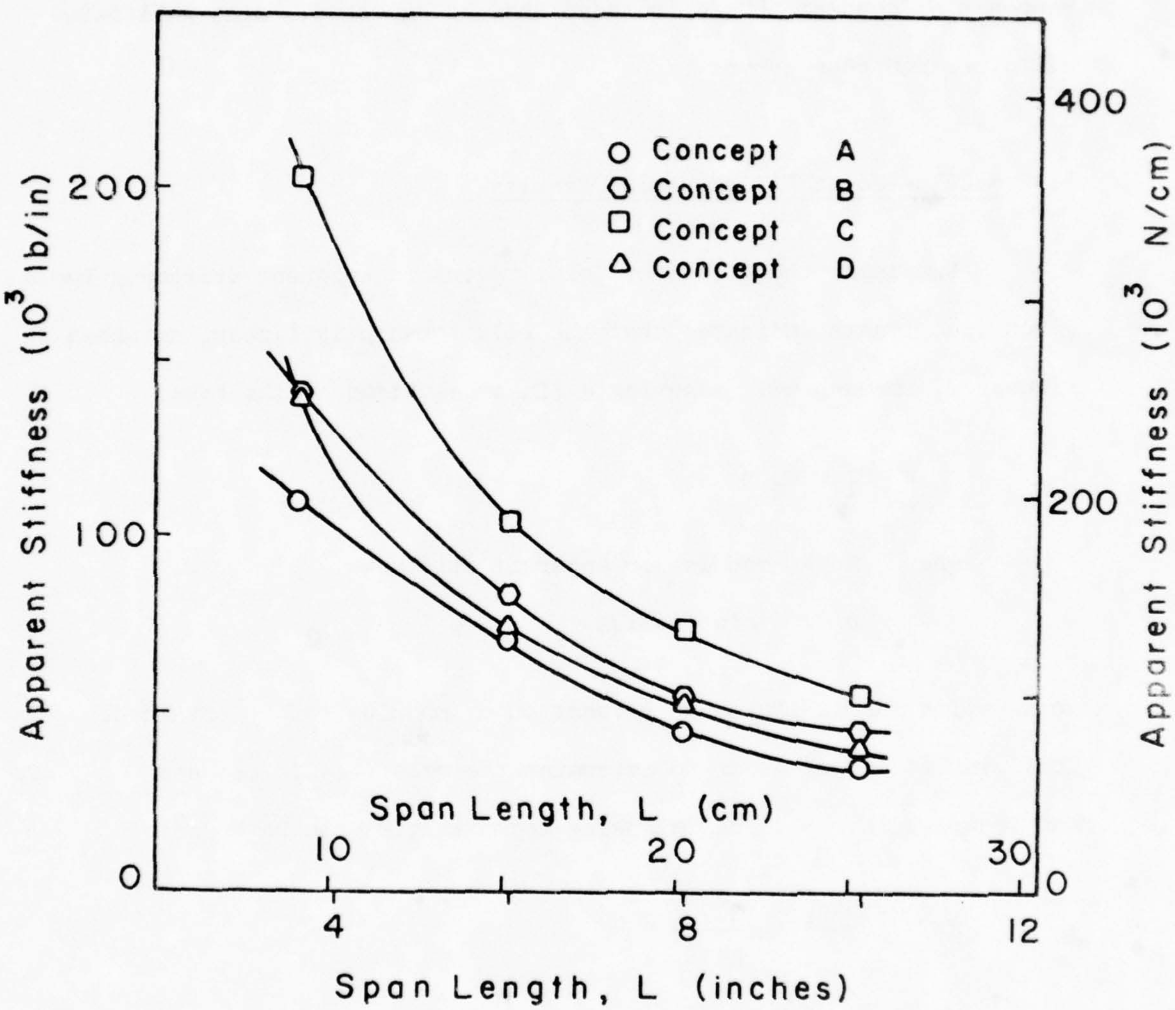

Figure 35: Experimental Determination of the Influence of Geometry and Span on Modulus

when predicted modulus-span responses for concepts "A" through "E" are plotted on a single graph (Figure 36), the same trends can be noted for the predicted results, however, the relative positions of the response curves for concepts "B" and "D" have been exchanged. Also the predicted response of concept "E" is included and, as expected, falls well below all other response curves.

4.4 Modulus-Joint Fillet Radius Results

Examining the effect of joint radius on apparent stiffness for a given span length indicates that the relationship is linear, as shown in Figures 37 through 40. Assuming a linear equation of the form

$$M = C_1 + C_2 r$$

where M = modulus or apparent stiffness

r = joint radius

an equation for stiffness as a function of modulus can be obtained. Utilizing trial and error to determine the relationship between C_1, C_2 and span length, S, the following approximation can be found:

$$M = \left(\frac{302}{S}\right) + \left(\frac{382}{S^{1.2}}\right) r \tag{3}$$

where M = modulus in 10^3 lb/in

S = span length in inches

r = joint fillet radius in inches

The maximum error between equation (3) and the finite element stiffness

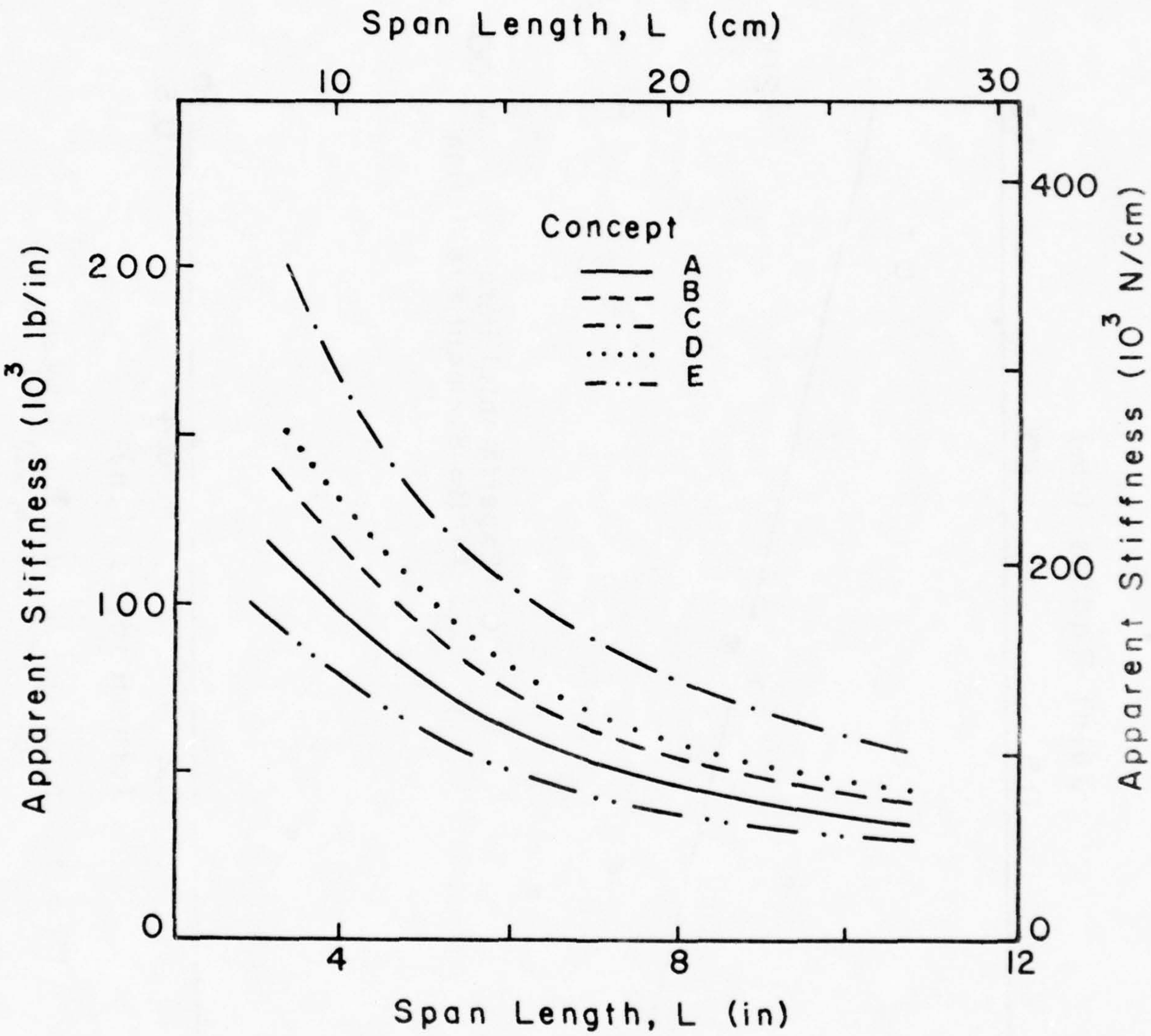

Figure 36: Finite Element Prediction of the Influence of Geometry and Span on Modulus

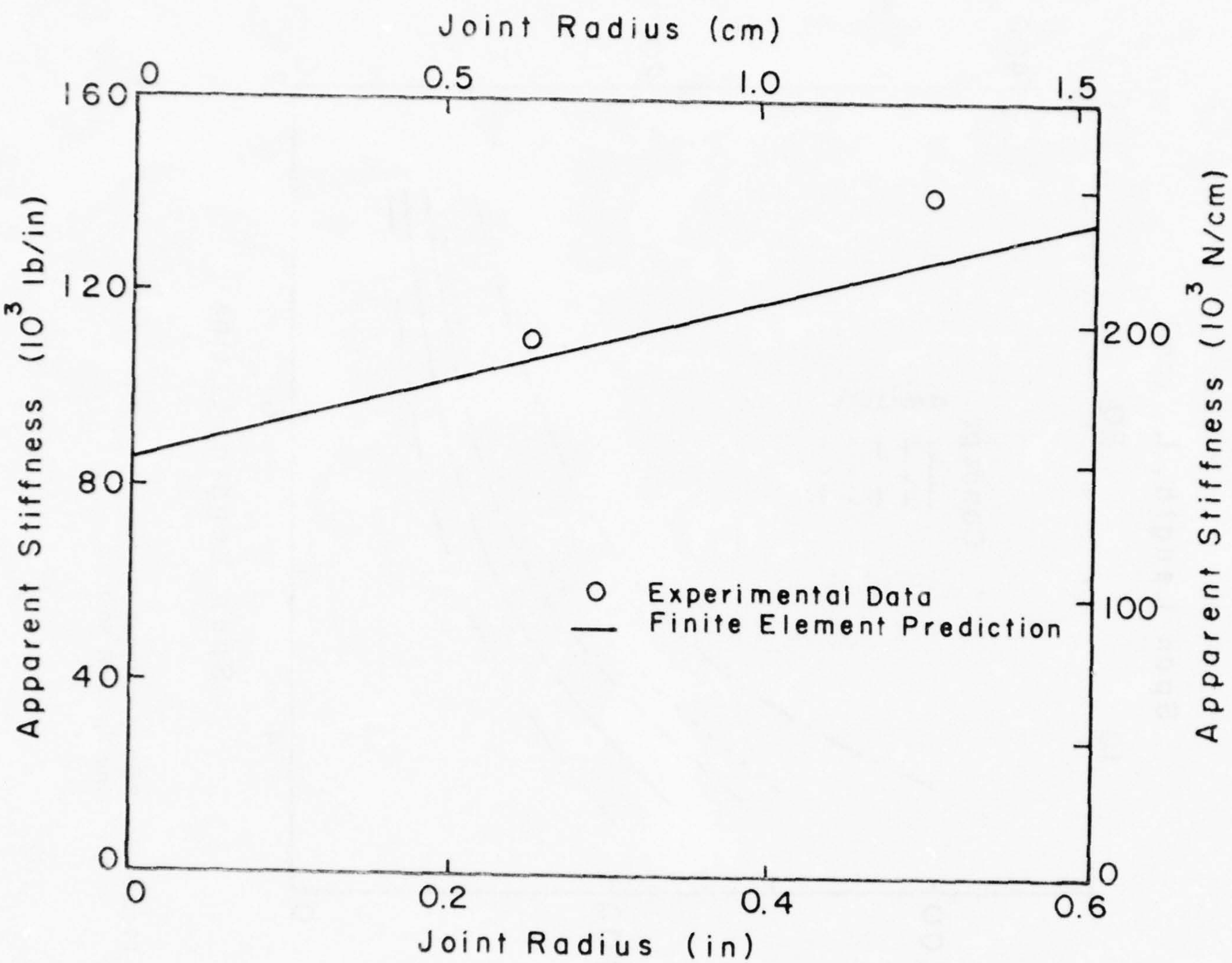

Figure 37: Influence of Joint Radius on Modulus
(Span Length = 3.6 inches)

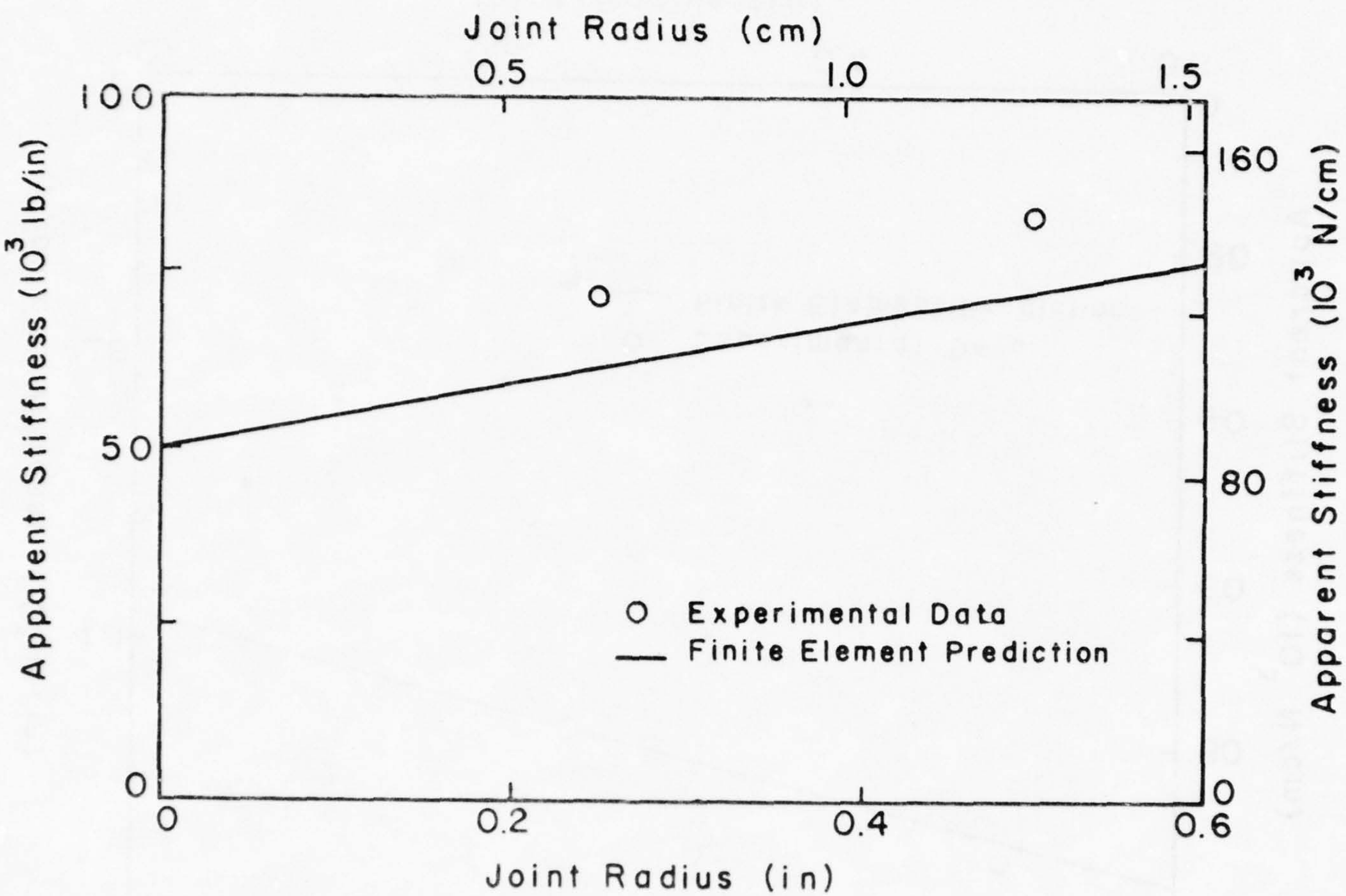

Figure 38: Influence of Joint Radius on Modulus
(Span Length = 6.0 inches)

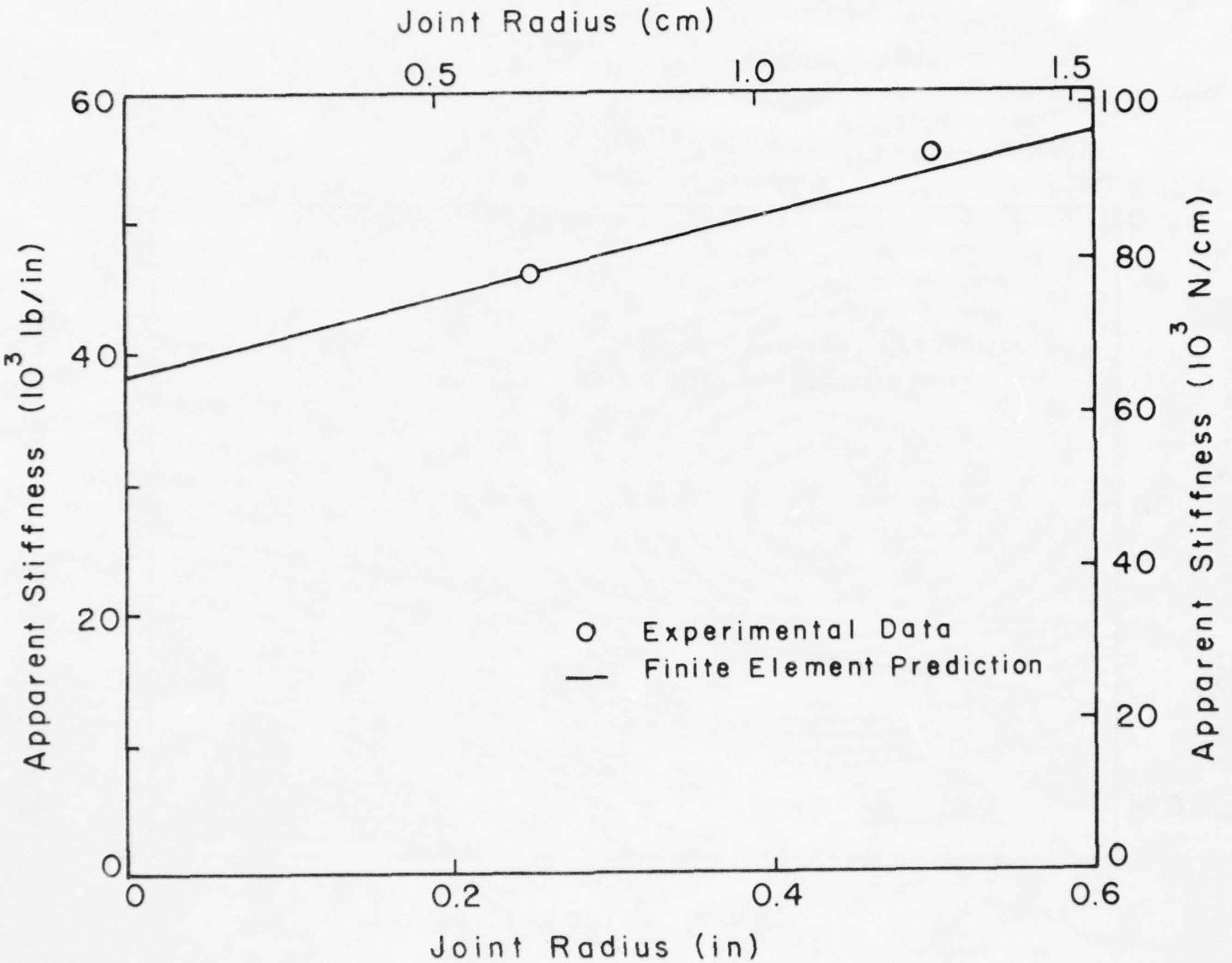

Figure 39: Influence of Joint Radius on Modulus
(Span Length = 8.0 inches)

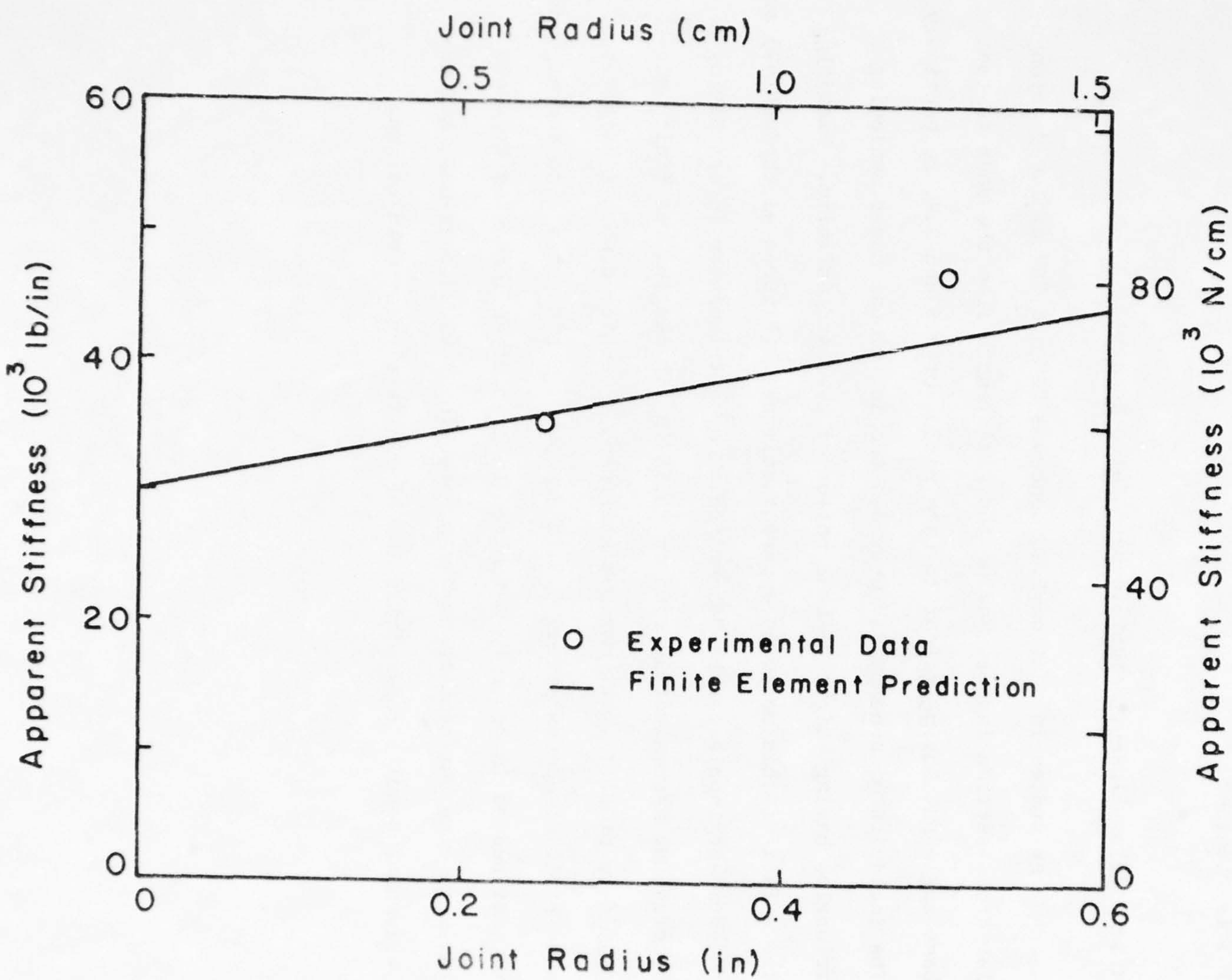

Figure 40: Influence of Joint Radius on Modulus
(Span Length = 10.0 inches)

prediction is 1% for all span and radius values investigated. Comparing equation (3) to experimental data, a maximum error of approximately 15% is obtained.

4.5 Modulus--Insert Height to Base Ratio Result

As stated in section 2.2, concepts "C" and "D" employed triangular cross-section inserts having the same length from the apex to the base angle but having height-to-base ratios of 0.5 and 2.4, respectively. The inclusion of concept "E" provides two additional cases employing triangles having height-to-base ratios of zero and infinity. Examining the effect of this ratio on apparent stiffness (Figures 41 through 44) an optimum apex angle can be determined. For a triangular insert having a hypoteneuse approximately 1.85 cm (0.73 in) in length, the finite element data predicts that maximum stiffness is achieved when a height-to-base ratio of approximately 0.5 is employed. This ratio also corresponds to that needed in order to maximize the area of an isosceles triangle having a constant hypoteneuse. As noted in previous sections, all experimental results fall within 10% of finite element predictions.

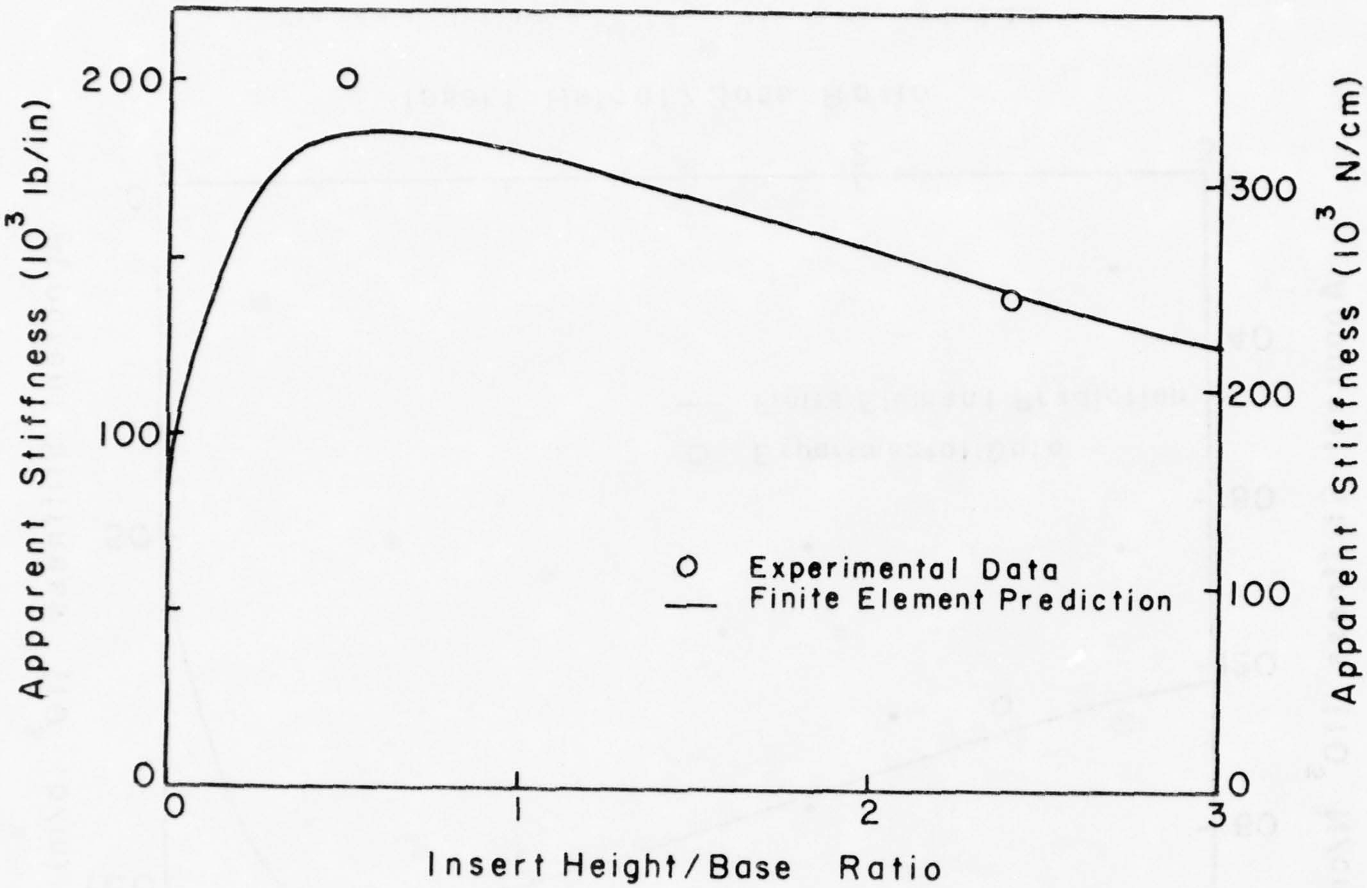

Figure 41: Influence of Height/Base Ratio on Modulus
(Span Length = 3.6 inches)

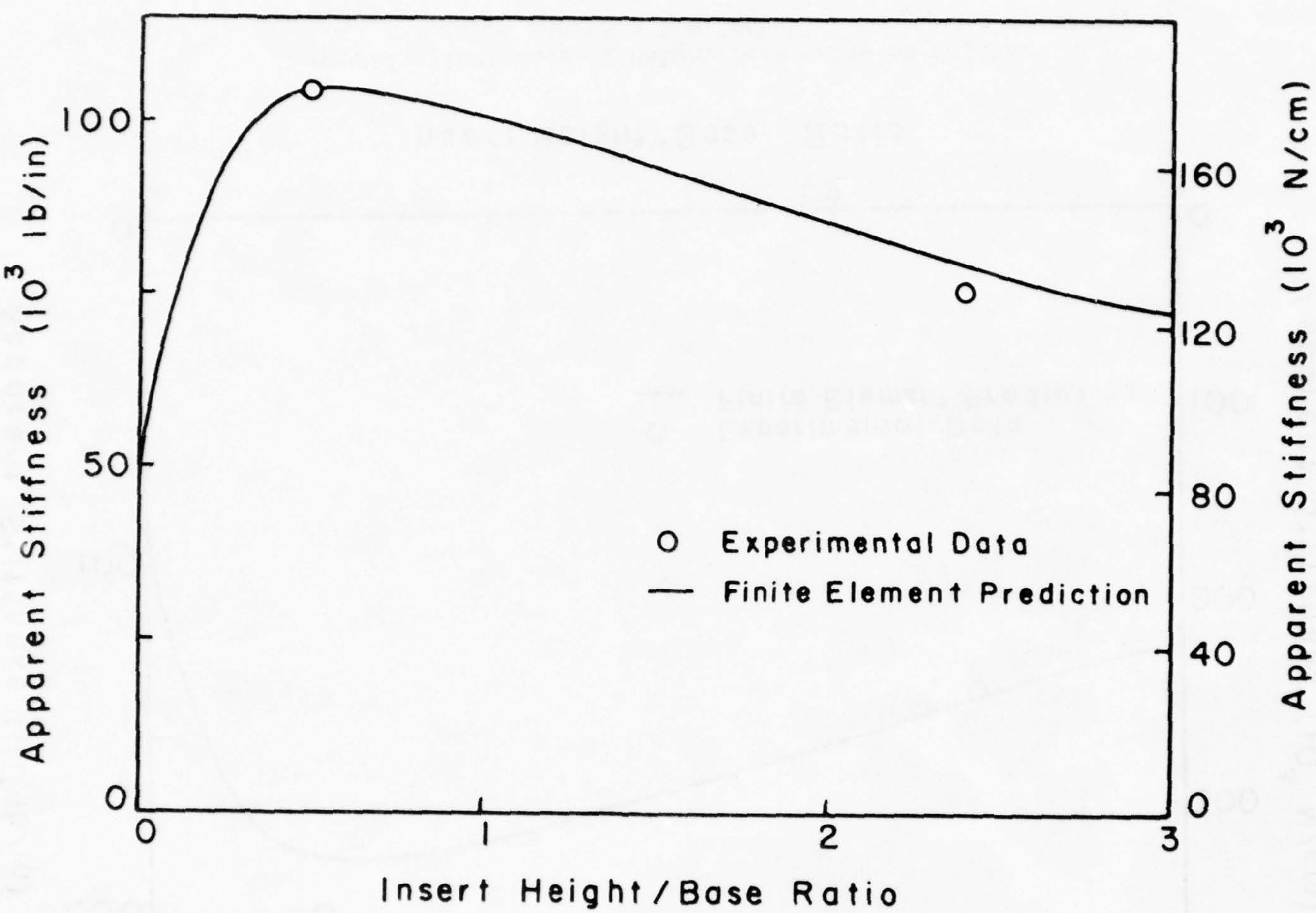

Figure 42: Influence of Height/Base Ratio on Modulus
(Span Length = 6.0 inches)

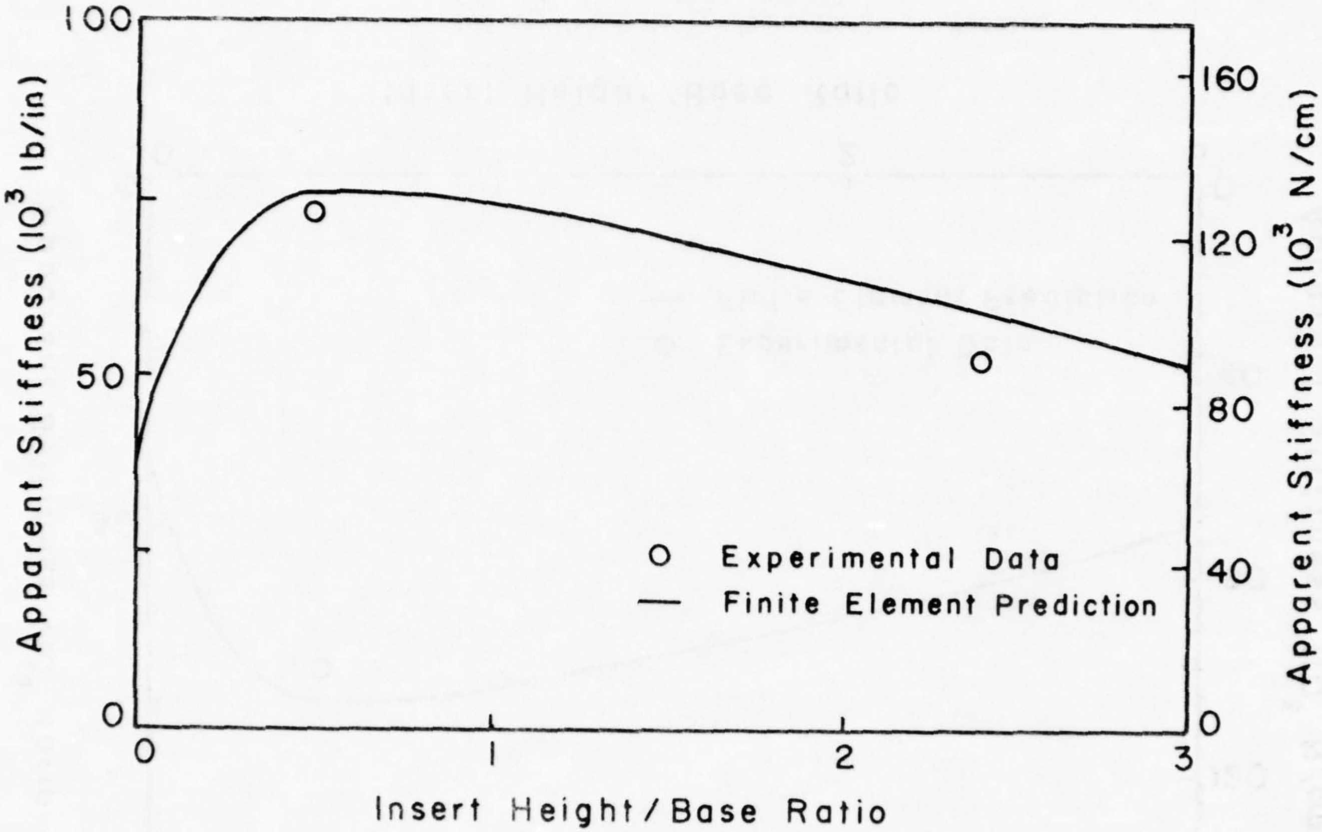

Figure 43: Influence of Height/Base Ratio on Modulus
(Span Length = 8.0 inches)

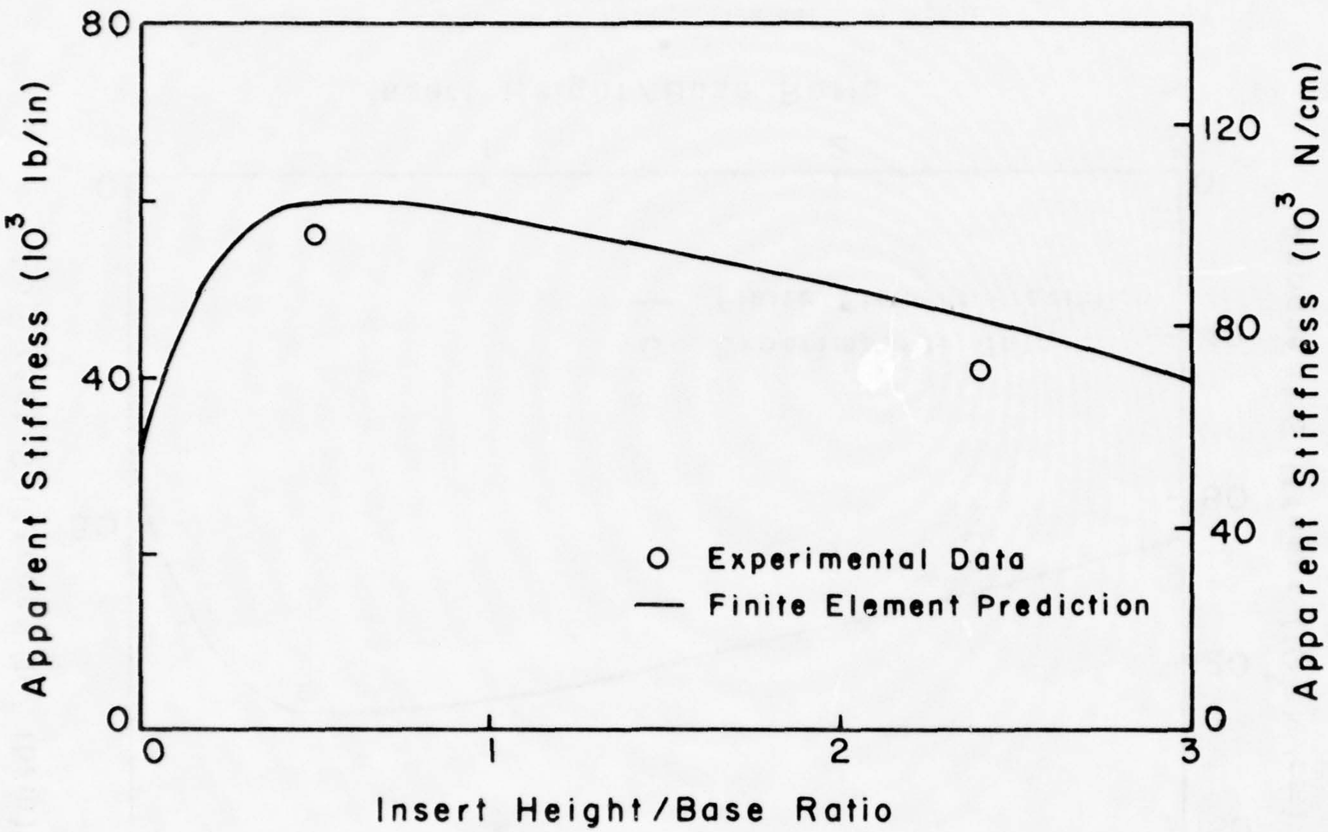

Figure 44: Influence of Height/Base Ratio on Modulus
(Span Length = 10.0 inches)

CHAPTER V

ANALYTICAL AND EXPERIMENTAL FAILURE RESULTS

5.1 Criteria for Failure

The second measure of concept evaluation and methodology comparison was the ultimate strength of the joint. Failure load for the experimental analysis was chosen as the maximum load achieved before catastrophic failure occurred; and therefore, did not necessarily represent the load at initial failure or crack propagation. Failure load for the finite element analysis was predicted by three different failure criteria. Elements in the vicinity of the joint, exclusive of the isotropic insert, were evaluated by both the Tsai-Wu and maximum stress failure criteria. The isotropic insert was analyzed using the maximum shear failure criterion. All three criteria employed assumed that ultimate failure and initial failure were simultaneous.

Ultimate strength allowables for individual sublaminates were obtained from the Air Force "Advanced Composite Design Guide" [3]. Reference was made for a high-strength graphite-epoxy composite and all strength values utilized are shown in Table 3. Interlaminar strengths were assumed to be equal to the transverse strengths of a unidirectional laminate. The isotropic shear strength of the adhesive used for the insert was that recommended by Gillespie and Pipes [1] and is also sup-

Table 3: Material Strength Allowables

	X_1^T MPa (ksi)	X_1^C MPa (ksi)	X_2^T MPa (ksi)	X_2^C MPa (ksi)	X_3^T MPa (ksi)	X_3^C MPa (ksi)	S_6 MPa (ksi)	S_4 MPa (ksi)
Unidirectional AS-3501-6 Graphite-Epoxy	1241 (180)	1241 (180)	55 (8)	207 (30)	55 (8)	207 (30)	83 (12)	83 (12)
$(\pm45/90_2)(0/\pm45/0)_2$ Graphite-Epoxy Laminates	641 (93)	538 (78)	358 (52)	345 (53)	55 (8)	207 (30)	83 (12)	83 (12)
$(0/\pm45/0)_n$ Graphite-Epoxy Laminates	703 (102)	703 (102)	138 (20)	248 (36)	55 (8)	207 (30)	83 (12)	83 (12)
$(\pm45/90_2)$ Graphite-Epoxy Laminates	138 (20)	248 (36)	703 (102)	703 (102)	55 (8)	207 (30)	83 (12)	83 (12)
$(\pm45/90_2)(0/\pm45/0)$ Graphite-Epoxy Laminates	483 (70)	469 (68)	483 (70)	469 (68)	55 (8)	207 (30)	83 (12)	83 (12)
$(\pm45)_n$ Graphite-Epoxy Laminates	152 (22)	152 (22)	152 (22)	152 (22)	55 (8)	207 (30)	83 (12)	83 (12)

Ultimate Adhesive Shear Strength $F^{SU}_{Adhesive} = 24.1$ MPa (3.5 ksi) plied in Table 3.

5.2 Tsai-Wu Failure Criterion

The Tsai-Wu failure criterion is a multiaxial failure analysis which utilizes all stress components in a single quadratic expression. For the lamina coordinate system, it is expressed in tensor notation as follows:

$$F_i \sigma_i + F_{ij} \sigma_i \sigma_j \geq 1 \qquad (i,j = 1,2,\ldots,5,6) \tag{4}$$

where F_i and F_{ij} are failure tensors which are functions of the material strength properties:

$$F_i = \frac{1}{X_i^t} - \frac{1}{X_i^c} \quad (i=1,2,3) \qquad F_i = \frac{1}{S_i^t} - \frac{1}{S_i^-} \quad (i=4,5,6)$$

$$F_{ii} = \frac{1}{X_i^t X_i^c} \quad (i=1,2,3) \qquad F_{ii} = \frac{1}{S_i^t S_i^-} \quad (i=4,5,6)$$

and

$$F_{ij} \leq \sqrt{F_{ii} F_{jj}} \qquad (i,j=1,2,\ldots,5,6) .$$

Failure is predicted when equation (4) is satisfied (the left-hand side of the equation exceeds 1.0). Applying this criterion for a state plane stress, equation (4) reduces to:

$$F_2 \sigma_2 + F_3 \sigma_3 + F_{22} \sigma_2^2 + F_{33} \sigma_3^2 + F_{44} \sigma_{23}^2 + 2F_{23} \sigma_2 \sigma_3 + 2F_{34} \sigma_3 \sigma_{23} + 2F_{24} \sigma_2 \sigma_{23} \geq 1 \tag{5}$$

where

$$F_2 = \frac{1}{X_2^t} - \frac{1}{X_2^c} \qquad F_{22} = \frac{1}{X_2^t\, X_2^c} \qquad F_{23} = \sqrt{F_{22}\, F_{33}}$$

$$F_3 = \frac{1}{X_3^t} - \frac{1}{X_3^c} \qquad F_{33} = \frac{1}{X_3^t\, X_3^c} \qquad F_{34} = \sqrt{F_{33}\, F_{44}}$$

$$F_{44} = \frac{1}{S_4^2} \qquad F_{24} = \sqrt{F_{22}\, F_{44}}$$

and X_i^t , X_i^c , S_i are supplied in Table 3. This quadratic expression can be solved to obtain the factor of safety, N , where

$$N = \frac{-b \pm \sqrt{b^2 - 4ac}}{2a} \tag{6}$$

and

$$N = \text{Factor of Safety} = \frac{\text{Failure Load}}{\text{Applied Load}}$$

$$a = F_{22}\,\sigma_2^2 + F_{33}\,\sigma_3^2 + F_{44}\,\sigma_{23}^2 + 2F_{23}\,\sigma_2\,\sigma_3$$

$$+ 2F_{34}\,\sigma_3\,\sigma_{23} + 2F_{24}\,\sigma_2\,\sigma_{23}$$

$$b = F_2\,\sigma_2 + F_3\,\sigma_3$$

$$c = -1$$

Inputting the stress components σ_1 , σ_2 , σ_{23} resulting from a single point load at the top of the spar, the resulting factor of safety, N , is equal to the predicted failure load.

5.3 Maximum Stress Failure Criterion

The second failure criterion used to evaluate the graphite-epoxy sublaminates was maximum stress. This criterion predicts failure when any one of the stress components reaches or exceeds the corresponding material strength. For the lamina coordinate system, failure is predicted when at least one of the following three equations is satisfied,

$$\sigma_i \geq X_i^t \qquad (\sigma_i > 0) \qquad (i=1,2,3)$$

$$-\sigma_i \geq X_i^c \qquad (\sigma_i < 0) \qquad (i=1,2,3)$$

$$|\sigma_i| \geq S_i \qquad (i=4,5,6)$$

where X_i^t = maximum normal tensile stress

X_i^c = maximum normal compressive stress

S_i = maximum shear stress

Similar to the Tsai-Wu analysis, the predicted failure load can be obtained as the minimum ratio of the maximum material strength to the corresponding stress component due to a point load applied at the top of the spar or

$$N_1 = \frac{X_2^t}{\sigma_2} \ (\sigma_2 > 0) \qquad N_2 = -\frac{X_2^c}{\sigma_2} \ (\sigma_2 < 0)$$

$$N_3 = \frac{X_3^t}{\sigma_3} \ (\sigma_3 > 0) \qquad N_4 = -\frac{X_3^c}{\sigma_3} \ (\sigma_3 < 0)$$

$$N_5 = \frac{S_4}{|\sigma_{23}|}$$

where N = failure load

σ_i = stress due to applied point load

and ultimate load is the minimum N value obtained.

5.4 Maximum Shear Failure Criterion

Utilized only for the prediction of insert or adhesive failure, the maximum shear criterion requires that yielding of the insert material initiates failure. Therefore, failure was assumed to occur when the following equation was satisfied

$$\sigma_{23_{max}} \geq \frac{F^{tu}_{adh}}{2} = F^{su}_{adh}$$

where F^{tu}_{adh} = ultimate adhesive tensile strength

F^{su}_{adh} = ultimate adhesive shear strength

Obtaining σ_2, σ_3 and σ_{23} from the finite element analysis, $\sigma_{23_{max}}$ was defined as

$$\sigma_{23_{max}} = \left| \left[\left(\frac{\sigma_2 - \sigma_3}{2} \right)^2 + \sigma_{23}^2 \right]^{1/2} \right| .$$

The predicted failure load, N, was determined from

$$N = \frac{F^{su}_{adh}}{\sigma_{23_{max}}}$$

where $\sigma_{23_{max}}$ resulted from the application of a point load on the top of the spar.

A value of 12.0 MPa (1.75 ksi) was used for the ultimate adhesive shear strength as recommended by Gillespie and Pipes [1]. Although this shear strength yielded predicted failure loads which agreed qualitatively with observed crack initiation loads, it provided a poor prediction of the ultimate load for a given concept. However, utilizing a shear strength two times the above value, good quantitative predictions of joint ultimate load can be obtained.

5.5 Ultimate Load--Span Results

The predicted failure load for all three failure criteria and the average experimental results are plotted versus span length for all concepts in Figures 45 through 49. Numerical results are tabulated in Table 4. Examining the responses for concepts "A", "C" and "D" (Figures 45, 47 and 48, respectively), the maximum shear criteria predicts failure by interlaminar debonding between the insert and the graphite-epoxy overlap (see Figure 51 and section 5.6 for initial failure locations). Maximum stress and Tsai-Wu criteria predict in-plane failure at the top of the overlap above the lower corners of the insert (Figure 51) at a load greater than that for insert-overlap debonding. For all three concepts the Tsai-Wu prediction was conservative when compared to maximum stress, but the two criteria bound the experimental results. A different response was exhibited by concept "B" as shown in Figure 46. For this case, all predicted failure loads fell well below the experi-

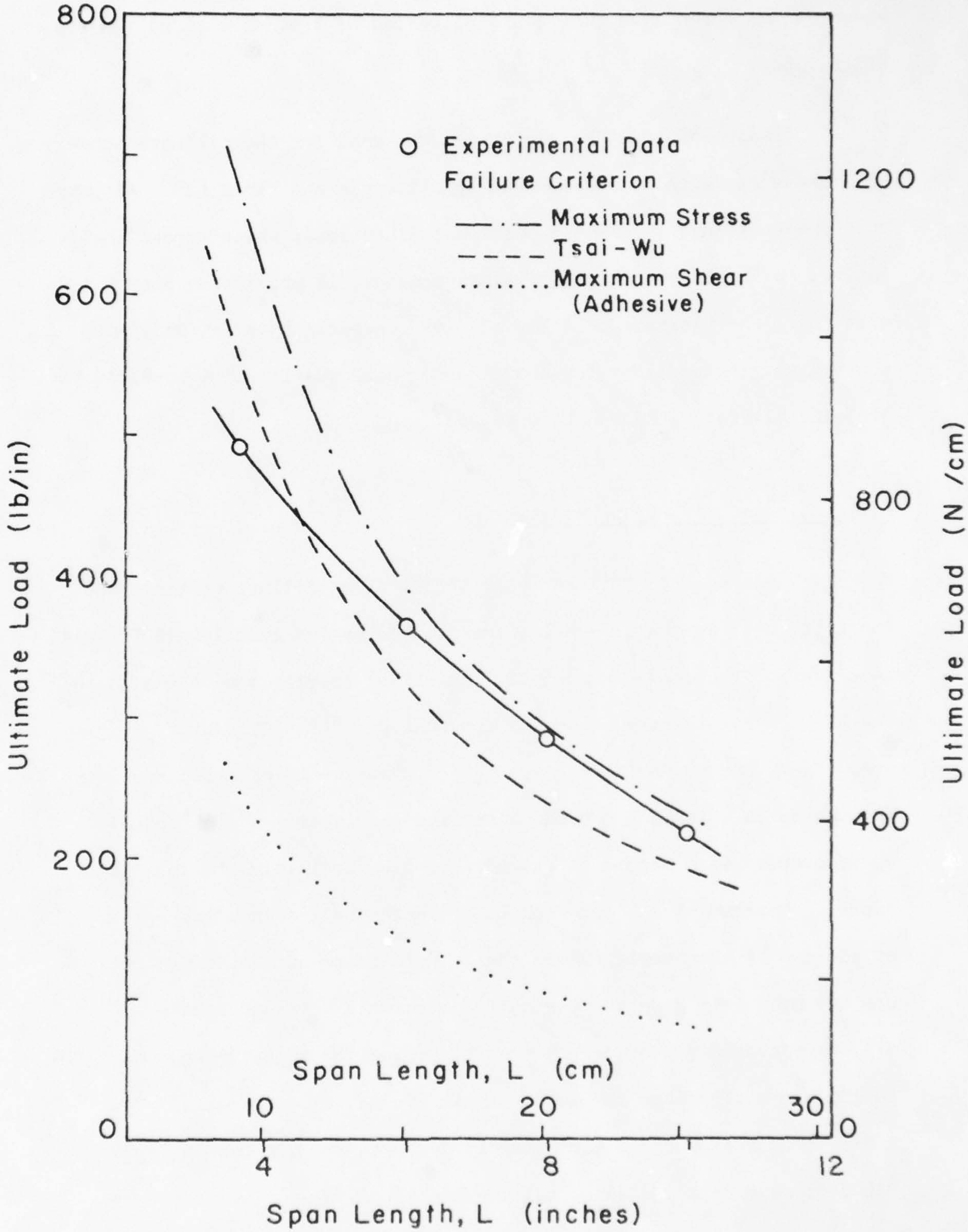

Figure 45: Influence of Span on Ultimate Load for Concept "A"

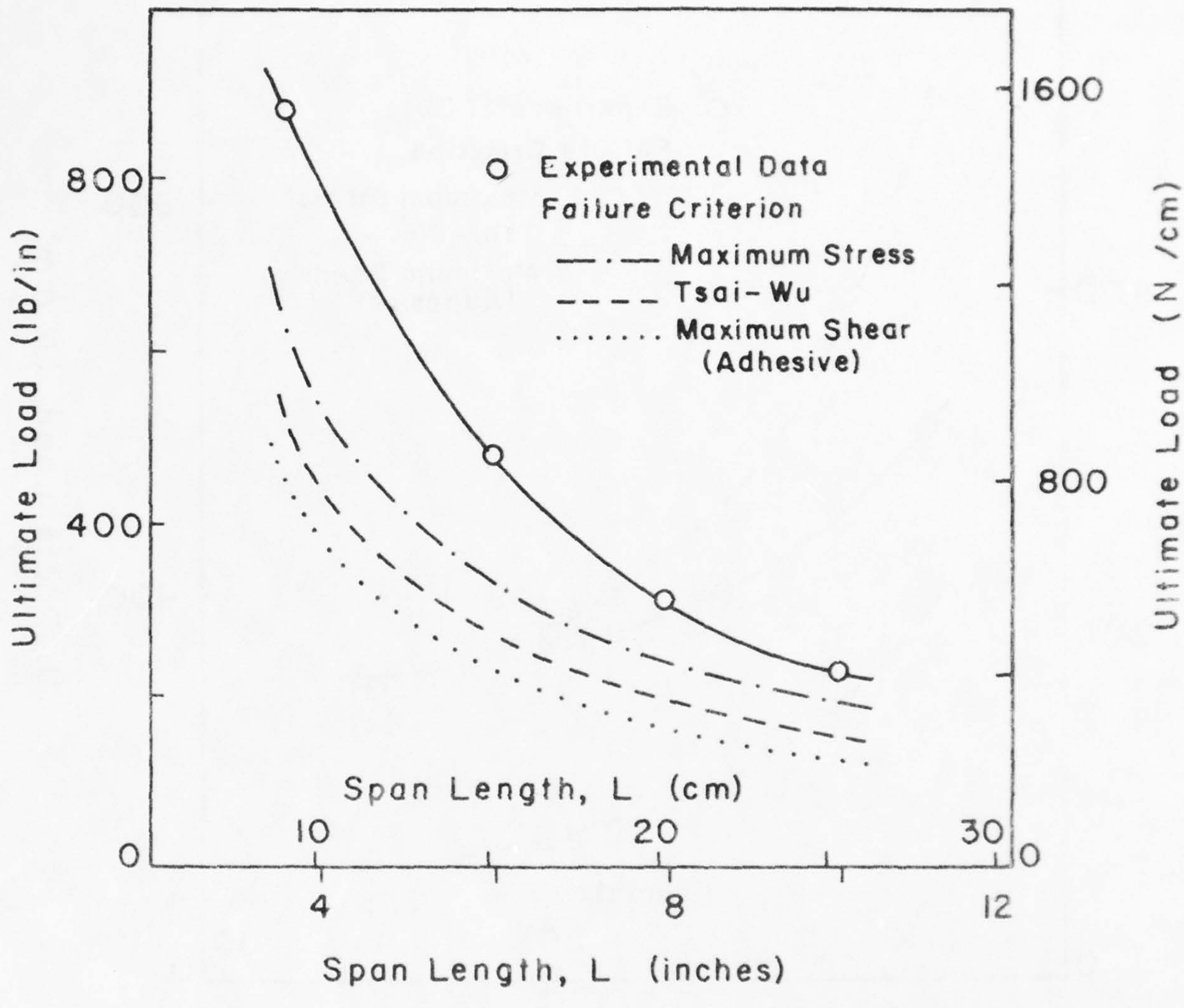

Figure 46: Influence of Span on Ultimate Load for Concept "B"

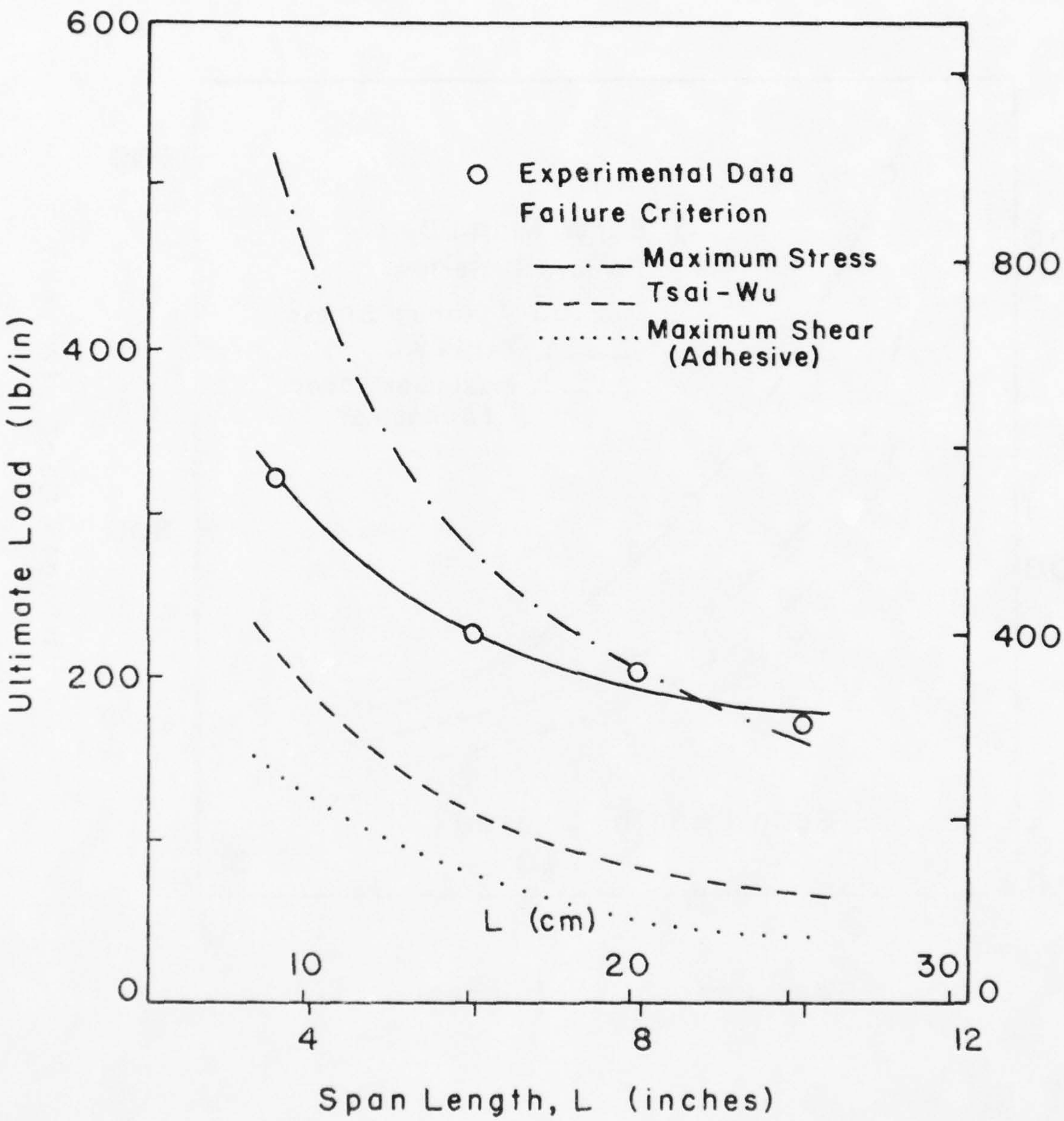

Figure 47: Influence of Span on Ultimate Load for Concept "C"

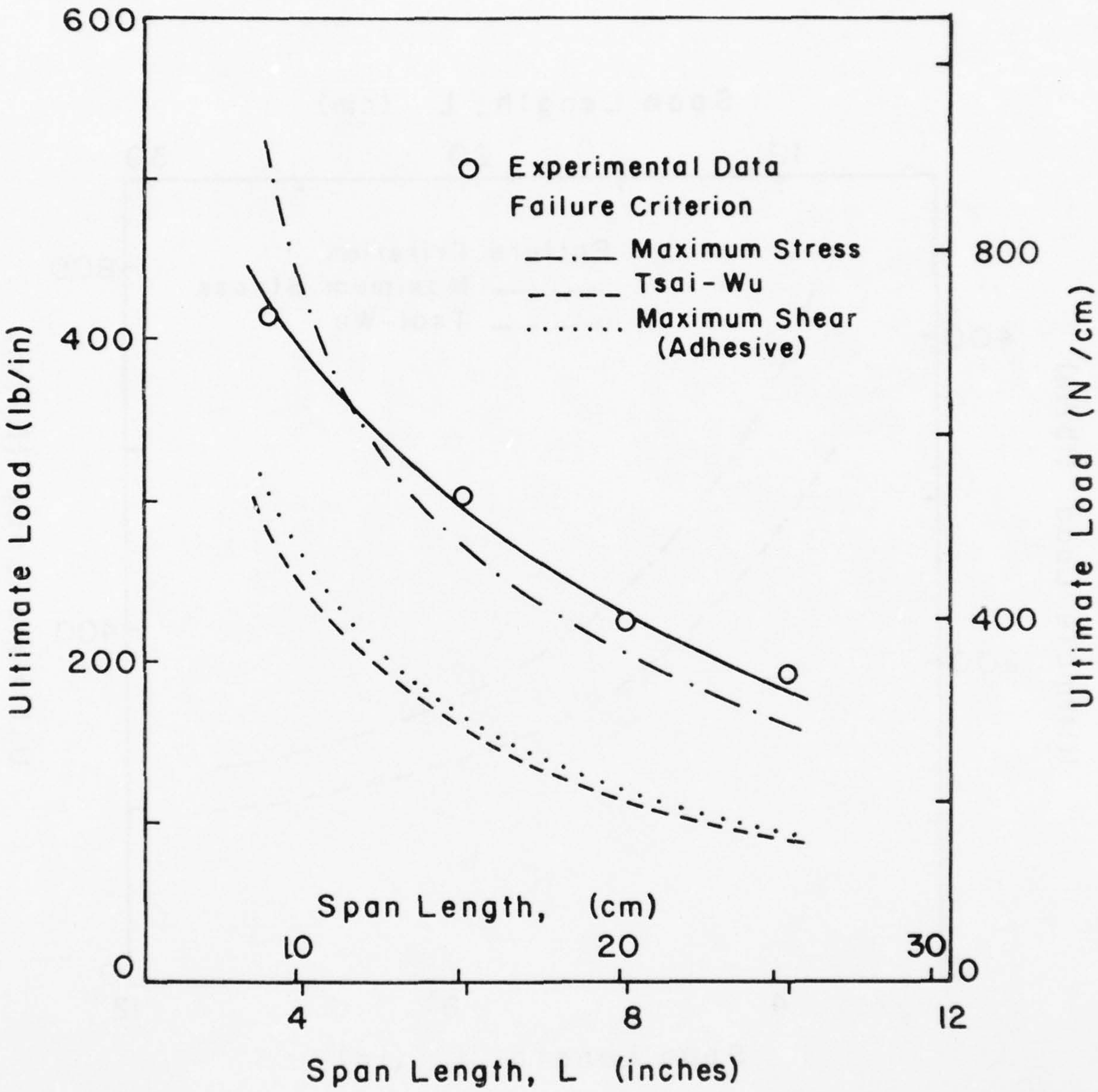

Figure 48: Influence of Span on Ultimate Load for Concept "D"

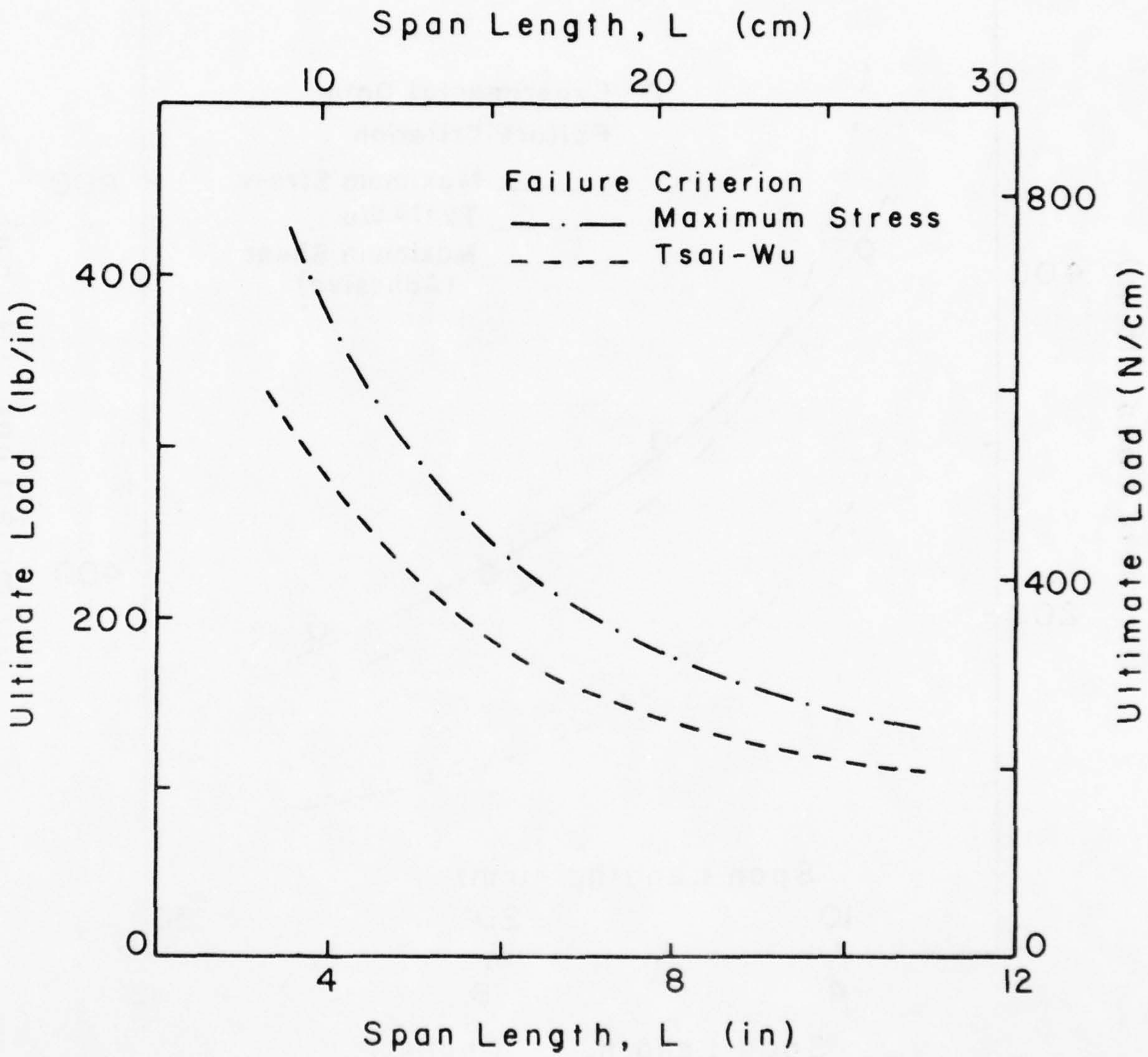

Figure 49: Influence of Span on Ultimate Load for Concept "E"

Table 4: Summary of Ultimate Load versus Span Results

Concept	Span	ULTIMATE STRENGTHS			
		Finite Element Results			Exper.
		Adhesive	Tsai-Wu	Max Strs	
	inches	lb/in	lb/in	lb/in	lb/in
A	3.6	247	562	680	491
A	6.0	138	322	393	365
A	8.0	101	238	290	284
A	10.0	80	189	230	217
B	3.6	451	515	619	882
B	6.0	225	272	330	479
B	8.0	159	195	238	311
B	10.0	123	152	186	231
C	3.6	137	215	507	319
C	6.0	74	115	277	224
C	8.0	54	83	200	200
C	10.0	42	65	157	170
D	3.6	300	278	495	412
D	6.0	165	156	270	301
D	8.0	118	114	201	223
D	10.0	93	90	159	190
E	3.6	-	297	395	-
E	6.0	-	184	236	-
E	8.0	-	139	176	-
E	10.0	-	112	141	-

mental findings.

For concept "E" (Figure 49), no experimental data was obtained. However, the predicted response curves show the same inverse relationship between strength and span as that exhibited by all other concepts. The Tsai-Wu criteria is conservative with respect to the maximum stress criteria for this concept as well.

Examination of all failure results for a given span indicate that predicted ultimate load-span responses are proportional to each other and, in general, are of the same form as experimental results as demonstrated by Table 5. For concept "B", the approximate relation between theoretical and experimental ultimate loads predicts failure load to within 10% of experimental findings. Although this error is indicative of most test values, one data point does differ by 40%.

Comparing experimental ultimate load results for all concepts and spans (Figure 50), two trends can be noted. First, the radial geometries possess the greatest strength with strength increasing as the insert radius increases (see section 5.7). For the triangular geometries, the insert of largest aspect ratio yielded the greatest strength (see section 5.8). As was the case with apparent stiffness, the influence of local joint geometry diminishes rapidly with increases in span length.

5.6 Failure Initiation Sites

Although finite element prediction of failure initiation sites was straight-forward, visual inspection during specimen testing was quite

Table 5: Proportionality of Ultimate Load versus Span Results

Concept	$\frac{F_{ad}}{F_{ms}}$	$\frac{F_{tw}}{F_{ms}}$	$\frac{F_{ex}}{F_{ms}}$
A	2.84	1.22	1.14
B	1.46	1.21	0.74
C	3.72	2.40	1.14
D	1.68	1.76	0.94
E	-	1.28	-

F_{ad} = Maximum shear failure load prediction (Adhesive)

F_{tw} = Tsai-Wu failure load prediction

F_{ms} = Maximum stress failure load prediction

F_{ex} = Experimental failure load

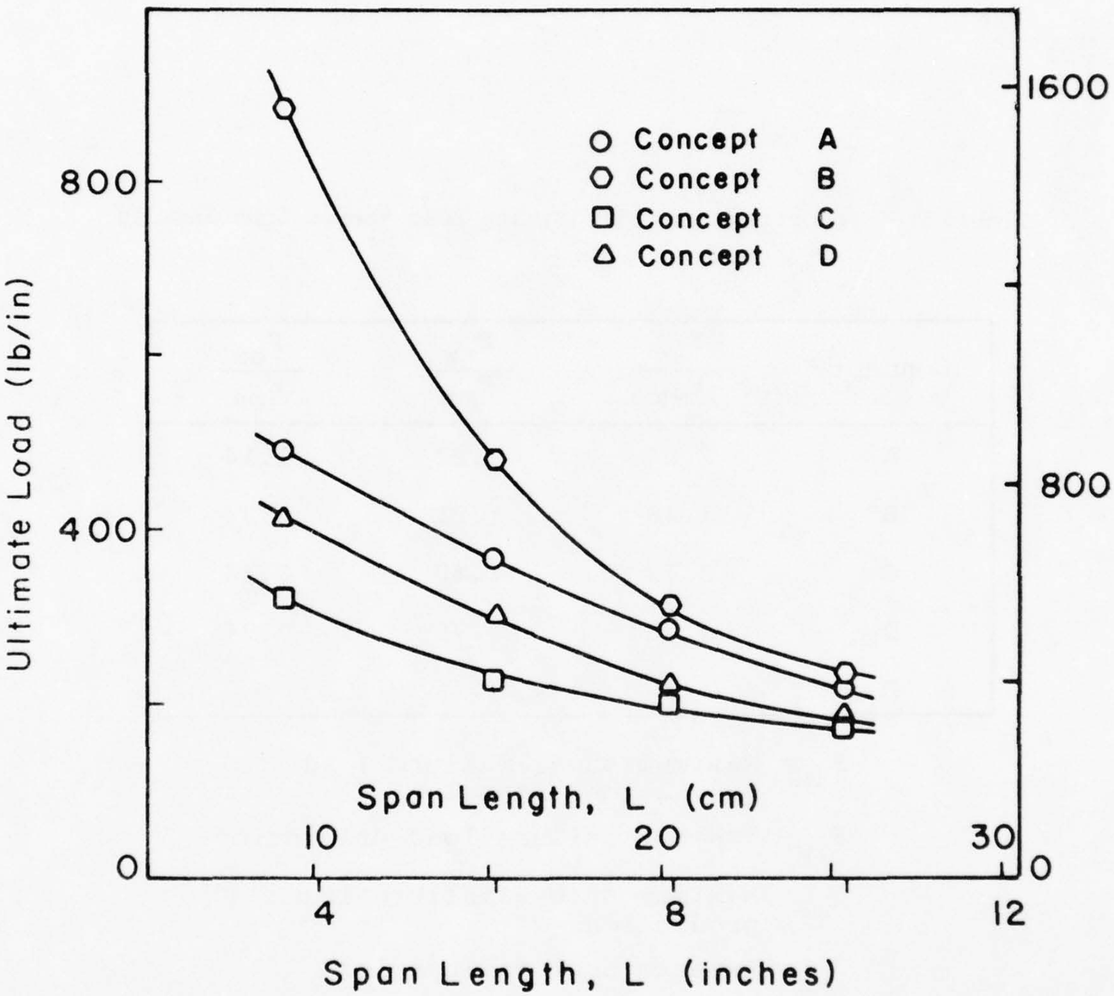

Figure 50: Experimental Determination of the Influence of Geometry and Span on Ultimate Load

inconclusive in determining sites of crack initiation. Initial failure locations are provided in Figure 51 for both the theoretical and experimental analysis. For most test specimens, insert debonding occurred at loads significantly below final joint failure.

Although Figure 51 is self-explanatory, several points should be noted. As indicated by experimental data scatter, the use of visual inspection must be regarded as only a good approximation. Due to the size of the area of interest, much difficulty was encountered in trying to distinguish first crack initiation.

Failures in concept "B" were, in general, catastrophic while crack initiation and propagation was noticeable in other concepts. As span length increased, failures became increasingly violent due to the large midspan deflections prior to failure. Inter-insert failures for concept "D" occurred at the insert "mold lines" for samples 12-1 through 12-4 (see section C.6). This inter-insert failure was not noted in samples having an insert fabricated in one step.

For concepts "A" through "D", Tsai-Wu and maximum stress criteria both predicted in-plane fiber failure at the upper surface of the overlap directly above the lower corners of the insert. Only for concept "E" did the two criteria differ. For this concept, maximum stress predicted an interlaminar failure at the center of the spar adjacent to the wingskin, while the Tsai-Wu criterion predicted an in-plane failure where the top of the overlap meets the spar.

Examination of failed specimens (Figures 52 through 91) offers

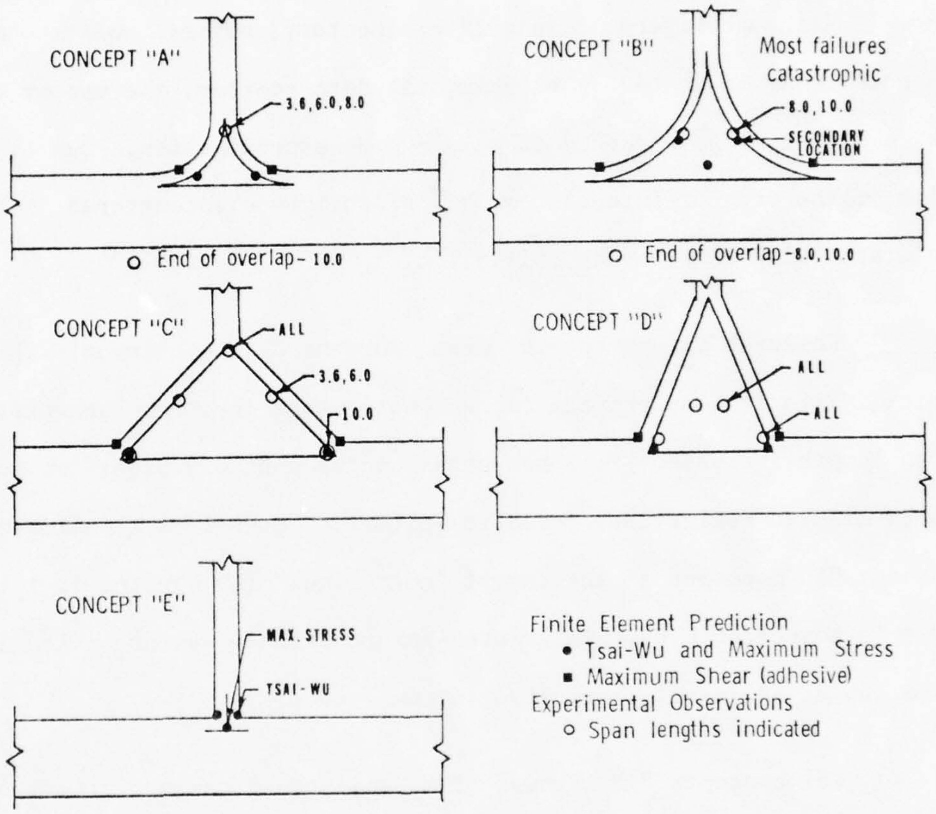

Figure 51: Initial Failure Locations

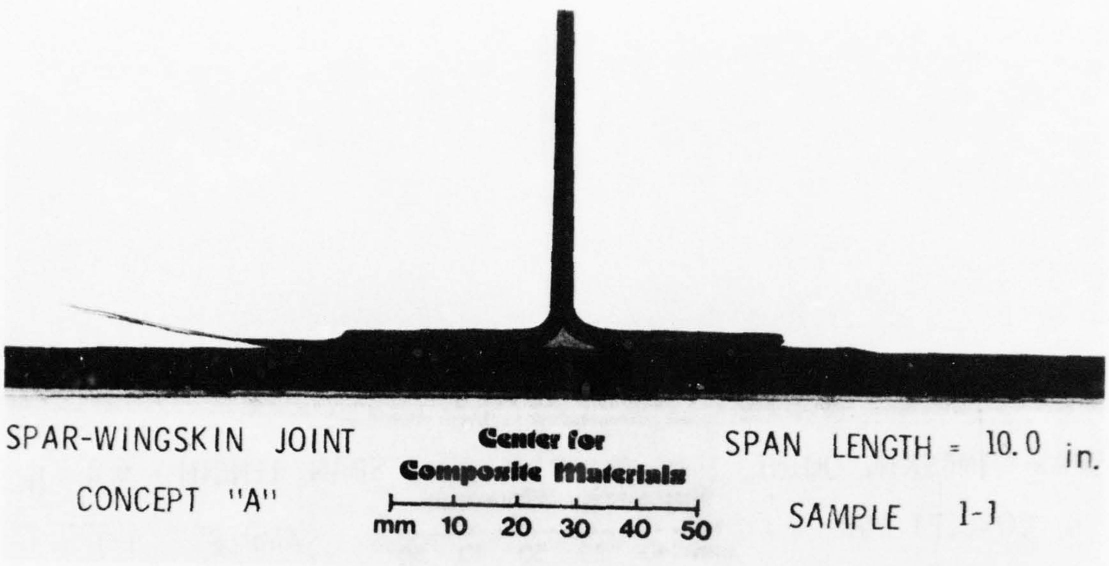

Figure 52: Specimen 1-1; Failed (Concept A; 10.0 inch span)

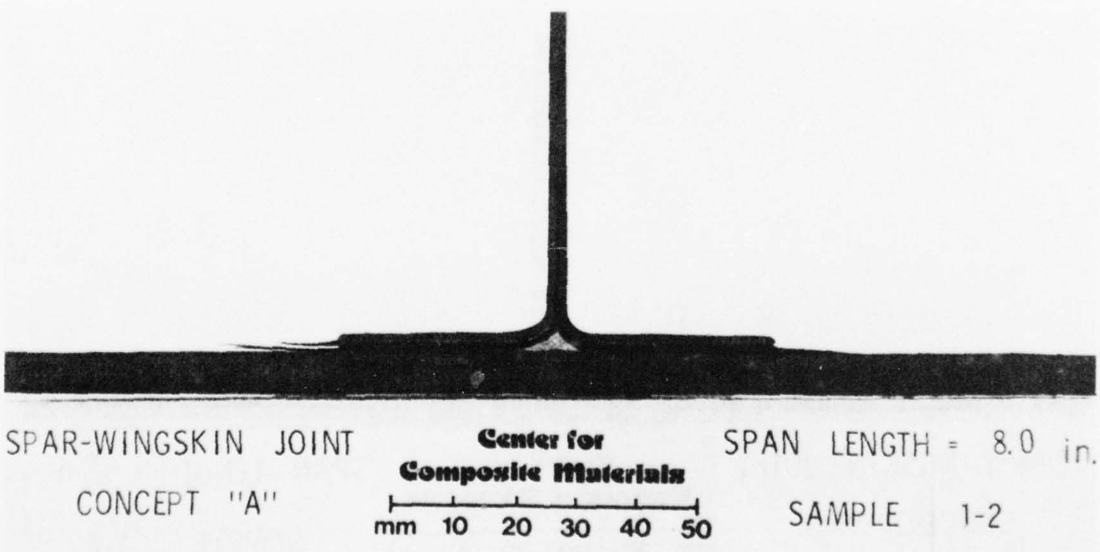

Figure 53: Specimen 1-2; Failed (Concept A; 8.0 inch span)

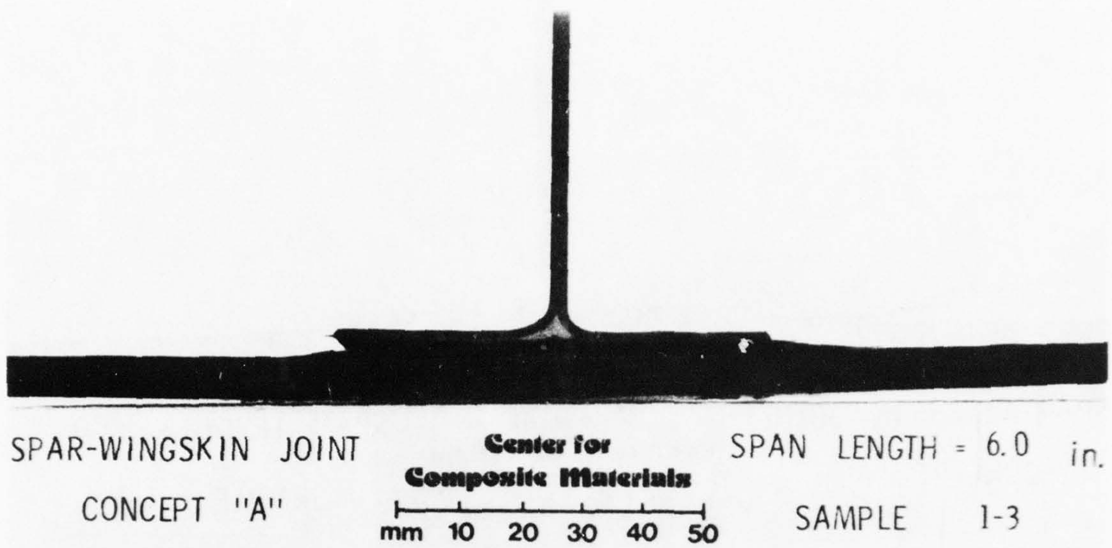

Figure 54: Specimen 1-3; Failed (Concept A; 6.0 inch span)

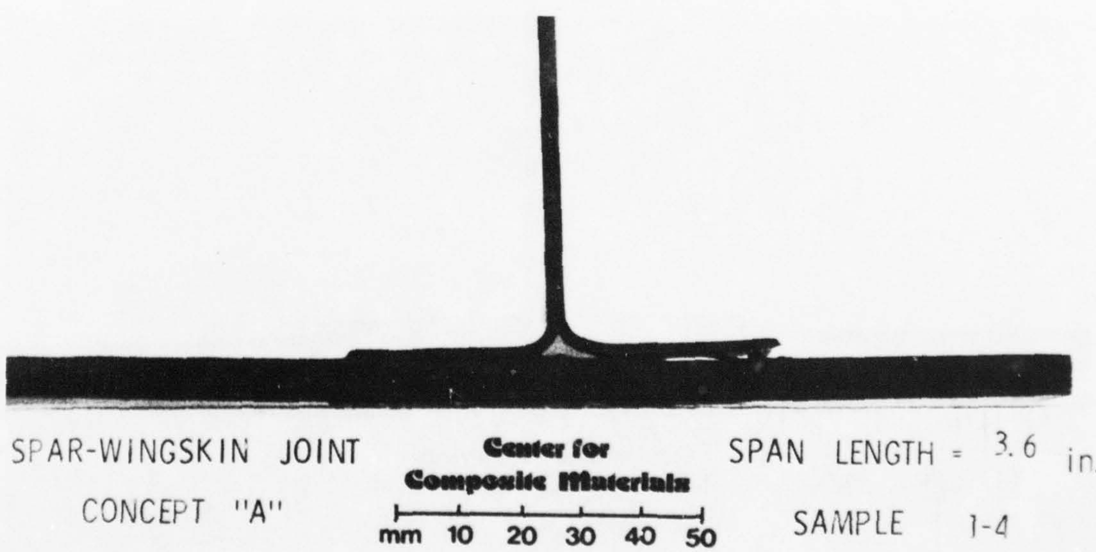

Figure 55: Specimen 1-4; Failed (Concept A; 3.6 inch span)

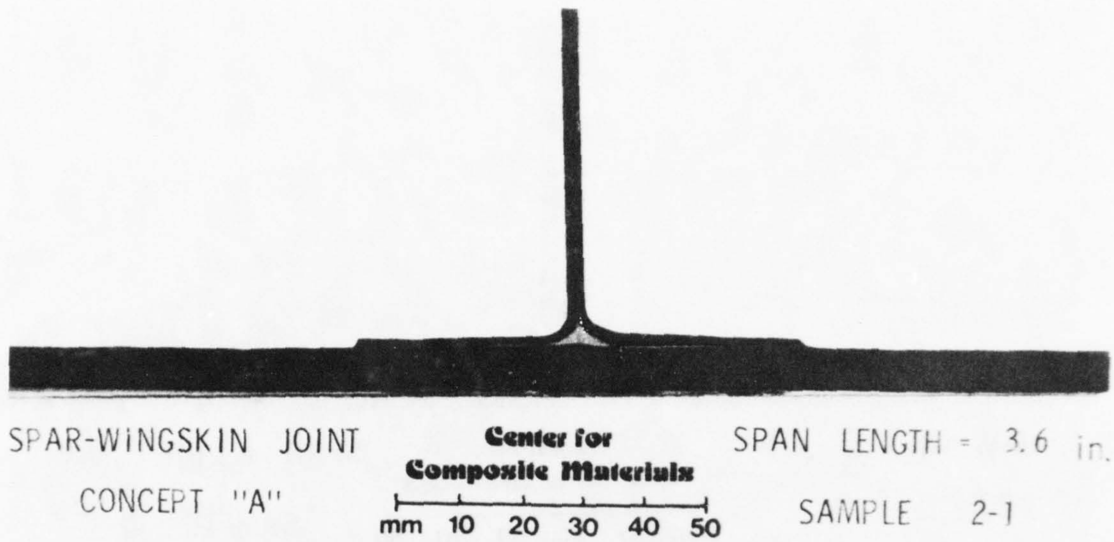

Figure 56: Specimen 2-1; Failed (Concept A; 3.6 inch span)

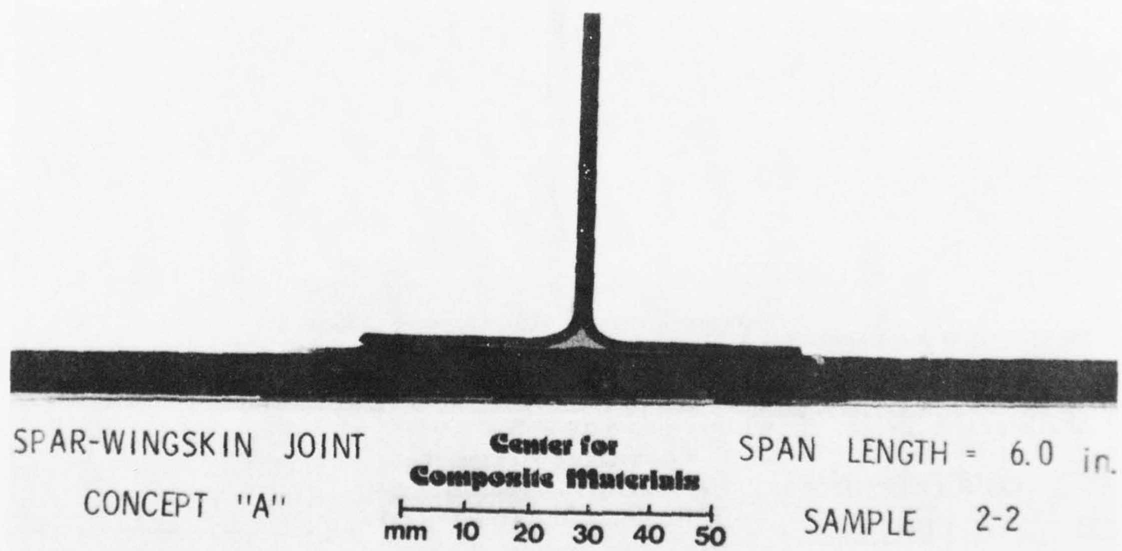

Figure 57: Specimen 2-2; Failed (Concept A; 6.0 inch span)

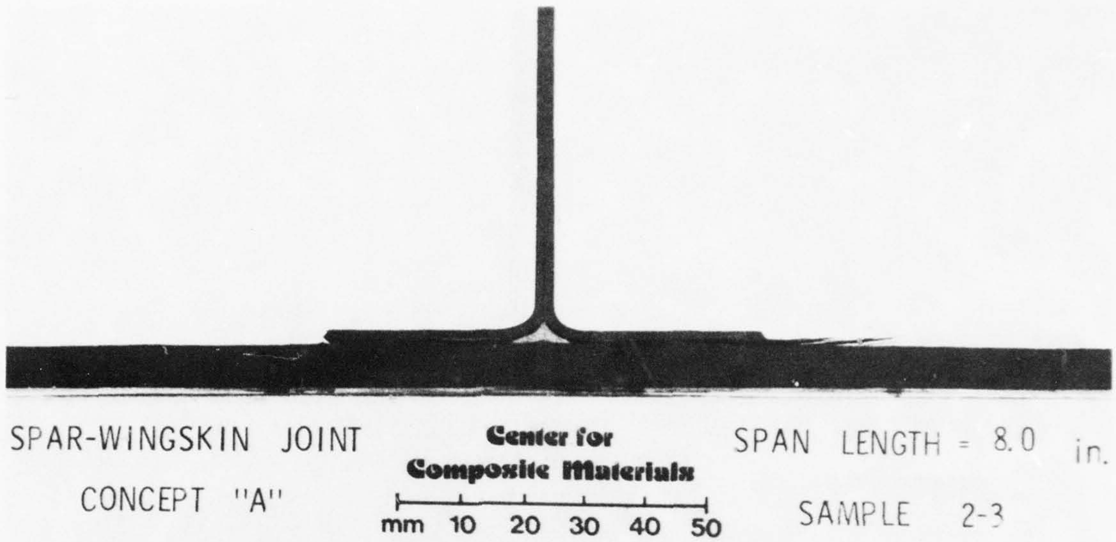

Figure 58: Specimen 2-3; Failed (Concept A; 8.0 inch span)

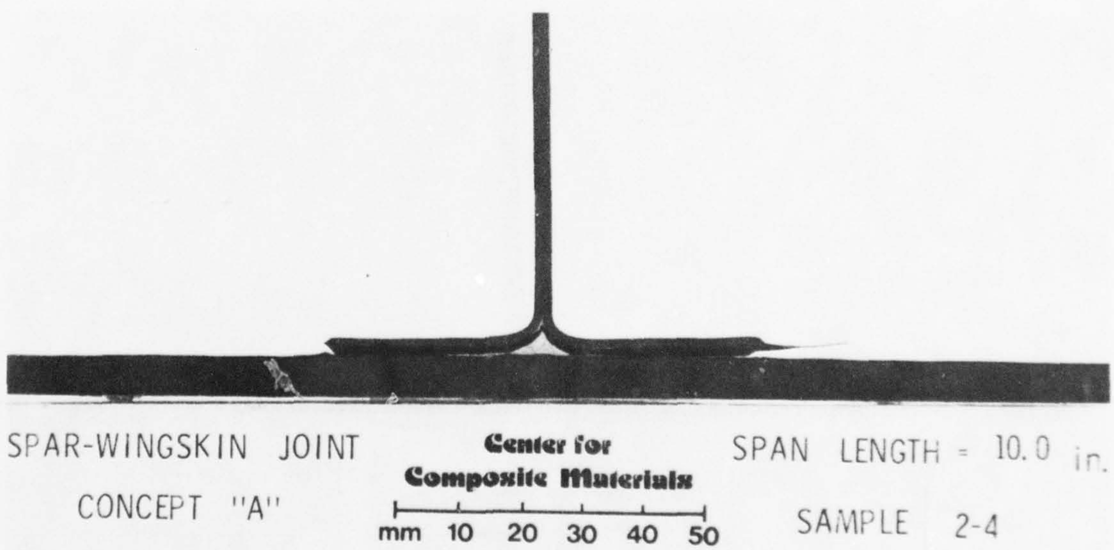

Figure 59: Specimen 2-4; Failed (Concept A; 10.0 inch span)

AD-A072 426 DELAWARE UNIV . NEWARK CENTER FOR COMPOSITE MATERIALS F/G 13/5
DESIGN OF THE SPAR-WINGSKIN JOINT.(U)
MAR 79 R D COPE, R B PIPES F33615-77-C-3132
UNCLASSIFIED AFFDL-TR-79-3015 NL

2 OF
AD
A072426

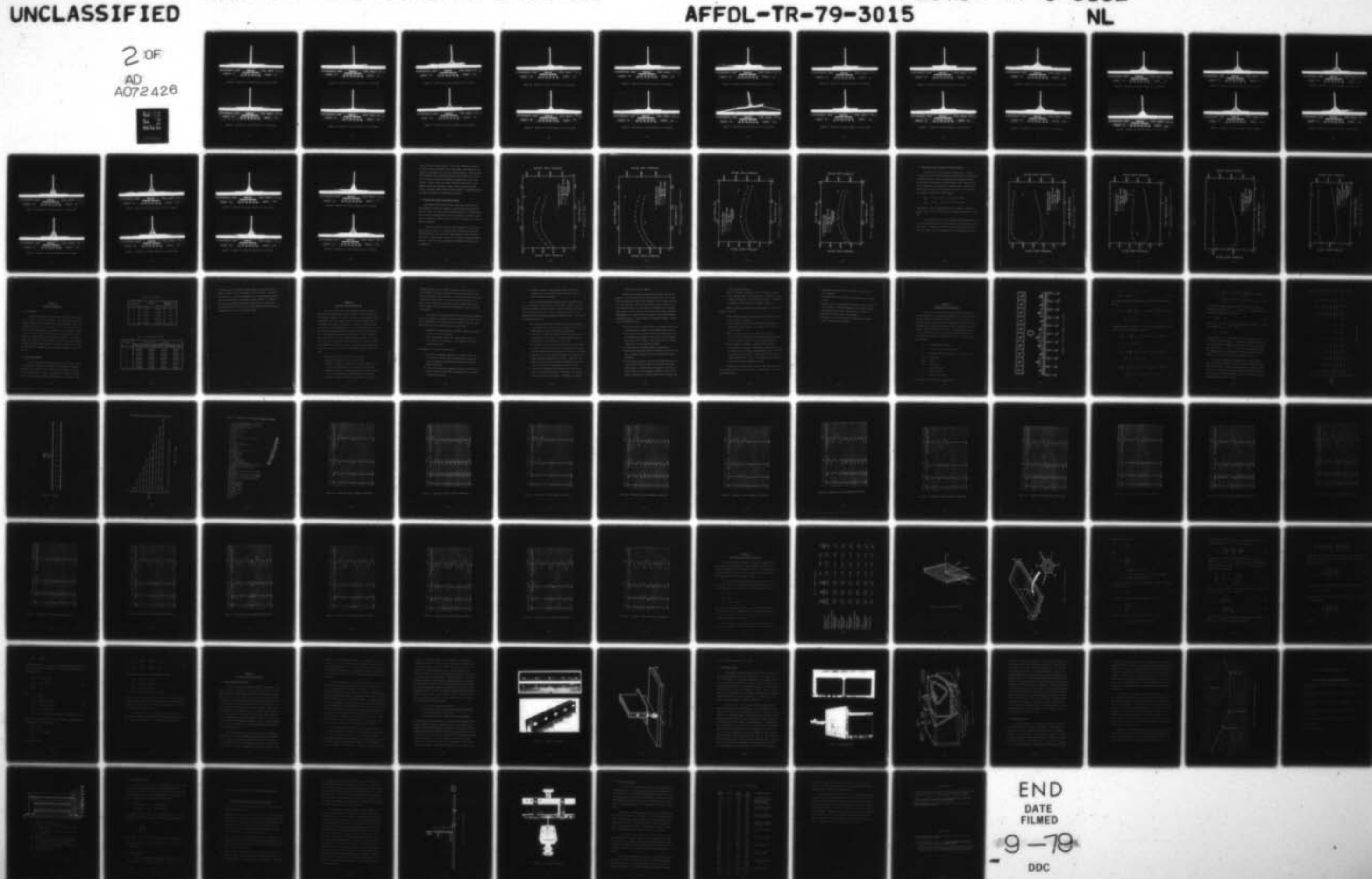

END
DATE
FILMED
9-79
DDC

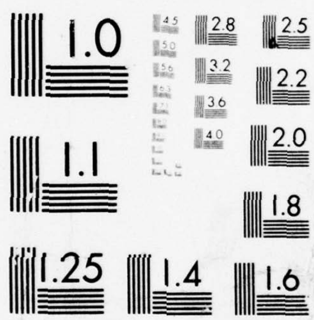

MICROCOPY RESOLUTION TEST CHART
NATIONAL BUREAU OF STANDARDS-1963-A

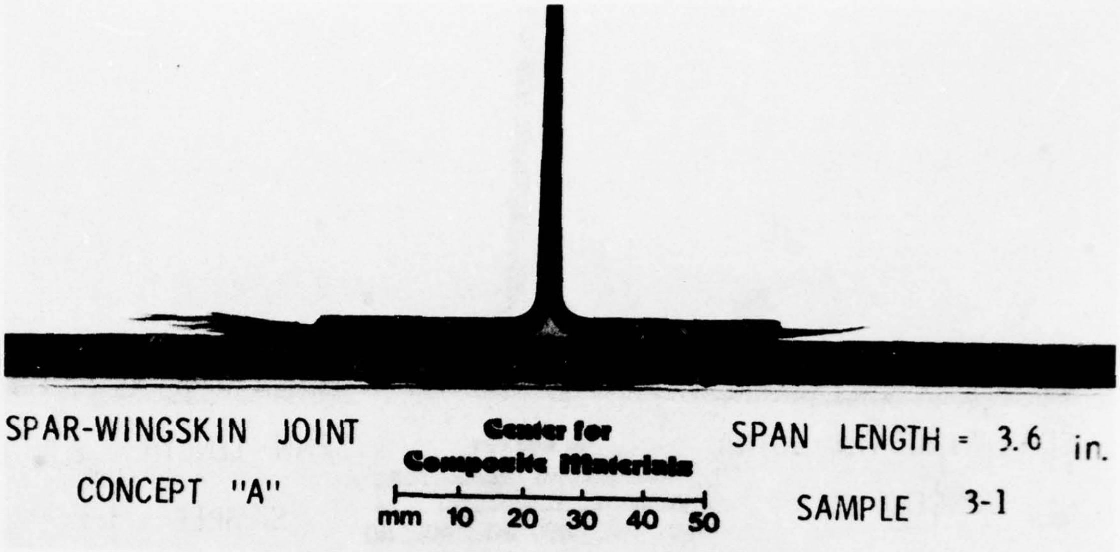

Figure 60: Specimen 3-1; Failed (Concept A; 10.0 inch span)

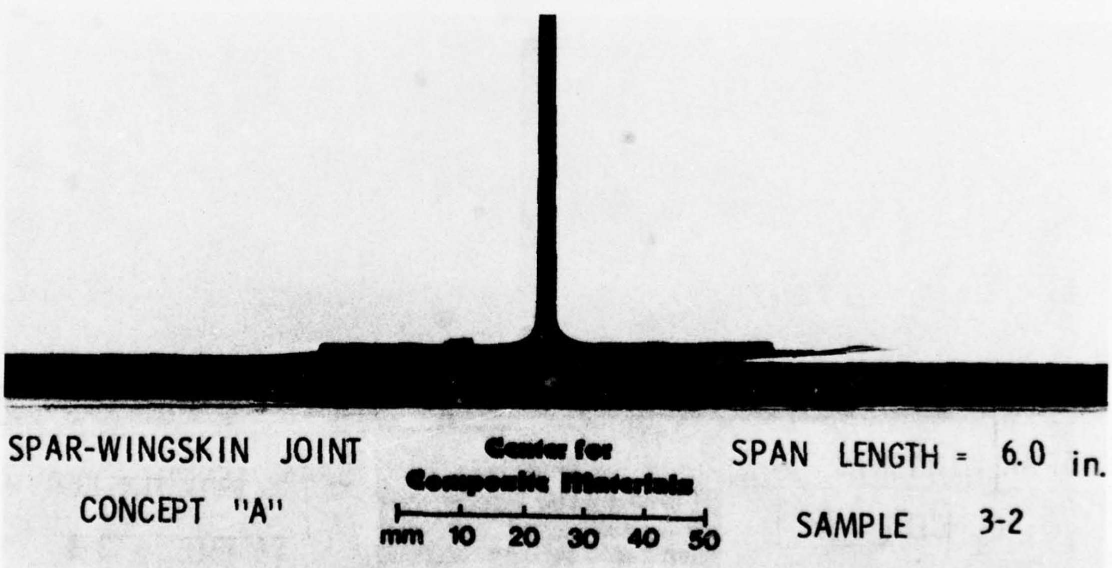

Figure 61: Specimen 3-2; Failed (Concept A; 8.0 inch span)

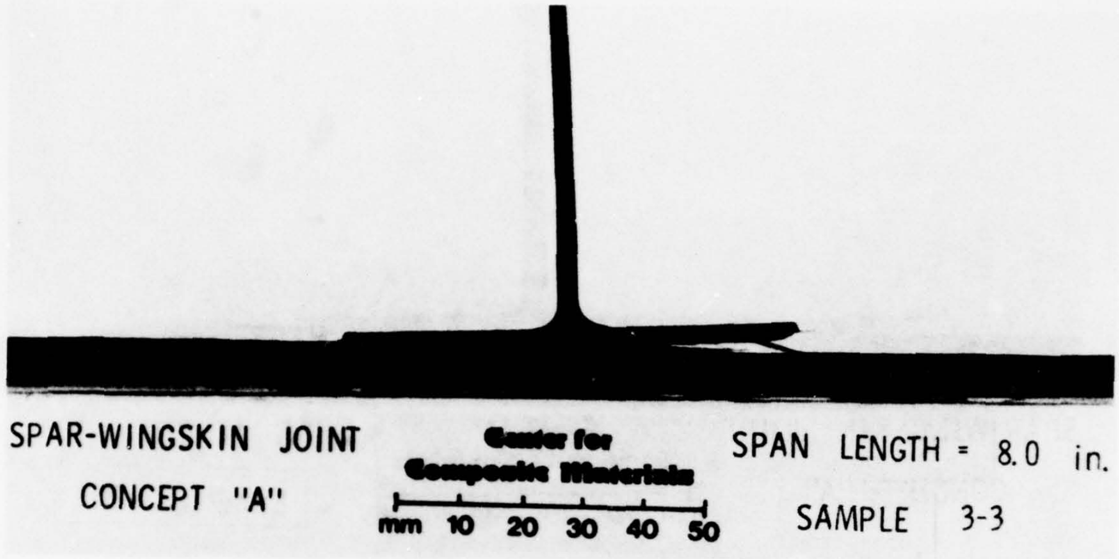

Figure 62: Specimen 3-3; Failed (Concept A; 6.0 inch span)

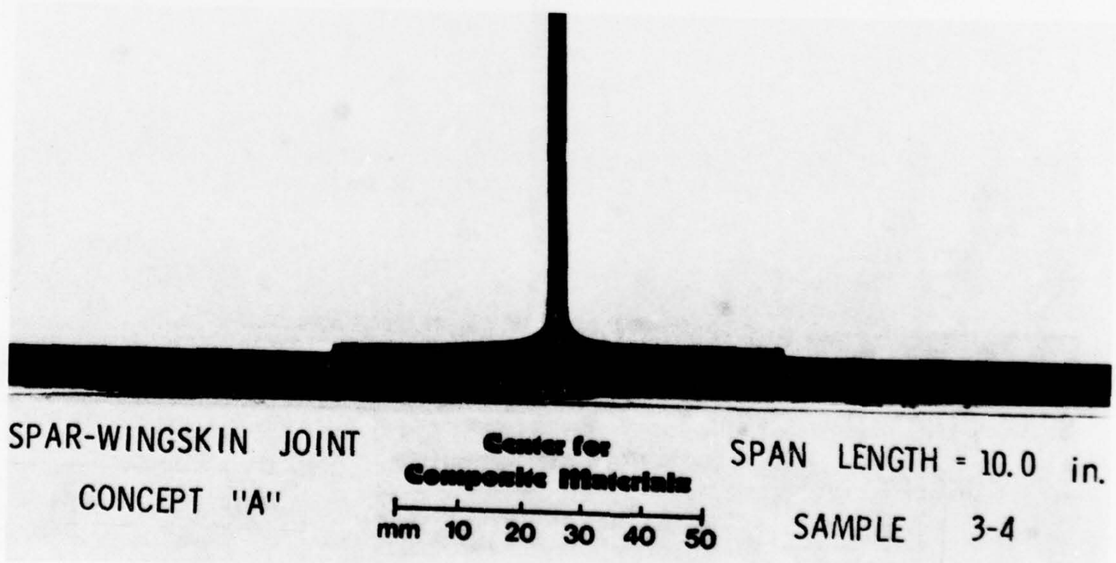

Figure 63: Specimen 3-4; Failed (Concept A; 3.6 inch span)

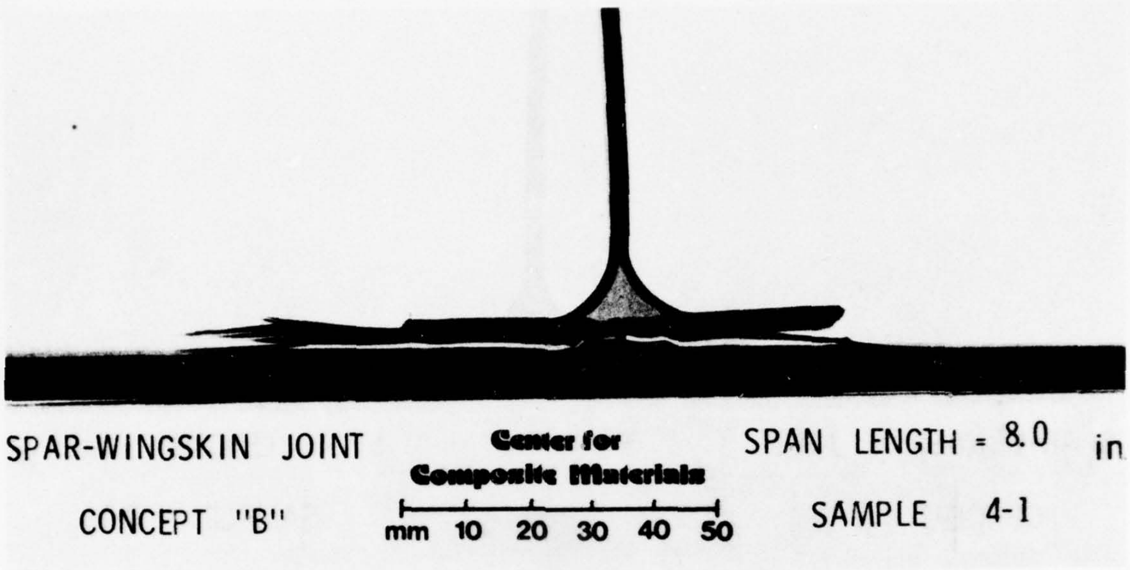

Figure 64: Specimen 4-1; Failed (Concept B; 8.0 inch span)

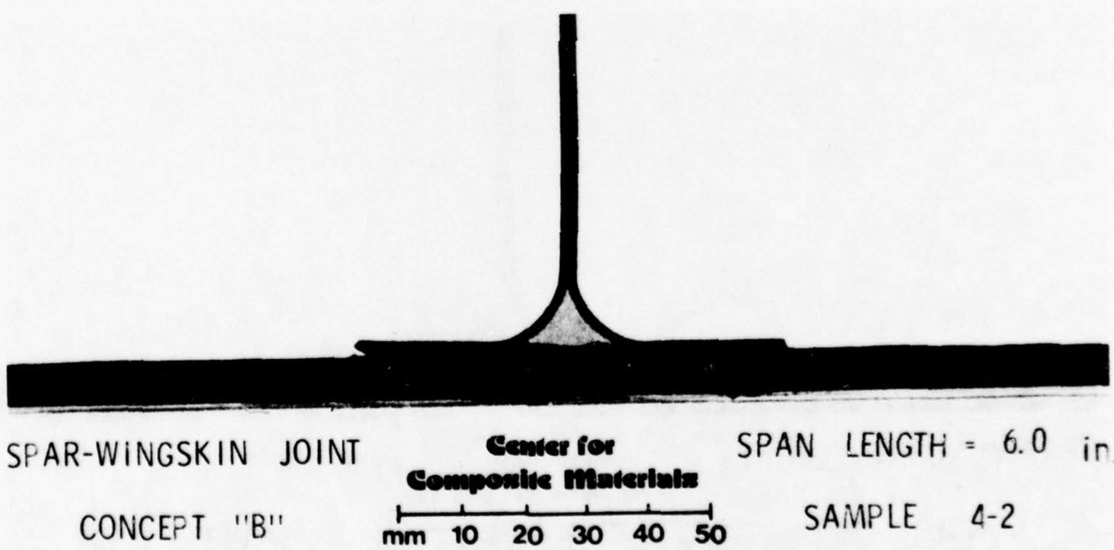

Figure 65: Specimen 4-2; Failed (Concept B; 6.0 inch span)

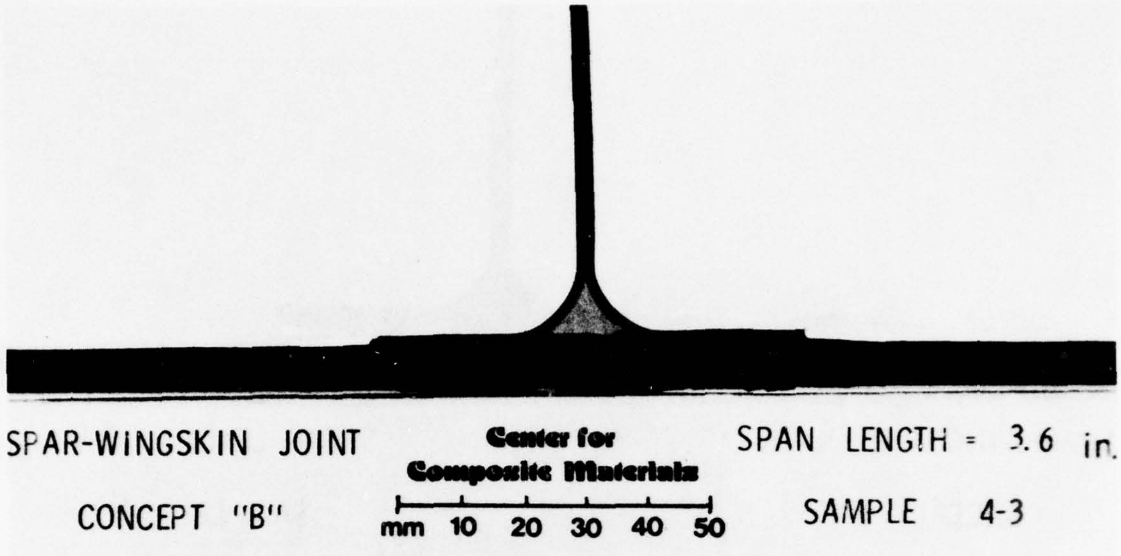

Figure 66: Specimen 4-3; Failed (Concept B; 3.6 inch span)

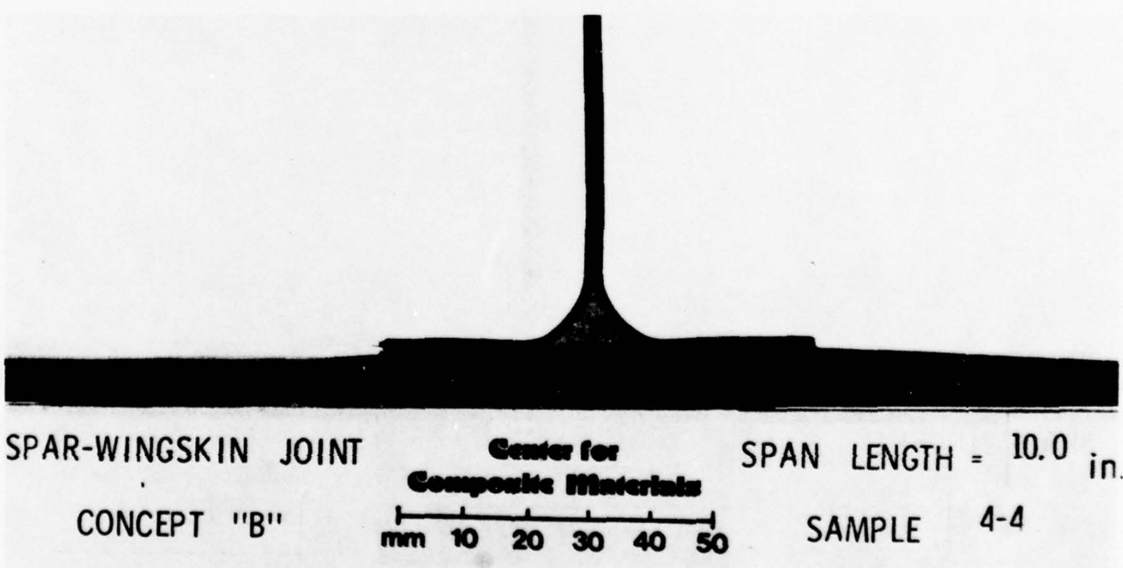

Figure 67: Specimen 4-4; Failed (Concept B; 10.0 inch span)

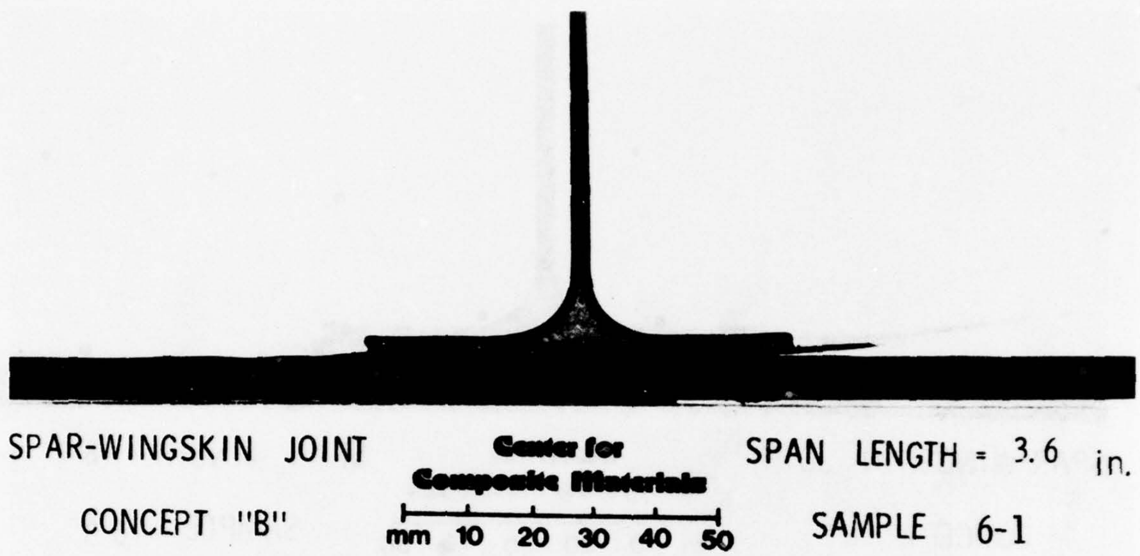

Figure 68: Specimen 6-1; Failed (Concept B; 3.6 inch span)

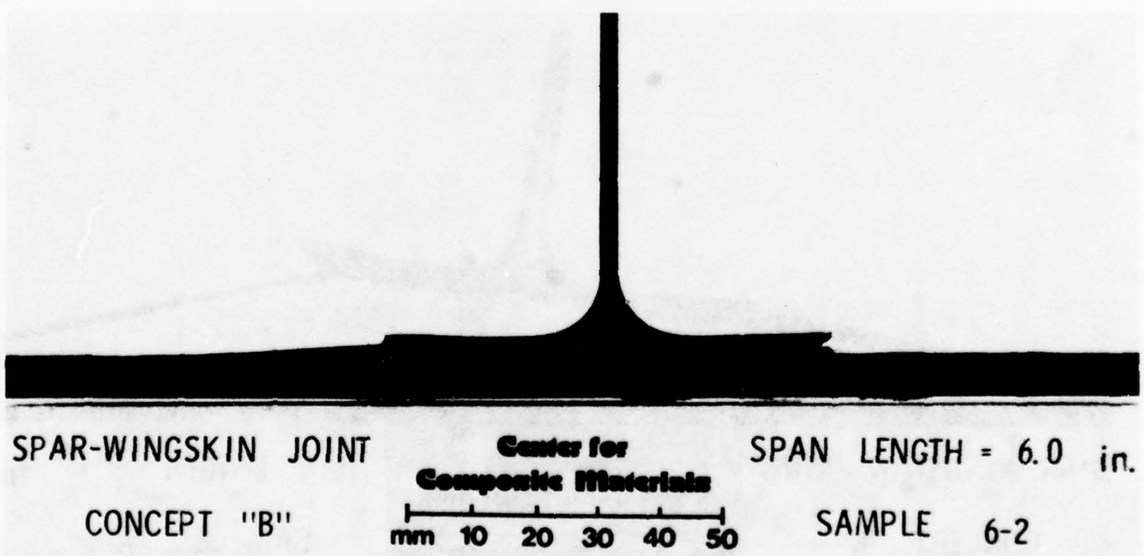

Figure 69: Specimen 6-2; Failed (Concept B; 6.0 inch span)

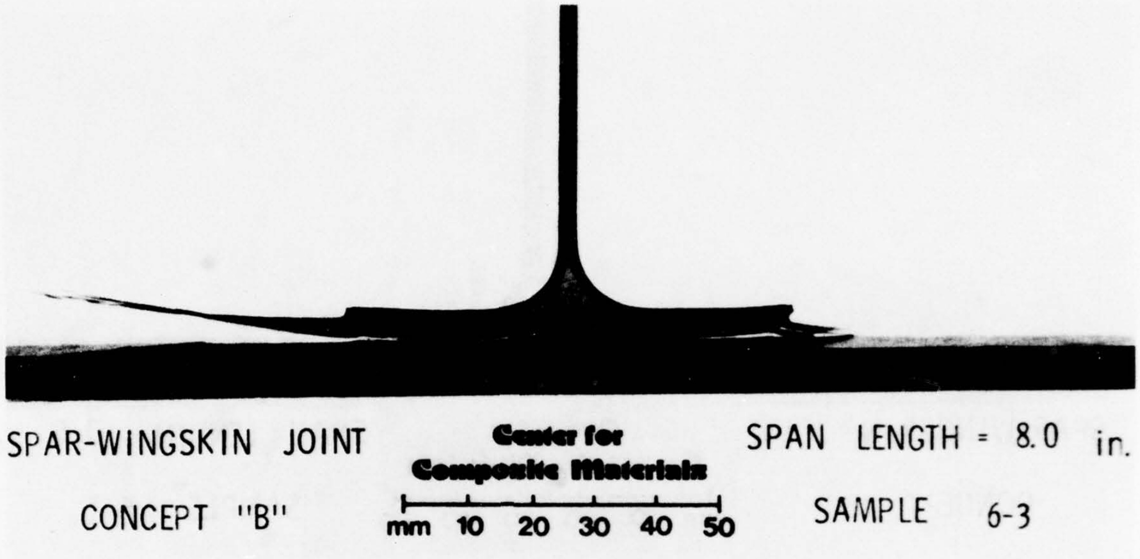

Figure 70: Specimen 6-3; Failed (Concept B; 8.0 inch span)

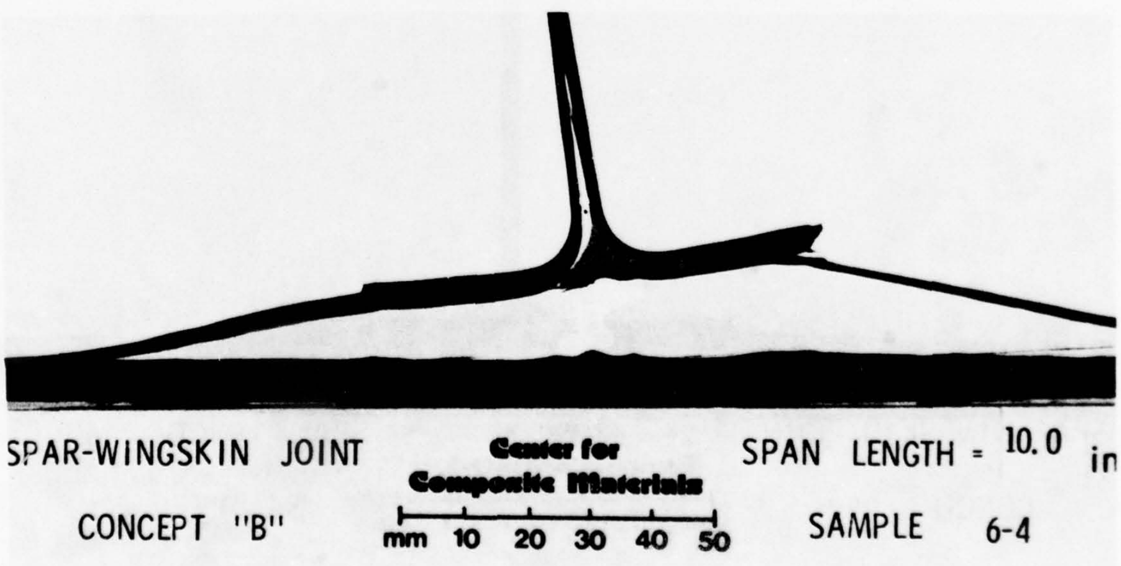

Figure 71: Specimen 6-4; Failed (Concept B; 10.0 inch span)

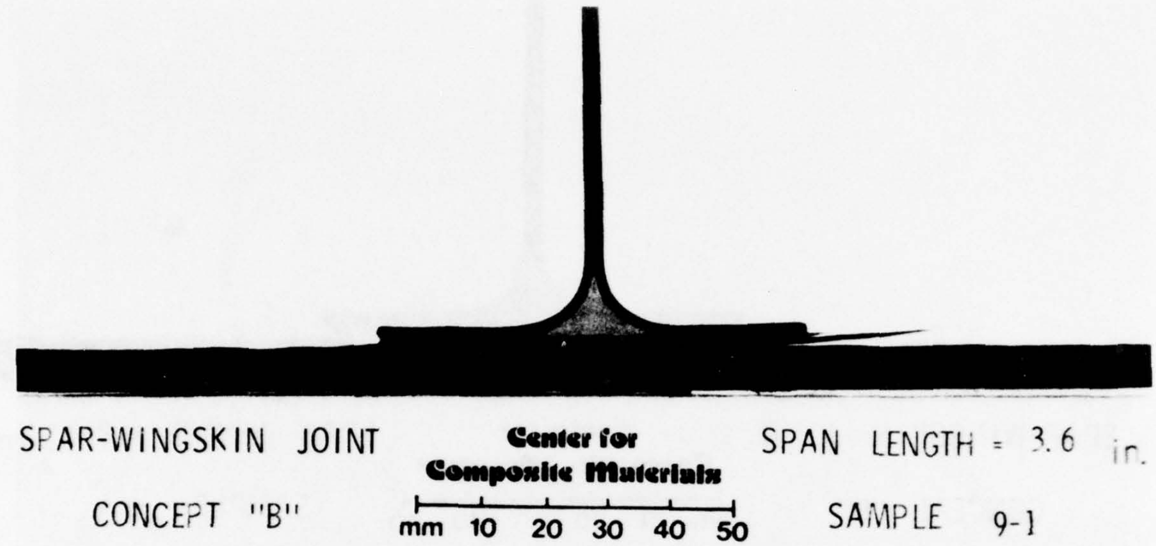

Figure 72: Specimen 9-1; Failed (Concept B; 3.6 inch span)

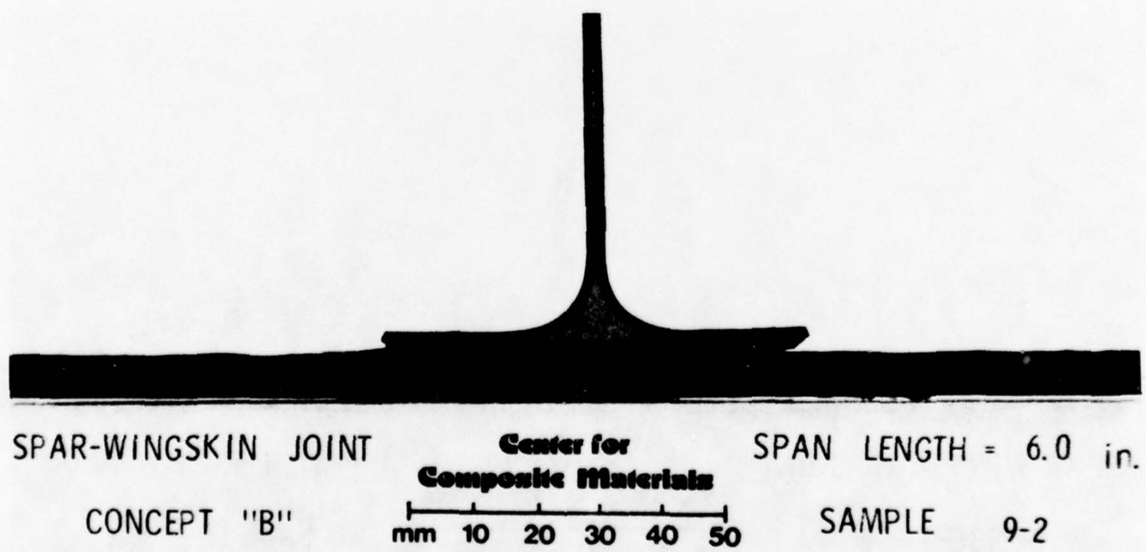

Figure 73: Specimen 9-2; Failed (Concept B; 6.0 inch span)

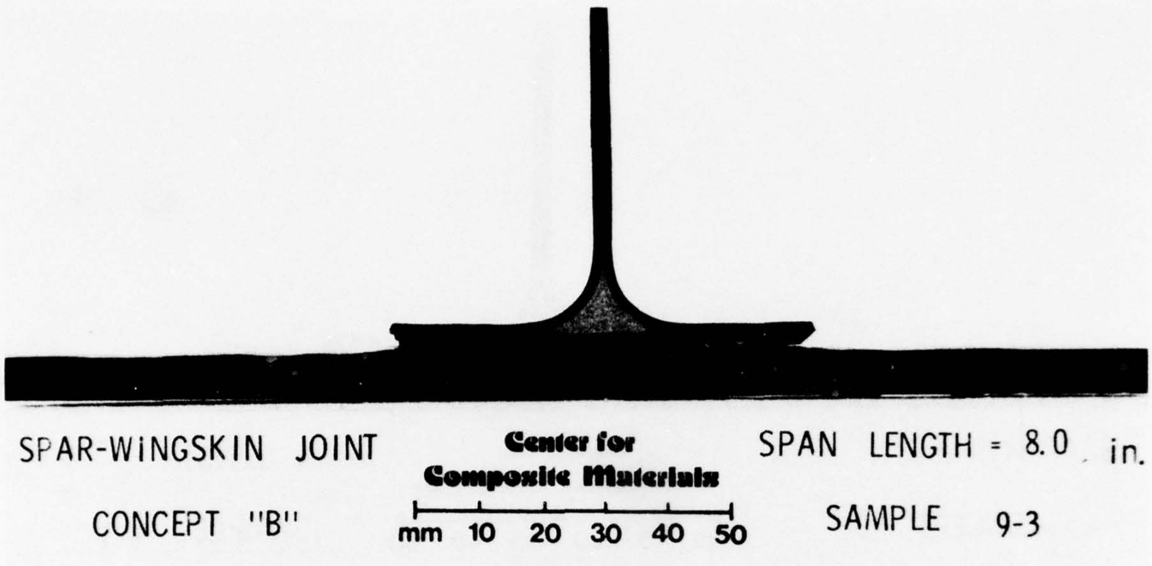

Figure 74: Specimen 9-3; Failed (Concept B; 8.0 inch span)

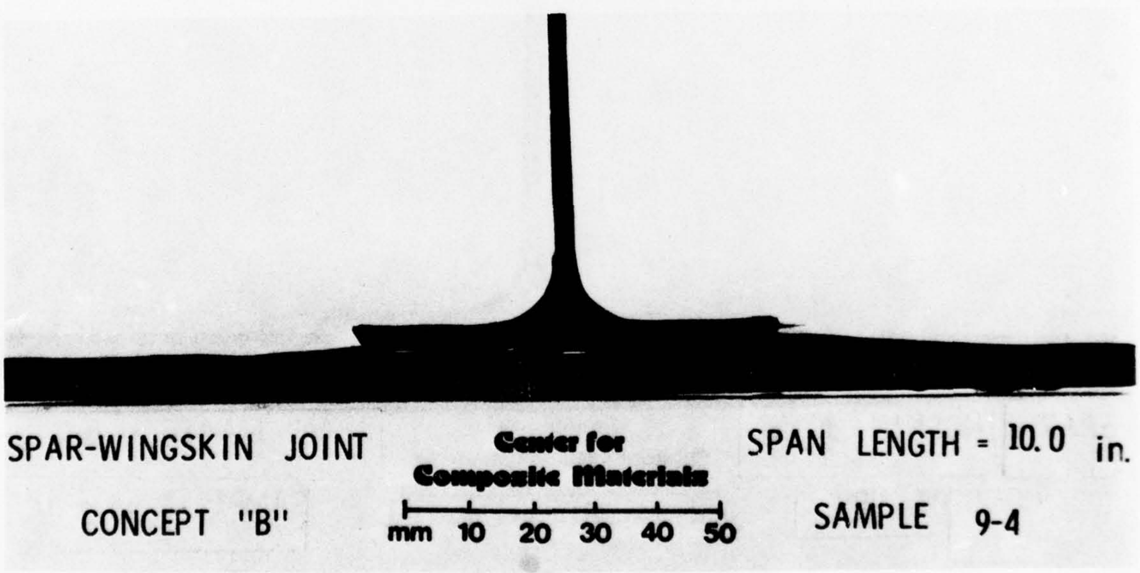

Figure 75: Specimen 9-4; Failed (Concept B; 10.0 inch span)

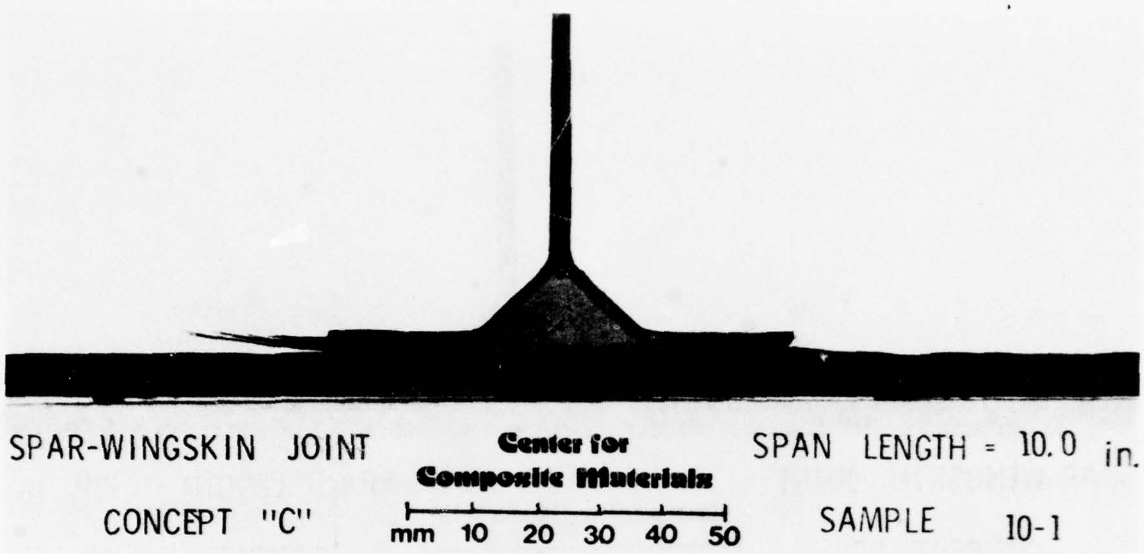

Figure 76: Specimen 10-1; Failed (Concept C; 10.0 inch span)

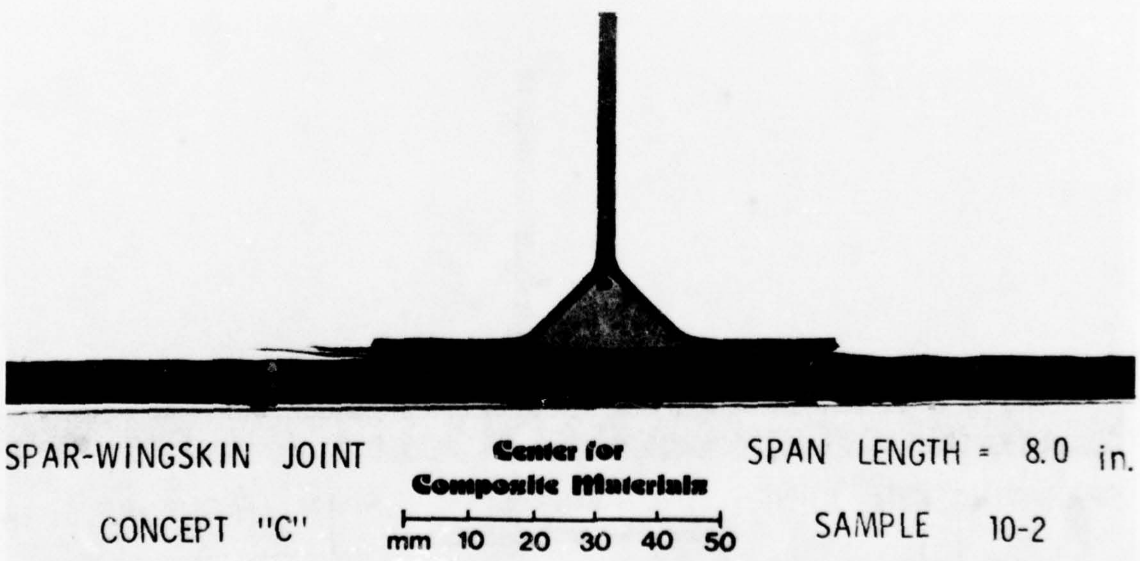

Figure 77: Specimen 10-2; Failed (Concept C; 8.0 inch span)

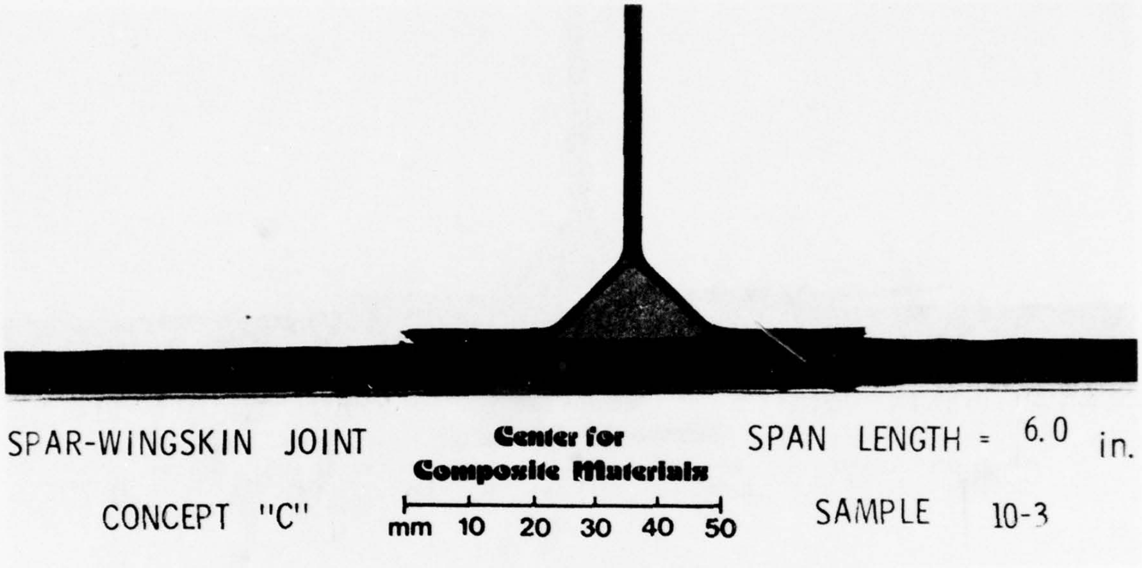

Figure 78: Specimen 10-3; Failed (Concept C; 6.0 inch span)

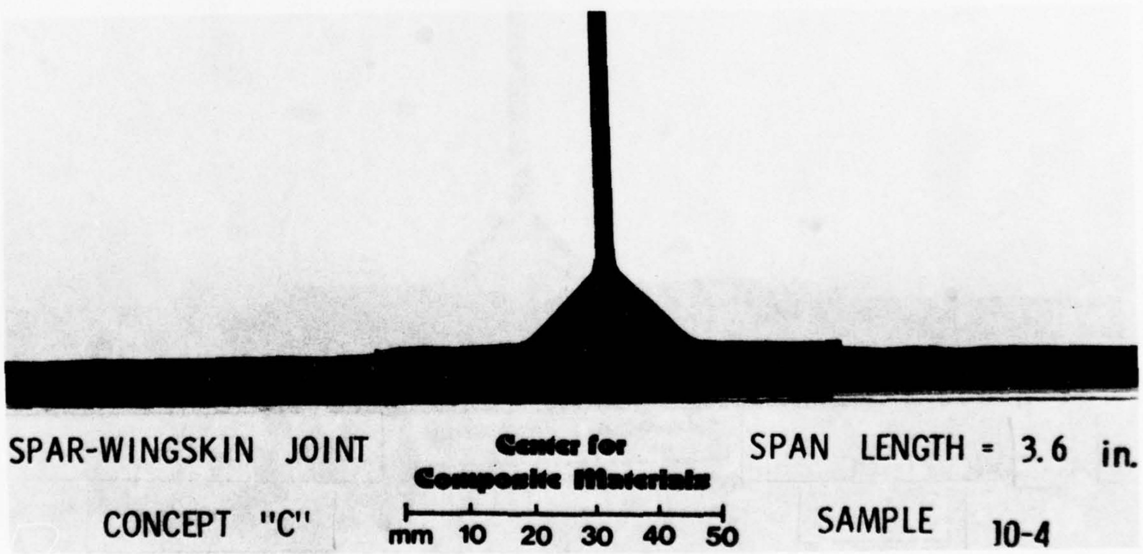

Figure 79: Specimen 10-4; Failed (Concept C; 3.6 inch span)

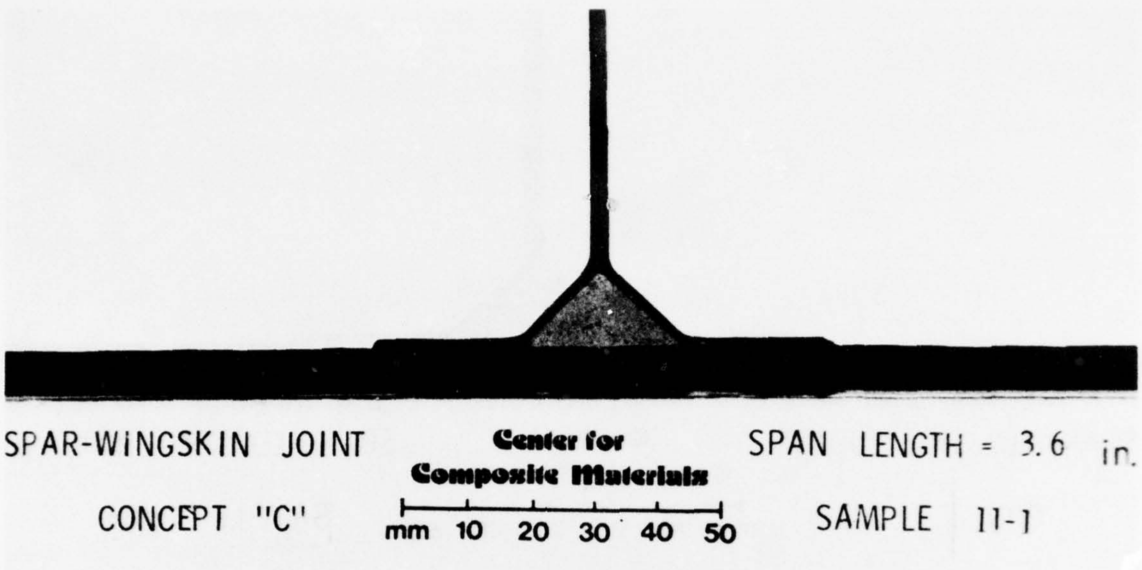

Figure 80: Specimen 11-1; Failed (Concept C; 3.6 inch span)

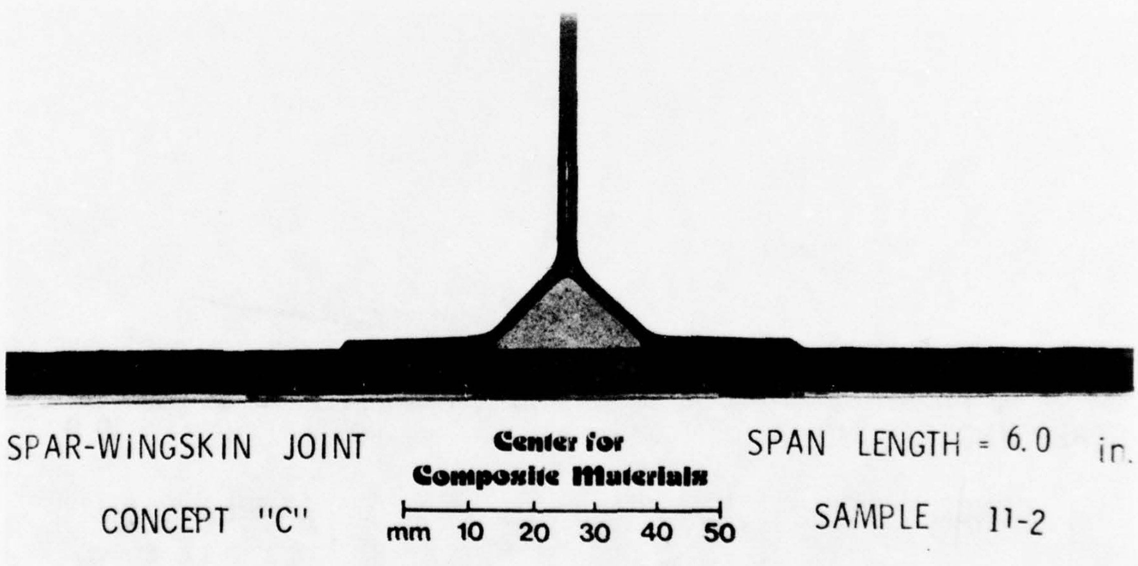

Figure 81: Specimen 11-2; Failed (Concept C; 6.0 inch span)

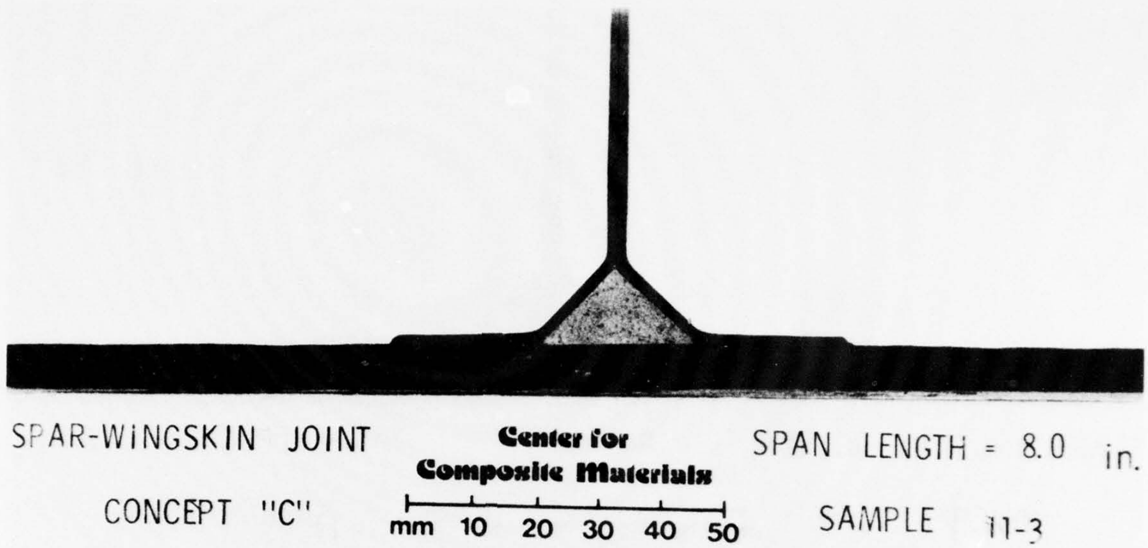

Figure 82: Specimen 11-3; Failed (Concept C; 8.0 inch span)

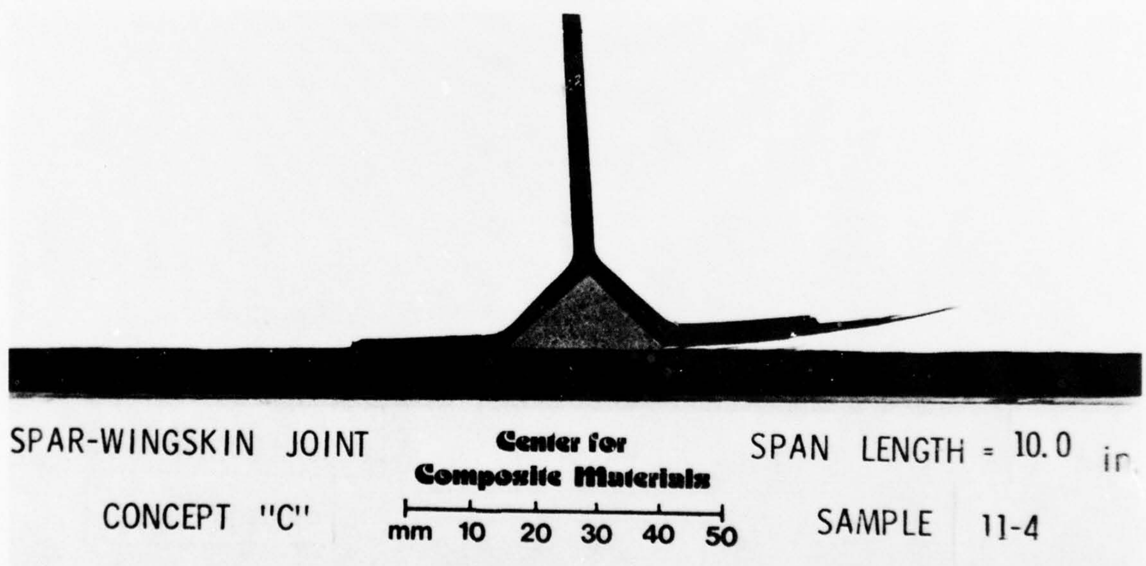

Figure 83: Specimen 11-4; Failed (Concept C; 10.0 inch span)

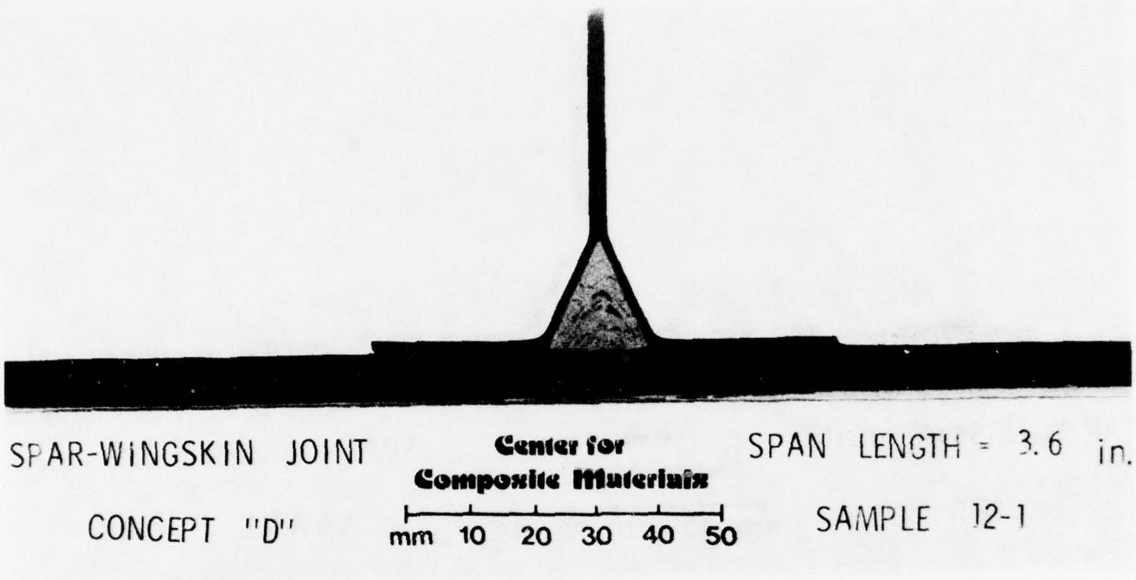

Figure 84: Specimen 12-1; Failed (Concept D; 3.6 inch span)

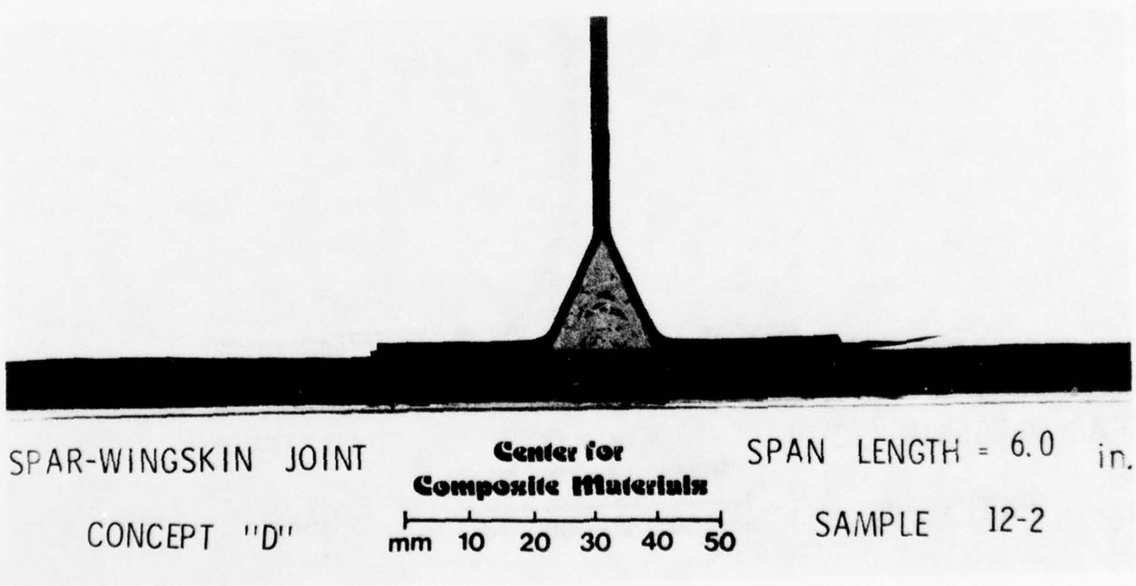

Figure 85: Specimen 12-2; Failed (Concept D; 6.0 inch span)

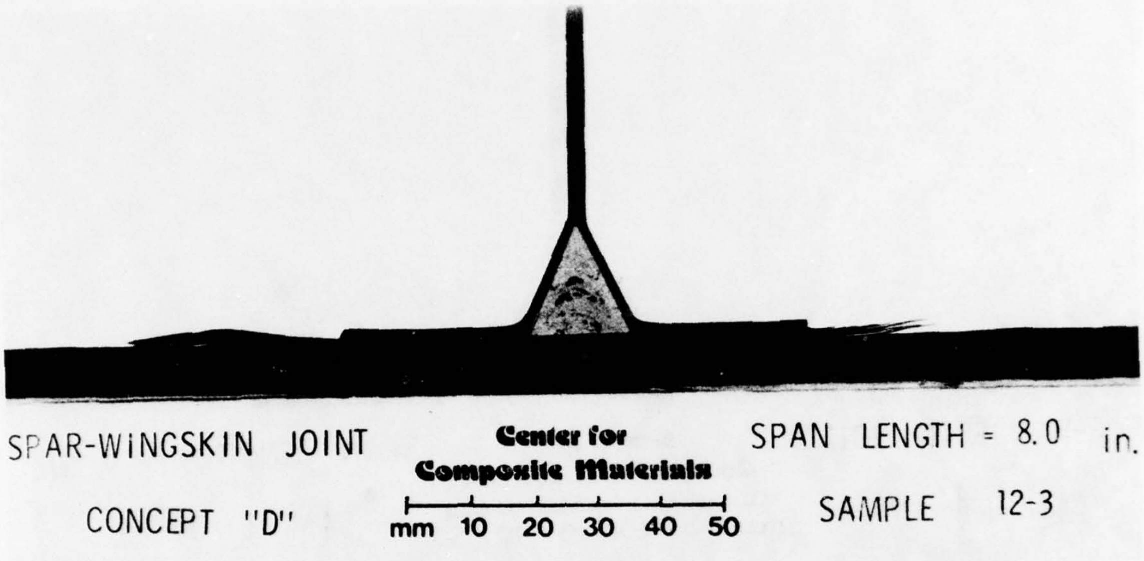

Figure 86: Specimen 12-3; Failed (Concept D; 8.0 inch span)

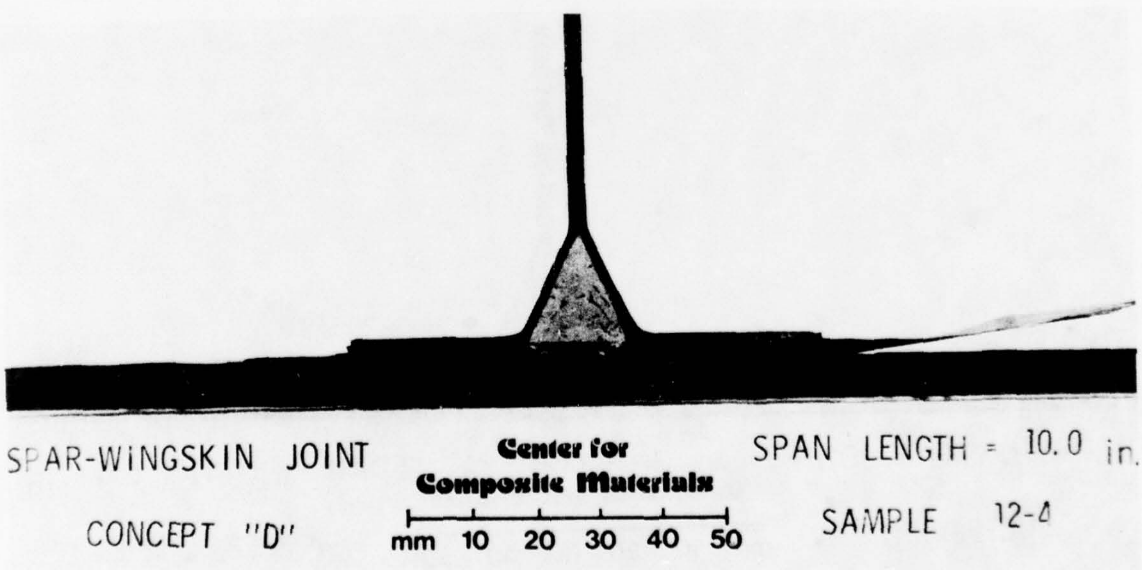

Figure 87: Specimen 12-4; Failed (Concept D; 10.0 inch span)

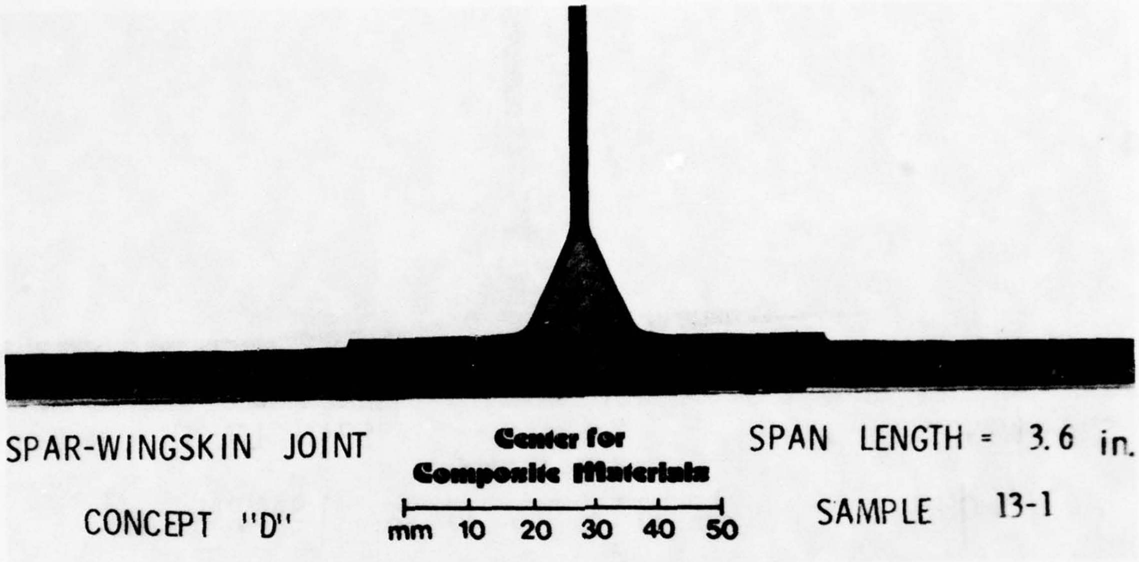

Figure 88: Specimen 13-1; Failed (Concept D; 3.6 inch span)

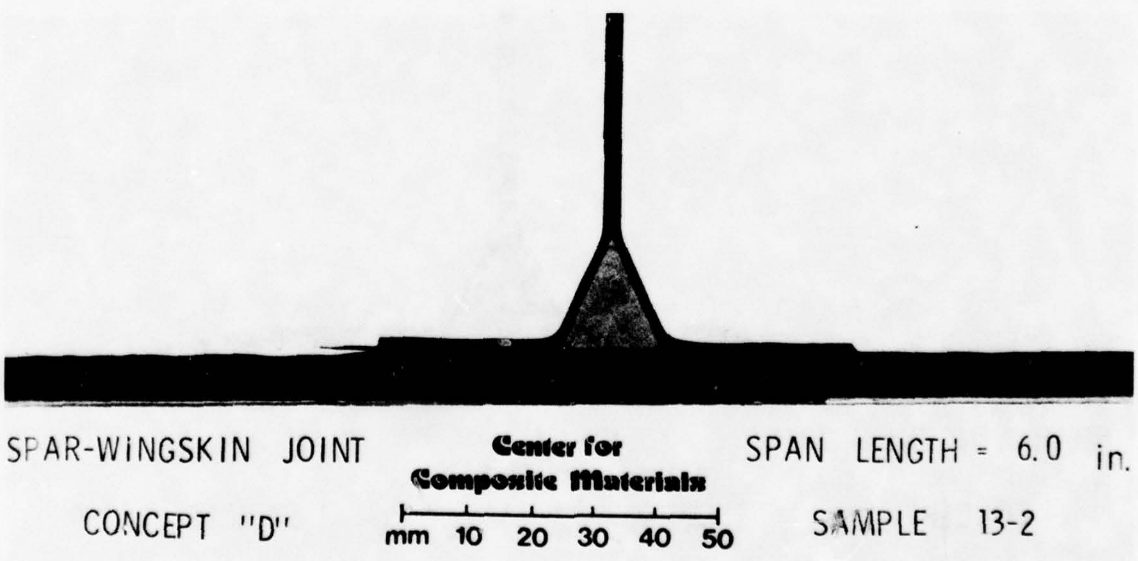

Figure 89: Specimen 13-2; Failed (Concept D; 6.0 inch span)

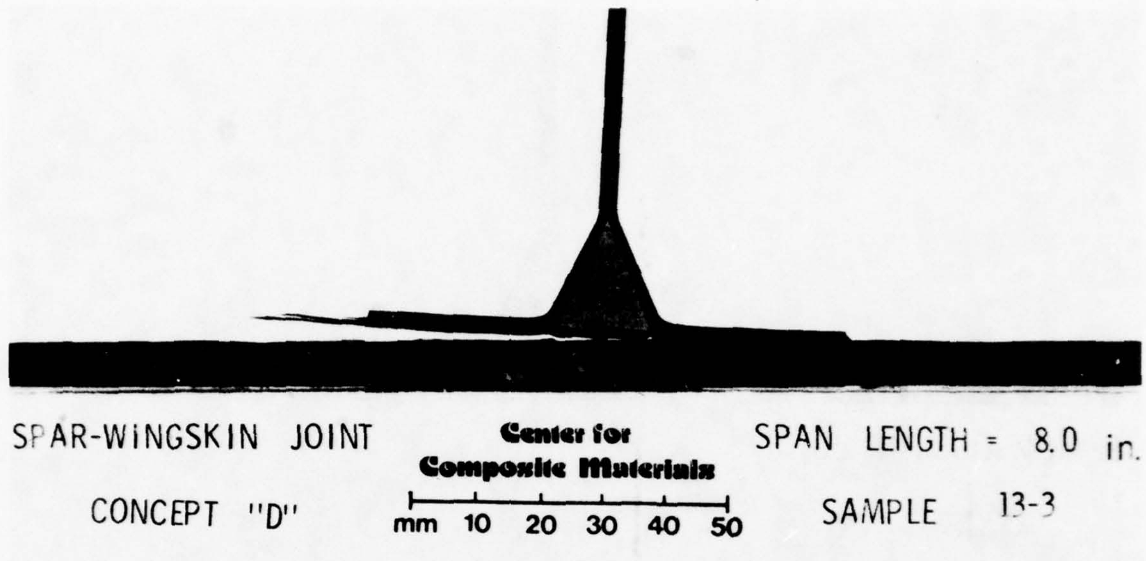

Figure 90: Specimen 13-3; Failed (Concept D; 8.0 inch span)

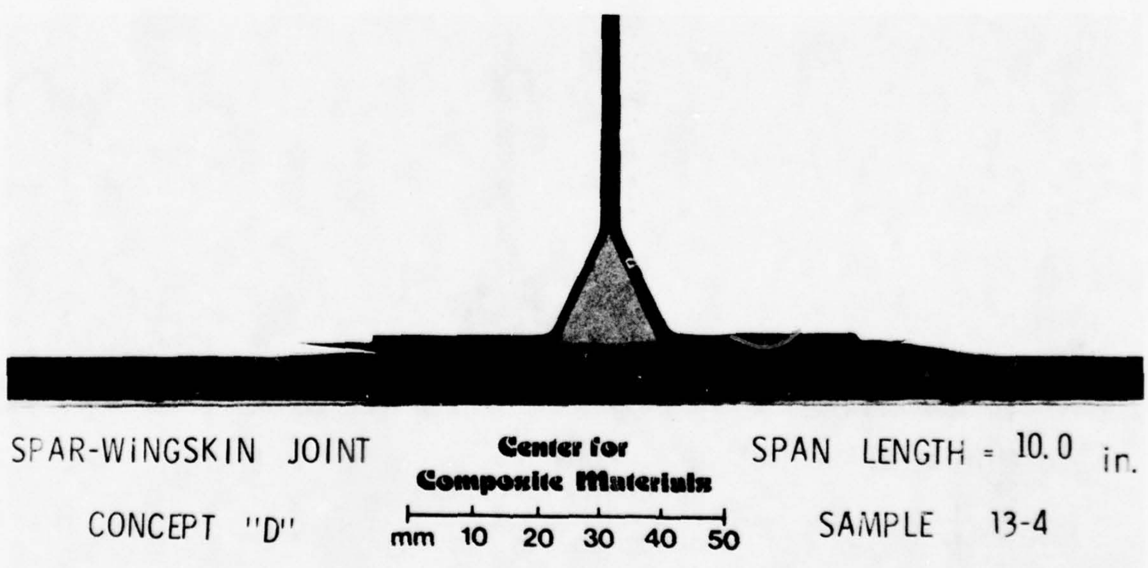

Figure 91: Specimen 13-4; Failed (Concept D; 10.0 inch span)

three additional failure details. First, insert debonding occurred at the insert-laminate interface except occasionally, when delamination occurred at a position one or two plies into the laminate. Over lap-wingskin debonding rarely occurred precisely at this interface but, in general, involved a delamination between the uppermost two plies of the wingskin. Finally, short span length specimens usually did not completely fracture and continued to carry a small load after failure; whereas, long span length specimen failures tended to completely separate the spar and overlap from the wingskin at failure.

5.7 Ultimate Load--Joint Fillet Radius Results

Investigation of the ultimate load versus joint radius for each span (Figures 92 through 95) suggests a relationship between predicted adhesive failure load and observed specimen failure load. Unfortunately, due to the lack of experimental data, the determination of such a mathematical relationship between the two sets of data is difficult and necessarily presumptuous.

Noting the ultimate load-joint radius responses for the two laminate failure criteria, it is apparent that no similarities exist with experimental data. Both Tsai-Wu and maximum stress criteria indicate a joint radius of approximately 0.76 cm (0.3 in) yields a maximum ultimate strength. Intuitively and in comparison to experimental results, this is unrealistic.

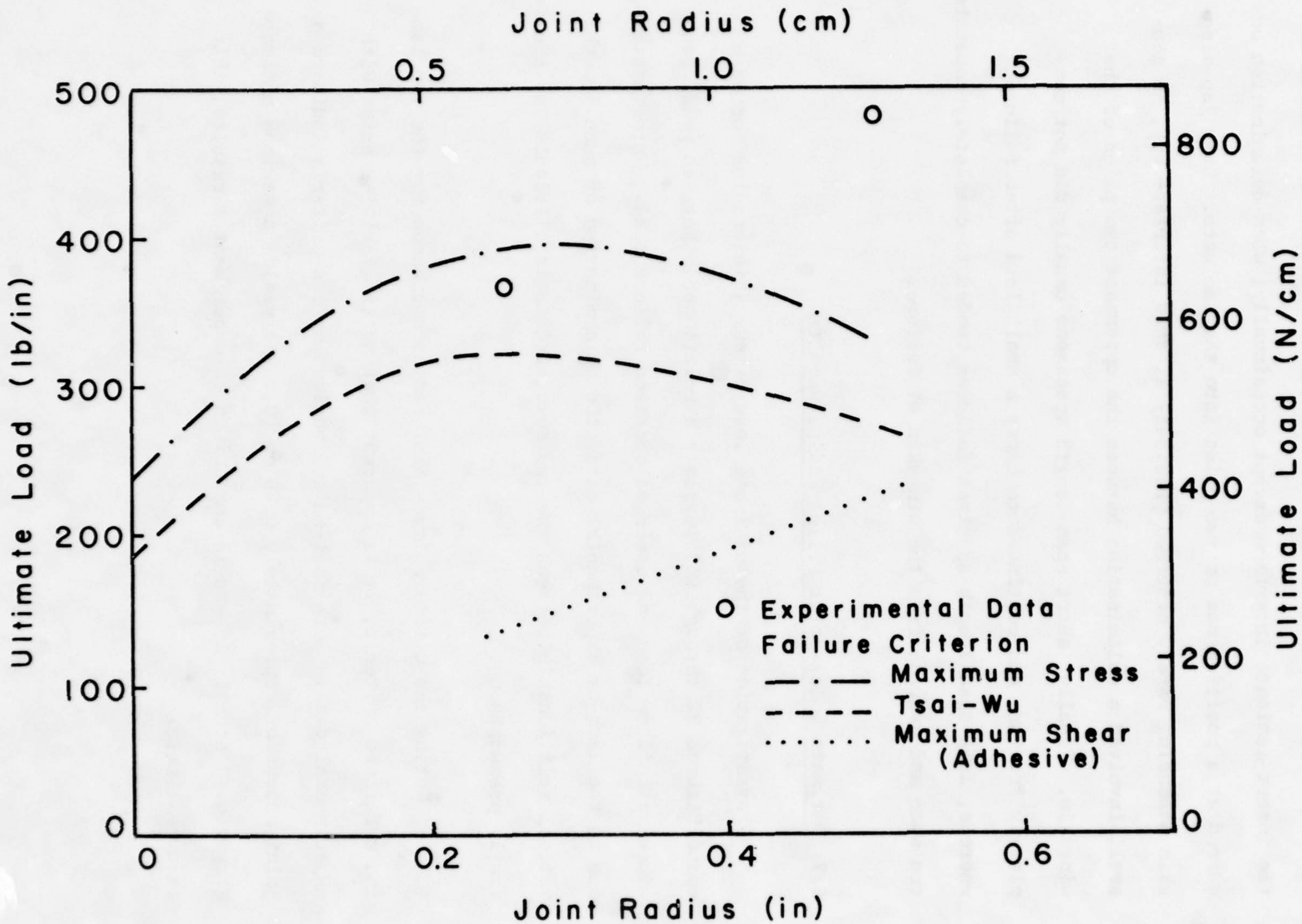

Figure 92: Influence of Joint Radius on Ultimate Load
(Span Length = 3.6 inches)

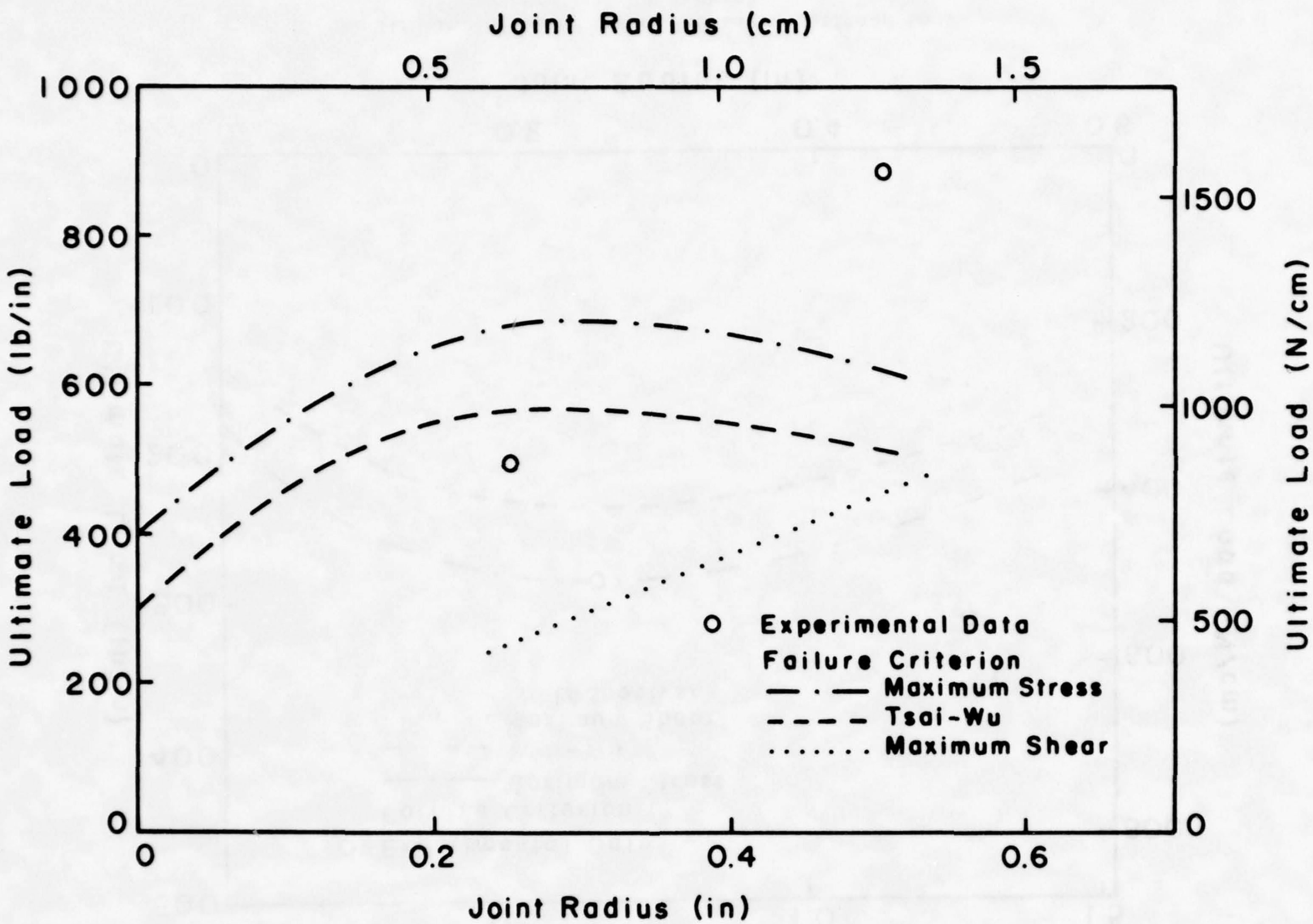

Figure 93: Influence of Joint Radius on Ultimate Load
(Span Length = 6.0 inches)

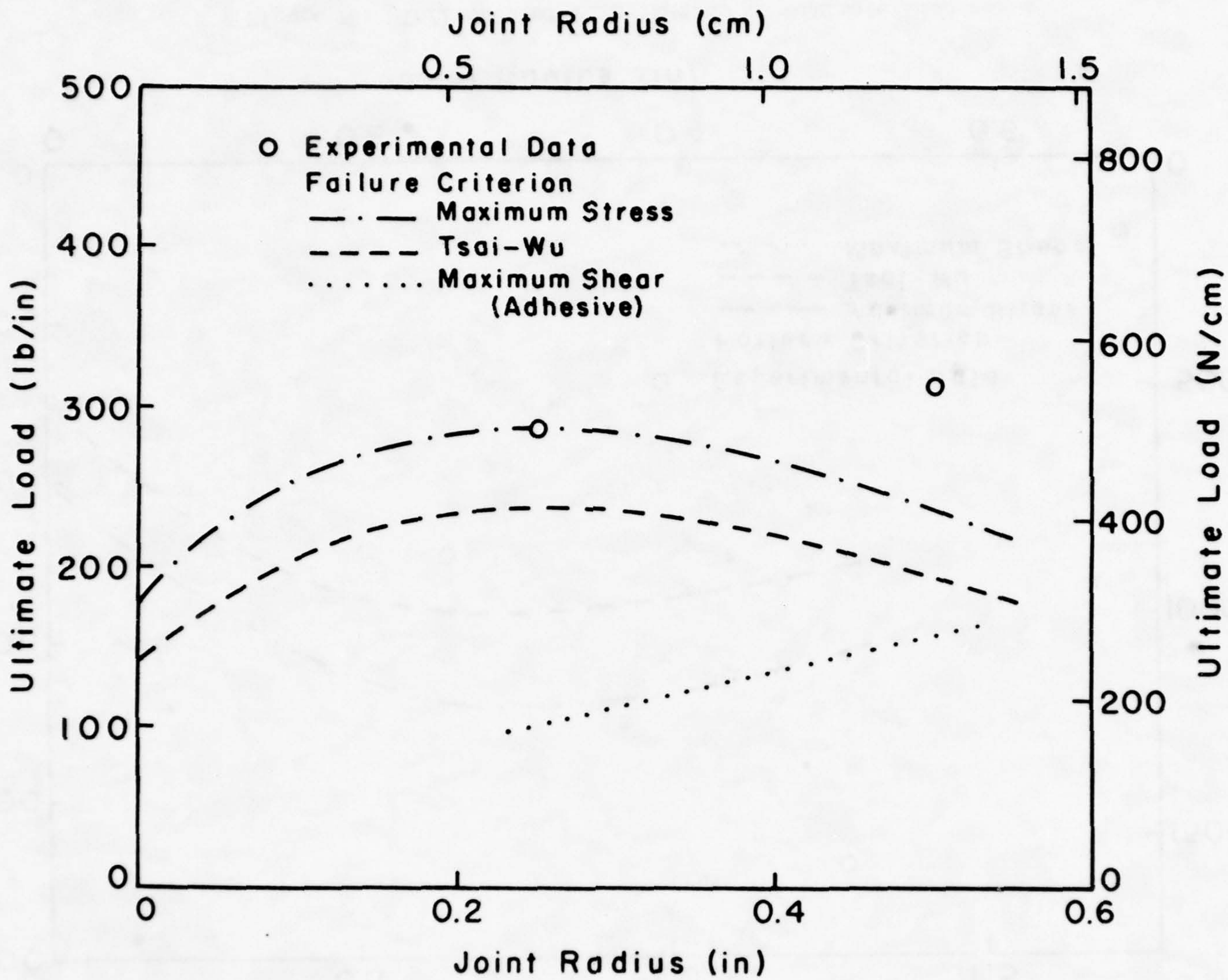

Figure 94: Influence of Joint Radius on Ultimate Load
(Span Length = 8.0 inches)

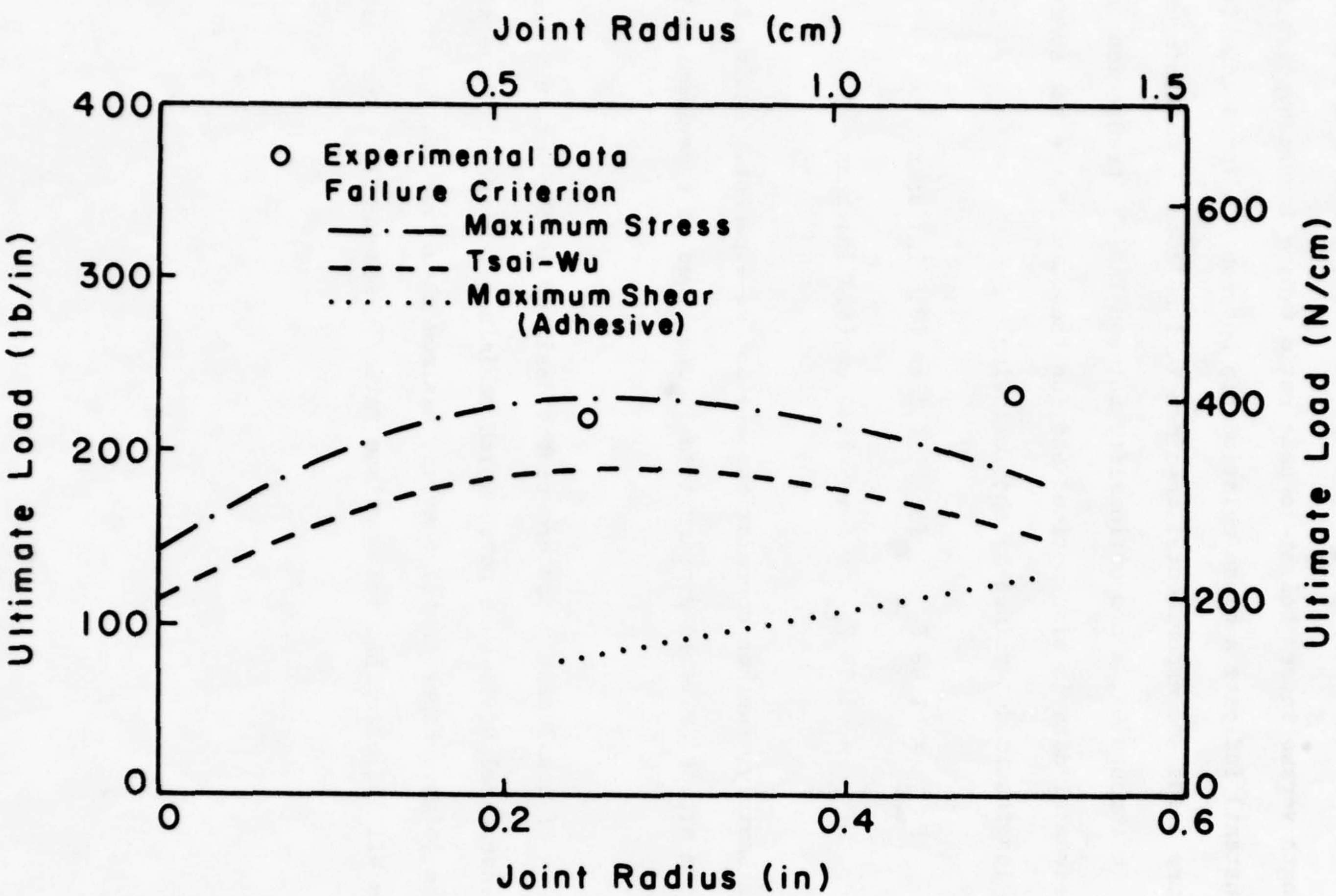

Figure 95: Influence of Joint Radius on Ultimate Load
(Span Length = 10.0 inches)

5.8 Ultimate Load--Insert Height To Base Ratio Results

As was the case in the previous section, plots of ultimate strength versus insert height-to-base ratio (where insert hypoteneuse is a constant) indicate a close relationship between predicted adhesive failure loads and experimental specimen failure loads. Examining Figures 96 through 99, a proportionality between Tsai-Wu predictions and experimental data is also noticed and for the case of the two shorter span lengths is determined by the following:

$$F_{exp} = 1.48\ F_{tw} \quad \text{for} \quad 9.1\ \text{cm}\ (3.6\ \text{in})\ \text{span}$$

$$F_{exp} = 1.94\ F_{tw} \quad \text{for} \quad 15.2\ \text{cm}\ (6.0\ \text{in})\ \text{span}$$

Unfortunately, further correlations are not so apparent. Again, the maximum stress criteria appears totally unrelated to experimental findings.

Of considerable concern to the designer is the determination of the insert height-to-base ratio which maximizes the out of plane strength of the joint. Experimental results, maximum shear and Tsai-Wu predictions all indicate that this optimum ratio is somewhat greater than 2.0.

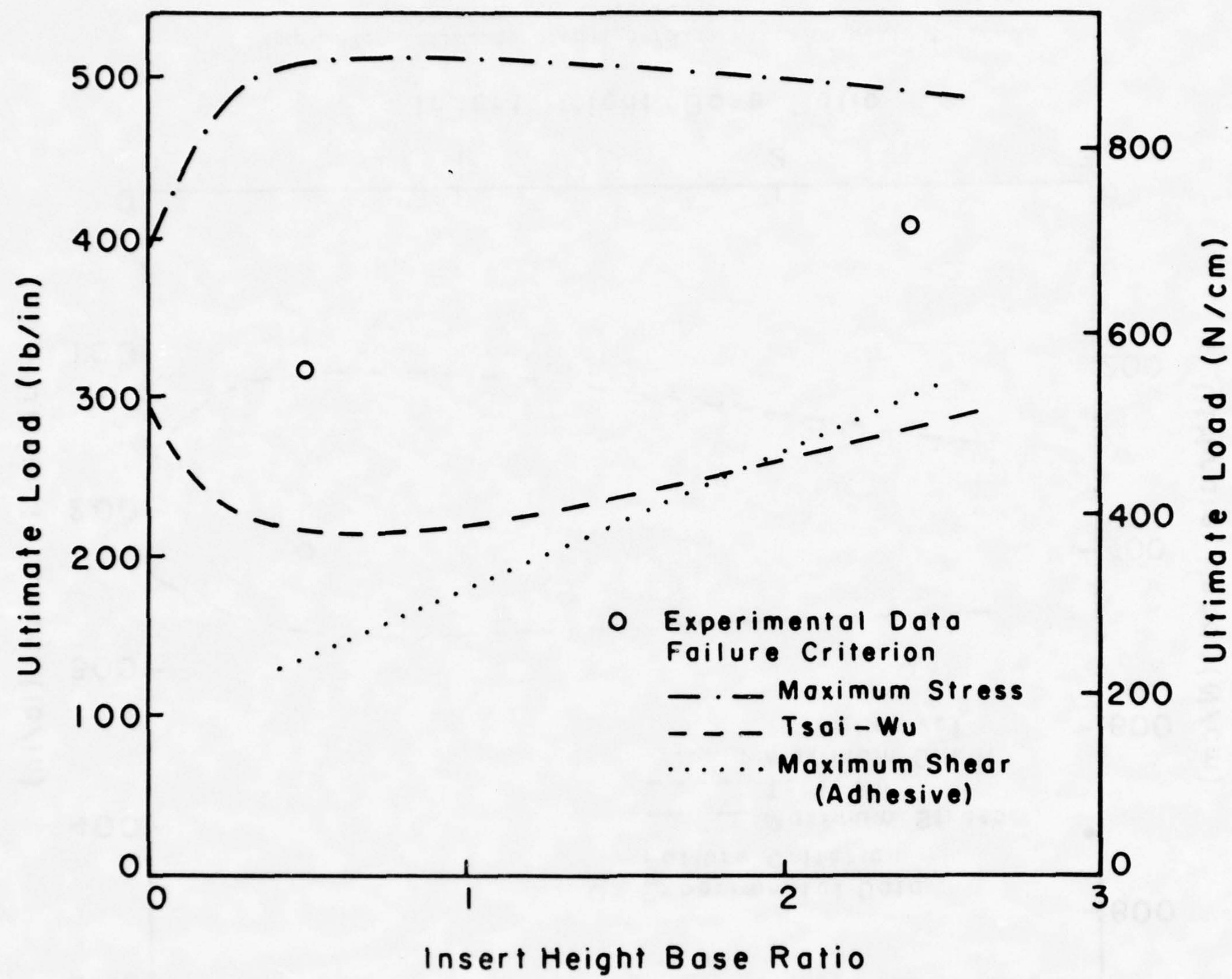

Figure 96: Influence of Height/Base Ratio on Ultimate Load
(Span Length = 3.6 inches)

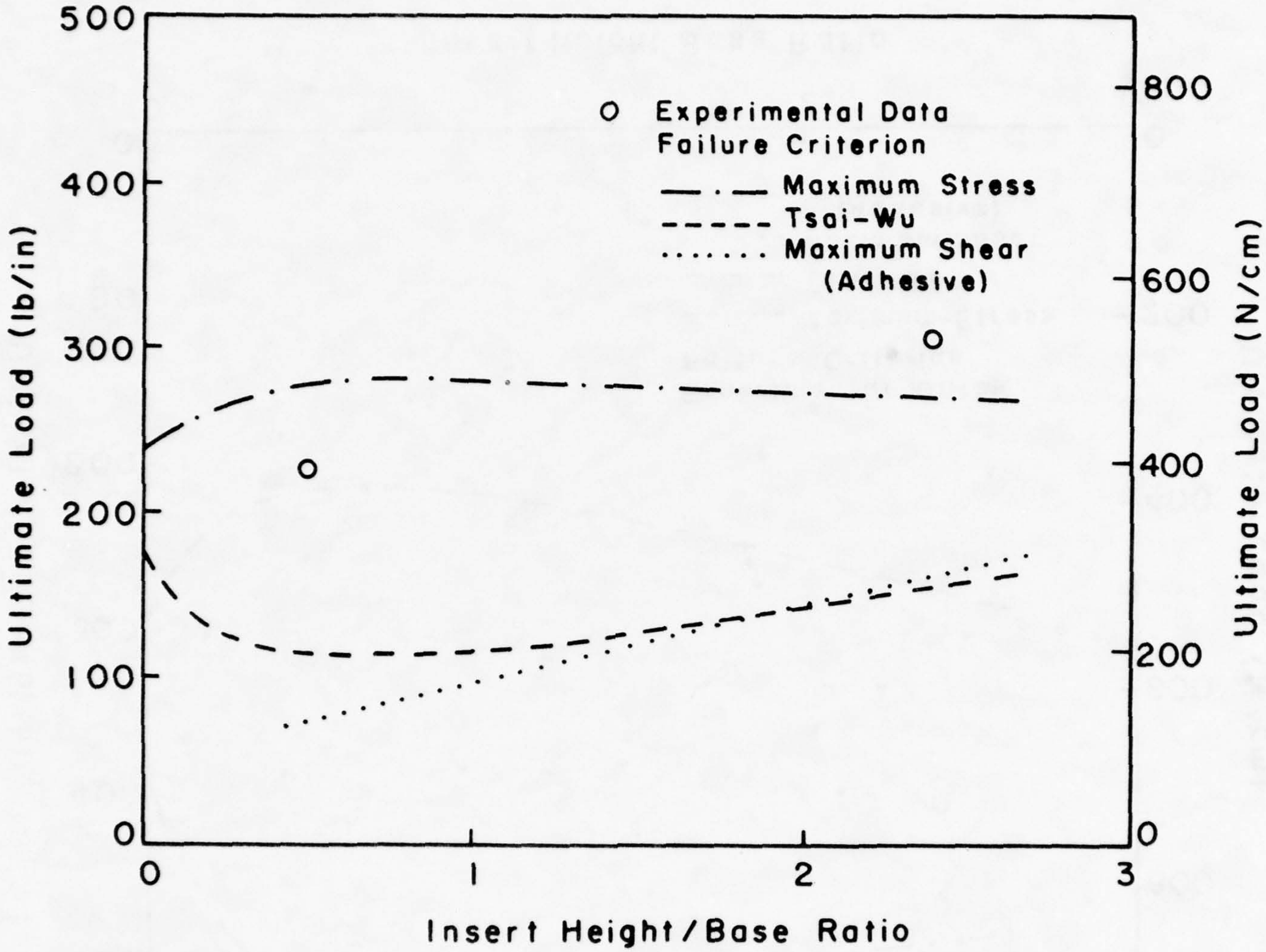

Figure 97: Influence of Height/Base Ratio on Ultimate Load
(Span Length = 6.0 inches)

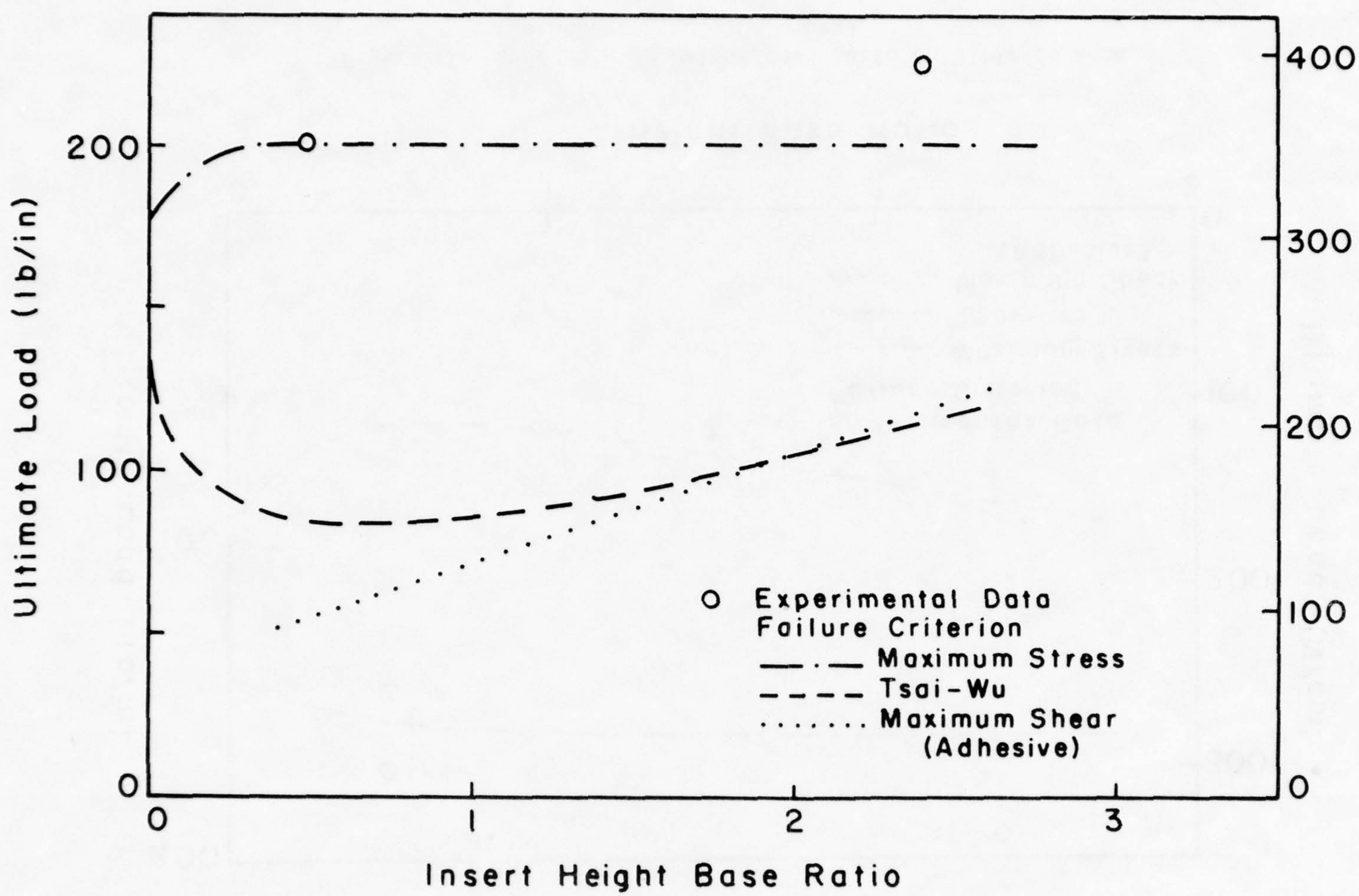

Figure 98: Influence of Height/Base Ratio on Ultimate Load
(Span Length = 8.0 inches)

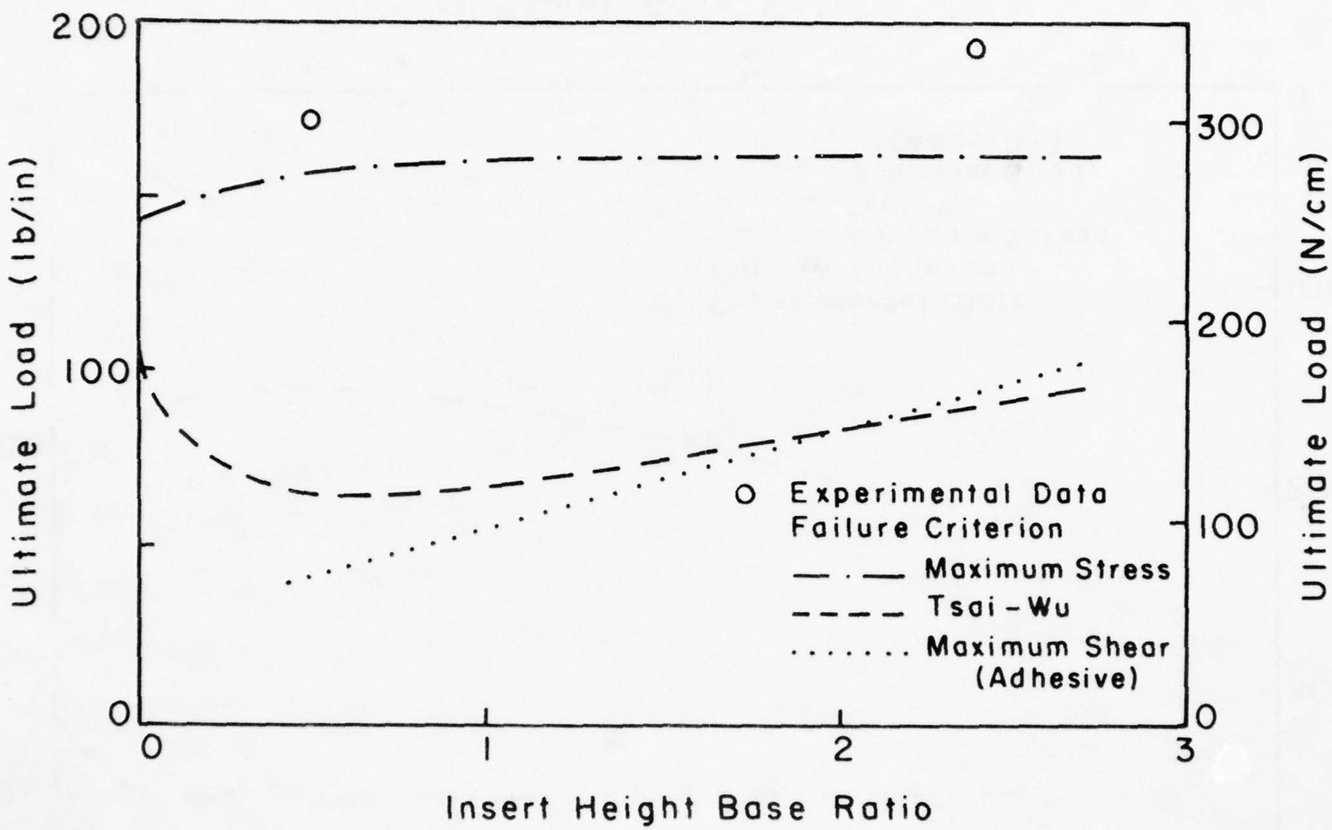

Figure 99: Influence of Height/Base Ratio on Ultimate Load
(Span Length = 10.0 inches)

CHAPTER VI

WEIGHT CONSIDERATIONS

6.1 Joint Weight

An important factor in the evaluation of a given joint concept is its influence upon structural weight. For this analysis the values computed correspond to the weight of the spar, overlap and insert. Calculations were based on a spar height of 5.1 cm (2.0 in), an overlap of 3.66 cm (1.44 in) in length, a ply thickness of 0.005 inches, a density of 0.0079 kg/cm^3 (0.059 lb/in^3) for the graphite-epoxy laminate, and a density of 0.0062 kg/cm^3 (0.046 lb/in^3) for the adhesive. All concept weights are supplied in Table 6 along with normalized values obtained by dividing the given concept weight by the weight of concept "E". Concept "C" was the joint of greatest weight followed in order by "D", "B", "A" and "E".

6.2 Span Length Effects

Since all concepts have been investigated over a range of spans, it is important to examine the influence of this parameter on weight. The weight values shown in Table 7 were obtained by adding to each of the spar weights given in Table 6 the weight of the wingskin of length equal to the spar-to-spar spacing corresponding to a given span. Per-

Table 6: Spar Weights

Concept	Weight N	Weight lb	Percent of concept "E"
A	0.109	0.0246	103
B	0.126	0.0284	119
C	0.149	0.0336	141
D	0.140	0.0314	132
E	0.106	0.0238	100

Table 7: Spar-Wingskin Weights

Concept	WEIGHT lb (% of "E")			
	3.6" span	6.0" span	8.0" span	10.0" span
A	0.164 (100.5)	0.257 (156.8)	0.334 (204.1)	0.412 (251.4)
B	0.168 (102.8)	0.260 (159.1)	0.338 (206.4)	0.415 (253.7)
C	0.174 (106.0)	0.266 (162.3)	0.343 (209.6)	0.420 (256.9)
D	0.171 (104.6)	0.264 (161.0)	0.341 (208.2)	0.418 (255.5)
E	0.164 (100.0)	0.256 (156.3)	0.333 (203.6)	0.411 (250.9)

centages indicate the relative concept weight for a given span as compared to concept "E" at a span length of 9.1 cm (3.6 in). In application of Table 7, it must be remembered that the spar-to-spar spacing is inversely proportional to the number of spars required. To support a 203 cm (80 in) wingskin requires only three spars at a spar-to-spar spacing equivalent to a 25.4 cm (10 in) span length while nine spars are required for the 9.1 cm (3.6 in) span length.

CHAPTER VII

CONCLUSIONS AND RECOMMENDATIONS

The use of linear-elastic finite-element analysis, supported and validated by experimental results, provides an excellent means for the design and analysis of a joint to carry out-of-plane loads and illustrated herein by a spar-wingskin joint. Five joint concepts were investigated. All concepts consisted of a $[(\pm 45)_6]_s$ spar which overlapped and was co-cured perpendicular to a $[(\pm 45/90_2)(0/\pm 45/0)_6]_s$ wingskin with the enclosed void at the base of the spar filled by an adhesive. The laminates were fabricated of Hercules' AS 3501-6 Graphite-Epoxy, and Reliable Manu. Inc. Reliabond 398 was employed as the adhesive. All joint concepts were identical except for the overlap geometry in the immediate vicinity of the base of the spar. The five geometries used from the apex of the insert to the overlap-wingskin contact point were:

- Concept "A" having a 0.64 cm (0.25 in) radius
- Concept "B" having a 1.27 cm (0.50 in) radius
- Concept "C" having a triangular cross-section insert 1.27 cm (0.50 in) in height and 2.54 cm (1.00 in) in base length
- Concept "D" having a triangular cross-section insert 1.75 cm (0.69 in) in height and 1.47 cm (0.58 in) in base length
- Concept "E" having no insert and a radius of zero length.

Loading conditions for each concept consisted of simple-supports positioned symmetrically about the spar on the top of the wingskin, with a tensile load applied through the spar. Four different span lengths were investigated ranging from 9.1 cm (3.6 in) to 25.4 cm (10.0 in). All concepts were evaluated via an extensive finite-element analysis with results compared to data obtained from experimental testing of concepts "A" through "D".

An elastomeric tooling consisting of two silicone rubber bladders fitted in an aluminum containment fixture was developed for the fabrication of experimental test specimens for each concept. From this fabrication experience the following conclusions can be made:

- Elastomeric tooling provides an excellent method for the fabrication of difficult geometries.
- For concepts having other than a smooth radial transition from the spar to the wingskin, it is necessary to pre-cure the adhesive insert.

Recommendations for future fabrication are:

- In addition to forming a radius on all interior corners of the bladders to prevent stress concentrations, a thick silicone ridge should be formed over the edge of the interior, bladder port washer.
- A caul plate having small perforations should be used to provide for more even resin flow and possibly omit the necessity of wingskin prebleeding.

- In order to obtain a smooth interior surface on the test specimen, the use of bladders faced with a thin sheet of metal should be investigated.

Analytical and experimental stiffness results showed a high degree of correlation. Defining modulus or apparent stiffness as the applied load divided by mid-span strain at the lower surface of the wingskin, a quantitative measure of joint stiffness was obtained. This measure can also be used when designing for maximum strain. Conclusions from modulus results are:

- The finite-element meshes utilized in this research provided an excellent model of each given joint concept for use in the determination of that joint's load-strain response.
- Joint concept stiffness or modulus increases linearly with increasing joint fillet radius. Mid-span strain is inversely proportional to joint radius for a given load.
- For triangular cross-section inserts having a constant length hypoteneuse, a height-to-base ratio of approximately 0.5 maximizes the modulus value and minimizes the mid-span strain value.
- Regardless of the cross-sectional geometry of the insert, the modulus decreases exponentially with span. Therefore, span lengths below 10.2 cm (4.0 in) must be employed if any benefits of individual joint geometries are to be realized.
- As expected, the greater the thickness of the joint at the base of the spar and the greater the distance over which the increased thickness region ranges, the greater the apparent

stiffness of the joint concept.

The Tsai-Wu and maximum stress failure criteria, used for the composite, and the maximum shear failure criterion, used for the adhesive, were employed to predict joint strength. For all cases, both the Tsai-Wu and maximum stress criteria predicted in-plane failure at the top of the spar above the lower corner of the insert and the maximum shear failure criteria predicted interlaminar insert-overlap debonding. Experimentally, all joint failures initiated as either insert-overlap interlaminar failure or overlap-wingskin interlaminar failure. Conclusions are summarized below:

- The Tsai-Wu failure criterion offers a conservative prediction of failure load as compared to the maximum stress criterion.
- The maximum shear criterion provides a reasonable prediction, as validated by experiment, of the initial site and approximate load for first failure. This failure does not, however, correspond to final catastrophic failure.
- As span increases, strength decreases exponentially.
- Smooth radial geometries provide a continuous load path and result in greater strengths than the discontinuous triangular geometries.
- For the radial geometries, the Tsai-Wu and maximum stress criterion offer a very poor prediction of ultimate load-joint radius response. Maximum shear does appear to model this response fairly well, but additional experimental work is required to determine the ultimate adhesive shear strength used

in the theoretical analysis.

- For the triangular geometries, both the Tsai-Wu and maximum shear criteria offer a good prediction of ultimate load-height to base ratio response. Again, experimental work is mandatory to determine better estimates of material strengths.

General conclusions concerning the overall design of the spar-wingskin joint are:

- Smooth radial geometries are far superior to triangular geometries in terms of strength.
- The use and/or investigation of different joint concepts is valid only for span lengths in the range of 7.6 to 10.2 cm (3.0 to 4.0 in).
- For the concepts investigated, concept "B", employing a 1.27 cm (0.5 in) radius at the spar-wingskin intersection provides the greatest strength without sacrificing stiffness.
- Joint strength is dependent on adhesive shear strength.
- In comparing joint concept strengths from several sources, one must take care to introduce a proportionality factor to account for variation in the moment of inertia values with changing wingskin thicknesses. A ratio of the cubes of the thicknesses has been used to obtain favorable results.

Throughout this research effort, several areas were suggested in which future research would be beneficial. Recommendations for such future research are:

- Investigate additional failure criterion to better predict joint strength.
- Investigate additional "smooth" insert geometries (i.e. ellipsoidal).
- Employ the use of an iterative finite-element model to predict joint strength. As failure progresses in one region, the region properties are modified and the model is reloaded. In this way, the failure path could be traced.
- Investigate the use of pultruded rods and helically wrapped tubes to replace adhesive inserts.

APPENDIX A

SINGULARITY FUNCTION ANALYSIS

In order to investigate the response of the full wingbox to a given pressure load, the structure was modeled as a multispan uniform beam and analyzed by singularity functions. As shown in Figure 100, the lower wingskin of the wingbox was isolated and modeled as an indeterminate beam of uniform cross-section simply supported at each spar-wingskin joint (every 20.3 cm [8.0 in]). A constant pressure load, P_i, was permitted in each cell (span between two adjacent supports) and pressure was allowed to vary from cell to cell. Using the following definitions:

v_i = displacement at support i

F_i = vertical force exerted by support i

P_i = pressure exerted from support i to support $i + 1$

$V(x)$ = shear force

$M(x)$ = moment

$v(x)$ = displacement

I = moment of inertia

E = Young's modulus

x = distance along beam

The boundary conditions for the multispan beam

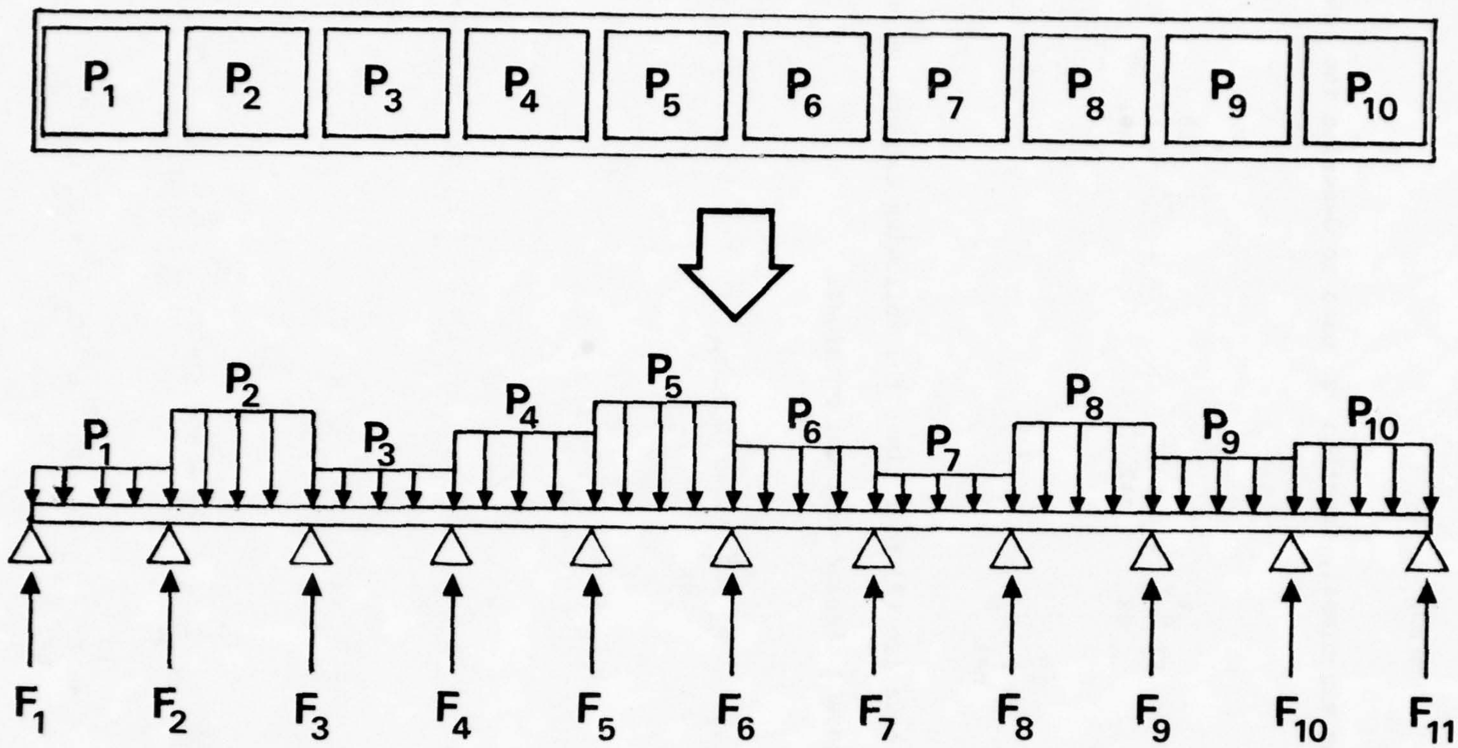

Figure 100: Reduction of Wingbox to Simple Beam

$$v_i = 0 \qquad i = 1, 2, \ldots, 10, 11$$

$$M(0) = M(80) = 0 \tag{7}$$

The following singularity function was used to describe the loading on the beam

$$P(x) = EI \frac{d^4 v}{dx^4} = \sum_{m=2}^{10} F_m <x - 8(m-1)>^{-1} - \sum_{n=1}^{10} P_n <x - 8(n-1)>^0$$

$$+ \sum_{n=1}^{10} P_n <x - 8n>^0 \tag{8}$$

Integrating equation (8) four times the following expressions for shear, moment, slope and displacement are obtained:

$$- V(x) = EI \frac{d^3 v}{dx^3} = F_m <x - 8(m-1)>^0 - P_n <x - 8(n-1)>^1 +$$

$$+ P_n <x - 8n>^1 + C_1 \tag{9}$$

$$M(x) = EI \frac{d^2 v}{dx^2} = F_m <x - 8(m-1)>^1 - \frac{1}{2} P_n <x - 8(n-1)>^2 +$$

$$+ \frac{1}{2} P_n <x - 8n>^2 + C_1 x + C_2 \tag{10}$$

$$EI \frac{dv}{dx} = \sum_{m=2}^{10} \frac{1}{2} F_m <x - 8(m-1)>^2 - \sum_{n=1}^{10} \frac{1}{6} P_n <x - 8(n-1)>^3 +$$

$$+ \sum_{n=1}^{10} \frac{1}{6} P_n <x - 8n>^3 + \frac{1}{2} C_1 x^2 + C_2 x + C_3 \tag{11}$$

$$EI\,v = \sum_{m=2}^{10} \frac{1}{6} F_m \langle x - 8(m-1)\rangle^3 - \sum_{n=1}^{10} \frac{1}{24} P_n \langle x - 8(n-1)\rangle^4 +$$

$$+ \sum_{n=1}^{10} \frac{1}{24} P_n \langle x - 8n\rangle^4 + \frac{1}{6} C_1 x^3 + \frac{1}{2} C_2 x + C_3 x + C_4 \quad (12)$$

Applying the boundary conditions stated in equation (7) yielded 13 simultaneous expressions in F_i , C_j and P_k . These expressions were represented in matrix form as follows:

$$[A]\{F\} = \{P\} \quad (13)$$

where $[A]$, $\{F\}$ and $\{P\}$ are given in Tables 8 through 10. Premultiplying equation (13) by $[A]^{-1}$ yielded:

$$\{F\} = [A]^{-1}\{P\}$$

where the vector $\{P\}$ was specified for each load case and $[A]^{-1}$ is the constant coefficient matrix. Consequently, the support forces and the four constants of integration were determined for each load case. Substitution of the F_i and C_i values into the equations for pressure, shear, moment and displacement, yielded equations for all four quantities as a function of the distance along the beam, x .

The above procedure was programmed into a Hewlett-Packard model 9825 A portable computer which was tied into a Hewlett-Packard model 7221 A plotter. Using the program supplied in Table 11, twenty load cases were analyzed and plotted (Figures 101 through 118). Each figure supplies the specified loading along with the shear, moment and displacement induced by that loading.

$$
[A] = \begin{bmatrix}
0 & 0 & 0 & 0 & 0 & 0 & 0 & 0 & 0 & 0 & 0 & 0 & 24 \\
0 & 0 & 0 & 0 & 0 & 0 & 0 & 0 & 0 & 2048 & 768 & 192 & 24 \\
2048 & 0 & 0 & 0 & 0 & 0 & 0 & 0 & 0 & 16384 & 3072 & 384 & 24 \\
16384 & 2048 & 0 & 0 & 0 & 0 & 0 & 0 & 0 & 55296 & 6912 & 576 & 24 \\
55296 & 16384 & 2048 & 0 & 0 & 0 & 0 & 0 & 0 & 131072 & 12288 & 768 & 24 \\
131072 & 55296 & 16384 & 2048 & 0 & 0 & 0 & 0 & 0 & 256000 & 19200 & 960 & 24 \\
256000 & 131072 & 55296 & 16384 & 2048 & 0 & 0 & 0 & 0 & 442368 & 27648 & 1152 & 24 \\
442368 & 256000 & 131072 & 55296 & 16384 & 2048 & 0 & 0 & 0 & 702464 & 37632 & 1344 & 24 \\
702464 & 442368 & 256000 & 131072 & 55296 & 16384 & 2048 & 0 & 0 & 1048576 & 49152 & 1536 & 24 \\
1048576 & 702464 & 442368 & 256000 & 131072 & 55296 & 16384 & 2048 & 0 & 1492992 & 62208 & 1728 & 24 \\
1492992 & 1048576 & 702464 & 442368 & 256000 & 131072 & 55296 & 16384 & 2048 & 2048000 & 76800 & 1920 & 24 \\
0 & 0 & 0 & 0 & 0 & 0 & 0 & 0 & 0 & 0 & 2 & 0 & 0 \\
144 & 128 & 112 & 96 & 80 & 64 & 48 & 32 & 16 & 160 & 2 & 0 & 0
\end{bmatrix}
$$

Table 8: [A] Matrix

$$\{F\} = \left\{ \begin{array}{c} F_2 \\ F_3 \\ F_4 \\ F_5 \\ F_6 \\ F_7 \\ F_8 \\ F_9 \\ F_{10} \\ C_1 \\ C_2 \\ C_3 \\ C_4 \end{array} \right\}$$

Table 9: {F} Array

$$\{P\} = \left\{ \begin{array}{l}
0 \\
4096\,P_1 \\
61440\,P_1 + 4096\,P_2 \\
266240\,P_1 + 61440\,P_2 + 4096\,P_3 \\
716800\,P_1 + 266240\,P_2 + 61440\,P_3 + 4096\,P_4 \\
1511424\,P_1 + 716800\,P_2 + 266240\,P_3 + 61440\,P_4 + 4096\,P_5 \\
2748416\,P_1 + 1511424\,P_2 + 716800\,P_3 + 266240\,P_4 + 61440\,P_5 + 4096\,P_6 \\
4526080\,P_1 + 2748416\,P_2 + 1511424\,P_3 + 716800\,P_4 + 266240\,P_5 + 61440\,P_6 + 4096\,P_7 \\
6942720\,P_1 + 4526080\,P_2 + 2748416\,P_3 + 1511424\,P_4 + 716800\,P_5 + 266240\,P_6 + 61440\,P_7 + 4096\,P_8 \\
10096640\,P_1 + 6942720\,P_2 + 4526080\,P_3 + 2748416\,P_4 + 1511424\,P_5 + 716800\,P_6 + 266240\,P_7 + 61440\,P_8 + 4096\,P_9 \\
14086144\,P_1 + 10096640\,P_2 + 6942720\,P_3 + 4526080\,P_4 + 2748416\,P_5 + 1511424\,P_6 + 716800\,P_7 + 266240\,P_8 + 61440\,P_9 + 4096\,P_{10} \\
0 \\
1216\,P_1 + 1088\,P_2 + 960\,P_3 + 832\,P_4 + 704\,P_5 + 576\,P_6 + 448\,P_7 + 320\,P_8 + 192\,P_9 + 64\,P_{10}
\end{array} \right\}$$

Table 10: {P} Array

Table 11: Singularity Function Analysis Computer Program

```
0: dim A[13,13],I[13,13],P[10],F[13],C[13],D[4,321]
1: rew;trk 1;ldf 0,A[*],I[*]
2: "TEST":ent "DO YOU WANT A RUN? (1=YES:2=NO)",Z
3: if Z=2;stp
4: dsp "ENTER PRESSURES";wait 2000
5: for I=1 to 10
6: ent P[I]
7: next I
8: ent "PUT IN PAPER",Z
9: 0→F[1]
10: for I=1 to 10
11: 0→F[I+1]
12: for K=1 to I
13: I-K+1→J
14: F[I+1]+P[K]*((8*J)↑4-(8*(J-1))↑4)→F[I+1]
15: next K
16: next I
17: 0→F[12]
18: 0→F[13]
19: for L=1 to 10
20: F[13]+(21-L*2)*64*P[L]→F[13]
21: next L
22: mat I*F→C
23: for N=1 to 321
24: (N-1)/4→X
25: int(X/8)→I
26: C[10]/6*X↑3+C[11]/2*X↑2+C[12]*X+C[13]→V
27: C[10]→S
28: C[10]*X+C[11]→M
29: V-P[1]*X↑4/24→V
30: -P[1]→P
31: S-P[1]*X→S
32: M-P[1]/2*X↑2→M
33: for L=1 to I
34: if X<8;gto +7
35: if X=80;if L=10;gto +6
36: P+(P[L]-P[L+1])→P
37: S+C[L]+(P[L]-P[L+1])*(X-L*8)→S
38: M+C[L]*(X-L*8)+(P[L]-P[L+1])*(X-L*8)↑2/2→M
39: V+C[L]*(X-L*8)↑3/6+(P[L]-P[L+1])*(X-L*8)↑4/24→V
40: next L
41: V→D[1,N];M→D[2,N];-S→D[3,N];P→D[4,N]
42: next N
43: psc 505
44: pclr
45: -190→r1;60→r2;50→r3;5→r4;2→r5;1→r9;gsb "GRAPH"
46: plt -12,0,1
47: lbl "EIv"
48: -50→r1;75→r2;10→r3;2.5→r4;2→r5;2→r9;gsb "GRAPH"
49: lbl "M"
50: -25→r1;100→r2;5→r3;1→r4;5→r5;3→r9;gsb "GRAPH"
51: lbl "V"
52: -6→r1;94→r2;2→r3;1→r4;2→r5;4→r9;gsb "GRAPH"
53: lbl "P"
54: gto "TEST"
55: end
56: "GRAPH":pen# 1;fxd 0
57: scl -10,80,r1,r2
58: csiz 1.2,2,3/2,0
59: xax 0,8,0,80,5
60: yax 0,r4,-r3,r3,r5
61: pen# 2
62: for N=1 to 321
63: plt (N-1)/4,D[r9,N]
64: next N
65: pen# 1
66: csiz 2.5,2,3/2,0
67: plt 77.5,1,1
68: lbl "X"
69: plt -9,0,1
70: ret
*22023
```

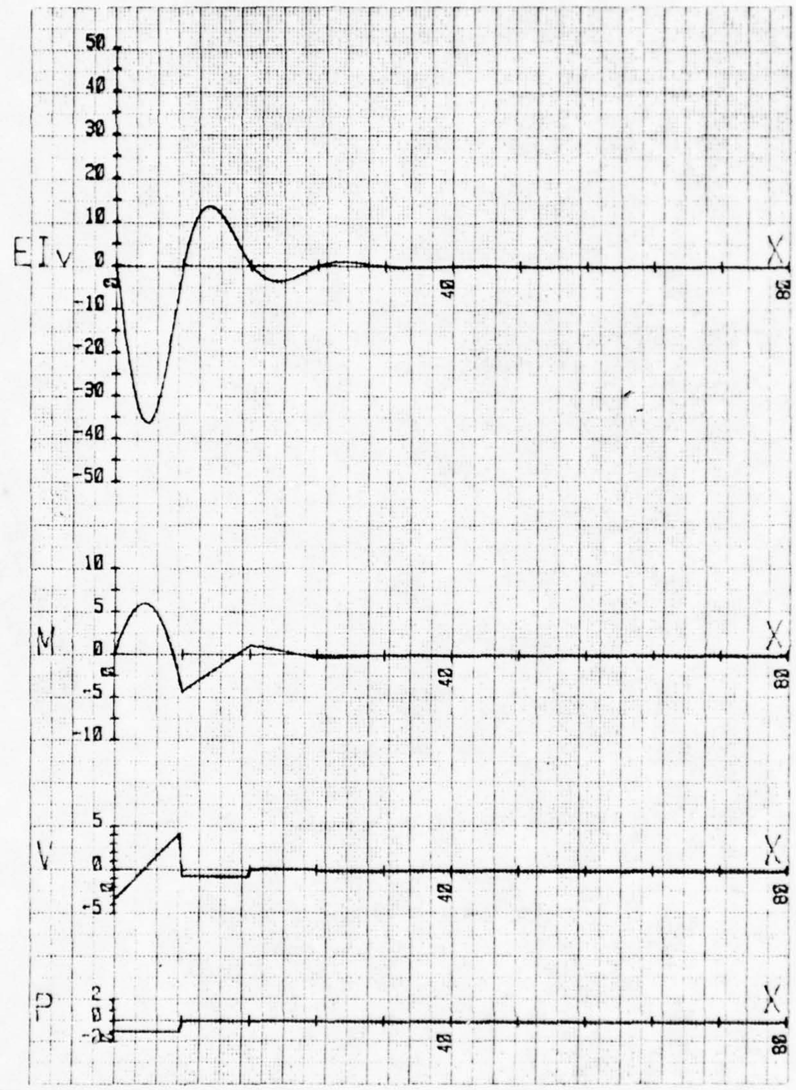

Figure 101: Singularity Function Analysis--Load Case 1

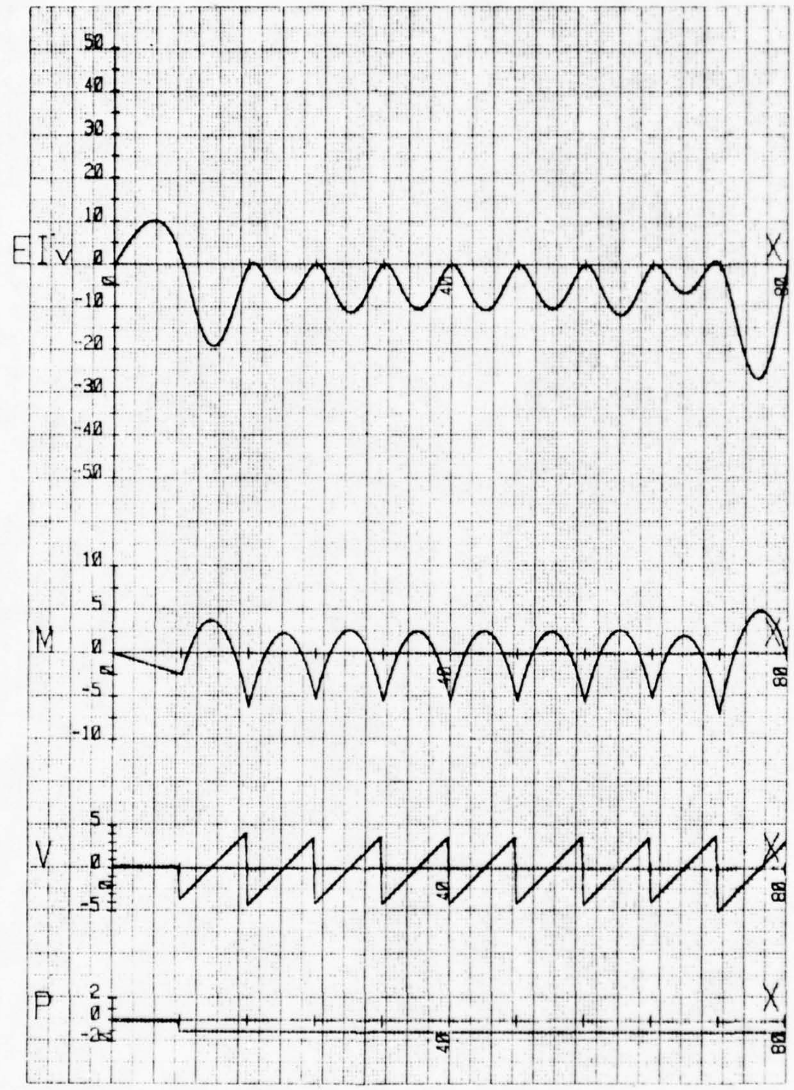

Figure 102: Singularity Function Analysis--Load Case 2

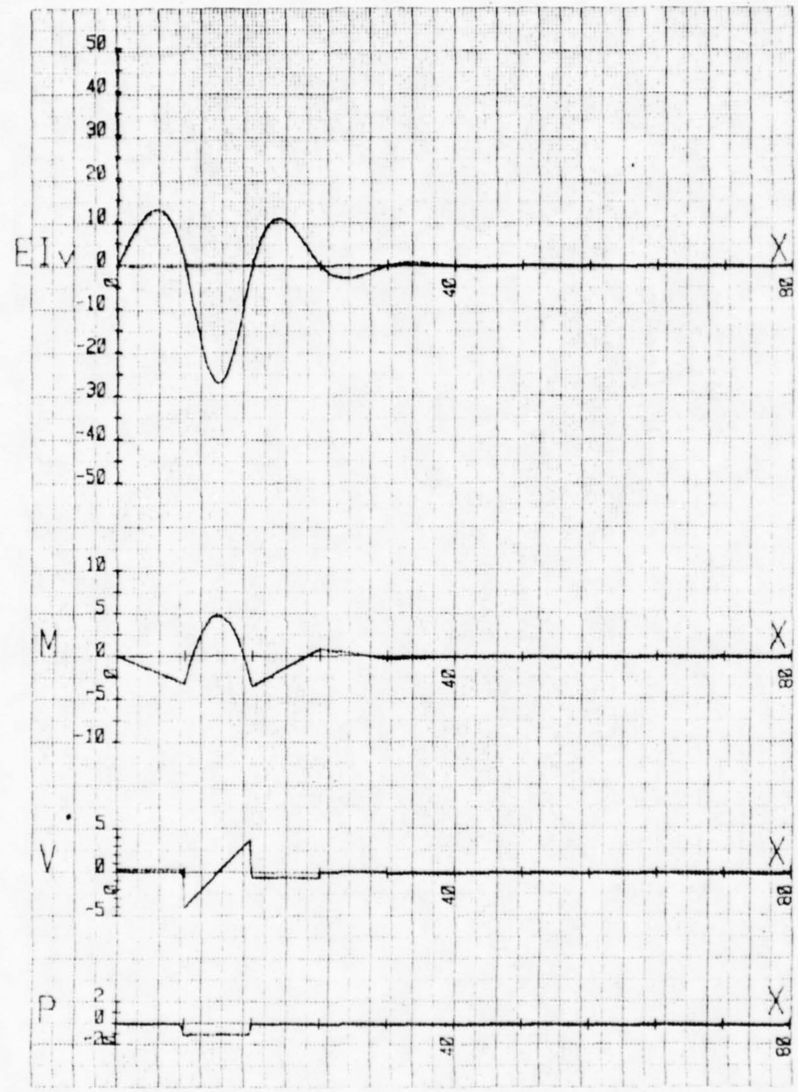

Figure 103: Singularity Function Analysis--Load Case 3

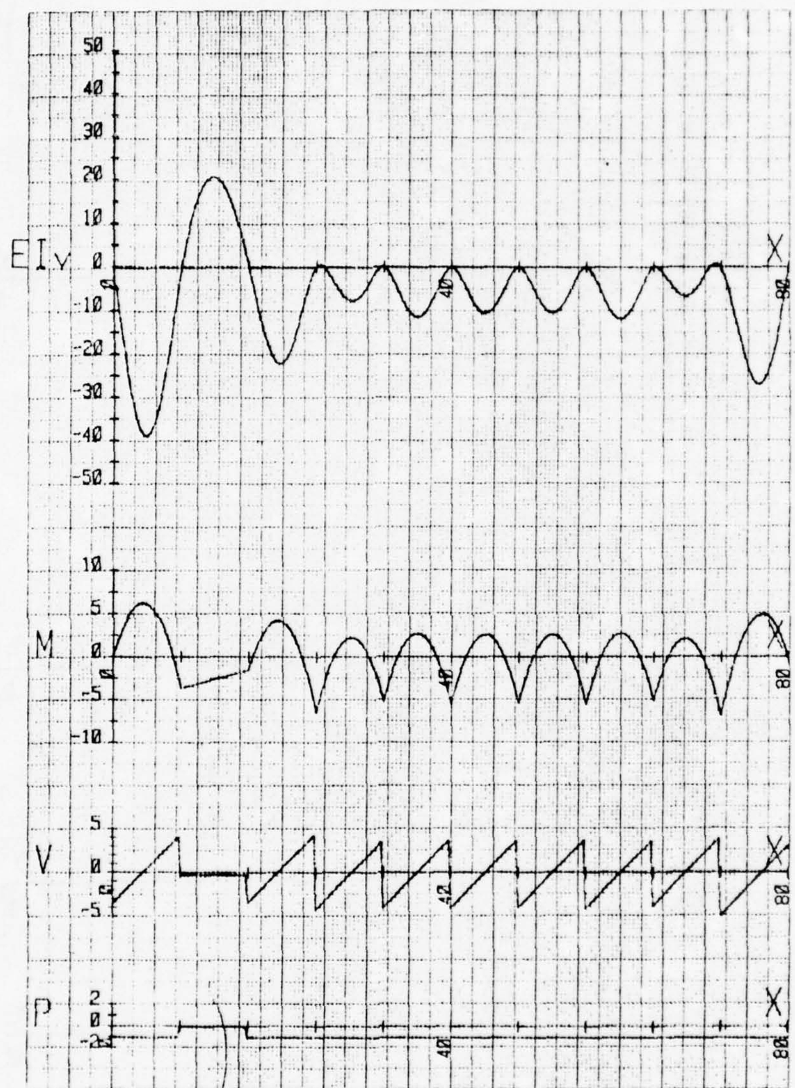

Figure 104: Singularity Function Analysis--Load Case 4

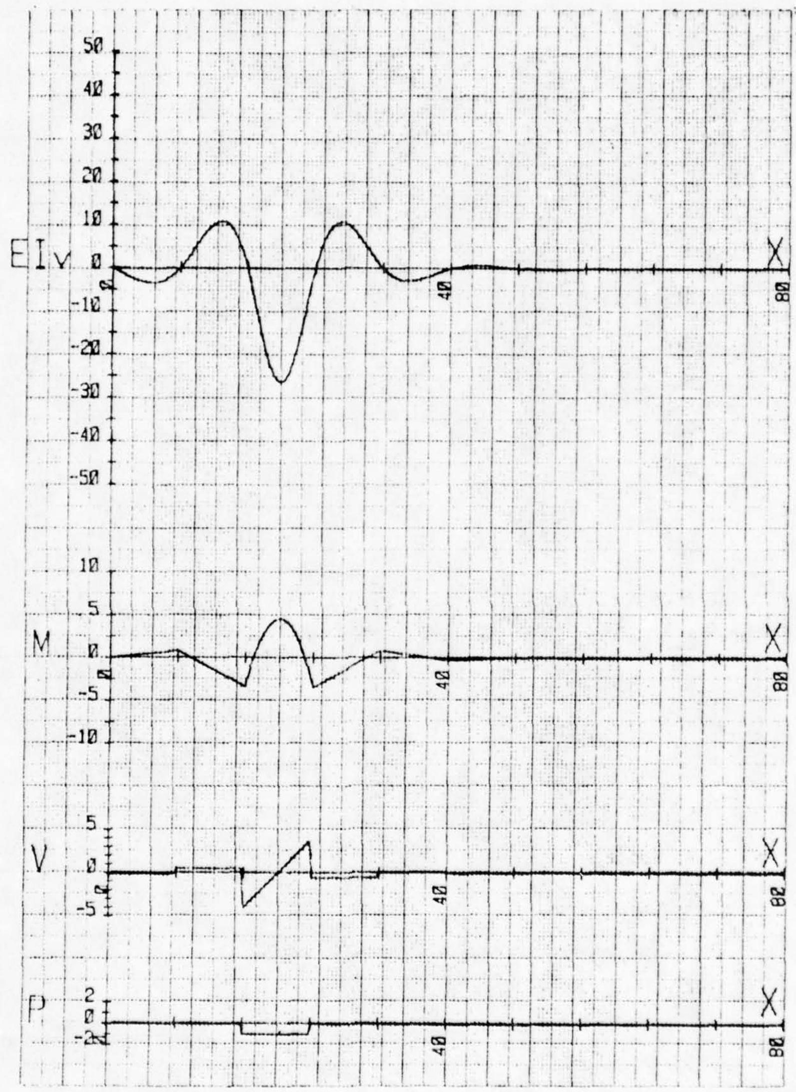

Figure 105: Singularity Function Analysis--Load Case 5

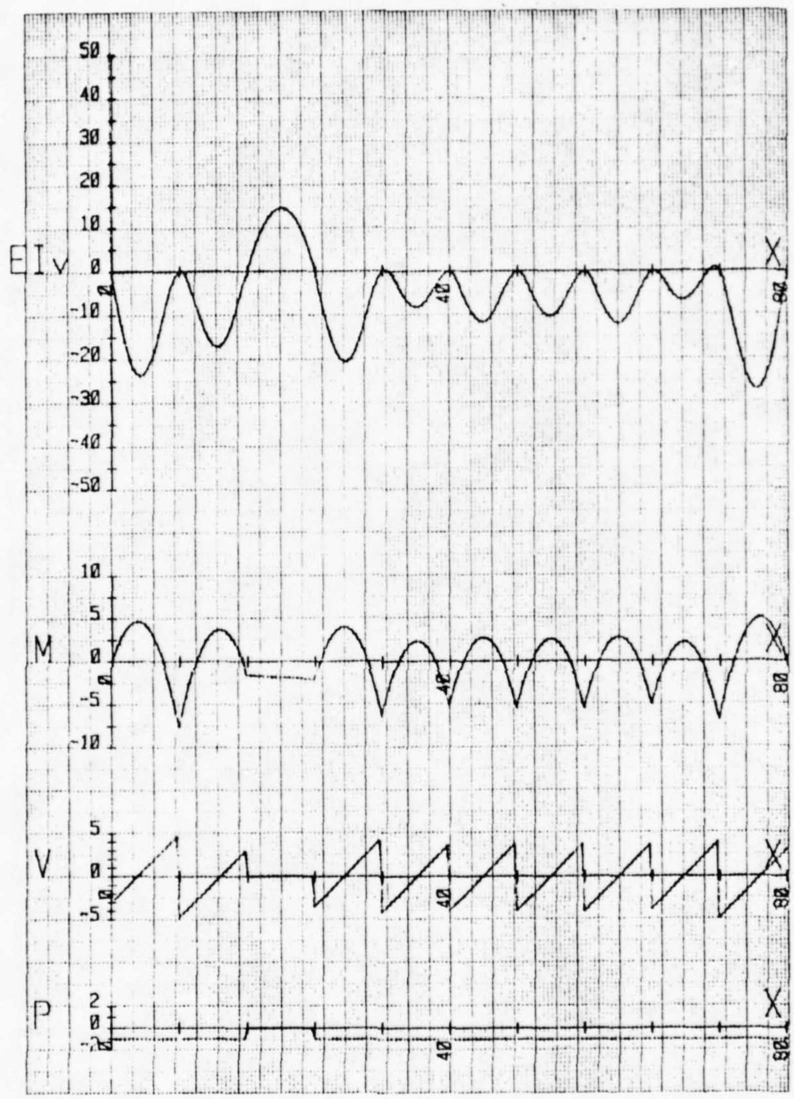

Figure 106: Singularity Function Analysis--Load Case 6

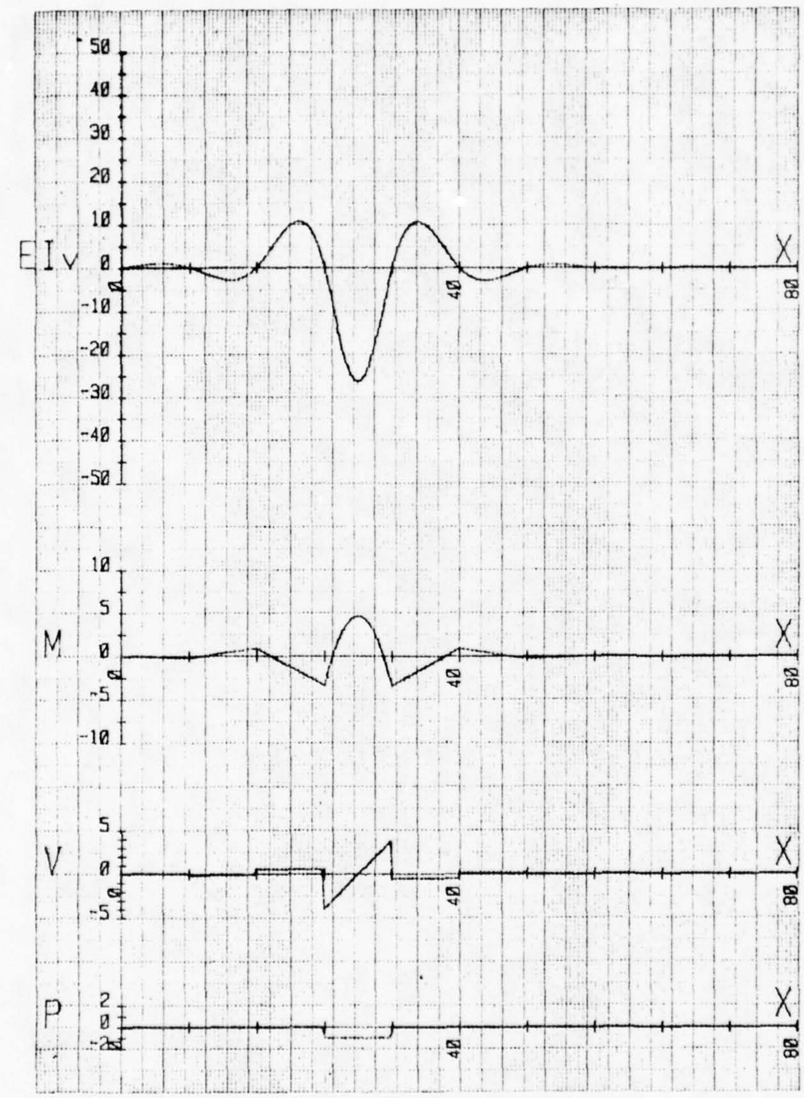

Figure 107: Singularity Function Analysis--Load Case 7

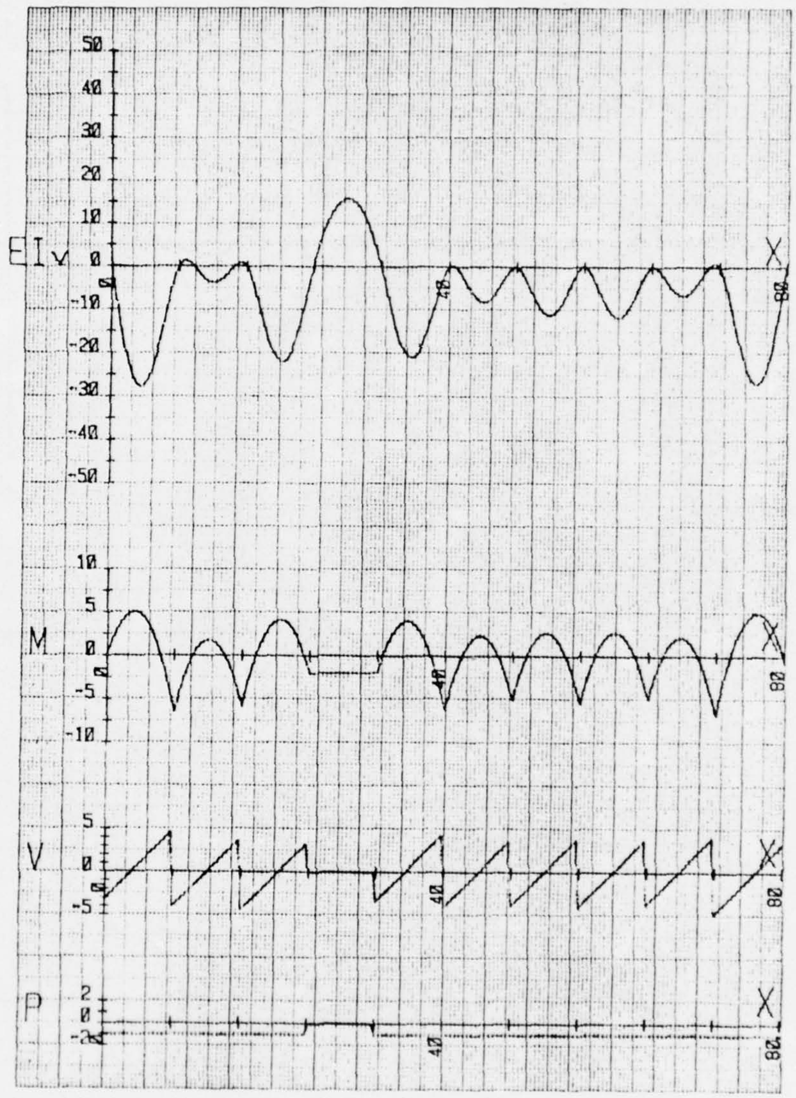

Figure 108: Singularity Function Analysis--Load Case 8

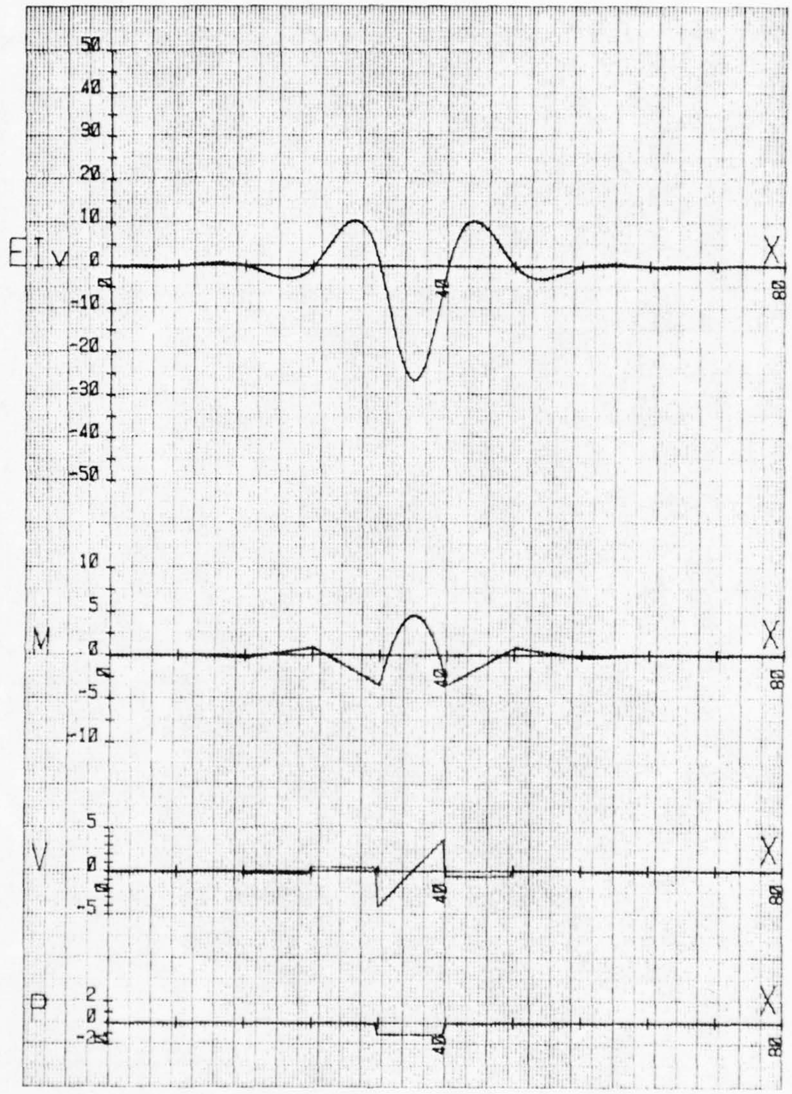

Figure 109: Singularity Function Analysis--Load Case 9

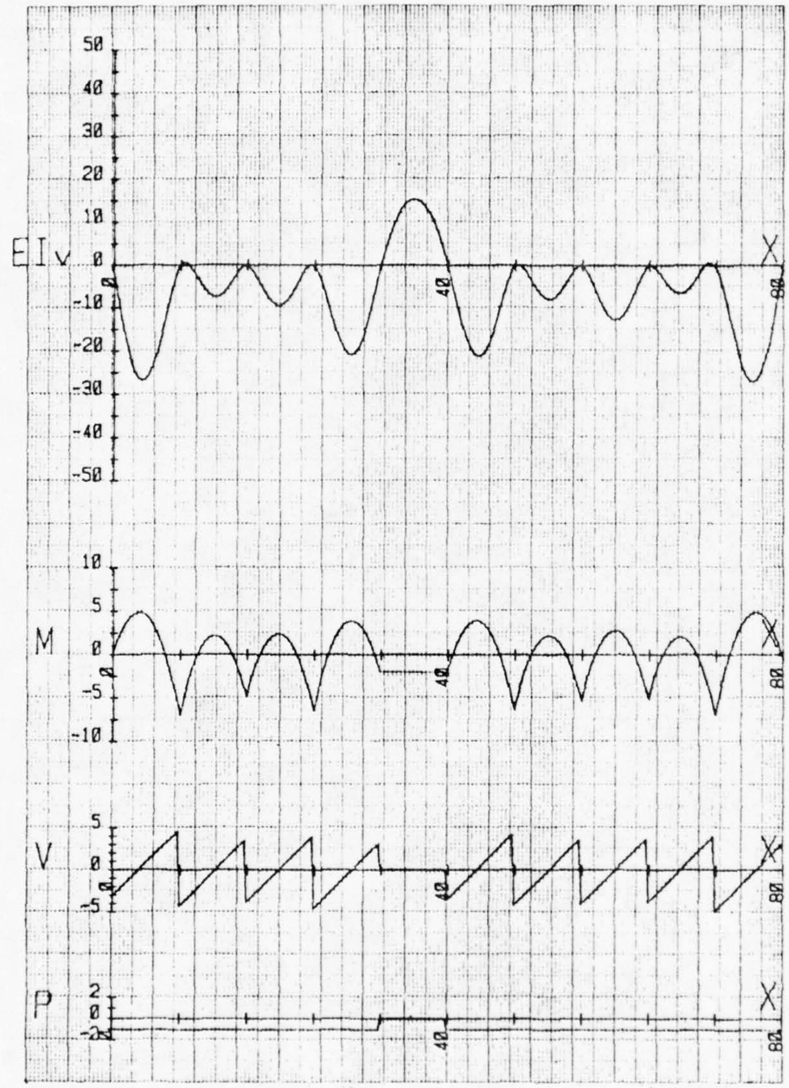

Figure 110: Singularity Function Analysis--Load Case 10

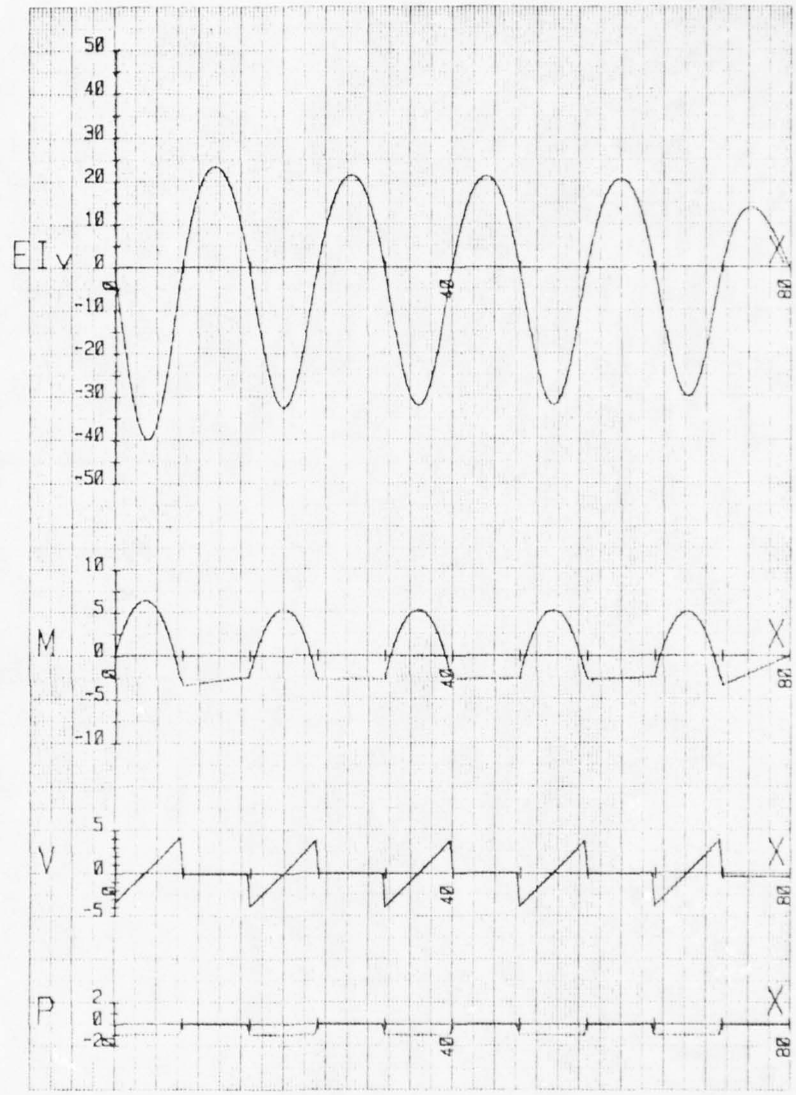

Figure 111: Singularity Function Analysis--Load Case 11

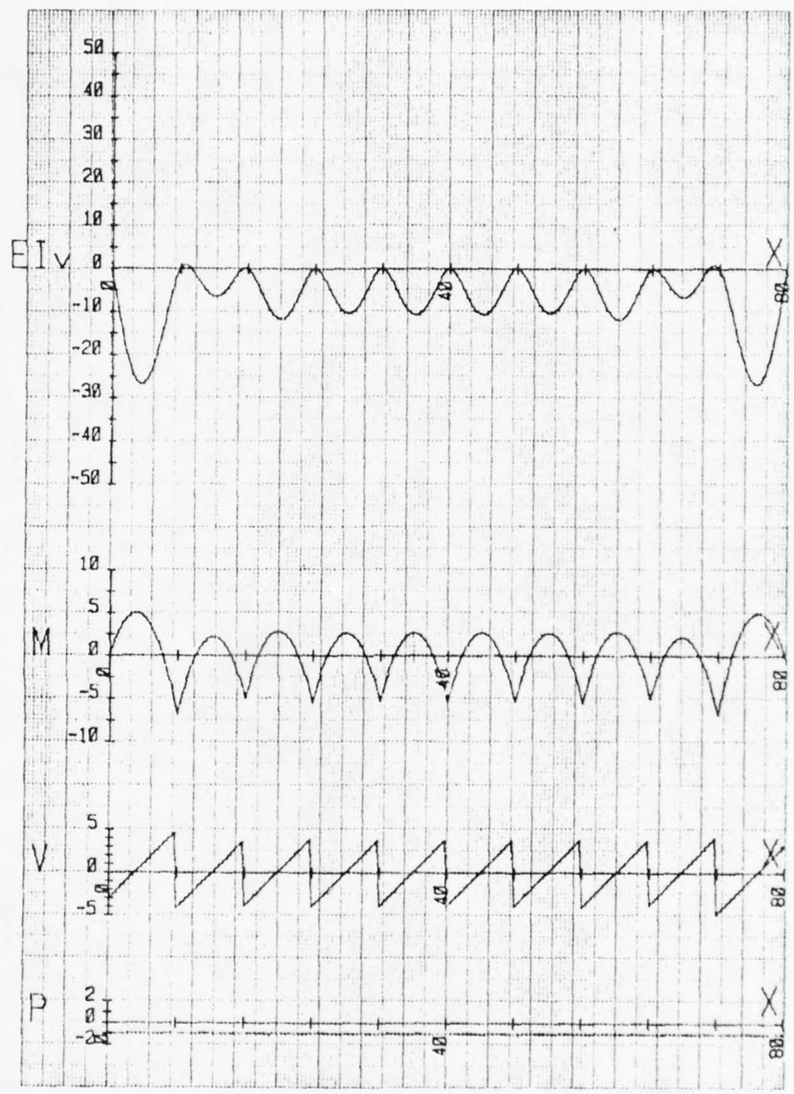

Figure 112: Singularity Function Analysis--Load Case 12

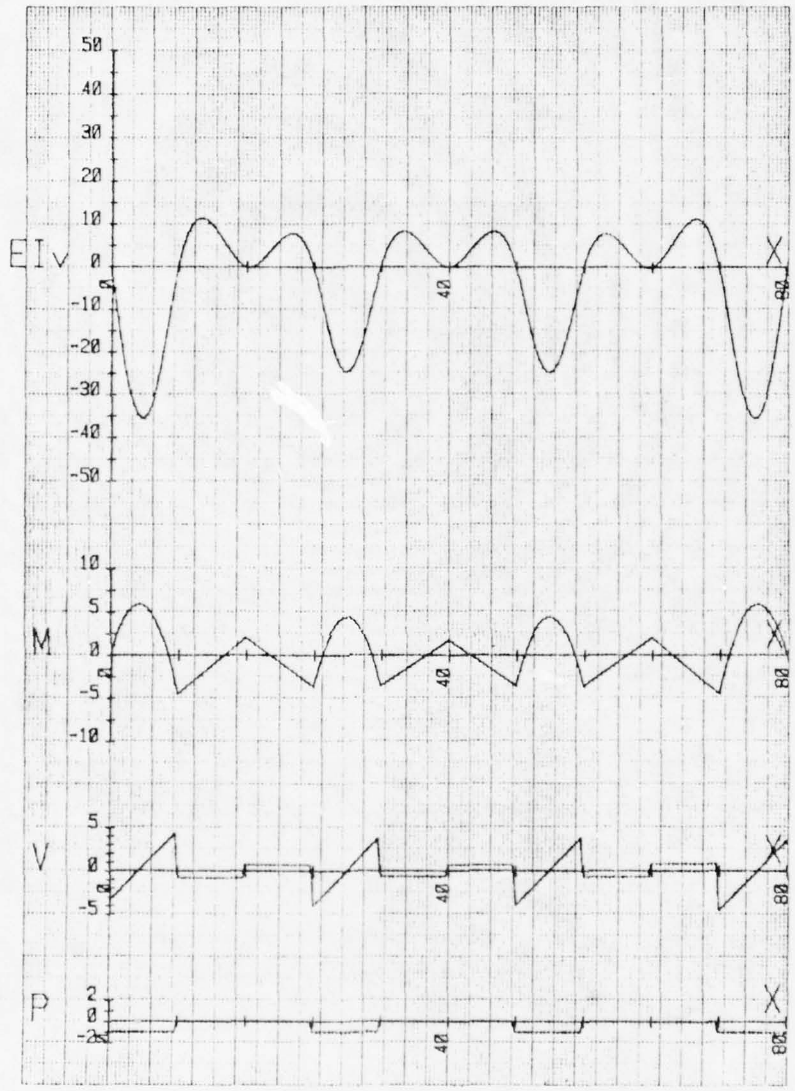

Figure 113: Singularity Function Analysis--Load Case 13

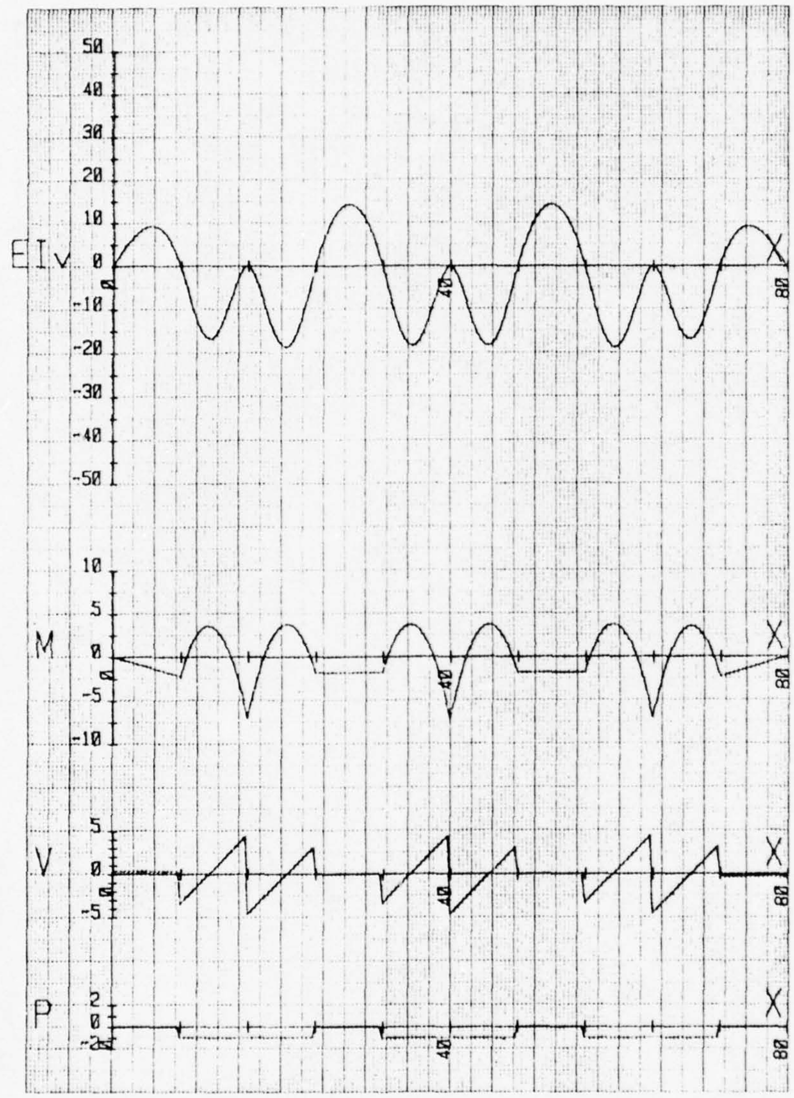

Figure 114: Singularity Function Analysis--Load Case 14

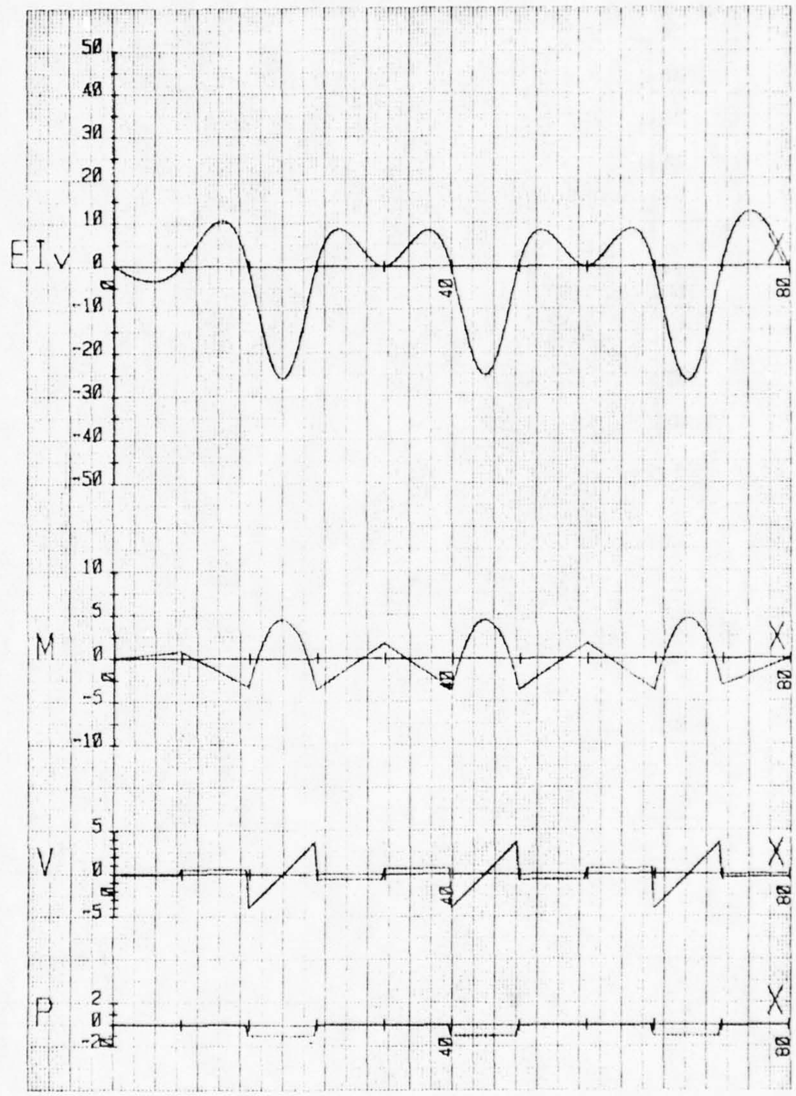

Figure 115: Singularity Function Analysis--Load Case 15

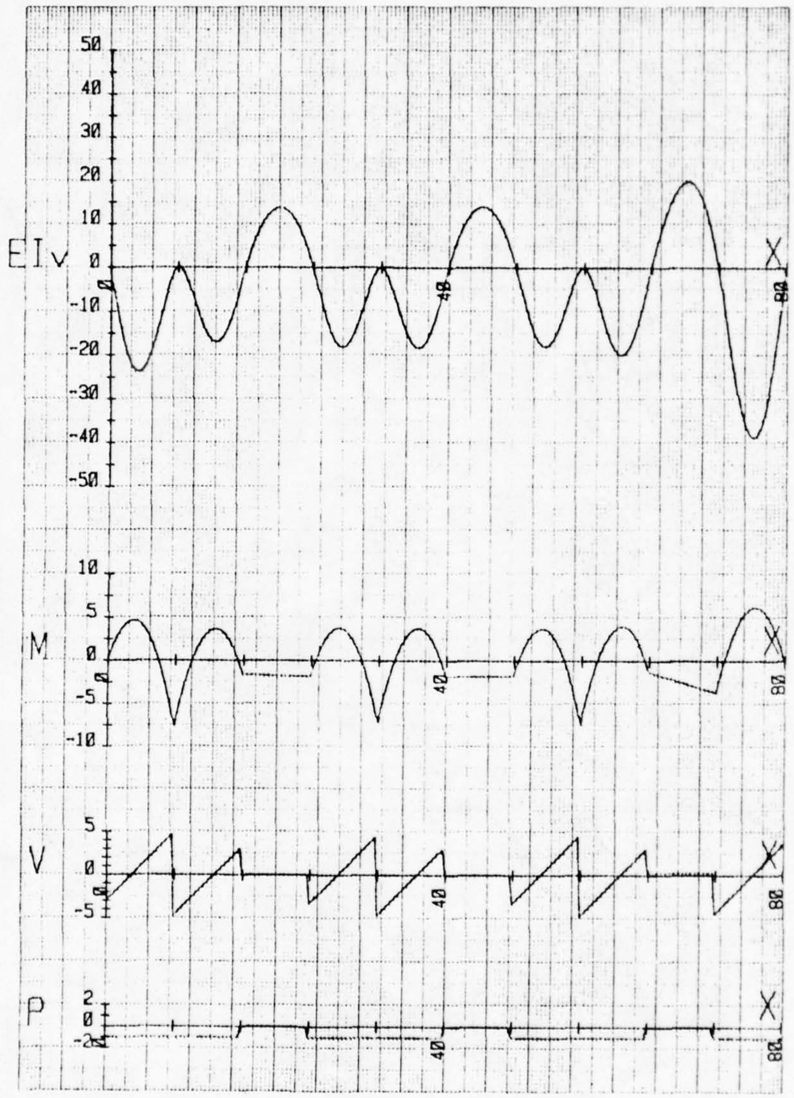

Figure 116: Singularity Function Analysis--Load Case 16

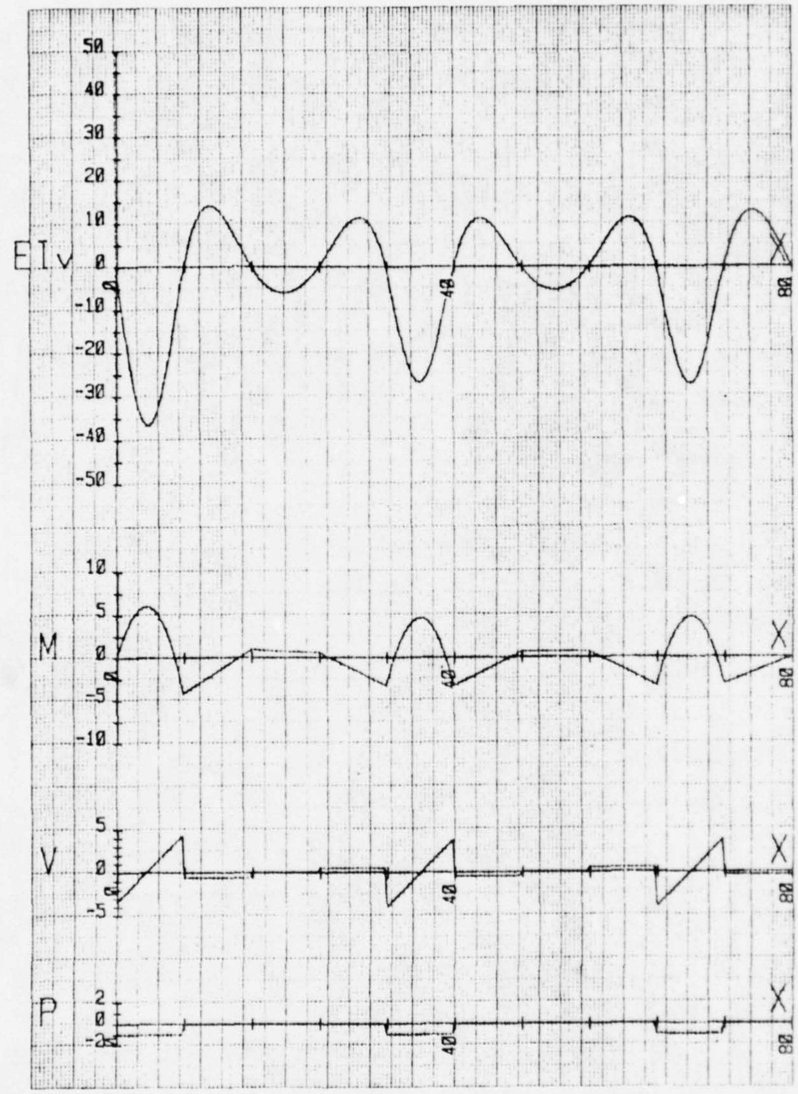

Figure 117: Singularity Function Analysis--Load Case 17

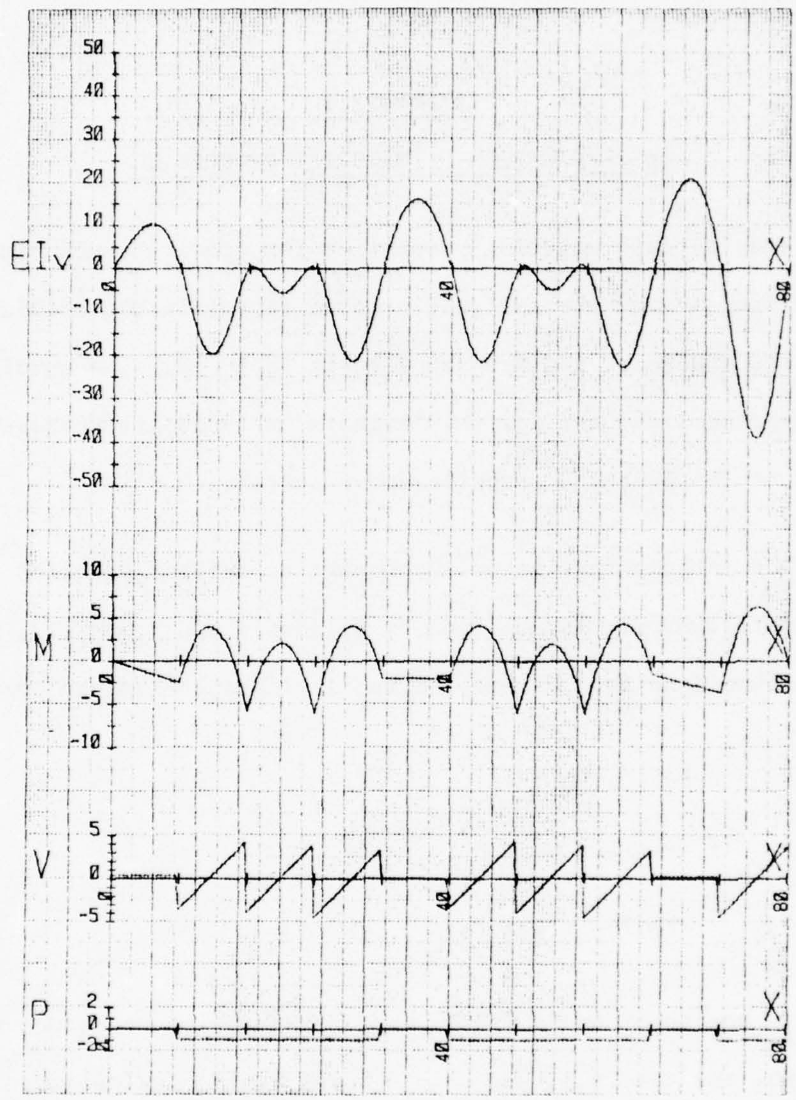

Figure 118: Singularity Functicn Analysis--Load Case 18

APPENDIX B

DETERMINATION OF MATERIAL PROPERTIES

The in-plane material properties for specific sublaminates were obtained from a laminate analysis program (Appendix D), utilizing laminate plate analysis, and are supplied in Table 12. The unidirectional material properties used for the laminate analysis are representative of the Hercules AS3501-6 graphite-epoxy system.

The interlaminar material properties are not provided by classical laminate theory. As outlined by Gillespie and Pipes [1], the following assumptions can be made for the lamina interlaminar properties:

$$E_3 \simeq E_2 \simeq E_z$$

$$\nu_{13} \simeq \nu_{12}$$

$$\nu_{23} \simeq \nu_f v_f + \nu_m(1-v_f)$$

where E_i are the Young's moduli and ν_{ij} are the Poisson's ratios of the lamina, and the i,j subscripts refer to the lamina coordinate system shown in Figure 119. Alphabetic subscripts refer to the laminate coordinate system shown in Figure 120.

The expression for the transverse Poisson ratio of a balanced and symmetric laminate was derived as shown [1]. The definition of the

Table 12: Material Properties

	E_x GPa (Msi)	E_y GPa (Msi)	E_z GPa (Msi)	ν_{xy}	ν_{yz}	ν_{zx}	G_{yz} GPa (Msi)
Unidirectional AS-3501-6 Graphite-Epoxy	137.2 (19.9)	9.6 (1.4)	9.6 (1.4)	0.015	0.300	0.015	4.1 (0.6)
$(\pm45/90_2)(0/\pm45/0)_2$ Graphite-Epoxy Laminates	53.0 (7.7)	33.7 (4.9)	9.6 (1.4)	0.237	0.217	0.032	4.1 (0.6)
$(0/\pm45/0)_n$ Graphite-Epoxy Laminates	77.4 (11.2)	22.3 (3.2)	9.6 (1.4)	0.199	0.241	0.010	4.1 (0.6)
$(\pm45/90_2)$ Graphite-Epoxy Laminates	13.7 (2.0)	38.8 (5.6)	9.6 (1.4)	0.687	0.076	0.169	4.1 (0.6)
$(\pm45/90_2)(0/\pm45/0)$ Graphite-Epoxy Laminates	41.2 (6.0)	45.0 (6.5)	9.6 (1.4)	0.286	0.200	0.047	4.1 (0.6)
$(\pm45)_n$ Graphite-Epoxy Laminates	14.9 (2.2)	14.9 (2.2)	9.6 (1.4)	0.803	0.057	0.037	4.1 (0.6)
Reliabond 398	3.4 (0.5)	3.4 (0.5)	3.4 (0.5)	0.300	0.300	0.300	4.1 (0.6)

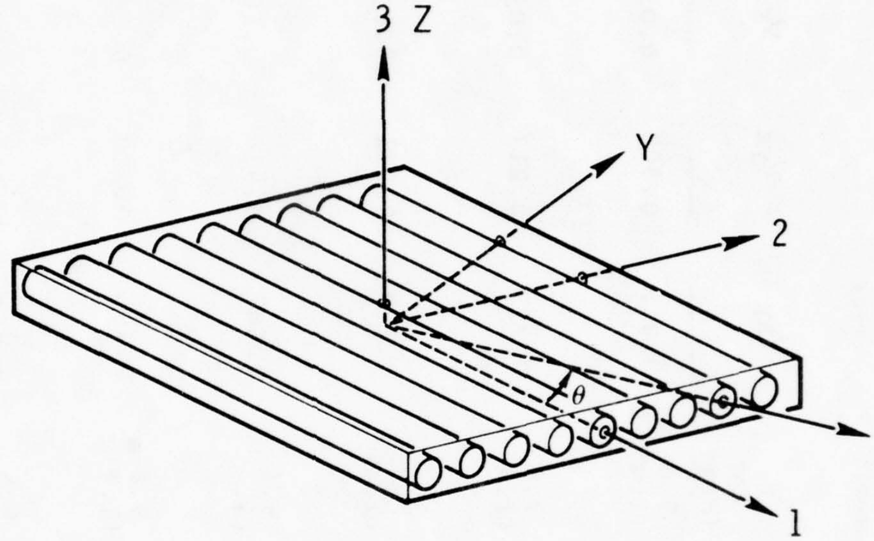

Figure 119: Lamina Coordinate System

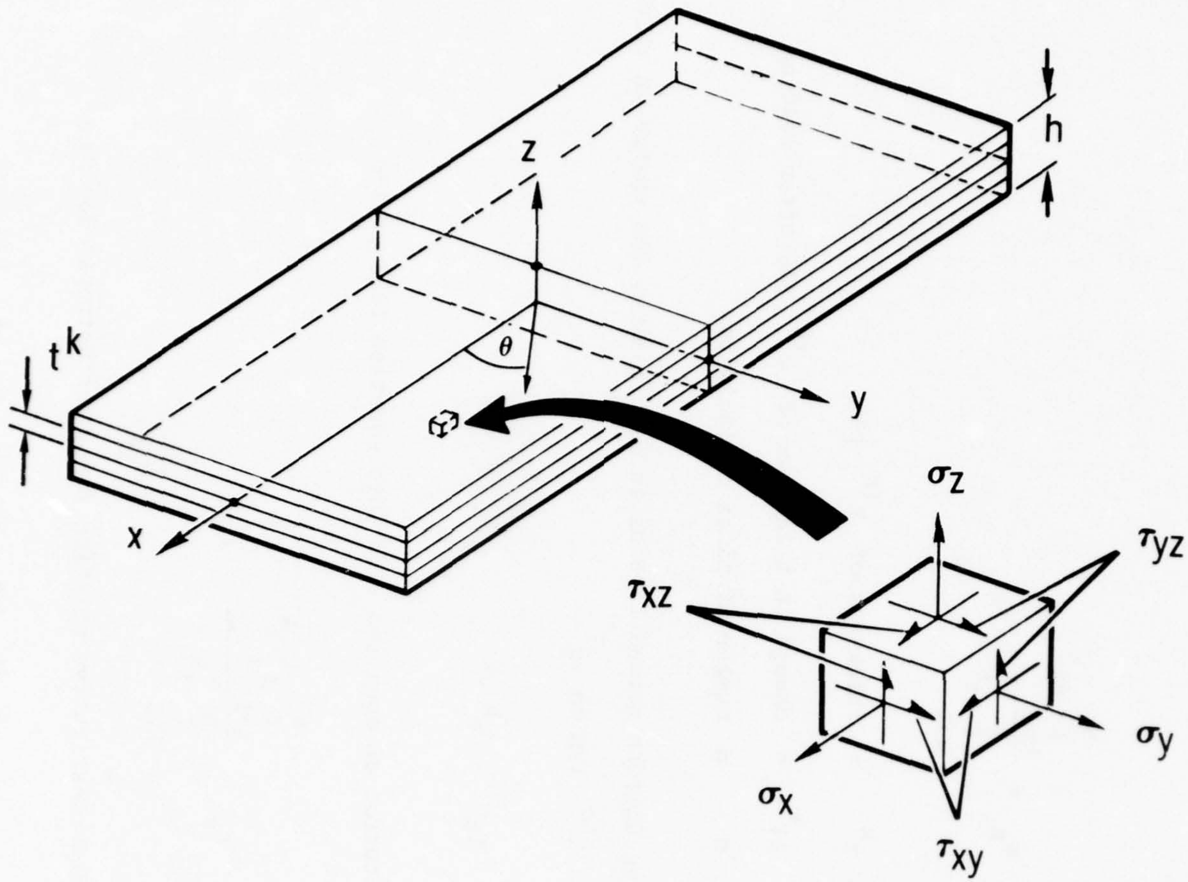

Figure 120 : Laminate Coordinate System

transverse Poisson ratio is

$$\nu_{iz} = -\frac{\varepsilon_z}{\varepsilon_i} \qquad i = x,y \tag{14}$$

where

$$\varepsilon_z = \frac{\sum_{k=1}^{n} \Delta t^k}{\sum_{k=1}^{n} t^k} \tag{15}$$

and t^k = thickness of k^{th} ply

Δt^k = change in thickness of k^{th} ply after loading

n = number of plies in laminate.

Assuming uniform normal strains in each lamina, the change in thickness of the k^{th} lamina is

$$\Delta t^k = \varepsilon_z^k \, t^k \ . \tag{16}$$

Substitution of equation (16) into equation (17) yields

$$\varepsilon_z = \frac{\sum_{k=1}^{n} \varepsilon_z^k \, t^k}{\sum_{k=1}^{n} t^k} \ . \tag{17}$$

From the constitutive relation for an orthotropic lamina,

$$\sigma_z = \bar{C}_{13}^k \varepsilon_x^k + \bar{C}_{23}^k \varepsilon_y^k + \bar{C}_{33}^k \varepsilon_z^k + \bar{C}_{36}^k \gamma_{xy}^k \ ,$$

and assuming plane stress $(\sigma_z = 0)$, the following relation between the strain components for the k^{th} layer is obtained.

$$\varepsilon_z^k = -\frac{\bar{C}_{13}^k \varepsilon_x^k}{\bar{C}_{33}^k} - \frac{\bar{C}_{23}^k \varepsilon_y^k}{\bar{C}_{33}^k} - \frac{\bar{C}_{36}^k \gamma_{xy}^k}{\bar{C}_{33}^k} \quad . \tag{18}$$

Examination of laminate theory provides expressions for the in-plane strains ε_x, ε_y and γ_{xy}. Subjecting a symmetric and balanced laminate to the loading, $N_y \neq 0$, $N_x = N_{xy} = 0$, the laminate plate theory yields the expression

$$\begin{bmatrix} 0 \\ N_y \\ 0 \end{bmatrix} = \begin{bmatrix} A_{11} & A_{12} & 0 \\ A_{12} & A_{22} & 0 \\ 0 & 0 & A_{66} \end{bmatrix} \begin{bmatrix} \varepsilon_x \\ \varepsilon_y \\ \varepsilon_{xy} \end{bmatrix} \tag{19}$$

where A_{ij} is the laminate extensional stiffness matrix. Equation (19) can be solved for ε_x and ε_y yielding

$$\varepsilon_y = \frac{A_{11} N_y}{A_{11} A_{22} - A_{12}^2} \tag{20}$$

$$\varepsilon_x = \frac{- A_{12} N_y}{A_{11} A_{22} - A_{12}^2} \quad . \tag{21}$$

Substituting equations (20) and (21) into equation (18) the normal strain, ε_z^k, in the k^{th} layer may be determined

$$\varepsilon_z^k = \frac{\bar{C}_{13}^k}{\bar{C}_{33}^k}\left(\frac{A_{12}\,N_y}{A_{11}\,A_{22}-A_{12}^2}\right) - \frac{\bar{C}_{23}^k}{\bar{C}_{33}^k}\left(\frac{A_{11}\,N_y}{A_{11}\,A_{22}-A_{12}^2}\right) \quad . \tag{22}$$

Equation (22) may be substituted into equation (17) and combined with equation (20) to give the final expression for the transverse Poisson's ratio of the laminate, ν_{yz}

$$\nu_{yz} = \frac{-\sum_{k=1}^{n}\left(\frac{\bar{C}_{13}^k}{\bar{C}_{33}^k}\frac{A_{12}}{A_{11}} - \frac{\bar{C}_{23}^k}{\bar{C}_{33}^k}\right)t^k}{\sum_{k=1}^{n} t^k} \quad . \tag{23}$$

From reciprocity we may determine the minor transverse Poisson's ratio,

$$\nu_{zy} = (\nu_{yz})(\varepsilon_z/\varepsilon_y) \quad .$$

The expression for the second Poisson's ratio, ν_{xz} , can be determined in a similar manner

$$\nu_{xz} = \frac{-\sum_{k=1}^{n}\left(\frac{\bar{C}_{23}^k}{\bar{C}_{33}^k}\frac{A_{12}}{A_{22}} - \frac{\bar{C}_{13}^k}{\bar{C}_{33}^k}\right)t^k}{\sum_{k=1}^{n} t^k} \tag{24}$$

and again

$$\nu_{zx} = \nu_{xz} \frac{E_z}{E_x} .$$

In order to evaluate ν_{yz} and ν_{xz} , the transformed material constants, $\bar{C}^k_{ij}$ (i,j=1,2,3) , must be determined. Coordinate transformation provides the following:

$$\begin{aligned}
\bar{C}^k_{13} &= m^2 C_{13} + n^2 C_{23} \\
\bar{C}^k_{23} &= n^2 C_{13} + m^2 C_{23} \\
\bar{C}^k_{33} &= C_{33}
\end{aligned} \tag{25}$$

where
$$\begin{aligned}
m &= \cos\theta \\
n &= \sin\theta \\
C_{13} &= E_2(\nu_{13}+\nu_{12}\,\nu_{23})/DET \\
C_{23} &= E_2(\nu_{23}+\nu_{31}\,\nu_{12})/DET \\
C_{33} &= E_2(1-\nu_{12}\,\nu_{21})/DET \\
DET &= (1-\nu_{12}\,\nu_{21}-\nu_{13}\,\nu_{31}-\nu_{23}\,\nu_{32}-\nu_{21}\,\nu_{13}\,\nu_{32}-\nu_{31}\,\nu_{12}\,\nu_{23}) .
\end{aligned} \tag{26}$$

Repeating the assumptions for the lamina interlaminar properties made at the beginning of this derivation

$$\begin{aligned}
\nu_{13} &\simeq \nu_{12} \\
\nu_{23} &\simeq \nu_f\, v_f + \nu_m(1-v_f) \\
E_3 &\simeq E_2 .
\end{aligned}$$

Employing reciprocity

$$\nu_{31} = \nu_{13}\frac{E_3}{E_1} \approx \nu_{12}\frac{E_3}{E_1} \approx \nu_{21}$$

$$\nu_{32} = \nu_{23}\frac{E_3}{E_2} \approx \nu_{ep}\frac{E_3}{E_2} \approx \nu_{ep} \quad . \tag{27}$$

Substituting equation (27) into equation (26) yields

$$C_{13} = E_2(\nu_{12}+\nu_{12}\ \nu_{ep})/DET'$$

$$C_{23} = E_2(\nu_{ep}+\nu_{21}\ \nu_{12})/DET'$$

$$C_{33} = E_2(1-\nu_{12}\ \nu_{21})/DET'$$

$$DET' = (1-2\nu_{12}\ \nu_{21}-\nu_{ep}^2-2\nu_{12}\ \nu_{21}\ \nu_{ep}) \quad .$$

The expressions for the interlaminar Poisson ratio are now completely defined. The above equations were incorporated into the laminate analysis program in Appendix D which was used in determination of all laminate properties supplied in Table 12.

As noted previously, the Reliabond 398 adhesive insert was modeled as an isotropic material with the properties indicated in Table 12. Values used correspond to the manufacturer's recommendation.

APPENDIX C

SPECIMEN FABRICATION AND TESTING

C.1 Prepreg Laminate Construction

In order to verify the theoretical analysis, several test specimens were fabricated and tested. Initially, a 25 × 30 cm (10 × 12 in) prepreg wingskin was fabricated using unidirectional AS3501-6 graphite-epoxy, 30 cm (12 in) wide, prepreg tape. As the 0° laminate direction was parallel to the short axis of the rectangular prepreg laminate, the 0° plies could be cut directly from the 30 cm (12 in) wide tape. 90° plies required some trimming but were easily obtained. The 45° plies were obtained by first constructing ± 45° and ∓ 45° prepreg laminates 74 cm (29 in) in width and 101 cm (40 in) in length. Each large ± 45° or ∓ 45° laminate was then cut into seven 25 × 30 cm (10 × 12 in) sections, for use in the wingskin, and twelve 13 cm (5 in) square sections. The 13 cm (5 in) squares were utilized in fabrication of the spar and will be discussed later.

After all wingskin plies had been cut the 56 ply wingskin was fabricated. Each ply was individually aligned with a fixed reference system to reduce misalignment and successive plies were rolled to reduce interlaminar voids. Special attention was taken in placement of the ± 45° plies to insure the symmetry of the finished wingskin. Upon completion of the entire prepreg wingskin, the laminate was cut into two 12 × 30 cm (5 × 12 in) sections for placement into the elastomeric tool used during processing. A conventional table saw was used to section the prepreg laminate, and the laminate was cooled to approximately 0°C (32°F) prior to cutting to reduce laminate damage and fouling of the saw blade.

With the prepreg wingskin completed, the next step was the construction of the spar and overlap. The spar was constructed of two $(\pm 45)_6$ laminates having an "L-shaped" cross-section. In order to achieve the desired shape, individual $\pm$ 45, 13 cm (5 in) square prepreg sheets were successively warmed to approximately 52°C (125°F) and formed around a sheet metal form of the desired geometry. To facilitate separation of the prepreg "L" and the metallic form, the form was covered with a teflon impregnated cloth, TX 1040, prior to the laminate forming operation. After completion of each spar sub-assembly, the entire assembly was cooled and the prepreg was trimmed to obtain a 3.66 cm (1.44 in) overlap length and a vertical spar height of 8.3 cm (3.25 in). Extra care was taken to insure that after mating of the two spar sub-assemblies, the desired symmetry of the spar laminate was obtained.

The next step was the fabrication of the Reliabond 398 insert. For the radial geometries (concepts "A" and "B") the insert was formed by rolling the uncured sheet adhesive into a cylindrical geometry. This solid adhesive cylinder was then pressed into the approximate radial insert geometry and any excess material trimmed. For the triangular geometries (concepts "C" and "D") it was necessary to pre-cure the insert in order to achieve the desired joint configuration and dimensions. Aluminum molds shown in Figure 121 were machined with a V-groove having an apex angle equal to that of the desired insert geometry and a depth equal to the corresponding insert depth. Vent ports were drilled through the bottom of the mold and aligned with the apex of the groove to allow an exit for entrapped air. The most successful results were achieved by laying in uncured strips of adhesive parallel to the sides of the groove until the groove was slightly overfilled. After curing all excess material was removed by machining and the insert was cut to a length of 13 cm (5 in). Due to surface contamination resulting from the insert-mold contact, it was necessary to treat the insert surface prior to spar-wingskin joining. Surface preparation for the pre-cured inserts involved the following steps:

1) sand lightly by hand with 400 grit
2) rinse several times with acetone until no residue remains
3) dry in vented oven at 52°C (125°F)
4) wrap with one layer of uncured Reliabond 398 adhesive

The final step in the construction of the prepreg spar-wingskin section was the joining of the two "L-shaped" spar halves, the insert and the wingskin. The insert was placed at the center of the top surface of the wingskin prepreg laminate with the insert axis perpendicular to the side of greatest length of the laminate and parallel to the principal laminate direction (Figure 122). The two "L-shaped" spar halves were joined along the spar centerline, centered over the wingskin and insert, and pressed into position. The spar-wingskin section was then ready to be

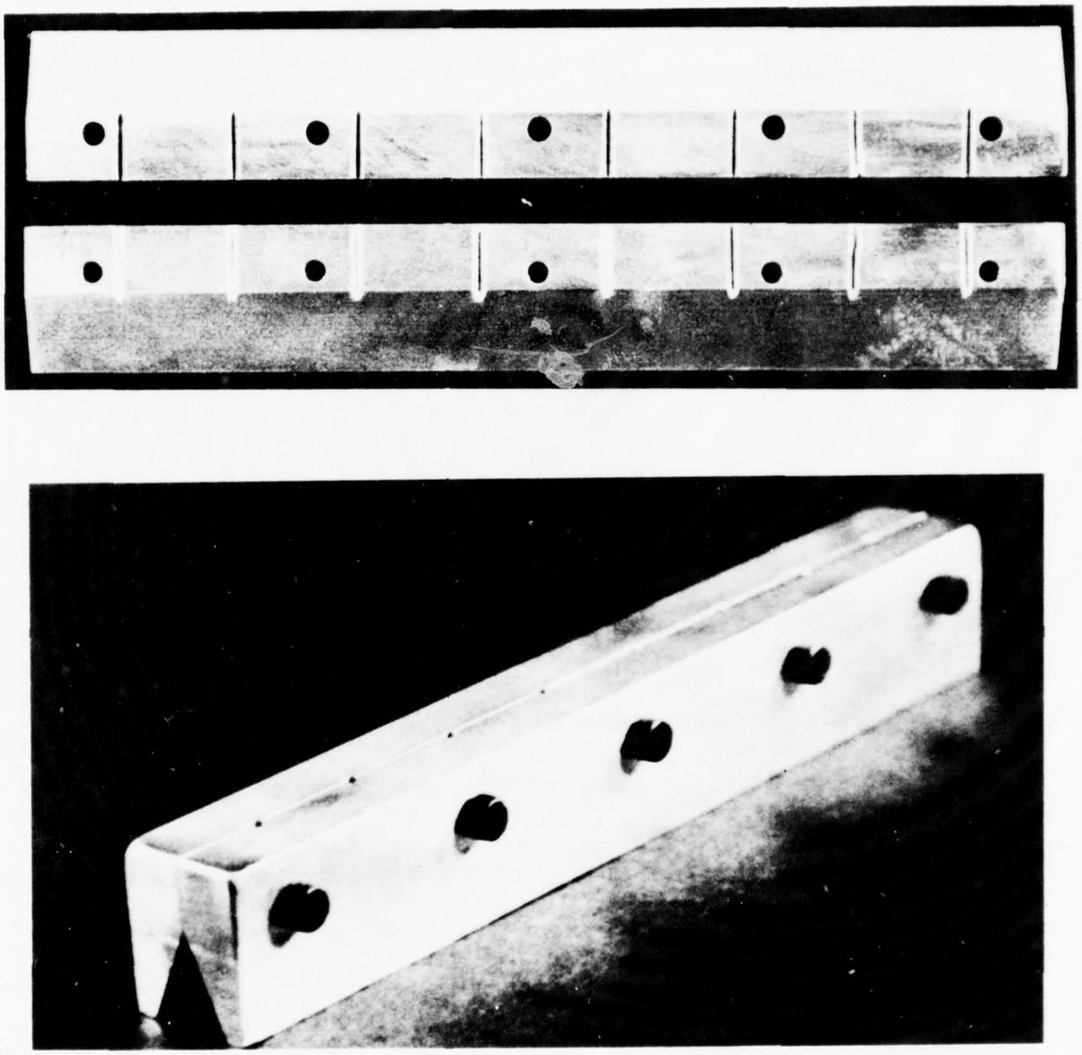

Figure 121: Aluminum Insert Molds

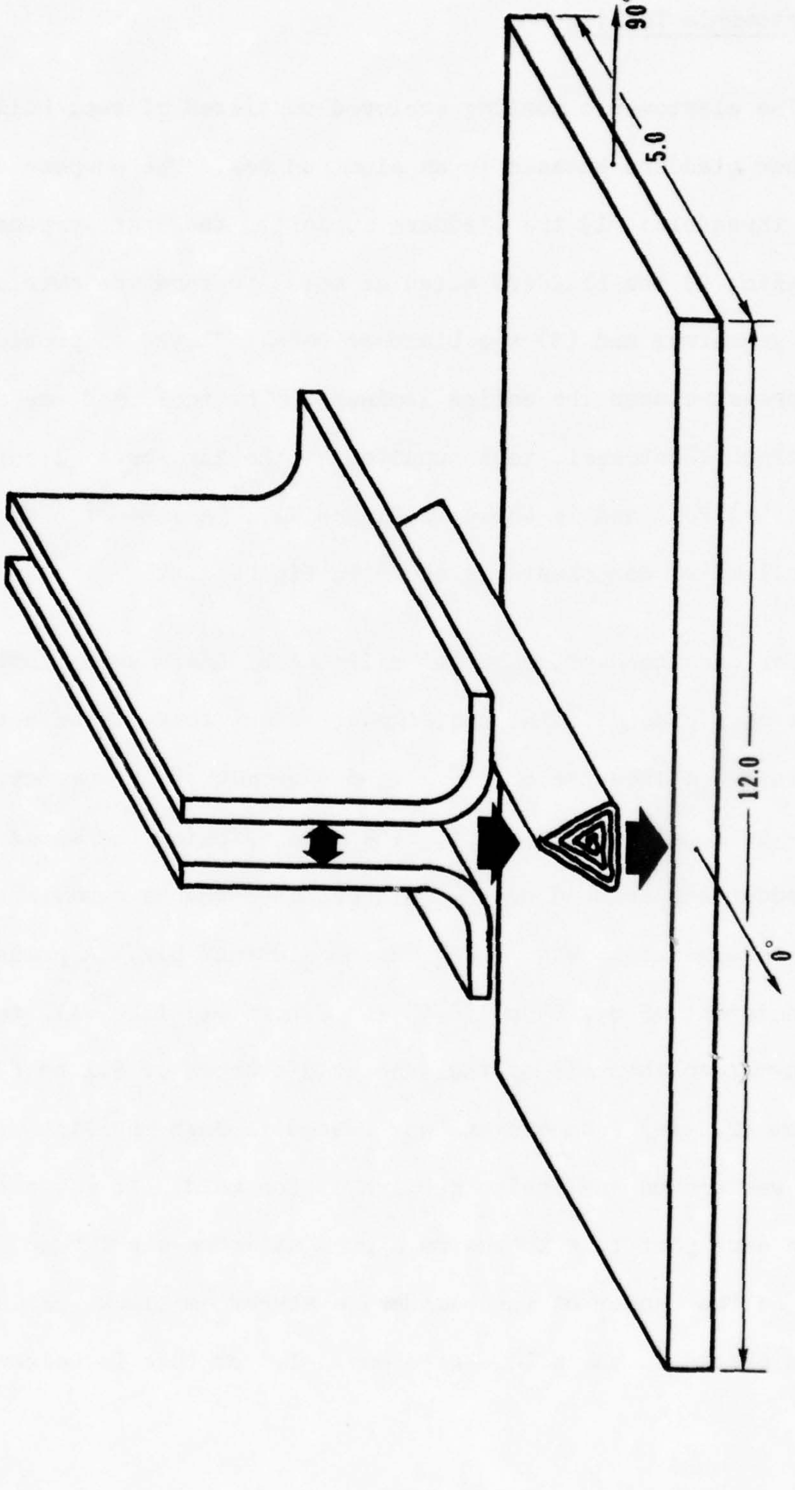

Figure 122: Prepreg Joint Assembly

placed in the elastomeric tool and cured.

C.2 Elastomeric Tooling

The elastomeric tooling employed consisted of two, hollow, silicone rubber bladders encased in an aluminum box. The purpose of the tool was threefold: 1) the bladders supported the spar perpendicular to the wingskin; 2) the bladders acted as molds to form the overlap to the intended geometry; and (3) the bladders were inflated to provide a semi-uniform pressure over the entire laminate. The tool used was a modified version of an elastomeric tool supplied by the Air Force Flight Dynamics Laboratory (AFFDL) and is shown in Figure 123. A schematic of the tool showing all major components is shown in Figure 124.

For each concept, a set of silicone bladders were fabricated such that when placed in the containment vessel they formed a mold conforming to the silhouette of the intended geometry. Construction of the bladders was a multistep process. The mold matching the shape of the desired bladder was created by the void obtained when a dummy specimen of appropriate dimensions was placed in the aluminum box. A pressurization port, consisting of a 0.64 cm (0.25 in) O.D. steel tube with two washers brazed normal to the axis of the tube at distances of 5.1 cm (2.0 in) and 6.4 cm (2.5 in) from one end was placed through one side of the box with the washers on the inside surface of the mold. It was necessary to acid etch each port tube to ensure a good silicone-steel bond. To create the void at the center of the bladder, a styrofoam block was cut such that when placed in the mold, there was a 1.3 cm (0.5 in) clearance, be-

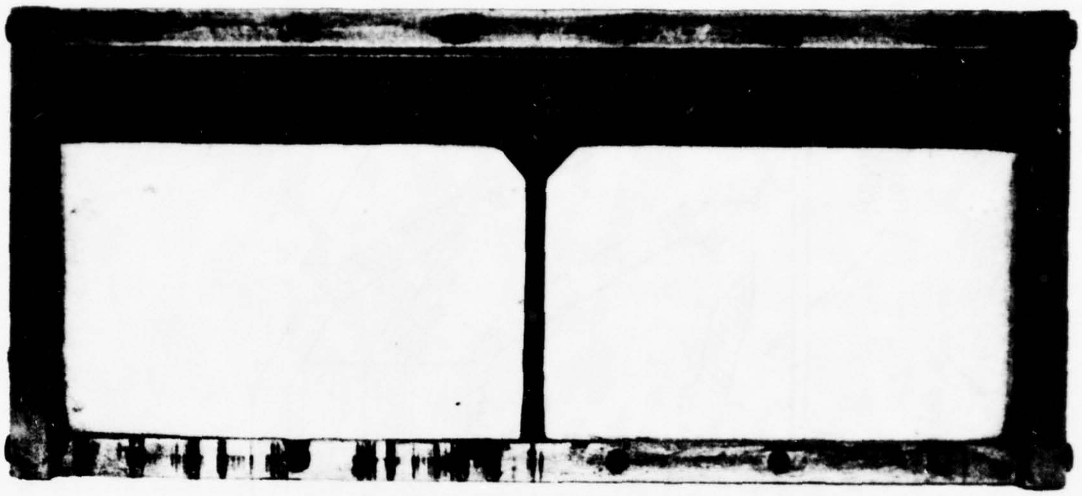

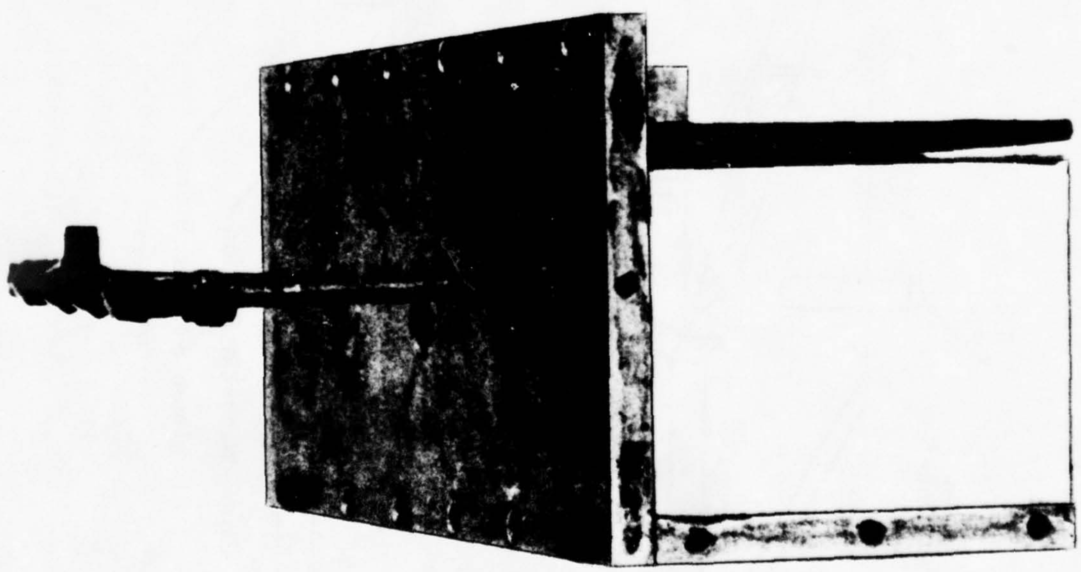

Figure 123: Elastomeric Tool

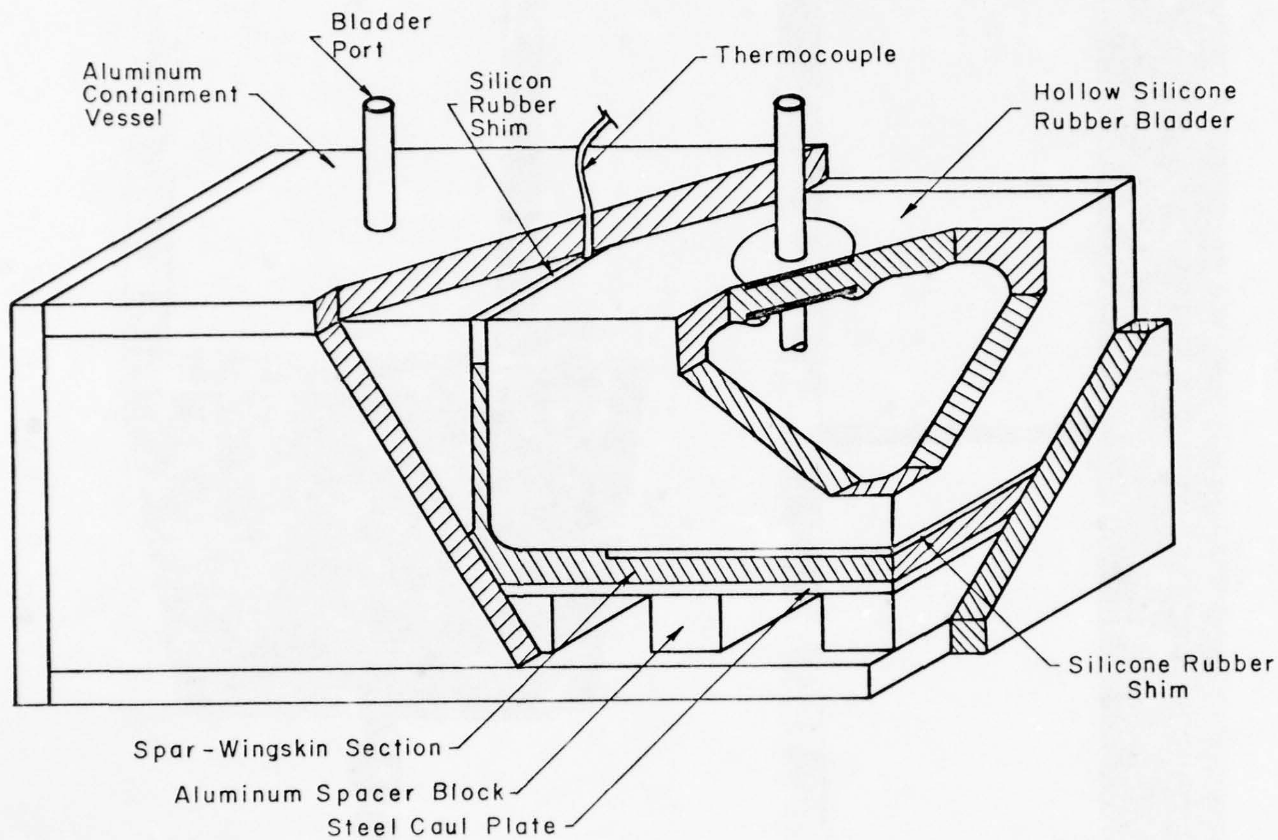

Figure 124: Schematic of Elastomeric Tool

tween block and mold, on all sides. To reduce stress concentrations on the inside surfaces of the bladder, all edges of the styrofoam block were rounded and a groove was placed where the edge of the innermost port washer met the block. With the styrofoam block centered in the mold and pressed over the portion of the port tube extending from the innermost washer, the bladder mold was complete and the bladder could be cast. The material used for casting of the bladder was Dow Corning Silastic® J RTV moldmaking rubber. Initially, only the bottom portion of the mold was filled. This was allowed to cure and thereby provided an anchor for the styrofoam. Following the final casting and complete cure of the bladder, the silicone-styrofoam block was heated to 177°C (350°F) for three hours to melt and consolidate the styrofoam yielding the desired hollow bladder. Any defects or surface imperfections in the bladder were then repaired with Dow Corning 732 adhesive. With the hollow bladders placed in the aluminum box, the elastomeric tool was completed and sample processing begun.

C.3 Material Processing

Following placement of the prepreg spar-wingskin laminate in the elastomeric tool, the laminate was cured in a conventional oven with pressure applied by inflation of the bladders with compressed nitrogen. Prior to placement in the tooling, all surfaces of the specimen were covered with teflon impregnated cloth, TX 1040, and all tool surfaces treated with a mold release agent. Two layers of fiberglass cloth were placed between the lower wingskin and the steel caul plate

(Figure 124) to act as resin bleeders. After insertion of the prepreg specimen in the tool, sheets of silicone rubber were placed where needed (Figure 124) to achieve the desired surface contours. The aluminum box was then fully assembled, placed in the oven, and pressure connections secured. A thermocouple was placed at the center of the top of the spar and was used to monitor sample temperature throughout the cure cycle. Figure 125 is a representative plot of specimen temperature versus time during cure. The recommended cure cycle was employed and is presented in Table 13.

In addition to the above processing, the first two samples processed employed a wingskin prebleed step prior to the joining of the spar, insert and wingskin. To prebleed the wingskin, the uncured laminate was vacuum bagged as indicated in Figure 126 and heated to approximately 93°C (200°F) under a minimum vacuum of 64 cm (25 in) of mercury. Temperature was maintained for one hour and then the sample was cooled. Although this process is necessary for very large laminates of high resin content, it was deemed unnecessary for the laminates used in this research and was consequently discontinued beginning with the processing of the third spar-wingskin section.

Processing of the precured inserts was the same as that given in Table 13 with the exception that the entire mold was vacuum bagged and held at a minimum of 64 cm (25 in) of mercury throughout the cure. Also, the applied pressure in steps 2 and 4 was altered to 482 kPa (70 psi).

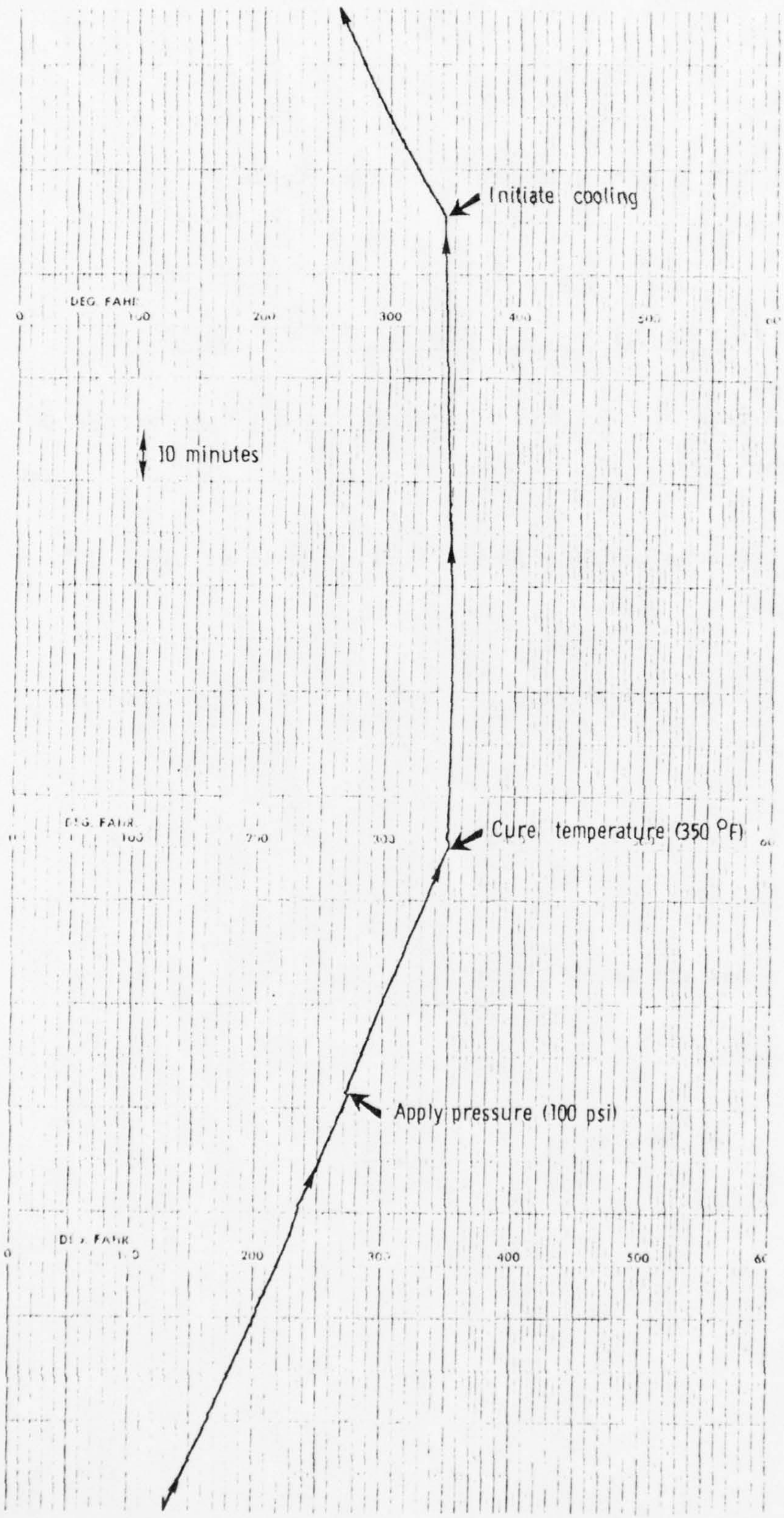

Figure 125: Cure Cycle Temperature versus Time Curve

Table 13: Graphite-Epoxy Cure Cycle

AS 3501-6 CURE CYCLE FOR ELASTOMERIC TOOLING

1. Heat at a rate of 2-3°C/min (3-5°F/min) to a temperature of 135 ± 3°C (275 ± 5°F).

2. Apply a pressure of 690 ± 35 kPa (100 ± 5 psi) at 135 ± 3°C (275 ± 5°F).

3. Heat at a rate of 2-3°C/min (3-5°F/min) to a temperature of 175 ± 3°C (350 ± 5°F).

4. Hold at 690 ± 35 kPa (100 ± 5 psi) and (175 ± 3°C (350 ± 5°F) for 120 ± 5 minutes.

5. Cool to a maximum of 65°C (150°F) in a minimum of 40 minutes.

6. Release pressure.

7. Remove tooling from oven.

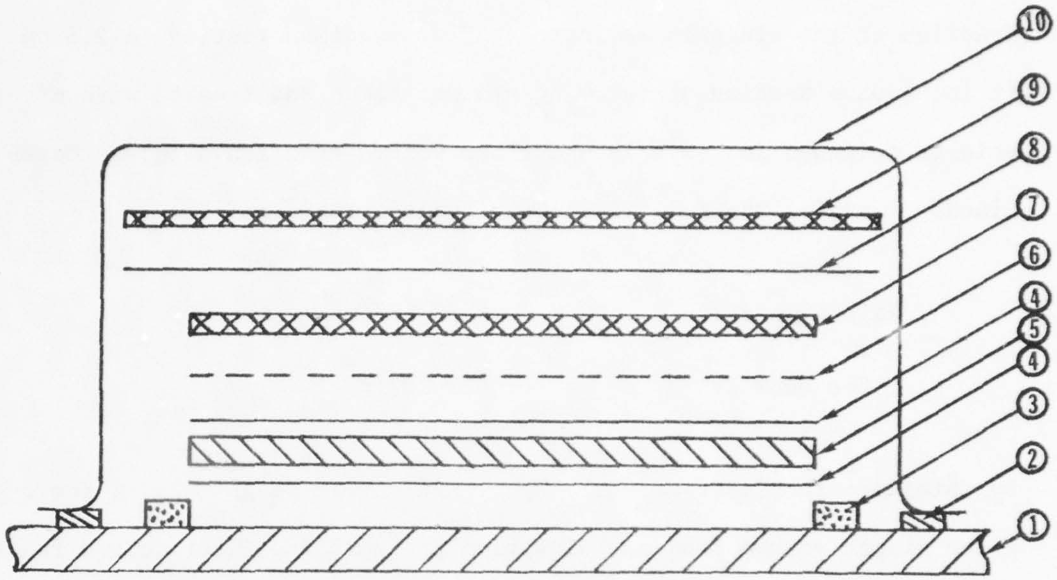

1- Aluminum processing plate

2- Vacuum bag sealer (Tacky Tape)

3- Coraprene cork dam material;must encircle laminate

4- Peel ply cloth;one piece on each side of laminate

5- Prepreg laminate

6- Porous teflon-impregnated cloth (TX1040)

7- 181 glass cloth;one ply of bleeder for every four plies of laminate

8- Clear teflon film;perforated (1 hole/in^2)

9- Vent cloth;181 glass cloth

10- Vacuum bag material

Figure 126: Prebleed Vacuum Bag Schematic

C.4 Fiber Volume Fraction

Chemical matrix digested was used to determine the fiber volume fraction of the wingskin laminate. After specimen testing, a 2.5 cm (1 in) square section of the wingskin was taken and treated with nitric acid as outlined in Table 14 and fiber volume fraction data was determined. Assuming the following constituent properties:

$$\text{matrix density} = \rho_m = 0.0457 \text{ lb/in}^3$$

$$\text{fiber density} = \rho_f = 0.0651 \text{ lb/in}^3 ,$$

by obtaining the fiber weight, W_f , and matrix weight, W_m , for a given sample volume from the digestion process; the fiber volume fraction is

$$v_f = \frac{W_f/\rho_f}{\dfrac{W_f}{\rho_f} + \dfrac{W_m}{\rho_m}}$$

where $\dfrac{W_i}{\rho_i}$ = volume of the i^{th} component for a given sample.

Results indicated an average fiber volume fraction of 0.68 for all specimens tested.

C.5 Test Procedure

Following the joint processing, the 12 × 30 cm (5 × 12 in) spar-wingskin unit was machined into four 2.54 × 30 cm (1.00 × 12 in)

Table 14: Fiber Volume Fraction by Chemical Matrix Digestion

FIBER VOLUME FRACTION BY CHEMICAL MATRIX DIGESTION

1. Take a 2.5 cm (1 in) square sample, and weigh it. Also weigh a dry Buchner funnel with filter.

2. Experimental set-up should be in a vented hood. Put on rubber gloves and goggles, and turn on the hood fan. Place the sample in a 400 mℓ beaker and pour in 200 mℓ of nitric acid; (use glass stirring rod for pouring acid). Heat the beaker with a bunsen burner until acid fumes--avoid boiling. Sample should visibly disintegrate leaving hair-like fibers; this should take about 20 min.

3. Insert the funnel into a large flask attached to a vacuum system. Transfer (wash) the acid and fibers into the funnel, and turn on the vacuum pump. Wash the fibers three times with 20 mℓ nitric acid and then follow with a water wash.

4. Remove the funnel and fibers, and dry in an oven at 100°C for at least 90 minutes. Break up fibers occasionally with a glass rod to facilitate drying. Remove and let cool in dessicator. Weigh funnel and fibers.

test specimens using a precision diamond saw. Each specimen was measured and average dimensions are shown in Figure 127. Specimens were then instrumented with precision strain gages (micro-measurement strain gage EA-06-125AC-350) applied at half and quarter-span points as indicated in Figure 6. The test span for a given specimen was random except that specimens obtained from a single processing cycle were tested at different span lengths. In this way, the influence of any processing variations on joint behavior could be minimized.

An Instron model TTC static testing machine, equipped with a test rig shown schematically in Figure 6, was utilized for all tests. As pictured in Figure 128, the actual test rig consisted of wedge action grips placed 5.7 cm (2.25 in) from the base of the spar applying a tensile load to the joint which was simply supported on two 1.11 cm (0.44 in) diameter steel bars poitioned symmetrically about the spar. The span length was easily adjusted and was maintained at a length of 9.14 (3.6), 15.24 (6.0), 20.32 (8.0) and 25.40 cm (10.0 in) by the horizontal spacer bars. A constant crosshead velocity of 0.25 cm/min (0.1 in/min) was maintained throughout all tests. Load data was recorded continually throughout the test using the test machine's strip chart recorder, and strain data was taken at 5 kg (11 lb) load intervals using a Datran II strain indicator. Crack initiation and propagation was noted by visual inspection during the loading. Ultimate load was taken as the maximum load achieved before catastrophic failure and does not necessarily correspond to the load at first failure or crack initiation.

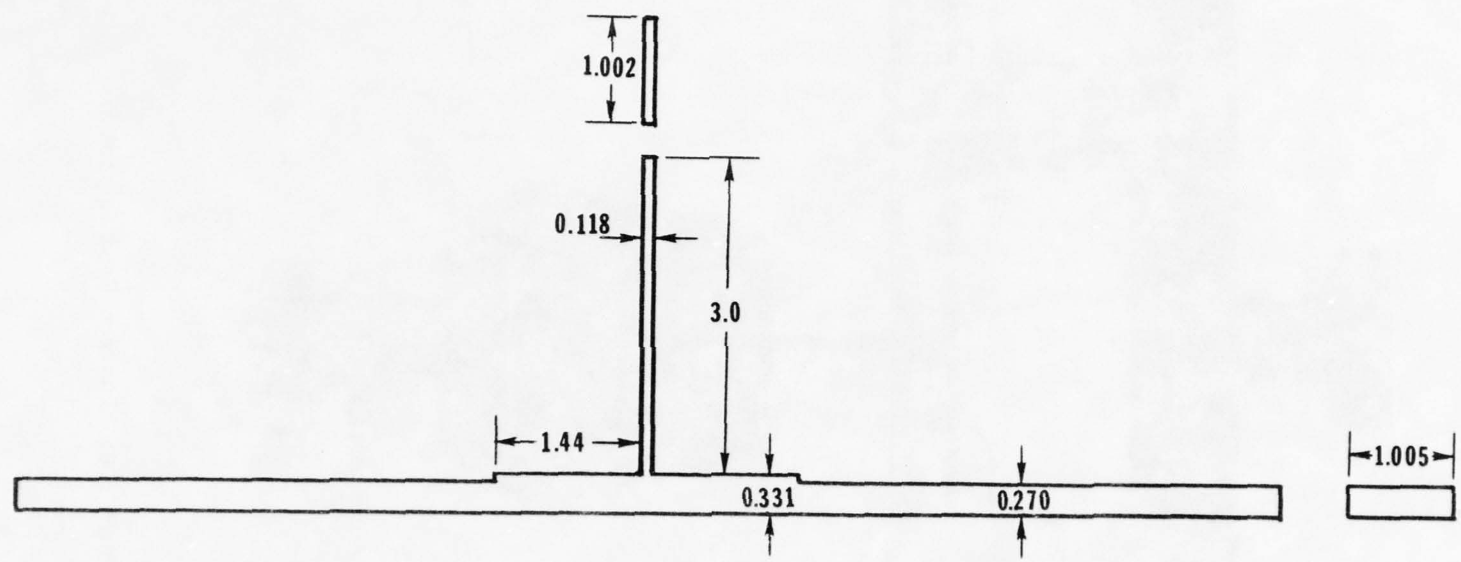

Figure 127: Average Specimen Dimensions

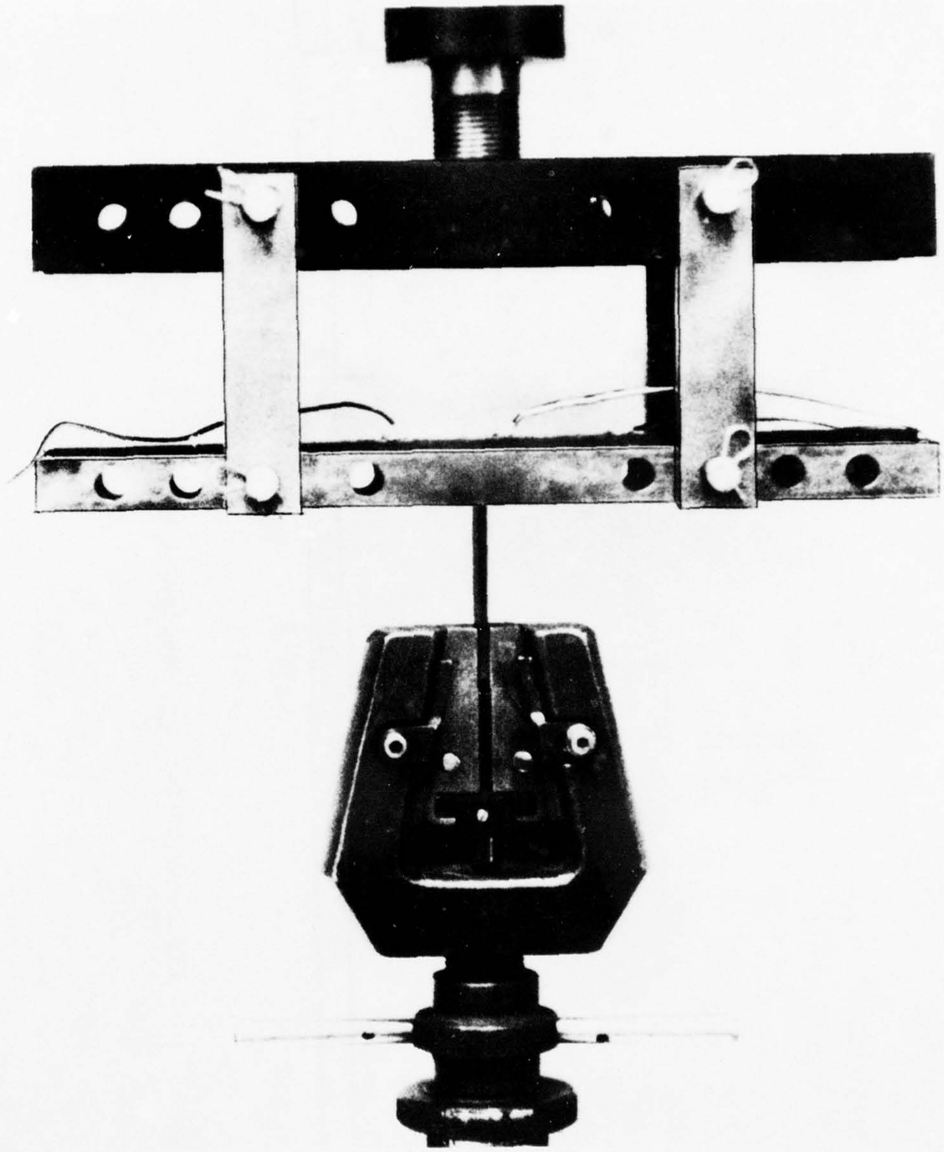

Figure 128: Instron Test Apparatus

C.6 Test Specimen Results

A total of 52 test specimens were fabricated throughout the experimental analysis. Of these, eight specimens were discarded due to the application of insufficient pressure during the cure cycle. Four more specimens were tested but not recorded due to improper, insert surface preparation resulting in complete insert debonding prior to testing. All pertinent information for the remaining 40 samples is shown in Table 15.

As noted in the comment column of Table 15, some wingskin warpage was noted for samples 1-1 through 1-4. This occurred due to movement of the caul plate supports (Figure 124) allowing caul plate, and consequently the skin, to warp when pressure was applied during the cure. These samples were tested, with special care taken, to insure that all wingskin warpage was outside of the test span length.

The fourth cure cycle (samples 4-1 to 4-4) utilized the silicone bladders fabricated for concept "C" and an uncured insert. Upon pressurization, the bladders were forced into a radial geometry matching that of concept "B" and the resulting samples were tested as such. Following this result, all triangular inserts were necessarily precured.

The precured triangular inserts used in the fabrication of samples 12-1, 2, 3 and 4 were made in two steps. The first insert cured for these samples had the proper triangular cross-section except the apex was rounded off. This defective insert was then sanded, cleaned

Table 15: Test Specimen Summary

SAMPLE NUMBER	CONCEPT	SPAN LENGTH (in)	FAIL LOAD (psi)	GENERAL COMMENTS
1-1	A	10.0	236	Radius = 0.25 inches
1-2	A	8.0	334	Wingskin prebled
1-3	A	6.0	398	Some skin warpage
1-4	A	3.6	646	
2-1	A	3.6	523	Radius = 0.25 inches
2-2	A	6.0	361	Wingskin prebled
2-3	A	8.0	292	
2-4	A	10.0	231	
3-1	A	10.0	183	Radius = 0.25 inches
3-2	A	8.0	225	0.4% moisture content
3-3	A	6.0	336	
3-4	A	3.6	306	
4-1	B	8.0	282	Radius = 0.44 inches
4-2	B	6.0	486	Concept "C" bladders used
4-3	B	3.6	937	
4-4	B	10.0	221	
6-1	B	3.6	886	Radius = 0.44 inches
6-2	B	6.0	487	
6-3	B	8.0	344	
6-4	B	10.0	241	
9-1	B	3.6	822	Radius = 0.41 inches
9-2	B	6.0	465	
9-3	B	8.0	307	
9-4	B	10.0	230	
10-1	C	10.0	202	Precured insert
10-2	C	8.0	230	
10-3	C	6.0	266	
10-4	C	3.6	338	
11-1	C	3.6	300	Precured insert
11-2	C	6.0	183	
11-3	C	8.0	169	
11-4	C	10.0	137	
12-1	D	3.6	450	Two piece precured insert
12-2	D	6.0	352	
12-3	D	8.0	251	
12-4	D	10.0	188	
13-1	D	3.6	373	Precured insert
13-2	D	6.0	250	
13-3	D	8.0	195	
13-4	D	10.0	194	

covered with several addition layers of adhesive, and cured a second time. The resulting insert matched the desired cross-section and was utilized in the twelfth spar-wingskin fabrication.

Although samples 3-1 through 3-4 exhibited load-strain responses similar to those for previously tested concept "A" specimens, the ultimate load values were somewhat inferior. Due to the time span between fabrication and testing, and the local atmospheric conditions, the specimen moisture content was indicated as a probable cause for the ultimate load discrepancy. Consequently, the sample was heated to 120°C (250°F) in a vented oven for 24 hours with weight measurements taken every 12 hours. Assuming that the total weight loss equaled the moisture content, a moisture content of 0.4% by weight was determined.

LIST OF REFERENCES

1. J. W. Gillespie, Jr., "Evaluation of the Embedded Spar Composite Design Concept," Master's Thesis, Department of Mechanical and Aerospace Engineering, University of Delaware, Newark, Delaware, (1978).

2. Bathe, K. and Wilson, E., SAP V: A Structural Analysis Program for Static and Dynamic Response of Linear Systems.

3. Advanced Composite Design Guide. Advanced Division (Dayton, Ohio: AFML, 1973), Vol. 1 and 2.

BIBLIOGRAPHY

Advanced Composite Design Guide. Advanced Division (Dayton, Ohio: AFML, 1973), Vol. 1 and 2.

Bathe, K. and Wilson, E., SAP V: A Structural Analysis Program for Static and Dynamic Response of Linear Systems.

J. W. Gillespie, Jr., "Evaluation of the Embedded Spar Composite Design Concept," Master's Thesis, Department of Mechanical and Aerospace Engineering, University of Delaware, Newark, Delaware, (1978).

☆U.S.Government Printing Office: 1979 — 657-002/615